

NASA CR-54118

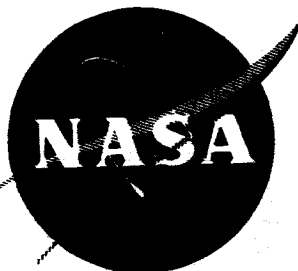
TRW ER-5838

GPO PRICE \$ _____

OTS PRICE(S) \$ _____

Hard copy (HC) \$ 6.00

Microfiche (MF) \$ 1.25



BRAYTON CYCLE SOLAR COLLECTOR DESIGN STUDY

Prepared for
NATIONAL AERONAUTICS AND SPACE ADMINISTRATION
MARCH 1964

CONTRACT NAS 3-2789

| | | |
|-------------------|-------------------------------|------------|
| FACILITY FORM 802 | N 65 14809 | |
| | (ACCESSION NUMBER) | (THRU) |
| | 206 | 1 |
| | (PAGES) | (CODE) |
| | CR 54118 | Q3 |
| | (NASA CR OR TMX OR AD NUMBER) | (CATEGORY) |

TRW

THOMPSON RAMO WOOLDRIDGE INC.
CLEVELAND, OHIO

NOTICE

This report was prepared as an account of Government sponsored work. Neither the United States, nor the National Aeronautics and Space Administration (NASA), nor any person acting on behalf of NASA:

- A.) Makes any warranty or representation, expressed or implied, with respect to the accuracy, completeness, or usefulness of the information contained in this report, or that the use of any information, apparatus, method, or process disclosed in this report may not infringe privately owned rights; or
- B.) Assumes any liabilities with respect to the use of, or for damages resulting from the use of any information, apparatus, method or process disclosed in this report.

As used above, "person acting on behalf of NASA" includes any employee or contractor of NASA, or employee of such contractor, to the extent that such employee or contractor of NASA, or employee or such contractor prepares, disseminates, or provides access to, any information pursuant to his employment or contract with NASA, or his employment with such contractor.

CASE FILE COPY

FINAL REPORT

**BRAYTON CYCLE SOLAR COLLECTOR
DESIGN STUDY**

Prepared for
NATIONAL AERONAUTICS AND SPACE ADMINISTRATION
MARCH 1964

CONTRACT NAS 3-2789

Technical Management
NASA Lewis Research Center
Cleveland, Ohio
Solar and Chemical Power Branch
Thaddeus S. Mroz

TRW
THOMPSON RAMO WOOLDRIDGE INC.
CLEVELAND, OHIO

ABSTRACT

14809

Analyses of solar concentrator performance and thermal and structural requirements are presented along with the specific design recommendation for the Brayton cycle system. Fabrication considerations, which were limited to the stretch-forming technique, are discussed. Small specimen fabrication and inspection results are presented as well as the results of surface error evaluations for a complete stretch-formed solar concentrator.

The resulting recommended design geometry, weight and predicted performance are presented.

Author

FOREWARD

This is the Final Report on Contract NAS 3-2789 covering the period from 26 July 1963 through 10 April 1964. The work performed under this contract was administered under direction of the NASA Lewis Research Center. Technical coordination was provided by members of the NASA Lewis Solar and Chemical Power Branch, Mr. Robert L. Cummings, Head. The report covers the work performed by the Solar Energy Systems Group of TRW Electromechanical Division, New Product Research Department. Mr. Edward S. Kovalcik was the project lead engineer and is the major author of this report. Mr. Charles H. Castle provided assistance in the technical direction and performed the receiver analysis of Section 4.3. The structural analysis work was conducted by Mr. William H. Reinhart and he is the major author of Section 6.0. Mr. Richard R. Reimer performed the analysis and computations for the thermal characteristics of the solar concentrator. Dr. George L. Schrenk, of the University of Pennsylvania, provided consulting services in the use of the IBM 7094 computer program which he developed for solar reflector performance calculations. Analytical investigations of paraboloidal optics and reflective surface characteristic were performed by Dr. H. C. Nash, Consultant to TRW.

TABLE OF CONTENTS

| | | |
|---------|---------------------------------------------------------------------------------------|----|
| 1.0 | INTRODUCTION | 2 |
| 2.0 | SUMMARY | 3 |
| 3.0 | COLLECTOR DESIGN SPECIFICATIONS | 7 |
| 3.1 | Performance Specifications | 7 |
| 3.1.1 | Nominal Cycle Specifications | 7 |
| 3.1.2 | Geometry and Construction Specifications | 7 |
| 3.1.3 | Orientation Specifications | 7 |
| 3.2 | Environmental Specification | 7 |
| 3.2.1 | Shock | 8 |
| 3.2.2 | Vibration | 8 |
| 3.2.3 | Acoustic | 8 |
| 3.2.4 | Acceleration | 8 |
| 3.2.5 | Orbit. | 8 |
| 3.3 | Derived System Requirements | 9 |
| 4.0 | PERFORMANCE ANALYSIS | 10 |
| 4.1 | Concentrator-Receiver Loss Analysis | 10 |
| 4.2 | Concentrator Performance Analysis | 14 |
| 4.2.1 | Optical Accuracy Considerations for the Selection of an Analytical Model | 14 |
| 4.2.1.1 | Geometric Surface Deviations | 14 |
| 4.2.1.2 | Surface Specularity | 18 |
| 4.2.1.3 | Surface Reflectivity | 19 |
| 4.2.2 | Concentrator Theoretical Analysis | 21 |
| 4.2.2.1 | Modified Silvern Analysis | 21 |
| 4.2.2.2 | Generalized Theoretical Analysis of Solar Reflectors | 21 |
| 4.2.2.3 | Concentrator Parametric Study Results | 22 |
| 4.3 | Receiver Performance Analysis | 40 |

TABLE OF CONTENTS (Continued)

| | | |
|---------|----------------------------------------------------------------------------------------------------|-----|
| 4.3.1 | Cavity Reflection Losses | 42 |
| 4.3.2 | Cavity Radiation Losses | 50 |
| 4.3.3 | Total Cavity Loss | 51 |
| 4.4 | Combined Concentrator Receiver Performance | 51 |
| 5.0 | SURFACE ERROR EVALUATION TESTING | 58 |
| 5.1 | Five Foot Diameter Concentrator Inspections | 58 |
| 5.2 | Honeycomb Markoff Investigation | 66 |
| 5.3 | Micrometeoroid Erosion Investigation | 70 |
| 5.3.1 | Specimen and Test Description and Results | 70 |
| 5.3.2 | Experimental Results Discussion | 73 |
| 5.3.3 | Predictions of Solar Mirror Degradation Due to Micrometeoroids | 79 |
| 6.0 | STRUCTURAL ANALYSIS AND DESIGN | 83 |
| 6.1 | Shell Membrane Analysis | 83 |
| 6.1.1 | Geometry | 83 |
| 6.1.2 | Membrane Stresses | 83 |
| 6.1.3 | Membrane Deflections | 86 |
| 6.1.4 | Validity of Membrane Solution | 89 |
| 6.2 | Support Ring Shell Discontinuity Considerations | 89 |
| 6.2.1 | Compatibility Equations | 89 |
| 6.2.2 | Shell Influence Coefficients | 94 |
| 6.2.3 | Ring Influence Coefficients | 94 |
| 6.2.4 | Shell Membrane Displacement and Rotation | 95 |
| 6.2.5 | Solving the Compatibility Equations | 96 |
| 6.2.6 | Shell Distortion Resulting from Temperature Difference Between the Ring and the Shell | 97 |
| 6.3 | Shell Stability | 99 |
| 6.3.1 | Equivalent Single-Thickness Shell for Honeycomb Construction | 99 |
| 6.3.2 | Overall Shell Stability | 101 |
| 6.3.3 | Other Approaches to Counteracting Shell Instability | 107 |
| 6.3.3.1 | Stabilization with Bag and Differential Pressure | 107 |

TABLE OF CONTENTS (Continued)

| | | |
|---------|--------------------------------------------------------|-----|
| 6.3.3.2 | Stabilization with Many Supports | 107 |
| 6.3.3.3 | Stabilization with Central Column | 108 |
| 6.3.3.4 | Rib-Stiffened Shells | 108 |
| 6.3.4 | Local Buckling Considerations | 108 |
| 6.4 | Thermal Stress and Distortion Considerations | 109 |
| 6.4.1 | Shell With Uniform Increase in Temperature | 109 |
| 6.4.2 | Shell With Thickness Temperature Gradient | 112 |
| 6.4.3 | Honeycomb Facing - Adhesive Considerations | 113 |
| 6.5 | The Brayton Cycle Environmental Specification. | 114 |
| 6.5.1 | Shell Instability Loads | 115 |
| 6.5.2 | High Stress Load | 116 |
| 6.5.2.1 | Shallow Shell Fundamental Frequency | 116 |
| 6.5.2.2 | Shock | 117 |
| 6.5.2.3 | Vibration | 117 |
| 6.5.3 | Load Summary | 117 |
| 6.6 | Sizing the Concentrator Shell | 117 |
| 6.7 | Sizing the Support Ring | 119 |
| 6.7.1 | The Inner Ring | 119 |
| 6.7.2 | The Edge Support Ring | 120 |
| 6.8 | Overall Structural Support Considerations | 122 |
| 6.9 | Detailed Design Considerations | 124 |
| 6.9.1 | Design Description | 124 |
| 6.9.2 | Concentrator Weight | 125 |
| 7.0 | ORBITAL THERMAL CHARACTERISTICS ANALYSIS | 126 |
| 7.1 | Concentrator Radiation Environment | 126 |
| 7.2 | Absorbed Radiation | 128 |
| 7.3 | Transient Heat Balance | 136 |
| 7.4 | Thermal Control Design | 141 |

TABLE OF CONTENTS (Continued)

| | | |
|-------|-----------------------------------------------------------------------------------------------|-----|
| 8.0 | FABRICATION CONSIDERATIONS | 145 |
| 8.1 | Sector Fabrication Process | 145 |
| 8.2 | Final Assembly of Full Paraboloid | 149 |
| 8.3 | Tooling | 152 |
| 8.3.1 | Master Tool | 154 |
| 8.3.2 | Assembly Tool | 154 |
| 8.4 | Inspection | 157 |
| 8.5 | Handling and Shipping Considerations | 158 |
| 8.5.1 | Fabrication, Assembly, and Test Handling | 158 |
| 8.5.2 | Shipping | 159 |
| 9.0 | DISCUSSION AND CONCLUSIONS | 161 |
| | REFERENCES | 163 |
| | NOMENCLATURE | 166 |
| | APPENDIX A EFFICIENCY DERIVATION BY LOSS ANALYSIS | 171 |
| | APPENDIX B EXTENSION OF SILVERN'S ANALYSIS | 176 |
| | APPENDIX C AN EXAMPLE OF ACTUAL VERSUS BLACK APERTURE RECEIVER LOSSES | 182 |
| | APPENDIX D COMPUTATION OF CONCENTRATOR SOLAR FLUX INCIDENT ON A RECEIVER SURFACE | 184 |
| | APPENDIX E REFLECTION EFFICIENCY FACTOR DERIVATION | 189 |
| | APPENDIX F BRAYTON CYCLE COLLECTOR WEIGHT ESTIMATE | 191 |

LIST OF FIGURES

| <u>Figure No.</u> | | <u>Page</u> |
|-----------------------|-------------------------------------------------------------------------------------|-------------|
| 1.0-1 | Brayton Cycle Space Power System | 1 |
| 4.2-1 | Sunflower Collector - Individual Characteristics of Surface Deviations | 16 |
| 4.2-2 | Comparison of Measured Distribution with Normal Distribution Models | 17 |
| 4.2-3 | Surface Accuracy Effects Upon Flux in the Focal Plane . . . | 25 |
| 4.2-4 | Surface Accuracy Effects Upon Concentrator Geometric Efficiency | 26 |
| 4.2-5 | Flux in the Focal Plane for Two Dimensional Error Model . . | 27 |
| 4.2-6 | Analytical Model Comparisons | 28 |
| 4.2-7 | IBM 7094 Computer Output Results - 50° Rim Angle | 29 |
| 4.2-8 | IBM 7094 Computer Output Results - 65° Rim Angle | 30 |
| 4.2-9 | IBM 7094 Computer Output Results - 50° Rim Angle 15' Misorientation | 31 |
| 4.2-10 | IBM 7094 Computer Output Results - 65° Rim Angle 15' Misorientation | 32 |
| 4.2-11 | Geometric Efficiency Vs Rim Angle | 33 |
| 4.2-12 | Misorientation Flux in the Focal Plane | 34 |
| 4.2-13 | Misorientation Effects Upon Concentrator Geometric Efficiency | 35 |
| 4.2-14 | Effects of Focal Distance Upon Flux Distribution | 36 |
| 4.2-15 | Effects of Focal Distance Upon Geometric Efficiency | 37 |
| 4.2-16 | Incident Solar Flux Profile on Receiver Brayton Concentrator Receiver | 38 |
| 4.3-1 | Receiver Configurations | 41 |
| 4.3-2 | Sphere Flux Profile and View Factor | 44 |
| 4.3-3 | Cone Flux Profile and View Factor | 45 |

LIST OF FIGURES (Continued)

| <u>Figure No.</u> | | <u>Page</u> |
|-----------------------|------------------------------------------------------------------------------------|-------------|
| 4.3-4 | Cylinder Flux Profile and View Factor | 46 |
| 4.3-5 | Reverse Cone No. 1 View Factor. | 47 |
| 4.3-6 | Reverse Cone No. 3 View Factor. | 48 |
| 4.3-7 | Receiver Reflectivity Efficiency Factor Versus Aperture Diameter | 49 |
| 4.3-8 | Receiver Radiation Loss Versus Aperture Diameter. | 52 |
| 4.3-9 | Cavity Losses Versus Surface Emissivity | 53 |
| 4.4-1 | Concentrator-Receiver Efficiency in the Sun Versus Aperture Diameter | 55 |
| 5.1-1 | Geometric Surface Error Inspection Rig. | 59 |
| 5.1-2 | Inspection Photographs. | 60 |
| 5.1-3 | Geometric Surface Error Inspection Rig Schematic. | 62 |
| 5.1-4 | Distribution of Surface Slope Errors in X and Y Coordinate Directions | 63 |
| 5.1-5 | Circumferential and Radial Error Distribution | 65 |
| 5.2-1 | Honeycomb Markoff Inspection Schematic | 67 |
| 5.2-2 | Proficorder Waviness Inspection Instrument | 68 |
| 5.2-3 | Proficorder Waviness Traces - "As Fabricated" | 69 |
| 5.2-4 | Proficorder Waviness Traces - At Orbital Equilibrium Temperature | 71 |
| 5.2-5 | Honeycomb Markoff Investigation Results | 72 |
| 5.3-1 | Shock Tube Erosion Specimen No. 12 | 74 |
| 5.3-2 | Specimen No. 12 Reflectance | 76 |
| 5.3-3 | Photomicrographs (500 X). | 77 |
| 5.3-4 | Photomicrograph Specimen No. 12 (1800 X). | 78 |
| 5.3-5 | Predicted Area Degradation By Micrometeoroids | 81 |

LIST OF FIGURES (Continued)

| Figure No. | | Page |
|---------------|---------------------------------------------------------------------------------------------------------------------------------------|------|
| 6.1-1 | Paraboloid Geometry | 82 |
| 6.1-2 | Force & Deflection Notation | 84 |
| 6.1-3 | Membrane Forces for Spherical Caps & Paraboloids | 85 |
| 6.1-4 | Membrane Displacement of Spherical Cap Loaded By Its Own Weight | 87 |
| 6.1-5 | Membrane Rotation of Spherical Cap Loaded By Its Own Weight | 88 |
| 6.2-1 | Edge Force and Displacements According to Membrane Theory | 91 |
| 6.2-2 | Membrane Reaction on Ring | 91 |
| 6.2-3 | Sign Convention Attached to Redundant Moment & Force | 92 |
| 6.2-4 | Example of Edge Influence Coefficient | 92 |
| 6.3-1 | Moment of Inertia as a Function of the Ratio of Either Flange Thickness to the Total Flange Thickness | 100 |
| 6.3-2 | Stability of Shallow Spherical Shells | 102 |
| 6.3-3 | Shell Thickness as a Function of Radius of Curvature for Pressure and Acceleration | 105 |
| 6.3-4 | Critical Loads for Large Diameter Concentrators | 106 |
| 6.3-5 | Monocell Buckling Stress | 110 |
| 6.7-1 | Support-Ring Concept | 121 |
| 6.8-1 | Concentrator Support Configurations | 123 |
| 7.1-1 | Incident Energy Levels for 300 Mile Orbit - Front Face and Back Face | 127 |
| 7.1-2 | Incident Receiver Radiation Radial Location at Orbit Time | 129 |
| 7.1-3 | Incident Radiator Energy Versus Radius | 130 |
| 7.2-1a | Total Absorbed Radiation - BTU/Hr for Unit Area at Center of Concentrator of 30' Diameter, 60° Rim Angle 300 NM Orbit | 131 |

LIST OF FIGURES (Continued)

| <u>Figure No.</u> | | <u>Page</u> |
|-----------------------|---------------------------------------------------------------------------------------------------------------------------------------------|-------------|
| 7.2-1b | Total Absorbed Radiation - BTU/Hr for Unit Area at 7.5'R of Concentrator of 30' Diameter, 60° Rim Angle, 300 NM Orbit | 132 |
| 7.2-1c | Total Absorbed Radiation - BTU for Unit Area at Rim of Concentrator of 30' Diameter, 60° Rim Angle, 300 NM Orbit | 133 |
| 7.2-2 | Planetary Radiation View Factor for Unit Area at Rim of Concentrator 30 Ft Diameter, 60° Rim Angle, 300 NM Orbit Front Side. | 134 |
| 7.2-3 | Planetary Radiation View Factor for Unit Area at Rim of Concentrator 30 Ft. Diameter, 60° Rim Angle, 300 NM Orbit Back Side | 135 |
| 7.3-1 | Transient Temperatures - 300 Mile Orbit | 137 |
| 7.3-2 | Transient Temperatures - 24 Hour Orbit | 138 |
| 7.3-3 | ΔT Versus Heat Rate Through Honeycomb in Vacuum | 139 |
| 7.3-4 | Transient Temperatures of Concentrator Honeycomb Construction 300 NM Orbit | 140 |
| 7.3-5 | Steady State Radial Temperature of Concentrator at End of Sun Time 300 NM Orbit. | 142 |
| 7.4-1 | Steady State Radial Temperature of Concentrator at End of Sun Time 300 NM Orbit. | 143 |
| 8.1-1 | Fabrication Sequence | 146 |
| 8.3-1 | Typical Master Tool and Stretch Forming Facility at TRW . | 153 |
| 8.3-2 | Typical Large Capacity Numerically Controlled Milling Machine Installation | 155 |
| 8.3-3 | Assembly Tooling Concept. | 156 |
| 8.5-1 | Typical Crating Concept | 160 |
| C-1 | Appendix C | 182 |
| D-1 | Appendix D | 185 |
| D-2 | Appendix D | 186 |

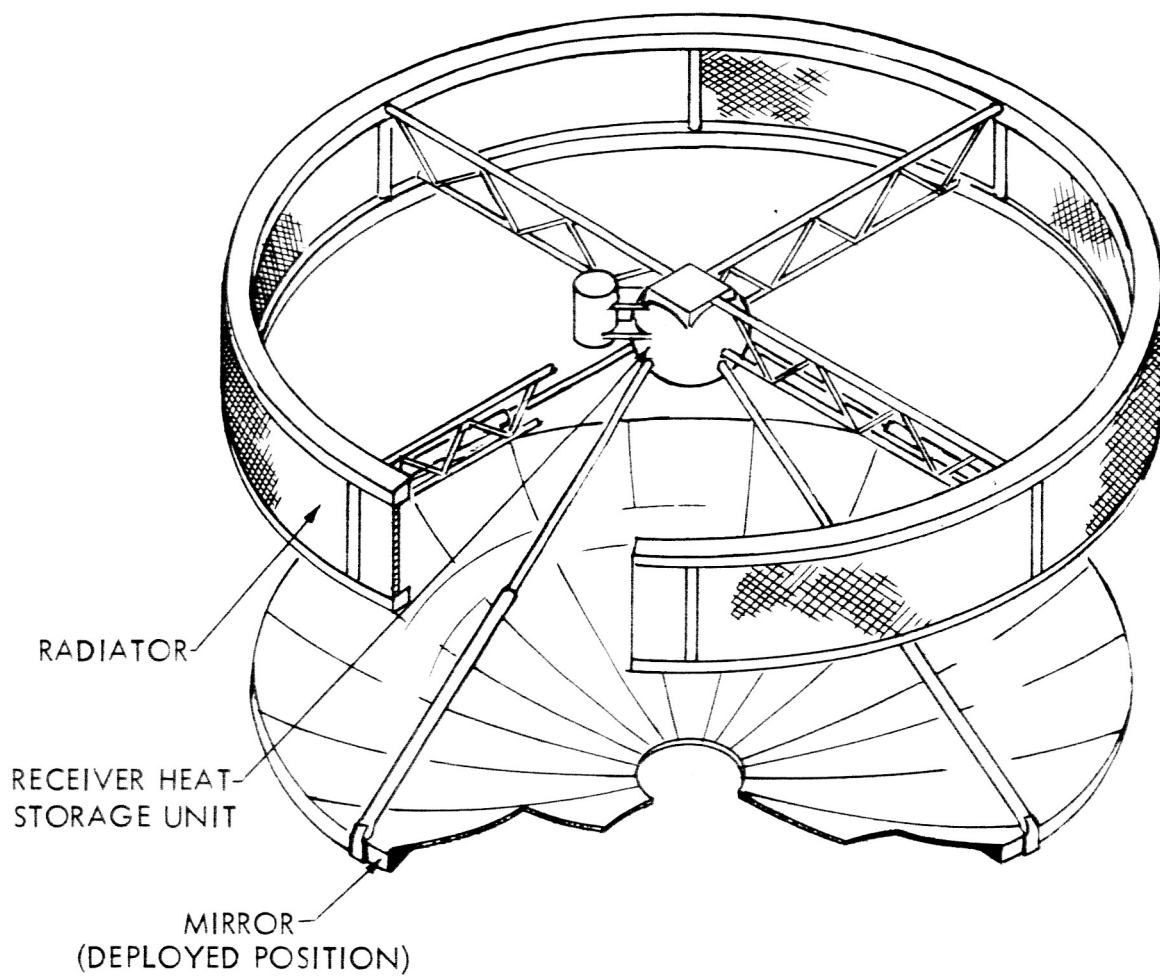
LIST OF FIGURES (Continued)

| <u>Figure No.</u> | | <u>Page</u> |
|-----------------------|----------------------|-------------|
| D-3 | Appendix D | 187 |
| D-4 | Appendix D | 188 |

LIST OF TABLES

| <u>Table No.</u> | | <u>Page</u> |
|------------------|--------------------------------------------------|-------------|
| 2.0-1 | Design Summary | 5 |
| 4.1-1 | Collection Losses (Earth Orbit) | 12 |
| 4.2-1 | Geometric Accuracy | 20 |
| 4.2-2 | Parametric Study Cases | 23 |
| 4.4-1 | Parametric Performance Study Cases | 56 |
| 5.1-1 | Measured Surface Error Characteristics | 64 |
| 5.3-1 | Shock Tube Erosion Results | 75 |
| C-1 | (Appendix C) | 183 |

FIGURE 1.0-1
BRAYTON CYCLE SPACE POWER SYSTEM



1.0 INTRODUCTION

The NASA Lewis Research Center is engaged in evaluating a Brayton cycle space power system utilizing solar energy as the heat source and an inert gas as the working fluid to produce electric power for various space applications. A typical power system concept is shown in Figure 1.0-1 and consists of a paraboloidal solar concentrator, cavity receiver-heat storage unit, turboalternator, radiator, and other heat transfer and control components.

It is seen that the concept utilizes a large single piece mirror to reflect and concentrate the intercepted solar energy. The Saturn S-4B and S-2 stage vehicles allow the system components to be designed as rigid structures with single piece concentrators of 20 ft and 30 ft diameter. The concentrator is nested inside the radiator annulus during launch and deployed to the proper focal length in orbit.

TRW was contracted to perform a design study to investigate one piece, rigid solar collectors employing stretch-formed aluminum construction for this system application.

2.0 SUMMARY

Parametric analysis of the solar concentrator performance and structural requirements was performed and resulted in a specific design recommendation for the Brayton cycle system.

The structural analysis showed that for the specified environmental loadings the structural efficiency of aluminum honeycomb sandwich material makes it a highly desirable structural concept. The resulting design is shown in drawing 818180 (see next page) and consists of a continuous 1/4 inch thick reflector shell made up of light weight aluminum honeycomb sandwich material. This reflector shell is supported at the outer diameter by a continuous flange and web type ring attached to the back of the shell and internally stiffened by honeycomb core material. The honeycomb mirror cross section is made up of an .008 inch stretch-formed aluminum reflective face which is supported by an adhesive bonded aluminum hexagonal cell core and .004 inch aluminum back skin.

It has been shown by specimen fabrication and inspections that with an .008 inch face material and proper fabrication process control, a high optical quality honeycomb structure can be obtained. Thermoelastic analysis and specimen testing with imposed thermal gradients have shown that the orbital thermal environment distortions are well within the optical quality requirements of the Brayton cycle concentrator.

Surface error evaluations for typical stretch-formed concentrators have resulted in the selection of a normal distribution surface error model for parametric performance calculations. Based upon computed results from a generalized theoretical analysis of solar reflectors, an optical geometry was selected and performance characteristics were predicted which include the effects of the cavity receiver configuration.

A summary of the recommended design geometry, weight, and predicted performance is shown in Table 2.0-1.

Fabrication considerations for such a design are discussed and include tooling, process, inspection, and shipping considerations.



TABLE 2.0-1
DESIGN SUMMARY

OPTICAL GEOMETRY

| | |
|-----------------------------------------------------|------------|
| Concentrator diameter | 30 ft. |
| Focal length | 14.25 ft. |
| Rim angle (Nominal) | 55° |
| Optimum aperture diameter | 7.0 inches |
| Nominal area concentration ratio | 2645 |
| Surface slope errors (Predicted) | |
| Maximum (radial) 95% of surface | 12 minutes |
| Maximum (circumferential) 95% of surface | 6 minutes |
| Standard deviation (radial) 68% of surface | 6 minutes |
| Standard deviation (circumferential) 68% of surface | 3 minutes |
| Reflectivity | 90% |

STRUCTURAL DESIGN

| | |
|--------------------------------------|------------------------------------------|
| Aluminum honeycomb sandwich material | |
| Mirror face thickness | .008 inches |
| Core size | 1/4" cell x .0015 wall x 1/4" thk. |
| Back face thickness | .004 inches |
| Support ring design | 8 point support |

WEIGHT

| | |
|-------------------------------|------------------|
| Honeycomb sandwich shell | 224.0 lbs |
| Joints and splices | 33.5 lbs |
| Support ring | 170.0 lbs |
| Total concentrator weight | 427.5 lbs |
| Specific weight (707 sq. ft.) | 0.60 lbs/sq. ft. |

TABLE 2.0-1 (Continued)

PERFORMANCE (AVERAGE)

| | |
|---------------------------------------------------------------------------------------|--------------|
| Misorientation (Anticipated time avg.) | 0.1° |
| Receiver surface temperature (average) | 1700°F |
| Receiver size (hemispherical) | 43.5 sq. ft. |
| Receiver surface absorptivity | 0.73 |
| Receiver surface emissivity | 0.60 |
| Overall blockage efficiency η_B | 94.5% |
| Concentrator geometric efficiency η_G | 97.0% |
| Receiver efficiency η_R | 95.0% |
| Combined concentrator-receiver efficiency (not including external receiver losses) | 79.0% |
| Time average efficiency (sun operation including external receiver losses) | 78.0% |
| Heat into the system and heat storage material for one hour in the sun | 244,820 BTU |

3.0 COLLECTOR DESIGN SPECIFICATIONS

Certain specifications of performance and usage were established as the basis for the study and design of the Brayton cycle solar collector. These specifications were explicitly stated in the study contract or through other communications with NASA, while other considerations were derived from system requirements or evolved from the study efforts.

The following section presents the major specification for which the concentrator was designed.

3.1 Performance Specifications

3.1.1 Nominal Cycle Specifications

| | |
|----------------------------|--------------------|
| Cycle working fluid | - Argon |
| Heat storage material | - Lithium Fluoride |
| Receiver exit temperature | - 1500°F |
| Receiver inlet temperature | - 986°F |

3.1.2 Geometry and Construction Specifications

Rigid construction - stretch formed
One piece structural design
Maximum diameters
 20 foot dia. (S-4B Saturn stage integration)
 30 foot dia. (S-2 Saturn stage integration)
Optical parameters of the collector are to be established so as to maximize system efficiency

3.1.3 Orientation Specifications

Misorientation not to exceed $1/4^\circ$
Time average misorientation - $.1^\circ$ to $.2^\circ$

3.2 Environmental Specification

The environmental conditions which were considered in the design study are

defined in NASA specification No. P0055-1. This specification covers the environments associated with manufacture, storage, transportation, lift-off, boost, orbit and orbital transfer. The major loads and design conditions may be summarized as follows.

3.2.1 Shock

4G to 35G applied along each of three mutually perpendicular axes
7G in orbit along flight-axis

3.2.2 Vibration

| | | |
|----------------|----------------------------|------------------|
| 2 - 10 cps | 0.40 inch double amplitude | } Transportation |
| 10 - 500 cps | 2.0G peak | |
| 16 - 100 cps | 6.0G peak | } Launch |
| 100 - 180 cps | .0118 d.a. | |
| 180 - 2000 cps | 19G peak | |
| 5 - 2000 cps | .25 peak | Orbit |

3.2.3 Acoustic

148 d.b. Re 0.0002 micro bar

3.2.4 Acceleration

7G - along boost axis
3G - along boost axis, opposite direction
4.5G - all directions normal to boost axis

| | |
|--------------------------------------------|---------|
| 3.5G - along boost axis | } Orbit |
| 1.0G - all directions normal to boost axis | |

.18G - nominal lateral due to spacecraft spin (while operating)

3.2.5 Orbit

300 to 20,000 nautical mile earth orbit
10,000 hours orbital life

In addition to these loading specifications, the collectors must be structurally capable of supporting their own weight under a 1-G environment during handling and testing, including a 20° tilt condition from the horizontal, without damage or distortion, during solar testing.

3.3 Derived System Requirements

Based upon overall system considerations the following specifications have been adopted into the design study:

Eight point support for the collector during the launch environments.

Four point support for the collector during the orbital operation.

System structure shadowing of the reflector on a quadrant basis (approximately 6 inch wide trusses).

Receiver internal cavity wall temperatures of 1550°F to 1850°F .

Complete aperture closure during the shade portion of orbit.

4.0 PERFORMANCE ANALYSIS

The performance of a solar energy collection device for the Brayton cycle space power system can be considered as the effectiveness with which the intercepted solar energy is reflected, concentrated, and retained for use in the power system.

A paraboloidal reflector in combination with a cavity receiver has been shown in many previous studies to be the most efficient concept approach and therefore it is the only type of collection device considered in this study.

4.1 Concentrator-Receiver Loss Analysis

The NASA Lewis Brayton cycle power system is based upon the maximum diameter single piece mirror which can be contained in large diameter launch vehicles. For this reason, the loss analysis and resulting efficiency relationships are based upon the maximum nominal area intercepted by this type mirror. The word "nominal" is used in this discussion to convey the fact that the total circular area of a 30 foot diameter concentrator is not really available to the concentrator designer. This total circular area and associated power is only nominally available and the true basis of collection efficiency is the actual power which arrives at the mirror surface after considerations for blockage and/or reflector configurations are made. The maximum nominal power available is,

$$AI_o = \frac{\pi D^2}{4} I_o \quad (4.1-1)$$

At any instant in time while the system is in the sun, the following losses from the maximum nominal power available will occur:

| | |
|------------------------------------------------------|-------------------------|
| Structure blockage (system design loss) | |
| Receiver blockage | } (Receiver losses) |
| Losses from external surfaces | |
| Emission out the aperture | |
| Reflection out the aperture | |
| Absorption during reflection | } (Concentrator losses) |
| Geometric inaccuracy scattering outside the aperture | |
| | |

Losses which occur in the shade portion of orbit are:

Receiver losses from external surfaces

Receiver losses from an open aperture or aperture
closure door - as the case may be

Losses in the shade are not considered in developing the concentrator-receiver efficiency relationships since this is considered to be an orbital mission factor - the losses being large for certain orbital inclinations and zero for full sun orbits. In this way, shade losses for any shade characteristic and shade time can be subtracted from the total power obtained from the sun operation. Also, the efficiencies thus derived have physical significance as an actual measure of performance for any instant in the sun - since they are not weighted by the shade characteristics.

Thus, the overall efficiency of the concentrator-receiver in the sun is defined as

$$\eta = \frac{\text{Net power to the system and heat storage material}}{\text{Maximum nominal power available}}$$

or

$$\eta = \frac{AI_o - L}{AI_o} \quad (4.1-2)$$

The total losses in the sun (L) are made up of the individual losses shown in Table 4.1-1. Typical values are also shown.

From the loss analysis the following expression for concentrator-receiver efficiency was derived (see Appendix A for derivation):

$$\eta = \eta_B \eta_C \eta_R^{-(1-\eta_X)} \quad (4.1-3)$$

where

$$\eta_B = 1 - (1 - \eta_r) - (1 - \eta_s) = \text{total blockage efficiency} = \frac{A_c}{A}$$

TABLE 4.1-1
COLLECTION LOSSES
(EARTH ORBIT)

| Type of Loss | Formula | Typical losses for 30 Ft. Dia Brayton | Typical losses for 20 Ft. Dia Brayton |
|-----------------------------------------------------------------------------|------------------------------------------|---------------------------------------------------------|---------------------------------------------------------|
| Structure blockage | $L_s = A_s I_o$ | 11,500 $\frac{\text{BTU}}{\text{Hr}}$ | 5,110 $\frac{\text{BTU}}{\text{Hr}}$ |
| Receiver blockage | $L_r = A_r I_o$ | 5,560 | 2,470 |
| Receiver ext. surface radiation | $L_x = A_x q_x$ | 2,550 | 1,130 |
| Concentrator absorption | $L_c = \alpha_c A_c I_o$ | 29,560 | 13,140 |
| Concentrator geometric scattering | $L_g = (1 - \eta_g) A_c \rho I_o$ | 7,980 | 3,540 |
| Receiver reflection out aperture | $L_p = (1 - \eta_p) \eta_g A_c \rho I_o$ | 700 | 310 |
| Receiver emission out aperture | $L_E = F_R A_R \sigma T_R^4$ | 9,960 | 4,420 |
| Total Losses | L | <u>67,810 $\frac{\text{BTU}}{\text{Hr}}$</u> | <u>30,120 $\frac{\text{BTU}}{\text{Hr}}$</u> |
| Maximum nominal power available | $P_{\max} = A I_o$ | 312,630 $\frac{\text{BTU}}{\text{Hr}}$ | 138,880 $\frac{\text{BTU}}{\text{Hr}}$ |
| Net Power to the system and heat storage material at any instant in the sun | | 244,820 $\frac{\text{BTU}}{\text{Hr}}$ | 108,830 $\frac{\text{BTU}}{\text{Hr}}$ |

$$\eta_r = \frac{A - A_r}{A} = \text{receiver blockage efficiency}$$

$$\eta_s = \frac{A - A_s}{A} = \text{structure blockage efficiency}$$

$$\eta_x = \frac{AI_o - L_x}{AI_o} = \text{external loss efficiency}$$

$$\eta_R = \frac{\text{net power into cavity walls incl. external losses}}{\text{energy thru the aperture}} = \frac{q_r}{q_l}$$

$$\eta_c = \rho \eta_G = \text{nominal concentrator efficiency}$$

$$\rho = \text{mirror reflectivity to solar radiation}$$

$$\eta_G = \frac{\text{energy thru the aperture}}{\text{total reflected energy}}$$

Equation 4.1-3 represents the efficiency of the Brayton cycle solar energy collection device. The primary parameters for optimizing the system are the concentrator geometric efficiency (η_G) and the receiver retention efficiency (η_R).

It is interesting to note that equation 4.1-3 reduces to,

$$\eta_{CR} = \eta_C \eta_R \quad (4.1-4)$$

For,

$$A_s = 0$$

$$\eta_s = 1$$

$$\eta_x = 1$$

$$\eta_B = \eta_r = \frac{A_c}{A}$$

where

$$\eta_{CR} = \frac{\text{Power collected and retained}}{I_o A_c}$$

which is the classical collector-receiver case.

4.2 Concentrator Performance Analysis

The performance analysis of the Brayton cycle concentrator is concerned with evaluating the concentrator efficiency (η_c);

where,

$$\eta_c = \rho \eta_G = f (\rho , \delta , \beta , \theta , \phi , \alpha')$$

It is seen that the concentrator performance involves geometry, optical accuracy, and the operating environment. Based on these parameters, an analytical model was selected for which a mathematical analysis could be established. Finally, computations were performed to investigate and optimize various parameters.

4.2.1 Optical Accuracy Considerations for the Selection of an Analytical Model

For study purposes, the optical accuracy of the concentrator has been estimated. Optical accuracy will be defined here as:

1. Geometric surface deviations
2. Surface specularity
3. Surface reflectivity

Surface reflectivity is considered as a general reduction in concentrator performance while geometric deviations determine the performance characteristic. Specularity will cause both effects - general reduction and modified performance characteristics.

4.2.1.1 Geometric Surface Deviations

To accurately determine the optical accuracy and associated performance characteristics of a solar concentrator, the magnitude and distribution of geometric surface deviations must be known. The magnitude and distribution are dependent upon both the fabrication and the orbital environment of the concentrator. As an example, Figure 4.2-1 presents the various types of error which were identified for the Sunflower solar concentrator which was fabricated by TRW under contract NAS 5-462. It is seen that both fabrication and environmental deviations were

measured or predicted analytically and that magnitudes and distribution characteristics varied. However, when the associated surface errors were combined algebraically at each radial location the resulting distribution is approximated by a normal distribution (see Figure 4.2-2). This can be expected from the statistical fact that the combination of many random distributions will approach a normal distribution.

An even closer approximation of the normal distribution of surface errors has been observed from the results of optical inspections of the five foot diameter stretch formed concentrator fabricated by TRW under Contract NAS 1-3216. Discussion of these inspection results and the results of other surface error evaluation tests are presented in Section 5.0. Typical normal distribution curves are shown in Figures 5.1-4 and 5.1-5.

Thus a normal distribution of surface errors can be anticipated for the Brayton Cycle concentrator and this error model has been selected for study purposes. A normal distribution of surface errors can be described by a single parameter, σ the standard deviation; and this parameter will be used throughout the study to represent the entire surface quality of various reflectors. To determine the magnitude of the deviations, both the fabrication process and orbital environment will be considered. The fabrication process is discussed in detail in Section 8.0. The following summary can be considered typical for the recommended concentrator design.

Brayton Concentrator Fabrication Process Outline

1. Stretch form front face over tool
2. Vacuum bag front face to tool
3. Apply core blanket and adhesive
4. Apply preformed back face
5. Vacuum bag sandwich and cure
6. Trim cured part
7. Specularity coat sectors
8. Vacuum metallize sectors
9. Assemble sectors into shell, vacuum bag and cure
10. Assemble ring to shell
11. Final assemble concentrator to power system

FIGURE 4.2-1
SUNFLOWER COLLECTOR
INDIVIDUAL CHARACTERISTICS OF SURFACE DEVIATIONS
(REF. 1)

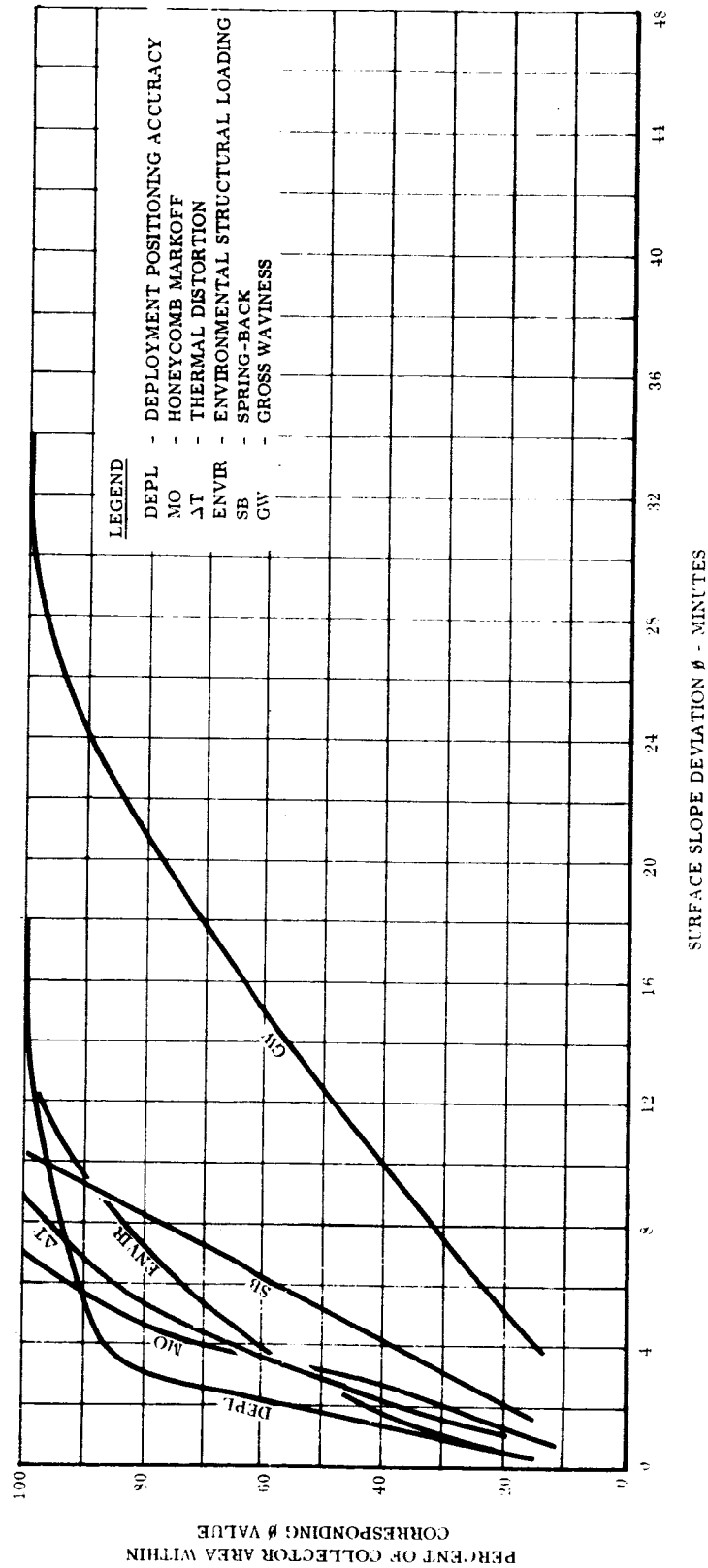
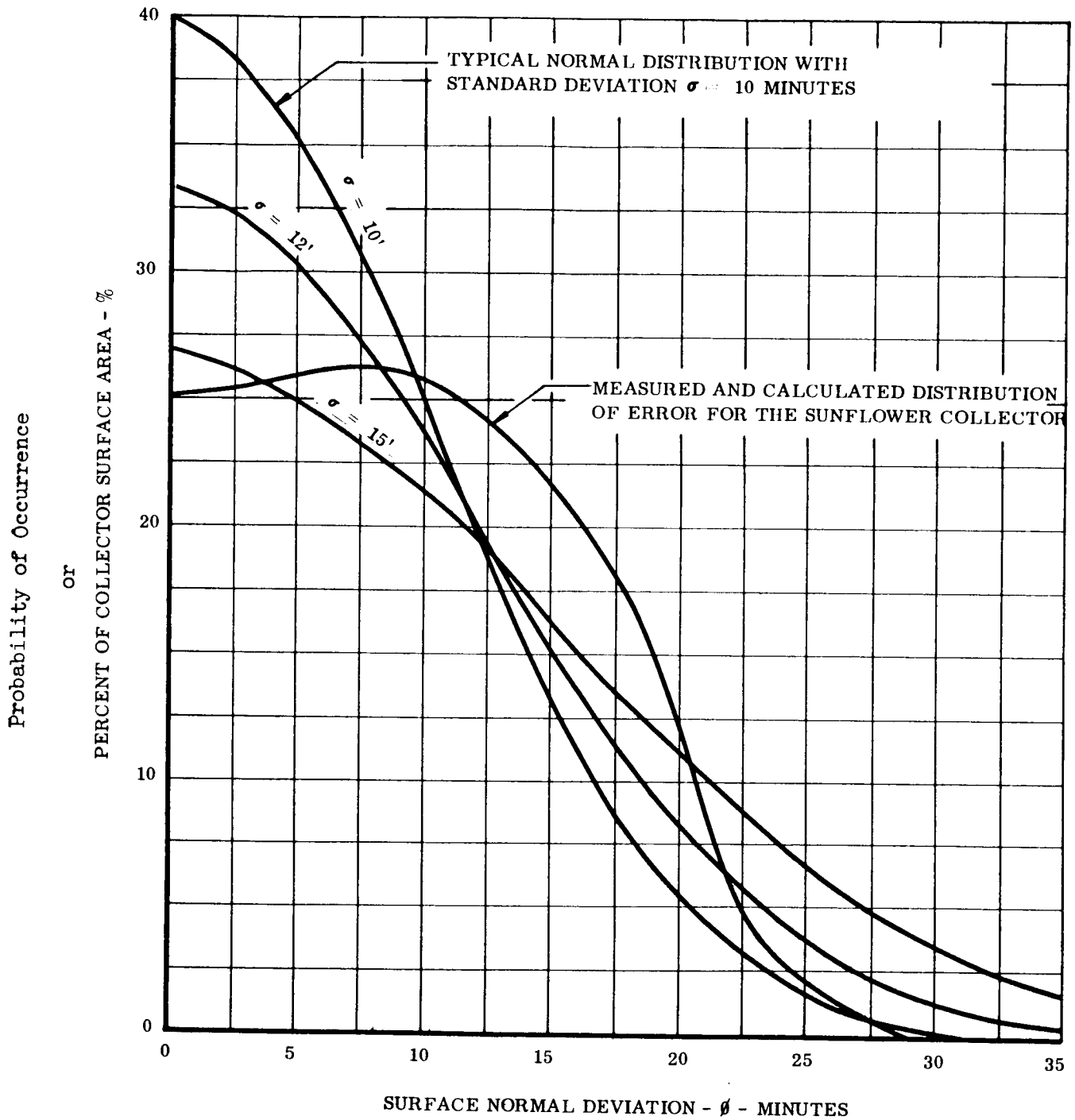


FIGURE 4.2-2
COMPARISON OF MEASURED DISTRIBUTION
WITH NORMAL DISTRIBUTION MODELS
(REF. 1)



From this process and from the results of the surface evaluation tests, the geometric fabrication errors have been estimated and are shown in Table 4.2-1. Environmental errors are also shown. This table presents the maximum estimated errors and the observed distribution characteristics. It is anticipated that, as in the case of Sunflower, the combination of these errors will result in a normal distribution representation of the Brayton concentrator optical quality. Also, it is assumed that the angular errors (ϕ_{\max}) will not necessarily combine directly but some will cancel others. The magnitude of the combined error, therefore, has been estimated from the combined normal distribution errors only, viz., master tooling errors (9'), stretch replication errors (6'), and assembly errors (3'). Assuming that this total maximum error (18') represents 95% (equal 2σ) of the surface area, then a standard deviation of 9' would represent the surface accuracy. This model has been extrapolated from existing inspection and test information and it is believed to be well within the present capabilities of the stretch formed aluminum concentrator technology. This model can also be considered to include the environmental errors of thermal distortion and other localized errors which involve small portions of the collector surface area and therefore are represented analytically in the tail of the normal distribution curve. Estimates of the higher geometric accuracy attainable with developmental improvement are also presented in Table 4.2-1.

It also might be pointed out that one of the basic conclusions determined from the five foot diameter concentrator inspections is the apparent relationship of the radial to circumferential error distributions. These results are shown in Figure 5.1-5 and the approximate 2:1 relationship has been assumed for the Brayton concentrator study purposes.

4.2.1.2 Surface Specularity

Specularity is defined as the amount and distribution of scattering of light when reflected by a surface. For aluminum reflecting surfaces, specularity has been improved by a thin epoxy coating before vacuum metallizing.

Thin sheet aluminum materials, similar to those recommended for construction of the Brayton concentrator, have been epoxy coated and aluminized successfully at TRW. Goniometric measurements of specularity (see reference 1) using a

monochromatic light source and a photo tube pickup has shown the reflector surface displays approximately a normal distribution of scattering with a standard deviation of less than 3 minutes. With a refined process, higher specularity is anticipated with a corresponding lower representative standard deviation (less than one minute); therefore, it is assumed that the nonspecular component of reflected light is well within the previously established surface accuracy model.

4.2.1.3 Surface Reflectivity

After obtaining a highly specular surface, a vacuum evaporated pure aluminum layer is provided to obtain maximum reflectivity. Reflectivity measurements have been made of typical thin aluminum specimens utilizing the facilities of the Thermal Radiation Laboratory at Space Technology Laboratories, Inc. Near normal direction total reflectance measurements are obtained with a modified Beckman DK-2A integrating sphere reflectometer; while the "diffuse" component of the reflectance is measured in a Gier-Dunkle integrating sphere at selected wave lengths within the solar spectrum. This "diffuse" component might be termed "gross diffuse" when compared to the previously discussed specularity considerations ($\sigma = 1'$ to $3'$) since the integrating sphere picks up non-specularity outside several angular degrees. Thus the information obtained from these combinations of measurements covers the full range of specularity and reflectance - with the small nonspecular characteristics being represented by a normal distribution and the measured "gross diffuse" being considered a general reduction in total reflectivity.

Measurements of typical specimens show that a reflectivity value of 90% (integrated over the solar spectrum) can be obtained and this value will be used for study purposes.

Finally, space degradation of reflectivity or specularity by vacuum, radiation, or micrometeoroid erosion is not well defined at this time and will not be considered in the present performance calculations. A discussion of investigations performed in this area are presented in Section 5.3.

TABLE 4.2-1
GEOMETRIC ACCURACY

| | | BRAYTON COLLECTOR ESTIMATED ERRORS | | | |
|------------------------------------------|----------------------------------------------------------------|------------------------------------|--------------------|-------------------------------------|-------------------------------------------------|
| | | | ϕ MAX. (95%) | | REFERENCE |
| | | DISTRIBUTION | PRESENT TECHNOLOGY | WITH DEVELOP. IMPROVEMENTS | |
| FABRICATION ERRORS | MASTER TOOLING ERRORS | NORMAL DISTRIBUTION | 9' | 6' | SPIN CAST OR NUMERICALLY MACHINED |
| | STRETCH REPLICATION ERRORS | NORMAL DISTRIBUTION | 6' | 4' | 60" LANGLEY (TABLE 5.1-1) (SCALING FACTOR 2.5X) |
| | SANDWICH SPRINGBACK | SHELL FLATTENING | SMALL | SMALL | ASSUMED |
| | HONEYCOMB MARKOFF ERRORS | UNIFORM | < 1/2' | < 1/4' | TEST SPECIMENS (FIGURE 5.2-5) |
| | TRIMMING & SEAM DISTORTION | LOCALIZED (2% OF AREA) | 6' | 4' | 60" LANGLEY (TABLE 5.1-1) |
| | ASSEMBLY POSITIONING ERRORS ASSEMBLY SPRINGBACK OR WAVINESS | NORMAL DISTRIBUTION | 3' | 2' | 60" LANGLEY (TABLE 5.1-1) |
| | FINAL ALIGNMENT ERRORS | CONSTANT | 1' | 1' | TOOLING ALIGNMENT |
| ENVIRONMENTAL ERRORS | THERMAL DISTORTION | | | | |
| | TEMPERATURE GRADIENT THRU THICKNESS | LOCALIZED AT RIM | .33' / °F | | THERMOELASTIC ANALYSIS (SECTION 6.4.2) |
| | RADIAL TEMPERATURE GRADIENT | UNIFORM | SMALL | | THERMOELASTIC ANALYSIS (SECTION 6.4.1) |
| | CIRCUMFERENTIAL TEMPERATURE GRADIENT | | NEGLIGIBLE | | THERMAL MAP CLACULATIONS (SECTION 7.2) |
| | RING-SHELL GRADIENT | LOCALIZED AT RIM | .45' / °F | | THERMOELASTIC ANALYSIS (SECTION 6.2.6) |
| | HONEYCOMB CELL THERMAL MARKOFF | UNIFORM | NEGLIGIBLE | | TEST SPECIMENS (FIGURE 5.2-5) |
| | CREEP DUE TO LONG TERM THERMAL CYCLING | UNIFORM STRAIN | NEGLIGIBLE | | CREEP LITERATURE (REF. 36) |
| | DEPLOYMENT POSITIONING | FOCAL LENGTH CHANGE | ± 1/2" ALLOWABLE | | PERFORMANCE ANALYSIS (SECTION 4.2.2.3) |
| SPACECRAFT SPIN INERTIAL LOAD DISTORTION | NON SYMMETRICAL | .000131 IN/G | | STRUCTURAL ANALYSIS (SECTION 6.1.3) | |
| ESTIMATED COMBINED ERROR DISTRIBUTION | | | | | |
| | STANDARD DEVIATION (RADIAL) σ _r | | 9' | 6' | |
| | STANDARD DEVIATION (CIRCUM) σ _c | | 4.5' | 3' | |
| | MAXIMUM DEVIATION ϕ max | | 18' | 12' | |

4.2.2 Concentrator Theoretical Analysis

It is seen in the previous sections that the normal or Gaussian distribution of surface errors has been established as the analytical model for the Brayton concentrator. Several methods of mathematical analysis of paraboloidal reflectors have been investigated during the study portion of the program.

4.2.2.1 Modified Silvern Analysis

Early in the study program, a literature survey showed that a differential equation had been developed by Silvern (2) for the energy distribution on the focal plane of paraboloidal mirrors as a function of a normal distribution of surface errors. To simplify the integration of the equation, Silvern neglected the misorientation terms and made several other broad small angle assumptions.

Appendix B presents the analytical work which was performed during the present study to solve Silvern's equation including misorientation and solar image parameters. The equation was successfully solved by explicit integration of one term and numerical integration of the remaining double integral over the solar disk.

Computed results for this analytical approach will be presented in Section 4.2.2.3 for comparison with an alternate approach.

4.2.2.2 Generalized Theoretical Analysis of Solar Reflectors

During the study program, a new and useful analytical tool became available, which consists of a generalized mathematical model of solar reflectors and an operative computer program for the model (3) (4). This model was developed by Allison in conjunction with the Aerospace Corporation for the Air Force.

It was decided to adopt this analytical tool for the Brayton cycle solar collector study program in order to accelerate calculations and because the accuracy and potential of this analysis is superior to the initial modified Silvern approach.

Dr. G. L. Schrenk, the principal author of the analysis, was contracted for consulting services, and a copy of the program was obtained from the Aerospace

Corporation. The TRW computer facilities which are available at TRW Space Technology Laboratories were utilized to compute the parametric study results.

The generalized analysis consists of a set of equations for determining the energy flux on any arbitrarily shaped focal surface from any arbitrarily shaped reflector surface; and it includes provisions for treating random reflector surface errors (including normal distribution), orientation errors, and vignetting of reflected radiation by a cavity opening. The computer programs evaluate these equations and print out the flux concentration on the focal surface and the fraction of total incident energy collected within various aperture diameters (η_g). For a detailed description of the theoretical development and the computer programs, see reference (4).

4.2.2.3 Concentrator Parametric Study Results

Upon the selection of the normal distribution analytical model and the adoption of the generalized mathematical analysis, a parametric study was established to investigate the following:

1. Surface accuracy
2. Concentrator diameter
3. Concentrator rim angle
4. Misorientation
5. Misplacement of the receiver
6. Receiver characteristics

Concentrator Diameter Considerations

The cases shown in Table 4.2-2 were computed for the 30 foot diameter Brayton concentrator. Since the same range of surface deviations can be assumed for the 20 foot Brayton concentrator, the results are plotted showing a dimensionless scale and also scales representing 20 and 30 foot diameter concentrators.

Surface Accuracy Comparisons

Surface accuracy for the normal distribution model is represented by the parameter σ which is the standard deviation (statistically, 68 per cent of the reflector surface area has smaller angular errors than the standard deviation).

TABLE 4.2-2
PARAMETRIC STUDY CASES

| <u>Rim Angle</u> | <u>Radial Std. Dev.</u> | <u>Circum. Std. Dev.</u> | <u>Misorien.</u> | <u>Focal Plane Misplacement (Axial)</u> |
|------------------|-----------------------------|------------------------------|------------------|---------------------------------------------|
| 45° | 9' | 0 | 0 | 0 |
| 50° | 9' | 0 | 0 | 0 |
| 55° | 9' | 0 | 0 | 0 |
| 60° | 9' | 0 | 0 | 0 |
| 65° | 9' | 0 | 0 | 0 |
| 70° | 9' | 0 | 0 | 0 |
| 50° | 9' | 0 | .25° | 0 |
| 60° | 9' | 0 | .25° | 0 |
| 65° | 9' | 0 | .25° | 0 |
| 55° | 9' | 4.5' | 0 | 0 |
| 55° | 9' | 4.5' | .25° | 0 |
| 55° | 6' | 3' | 0 | 0 |
| 55° | 6' | 3' | .25° | 0 |
| 55° | 6' | 0 | 0 | 0 |
| 55° | 6' | 0 | .25° | 0 |
| 55° | 0 | 0 | 0 | 0 |
| 55° | 0 | 0 | .25° | 0 |
| 55° | 4' | 0 | 0 | 0 |
| 55° | 4' | 0 | .25° | 0 |
| 55° | 6' | 3' | .10° | 0 |
| 55° | 6' | 3' | .5° | 0 |
| 55° | 6' | 3' | 0 | + .5" |
| 55° | 6' | 3' | 0 | +1.0" |
| 55° | 6' | 3' | .25° | +1.0" |

The effect of varying surface accuracy is seen in Figure 4.2-3 and 4.2-4 by considering only the radial standard deviations. When a two dimensional error model is considered, the flux characteristic is modified as shown in Figure 4.2-5. As mentioned previously, these results were computed using the generalized mathematical analysis and computer program. For comparison, Figure 4.2-6 shows a case computed from the modified Silvern analysis. Since the Silvern surface error model is actually a two dimensional model, no direct comparison was obtained at this time. All the remaining results presented in this section will be those computed from the generalized mathematical analysis.

Concentrator Rim Angle Optimization

To investigate the effect of concentrator focal length, and therefore rim angle, a series of cases which varied only this parameter were computed. Results for variations in rim angle are shown in Figures 4.2-7 and 4.2-8. These are reproductions of the actual computer data read-out sheets from the IBM 7094 computations for the generalized analysis. It can be seen that the results are tabulated, using floating decimal form, for the fraction of energy collected (η_G) at various aperture sizes in inches for the 30 foot diameter concentrator. Also, rough plots of the efficiency curve are printed out. Results for misoriented cases are shown in Figures 4.2-9 and 4.2-10.

Using these tabulated results, the maximum concentrator geometric efficiency range can be seen in Figure 4.2-11. This is a plot of geometric efficiency versus concentrator rim angle for various aperture sizes in the range of interest. It is seen that efficiency is maximized for this error model in the range of 53° to 55° even when the misoriented case is considered. It should be noted that geometric efficiency varies by only several per cent between 45° and 60° ; however, to maximize efficiency and based upon stowage considerations, a rim angle of 55° was selected for the Brayton concentrator configuration.

Rim angle optimization based upon concentrator geometric efficiency alone is a valid study approach since, as will be shown in Section 4.3, reflection losses from the cavity are small.

FIGURE 4.2-3
SURFACE ACCURACY EFFECTS
UPON FLUX IN THE FOCAL PLANE

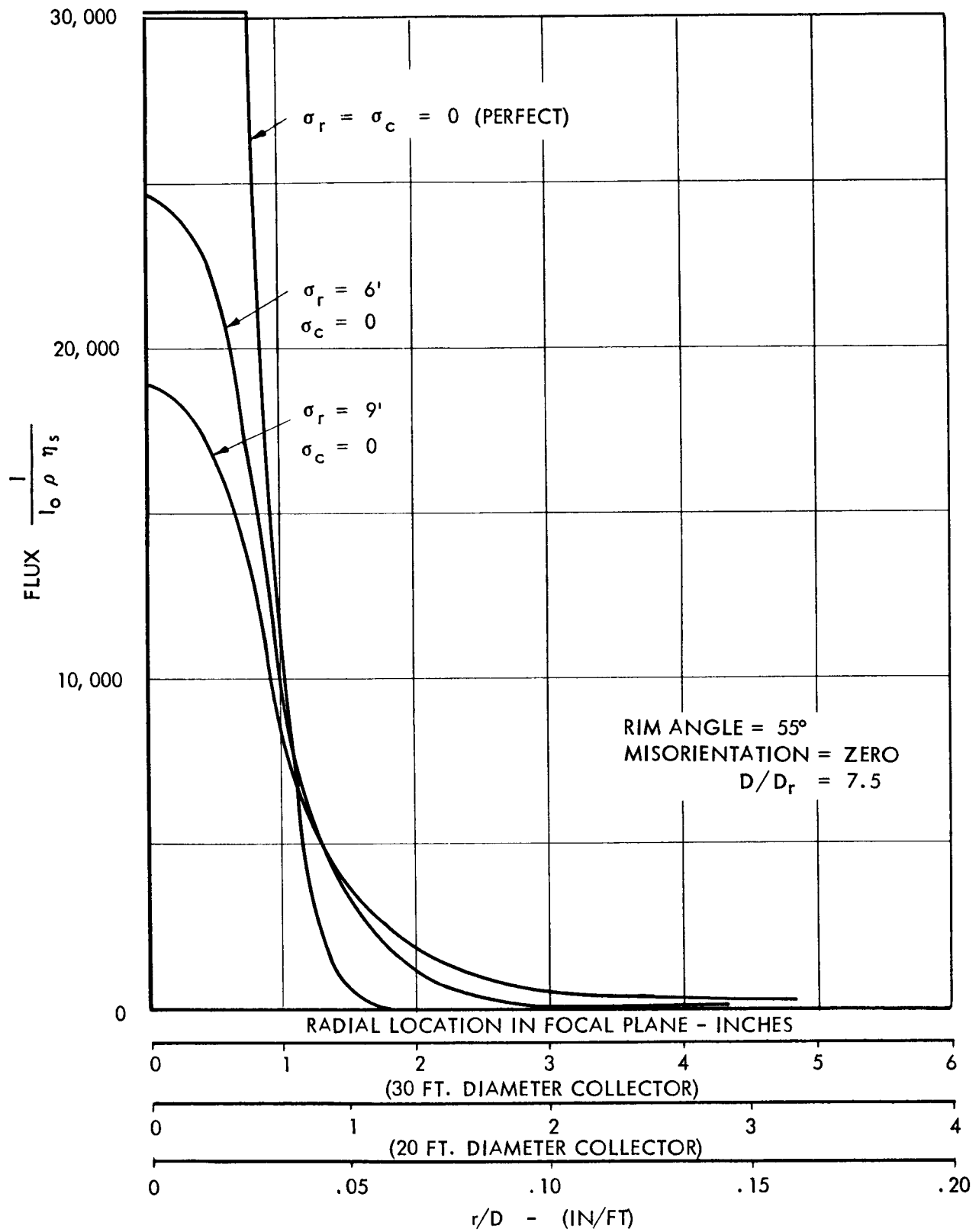


FIGURE 4.2-4
SURFACE ACCURACY EFFECTS UPON CONCENTRATOR GEOMETRIC EFFICIENCY

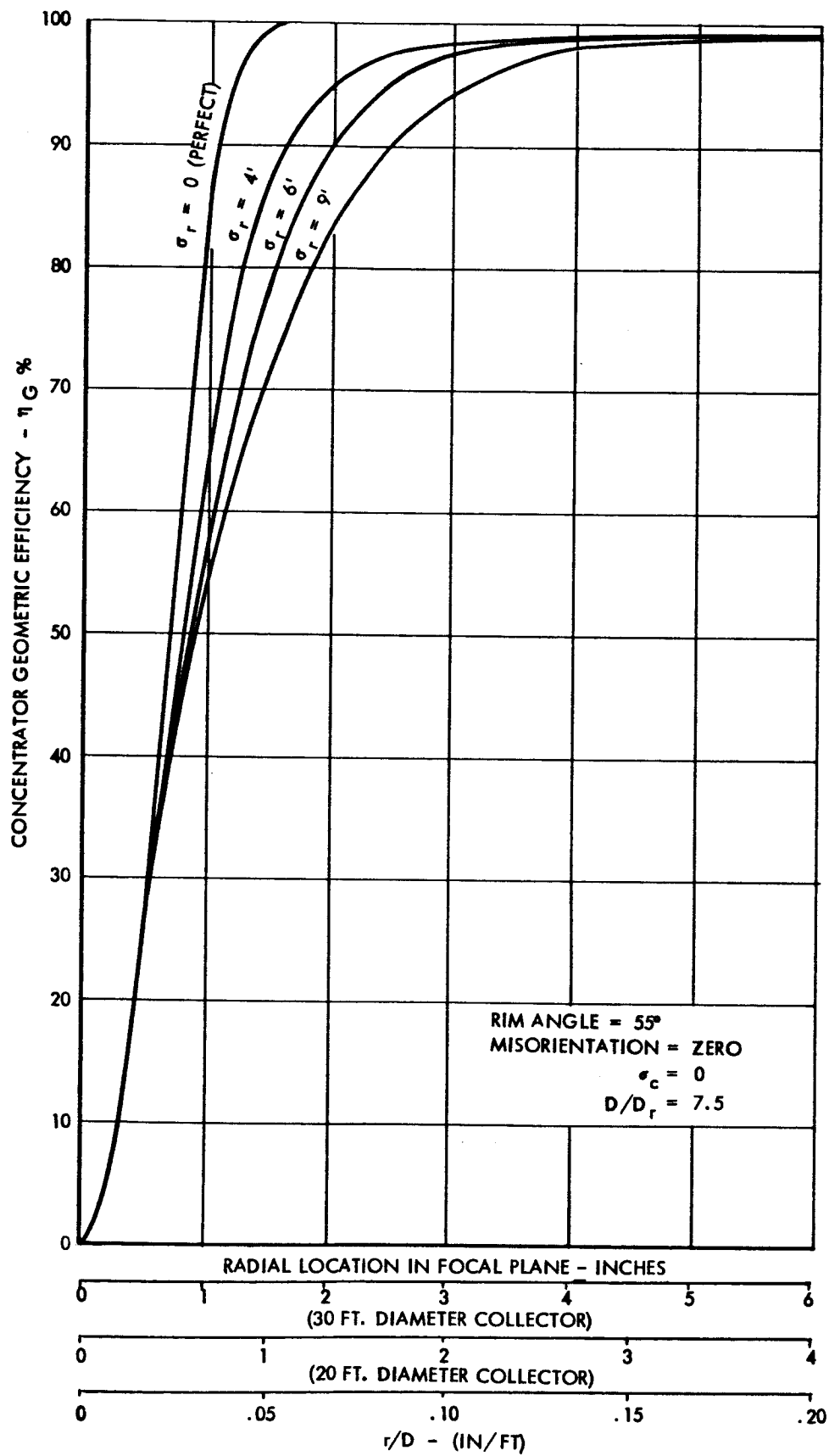


FIGURE 4.2-5

FLUX IN THE FOCAL PLANE
FOR TWO DIMENSIONAL ERROR MODEL

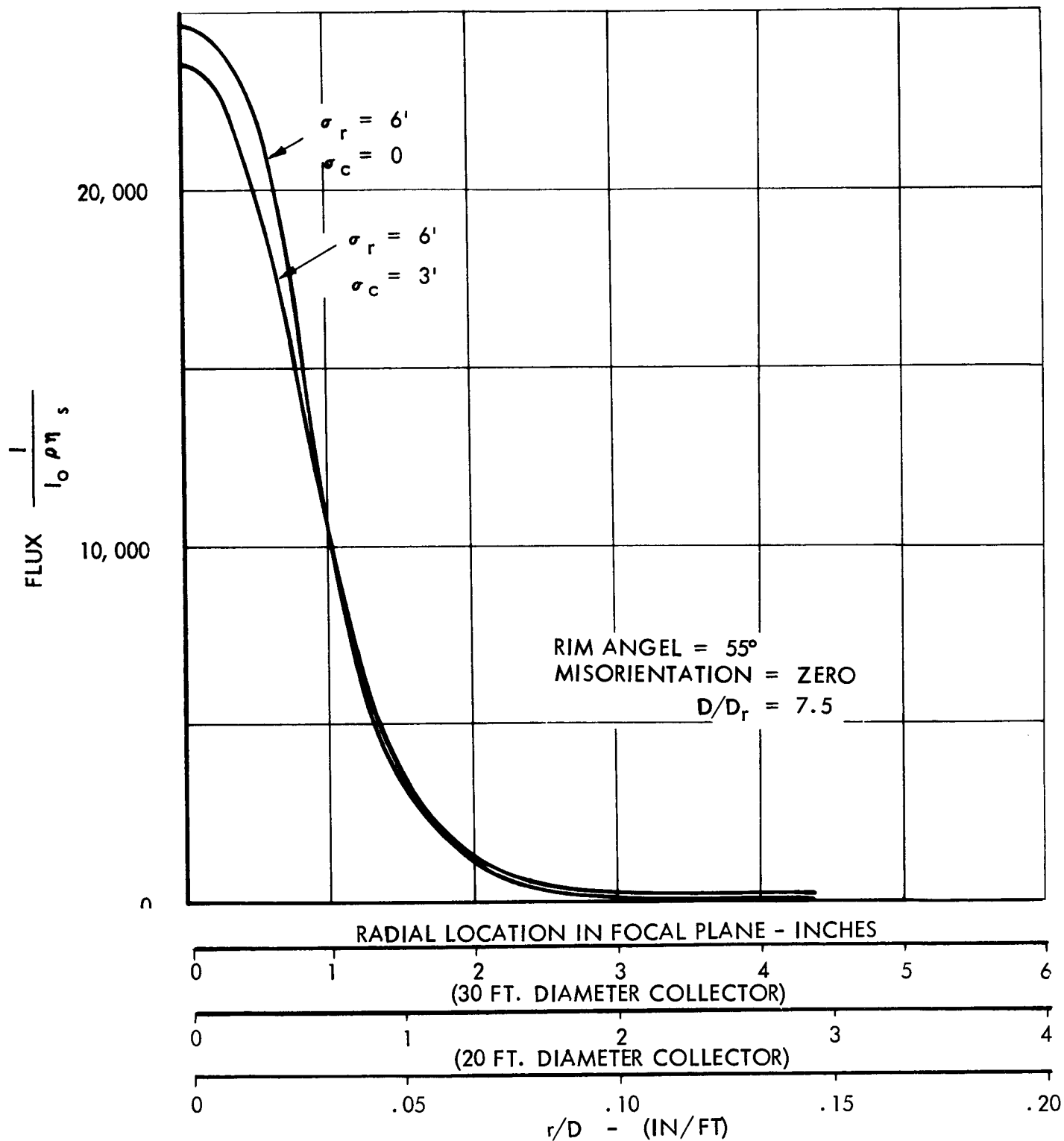


FIGURE 4.2-6
ANALYTICAL MODEL COMPARISONS

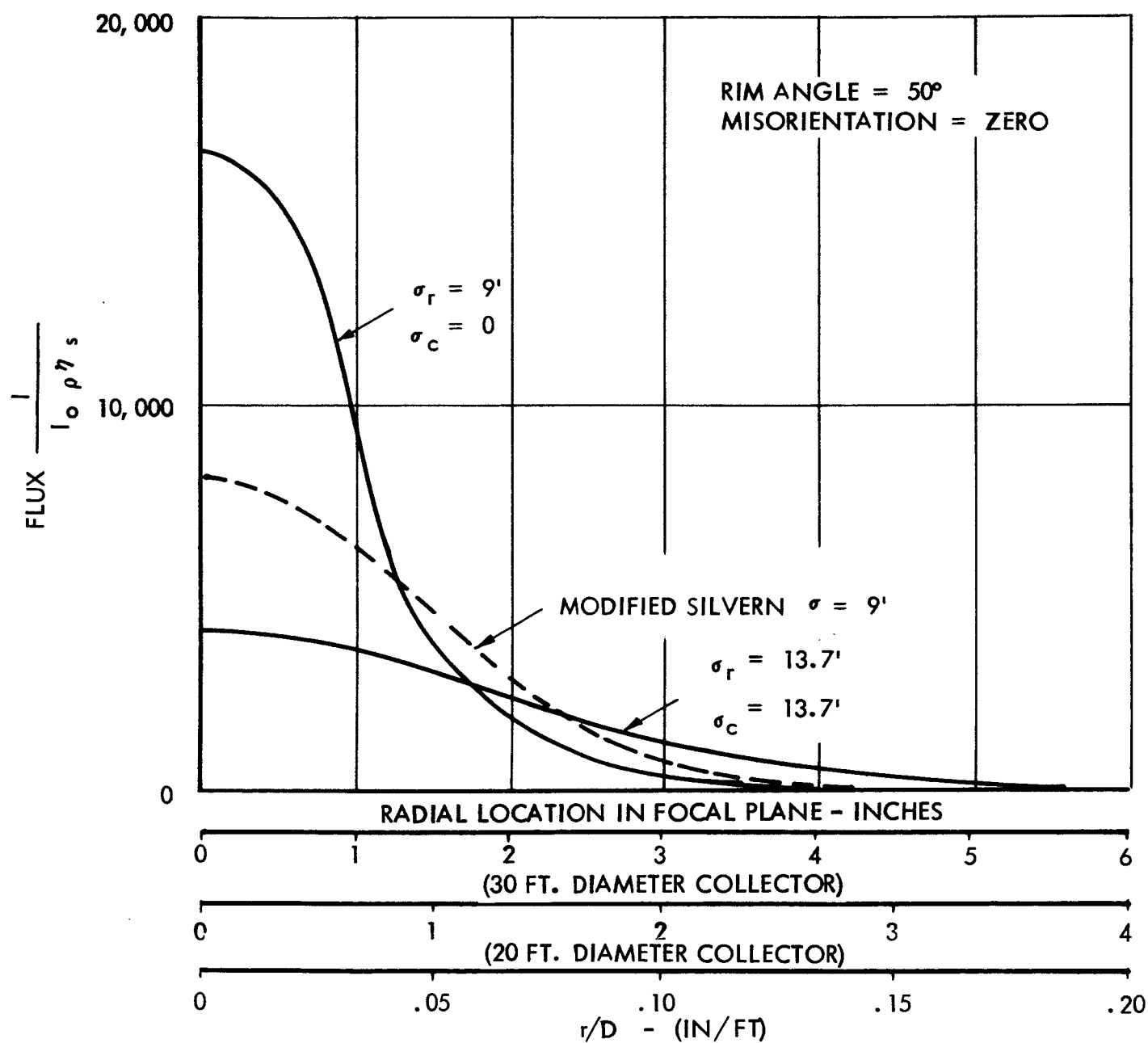


FIGURE 4.2-7
IBM 7094 COMPUTER OUTPUT RESULTS - 50° RIM ANGLE

| R | FRACTION OF TOTAL INCIDENT ENERGY COLLECTED |
|--------------|---------------------------------------------|
| 0.400000E-00 | 0.157683E-00 |
| 0.800000E-00 | 0.412138E-00 |
| 0.120000E 01 | 0.594780E 00 |
| 0.160000E 01 | 0.726465E 00 |
| 0.200000E 01 | 0.822045E 00 |
| 0.240000E 01 | 0.884947E 00 |
| 0.280000E 01 | 0.924448E 00 |
| 0.320000E 01 | 0.951312E 00 |
| 0.360000E 01 | 0.968329E 00 |
| 0.400000E 01 | 0.978405E 00 |
| 0.440000E 01 | 0.983963E 00 |
| 0.480000E 01 | 0.986764E 00 |
| 0.520000E 01 | 0.988048E 00 |
| 0.560000E 01 | 0.988770E 00 |
| 0.600000E 01 | 0.989177E 00 |

$\sigma_r = 9'$
 $\sigma_c = 0$
 $\beta = 0$

FIGURE 4.2-8
IBM 7094 COMPUTER OUTPUT RESULTS - 65° RIM ANGLE

FRACTION OF TOTAL INCIDENT ENERGY COLLECTED

| R | FRACTION OF TOTAL INCIDENT ENERGY COLLECTED |
|--------------|---------------------------------------------|
| 0.400000E-00 | 0.210921E-00 |
| 0.800000E-00 | 0.451483E-00 |
| 0.120000E 01 | 0.611788E 00 |
| 0.160000E 01 | 0.727814E 00 |
| 0.200000E 01 | 0.805791E 00 |
| 0.240000E 01 | 0.859523E 00 |
| 0.280000E 01 | 0.899073E 00 |
| 0.320000E 01 | 0.926804E 00 |
| 0.360000E 01 | 0.945060E 00 |
| 0.400000E 01 | 0.955874E 00 |
| 0.440000E 01 | 0.961779E 00 |
| 0.480000E 01 | 0.965977E 00 |
| 0.520000E 01 | 0.969005E 00 |
| 0.560000E 01 | 0.971149E 00 |
| 0.600000E 01 | 0.972641E 00 |
| 0.640000E 01 | 0.973660E 00 |
| 0.680000E 01 | 0.974344E 00 |

$\sigma_r = 9'$
 $\sigma_c = 0$
 $\beta = 0$

FIGURE 4.2-9
IBM 7094 COMPUTER OUTPUT RESULTS - 50° RIM ANGLE

$$\sigma_r = 9'$$

$$\sigma_c = 0$$

$$\beta = 15' \text{ MISORIENTATION}$$

| FRACTION OF TOTAL INCIDENT ENERGY COLLECTED | |
|---------------------------------------------|--------------|
| R | |
| 0. | 0. |
| 0.60000E 00 | 0.192765E-00 |
| 0.12000E 01 | 0.472661E-00 |
| 0.18000E 01 | 0.700940E 00 |
| 0.24000E 01 | 0.831713E 00 |
| 0.30000E 01 | 0.905370E 00 |
| 0.36000E 01 | 0.944312E 00 |
| 0.42000E 01 | 0.964723E 00 |
| 0.48000E 01 | 0.974764E 00 |
| 0.54000E 01 | 0.979728E 00 |
| 0.60000E 01 | 0.981346E 00 |
| 0.66000E 01 | 0.981943E 00 |
| 0.72000E 01 | 0.982025E 00 |

FIGURE 4.2-10
IBM 7094 COMPUTER OUTPUT RESULTS - 65° RIM ANGLE

$$\sigma_r = 9'$$

$$\sigma_c = 0$$

$$\beta = 15' \text{ MISORIENTATION}$$

FRACTION OF TOTAL INCIDENT ENERGY COLLECTED

| R | | |
|-------------|--------------|----|
| 0. | 0. | 0. |
| 0.60000E 00 | 0.250957E-00 | 0. |
| 0.12000E 01 | 0.550624E 00 | |
| 0.18000E 01 | 0.726607E 00 | |
| 0.24000E 01 | 0.830247E 00 | |
| 0.30000E 01 | 0.892719E 00 | |
| 0.36000E 01 | 0.931155E 00 | |
| 0.42000E 01 | 0.954237E 00 | |
| 0.48000E 01 | 0.966652E 00 | |
| 0.54000E 01 | 0.973185E 00 | |
| 0.60000E 01 | 0.976940E 00 | |
| 0.66000E 01 | 0.979100E 00 | |
| 0.72000E 01 | 0.980234E 00 | |
| 0.78000E 01 | 0.980845E 00 | |
| 0.84000E 01 | 0.980964E 00 | |

FIGURE 4.2-11
GEOMETRIC EFFICIENCY VERSUS RIM ANGLE

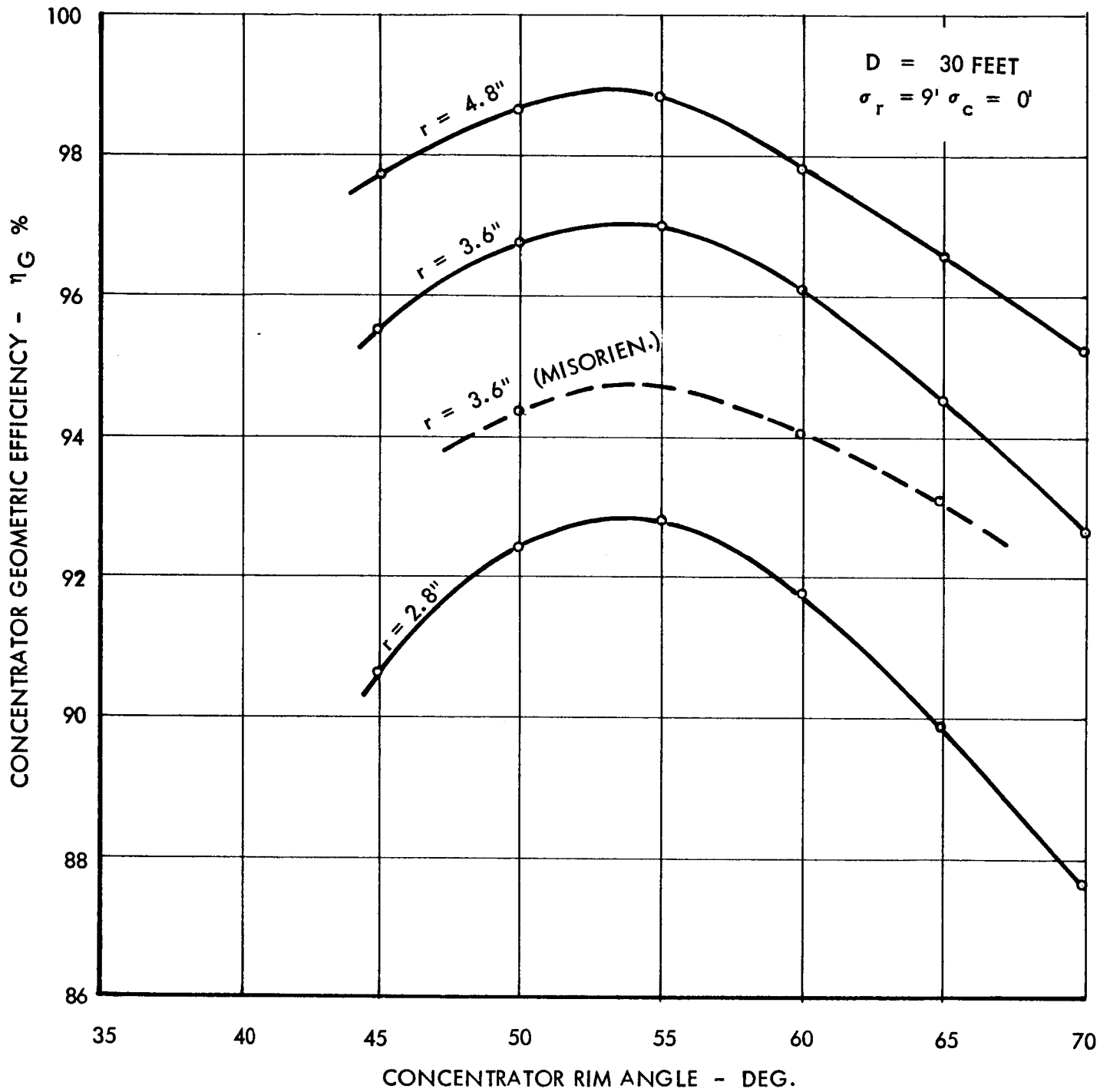


FIGURE 4.2-12
MISORIENTATION FLUX IN THE FOCAL PLANE

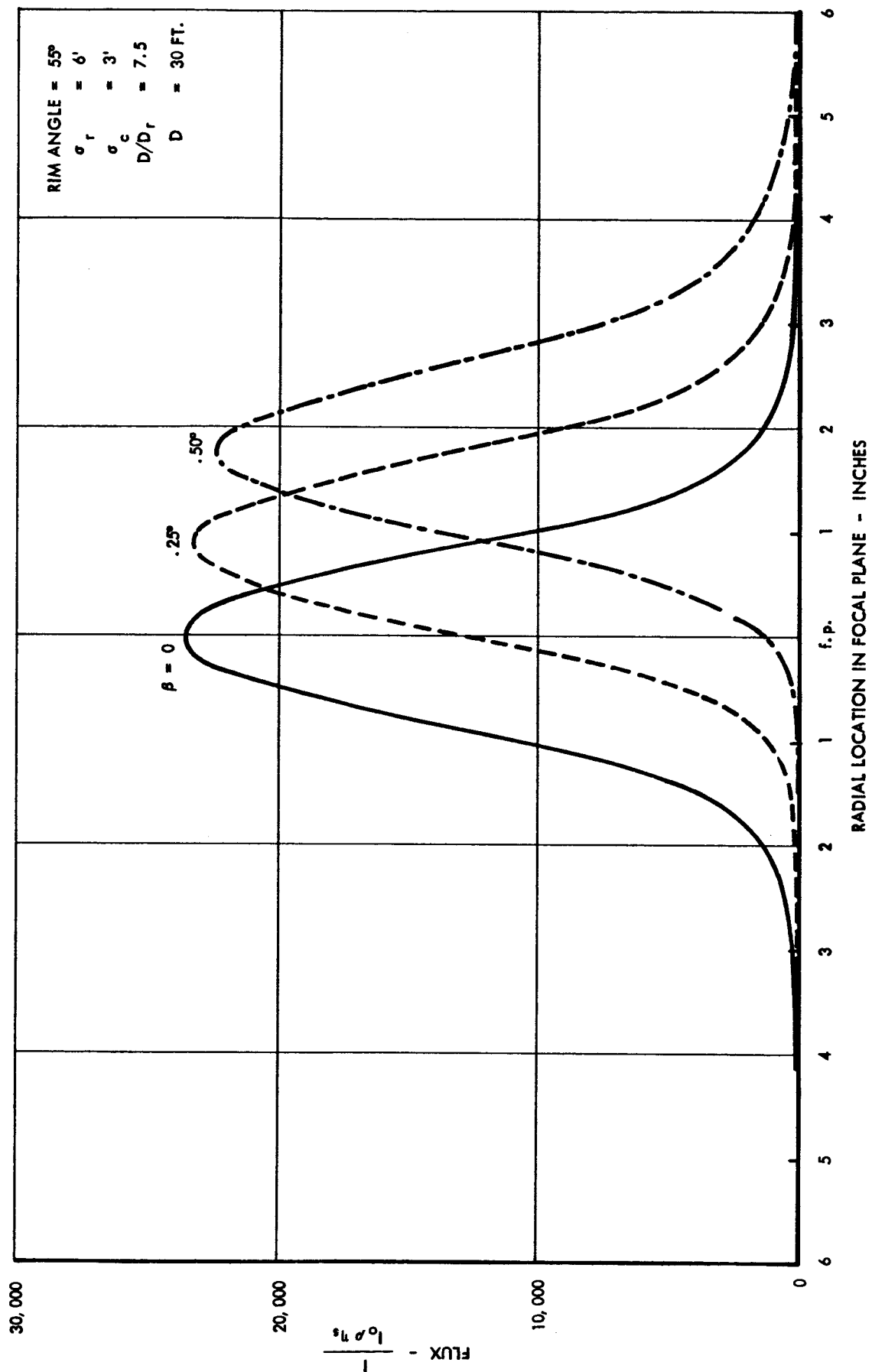


FIGURE 4.2-13

MISORIENTATION EFFECTS UPON CONCENTRATOR GEOMETRIC EFFICIENCY

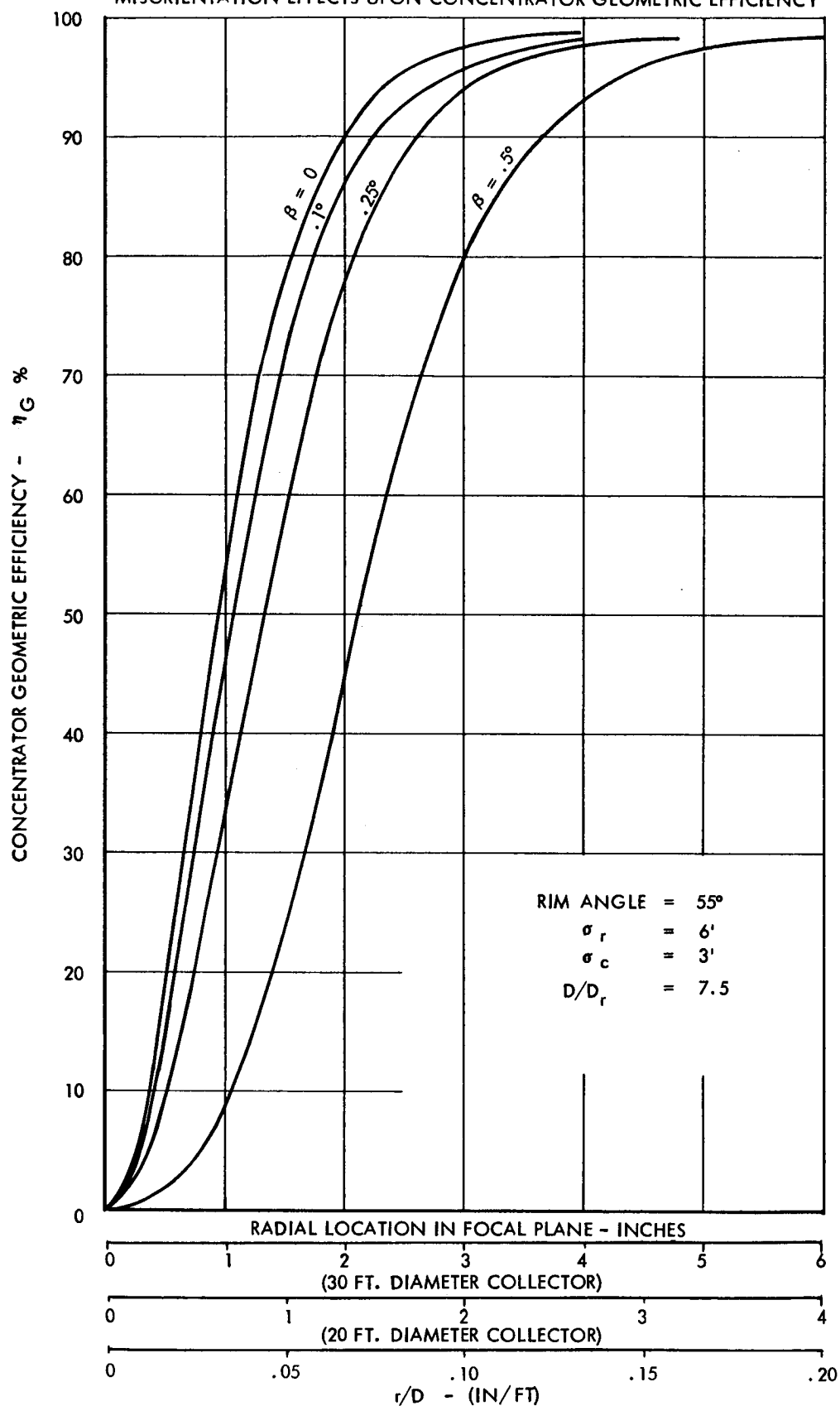


FIGURE 4.2-14
EFFECTS OF FOCAL DISTANCE UPON FLUX DISTRIBUTION

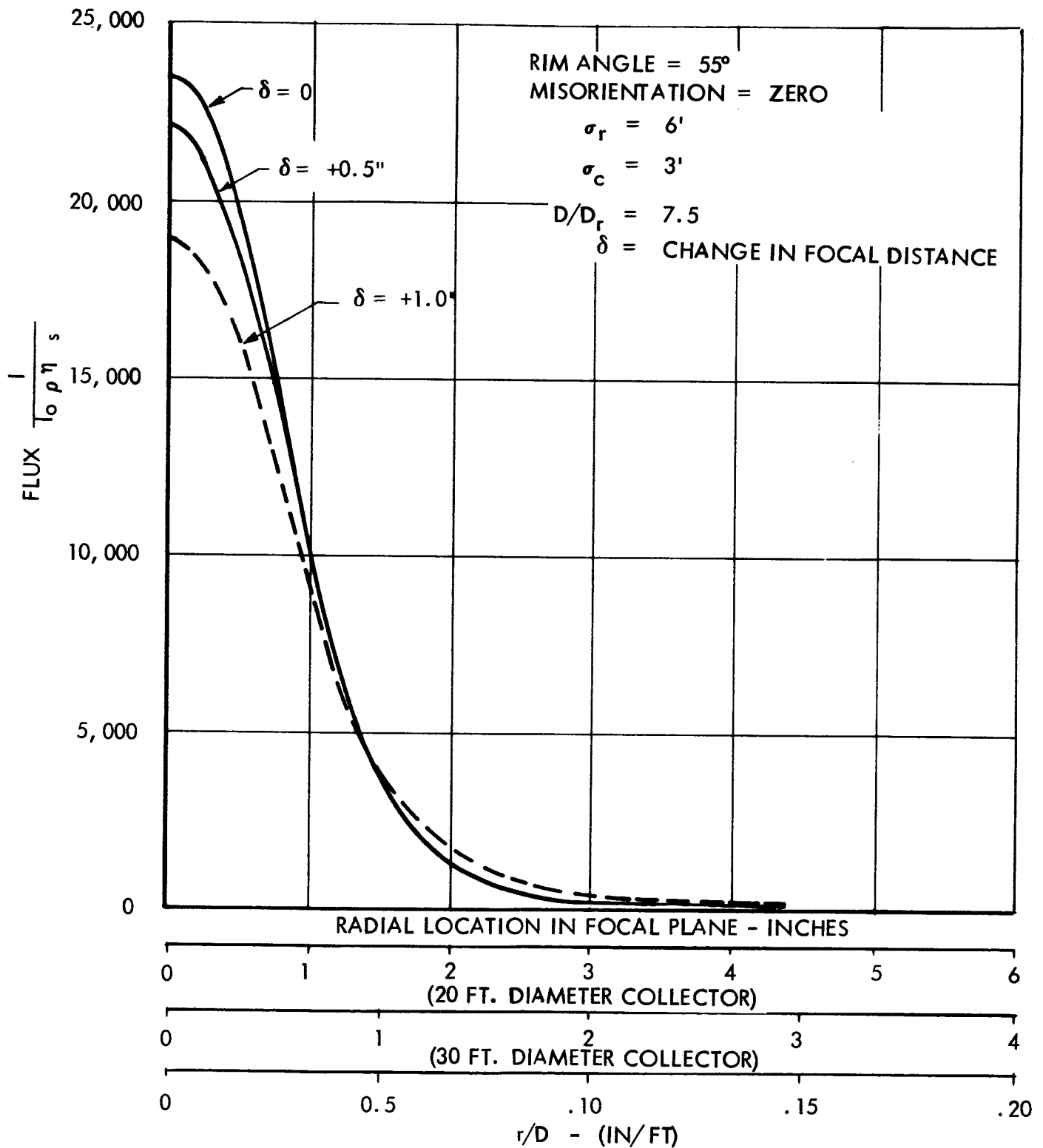
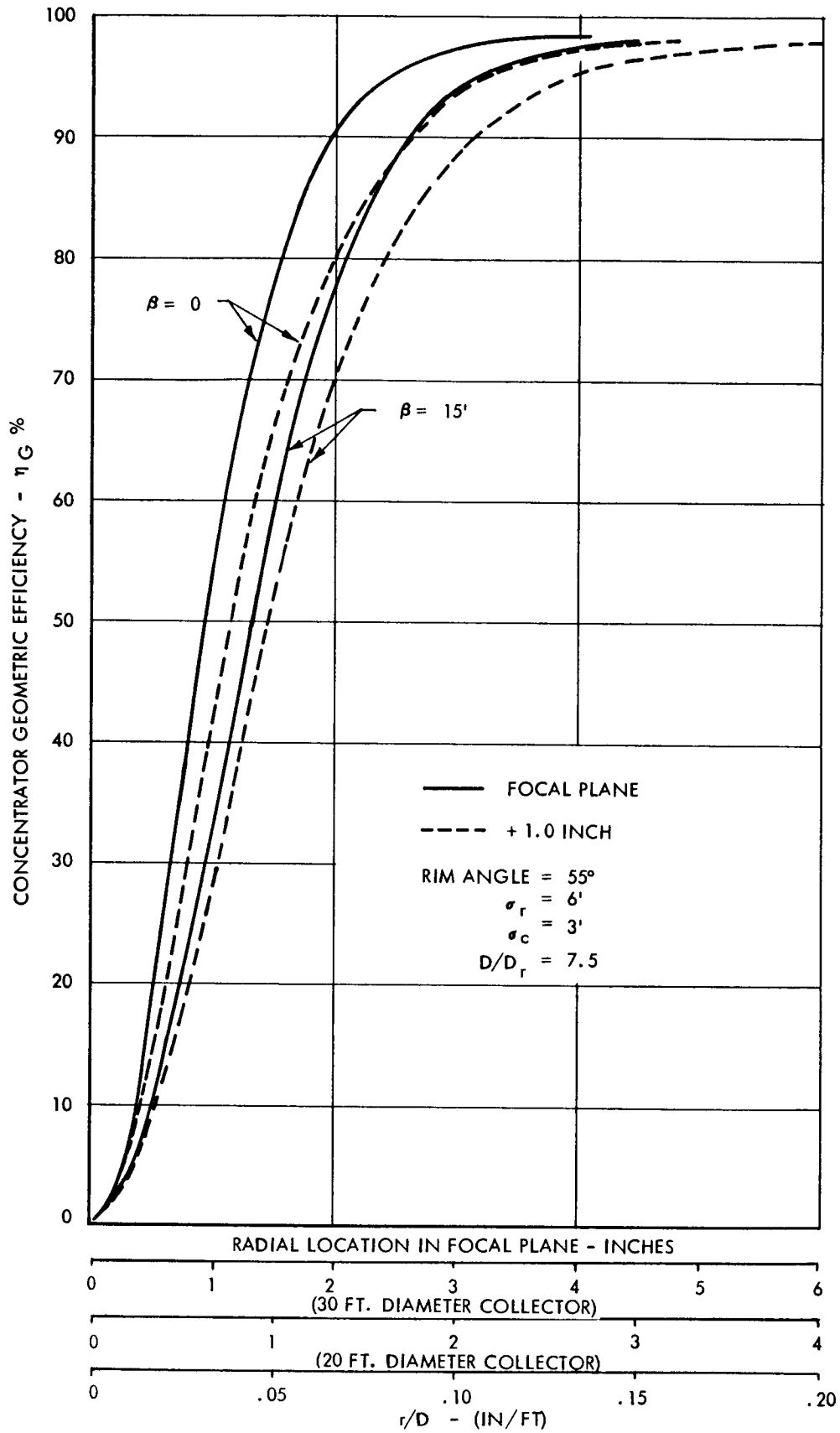


FIGURE 4.2-15
EFFECTS OF FOCAL DISTANCE UPON GEOMETRIC EFFICIENCY



Misorientation

Concentrator misorientation with respect to the sun will result in a reduction of efficiency. This is caused by the shifting and distortion of the flux profile in the focal plane as shown in Figure 4.2-12. The resulting changes in the fraction of energy collected through various aperture sizes is shown in Figure 4.2-13. These curves will be the basis for combined concentrator-receiver performance calculations to be presented in Section 4.4 and the effects of misorientation on overall efficiency will be discussed at that time.

Misplacement of the Receiver

Reduction in concentrator-receiver performance can occur due to changes in focal distances resulting from deployment errors and orbital thermal environment effects. Increase in focal distance parameters were investigated and the effect upon flux distribution is shown in Figure 4.2-14. A small change in the flux distribution is seen for the one half inch increase in focal distance. However, for the one inch case the efficiency drops off, especially in the misoriented position (see Figure 4.2-15). For $\delta = +.5$ inches, the efficiency decrease is less than one per cent.

It is concluded that changes in focal distance must be kept within a ± 0.5 tolerance. Calculation for several assumed telescoping support member configurations and typical temperature variations indicate that this tolerance (± 0.5 ") is attainable.

Receiver Flux Characteristics

As mentioned previously, the generalized analysis and computer program can be used to determine the energy flux distribution on any arbitrary receiver surface. The results of the collector computations are used in a complimentary computer program to determine the flux on the receiver surface including the effects of aperture vignetting.*

*The term vignetting refers to the energy in the focal plane which is blocked by the aperture plate and therefore does not pass through the aperture opening.

Computed results for the Brayton concentrator-receiver combination are plotted in Figure 4.2-16. This profile represents the first incident solar flux from the concentrator and it is the starting point for any receiver cavity heat balance analysis.

4.3 Receiver Performance Analysis

A parametric study of the Brayton receiver retention efficiency (η_R) was made in order to evaluate the overall concentrator-receiver efficiency (η). The parameters which enter into the evaluation are cavity geometry, surface absorptivity and emissivity characteristics and temperature. Several approaches to calculating the receiver retention efficiency are available. For example, Reference (5) presents a method which utilizes a radiosity approach to calculate the heat balance for a cavity receiver. The method starts with an arbitrary incident flux profile on the cavity walls from the solar collector and includes the heat transfer characteristics of the heat storage material in the heat balance as well as the interior wall emissivity and absorptivity effects. View factors are calculated on a zone basis and a computer has been used successfully to solve the heat balance equations resulting in a computed cavity temperature profile and the receiver retention efficiency.

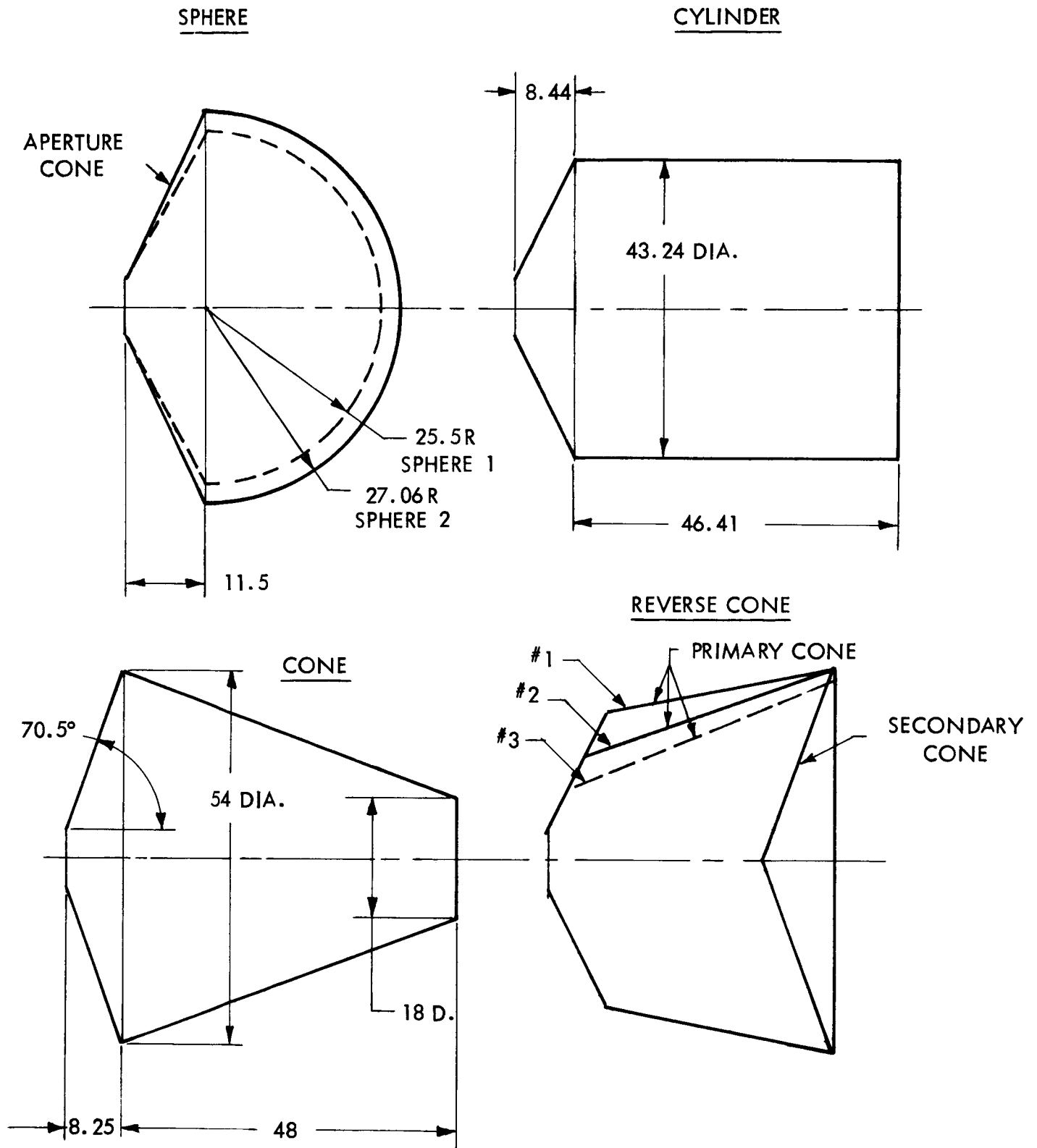
The present analysis treats only the reflection and radiation losses which pass out of the receiver aperture when a constant cavity wall temperature is assumed. This provides the receiver retention efficiency (η_R) for various assumed temperature conditions and allows a preliminary evaluation of several cavity geometries. Figure 4.3-1 shows the four basic shapes considered in the Brayton solar concentrator program, while all but the reverse cone were evaluated on the Brayton receiver study contract (NAS 3-2779).

The equation which ties in the receiver retention efficiency is obtained from equation (4.1-3) neglecting external receiver losses temporarily,

$$\eta = \eta_B \eta_C \eta_R = \eta_B \rho \eta_G \eta_R \quad (4.3-1)$$

The retention efficiency factor (η_R) has been defined as the heat rate passing into the receiver walls divided by the total concentrated solar flux

FIGURE 4.3-1
RECEIVER CONFIGURATIONS



passing through the cavity aperture, which is incident on the receiver surface,

$$\eta_R = \frac{q_R}{q_1} = \frac{q_1 - L_\rho - L_E}{q_1} \quad (4.3-2)$$

The heat losses are:

$$L_\rho = (1 - \eta_\rho) q_1 \quad (4.3-3)$$

$$L_E = A_R F_R \sigma T_R^4 \quad (4.3-4)$$

Substitution of equations (4.3-3) and (4.3-4) into (4.3-2) gives:

$$\eta_R = \eta_\rho - \frac{A_R F_R \sigma T_R^4}{q_1} = \eta_\rho - \frac{A_R F_R \sigma T_R^4}{I_o \rho A_c \eta_G} \quad (4.3-5)$$

It should be noted that the concentration efficiency (η_G) shows up in the right hand side of equation (4.3-5) and therefore the retention efficiency is dependent on concentrator efficiency.

Some receiver analyses assume that the receiver aperture exhibits black-body characteristics, wherein such a loss is assumed to be a maximum limit. This assumption is a close approximation for some cases but not all. Because of the common use of the black aperture loss, the actual receiver losses will be related to the black aperture loss for comparison in this analysis. It will be shown subsequently that the actual losses for the Brayton receiver configurations are between 1.058 to 1.074 times black aperture loss. Appendix C shows a comparison between an actual cavity and a black aperture and illustrates why the black aperture loss cannot be used as a maximum loss.

4.3.1 Cavity Reflection Losses

For ease of analysis in Appendix C, the incident concentrated solar flux on the cavity surface was assumed uniform. Thus an average view factor (F_{R-A}) could be used in equation D (Table C-1 of Appendix C) to calculate the reflection factor (η_ρ). Since the receiver shapes to be considered do not approach

this uniform incident flux assumption, the following analysis includes a method of more accurately calculating the reflection loss (L_p).

Actually, there are portions of the receiver surface which do not receive solar flux directly. By multiple reflections, they do enter into the reflection loss however. The aperture plate and the area on the receiving surface greater than the concentrator rim angle and less than the center section angle do not receive solar flux directly, at zero solar misorientation (see Figure 4.2-16).

The incident flux profiles on the receiver surface for three cavity geometries were computed as in Appendix D. Figures 4.3-2a, 4.3-3a and 4.3-4a show the profiles plotted in per cent of intercepted solar flux for equal length (but not area) zones on the receiver surface. Thus the incident zonal flux may be treated, rather than assuming a constant flux profile. To obtain the zone losses, the zonal view factors were determined and are shown in Figures 4.3-2b, 4.3-3b and 4.3-4b as view factor versus zone. They were obtained by graphical integration after the shadow method of Eckert (Reference 6). Although the three reverse-cone shapes in Figure 4.3-1 were not evaluated for efficiency, the view factors were determined for cases 1 and 3 and are shown in Figures 4.3-5 and 4.3-6.

The procedure for computing the reflection efficiency factor is as follows:

$$q_A = \sum q_Z (\alpha_s + X_Z F_R) \quad (4.3-6)$$

for the ten zones chosen. For each zone there is usually a different q_Z and X_Z . Equation (4.3-6) is derived in Appendix E. The reflectivity factor is then,

$$\eta_p = \frac{q_A}{q_i} = \frac{\sum q_Z (\alpha_s + X_Z F_R)}{I_o \rho A_c \eta_G} \quad (4.3-7)$$

This factor, for the three receiver shapes and a black aperture, is plotted versus aperture diameter (d) in Figure 4.3-7. The black aperture has a reflectivity factor of one. The ranking of receiver surface geometries to minimize reflection losses is the cylinder, cone and sphere in that order.

FIGURE 4.3-2a
SPHERE FLUX PROFILE

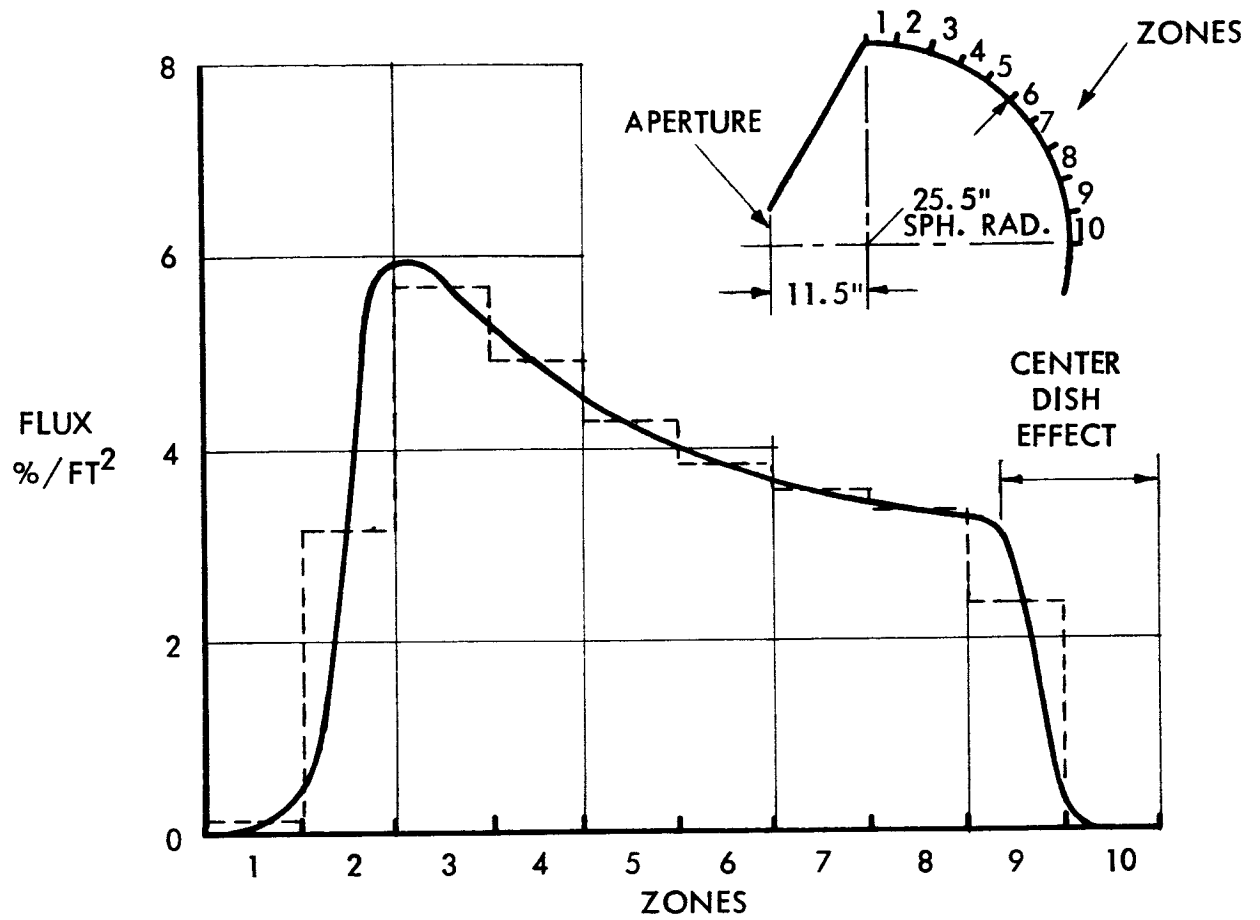


FIGURE 4.3-2b
SPHERE VIEW FACTOR

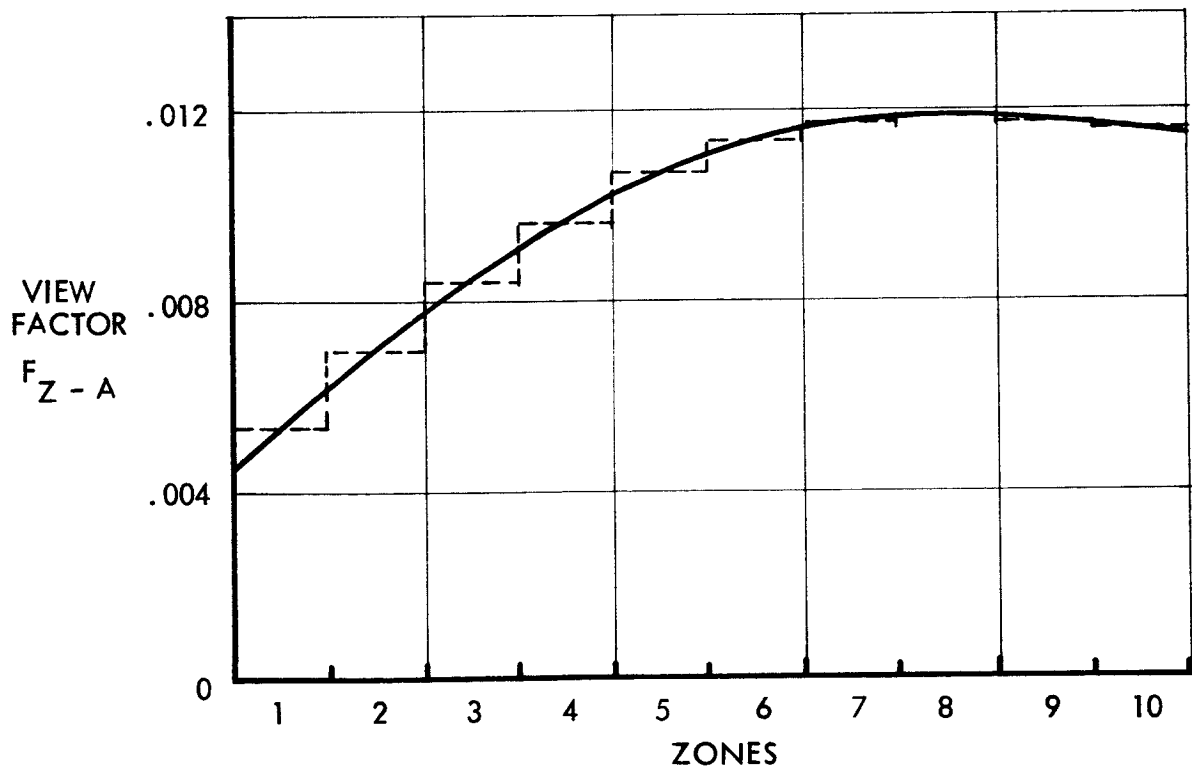


FIGURE 4.3-3a
CONE FLUX PROFILE

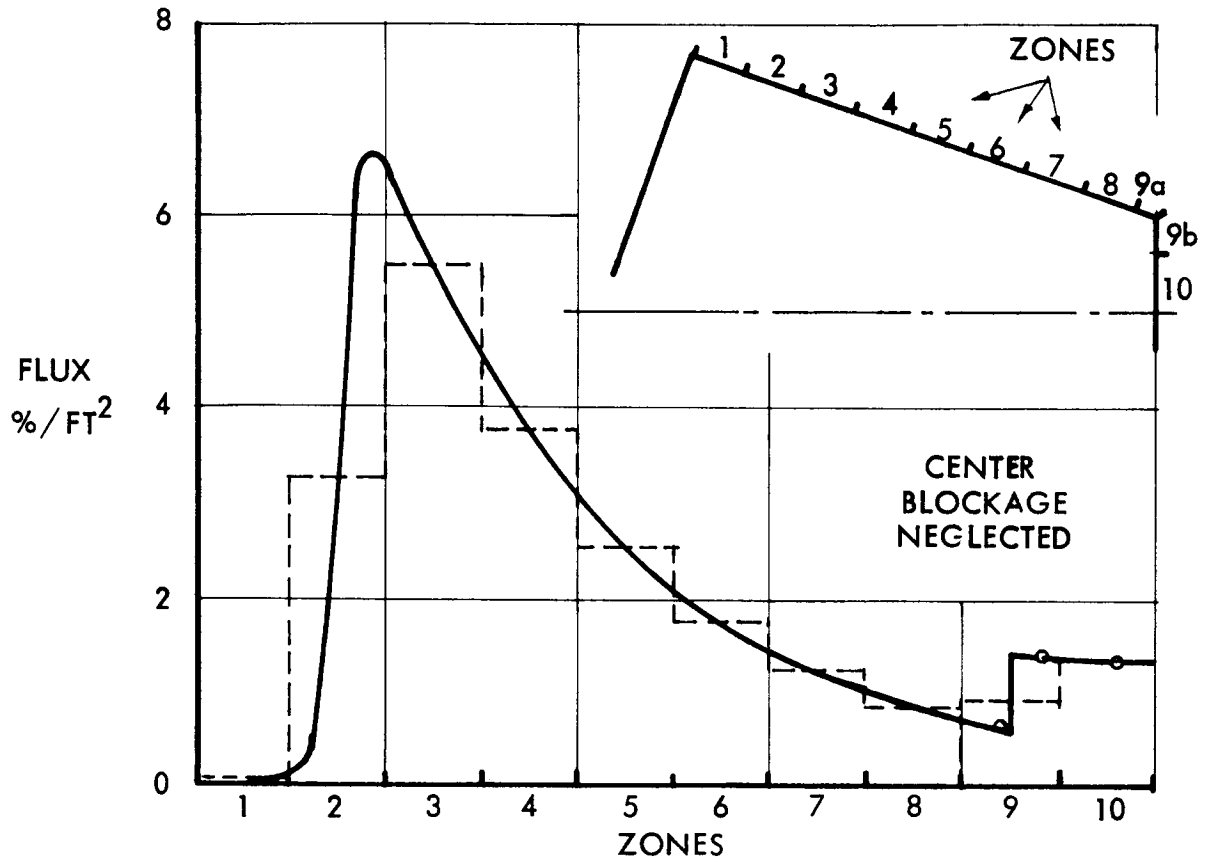


FIGURE 4.3-3b
CONE VIEW FACTOR

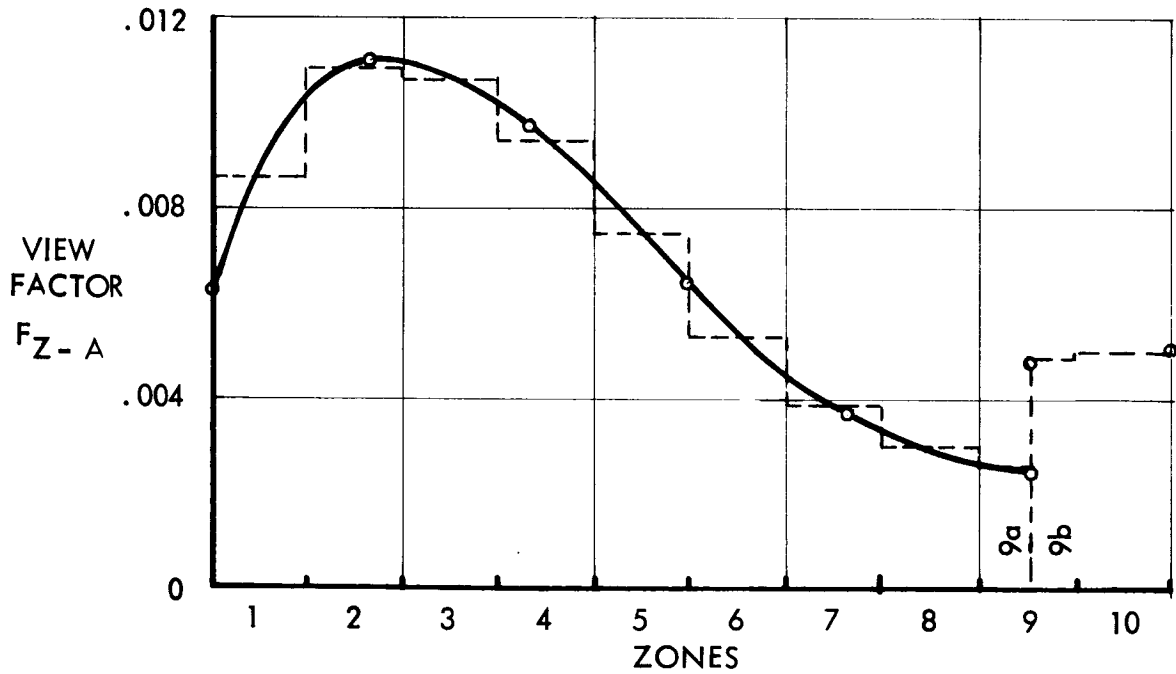


FIGURE 4.3-4a
CYLINDER FLUX PROFILE

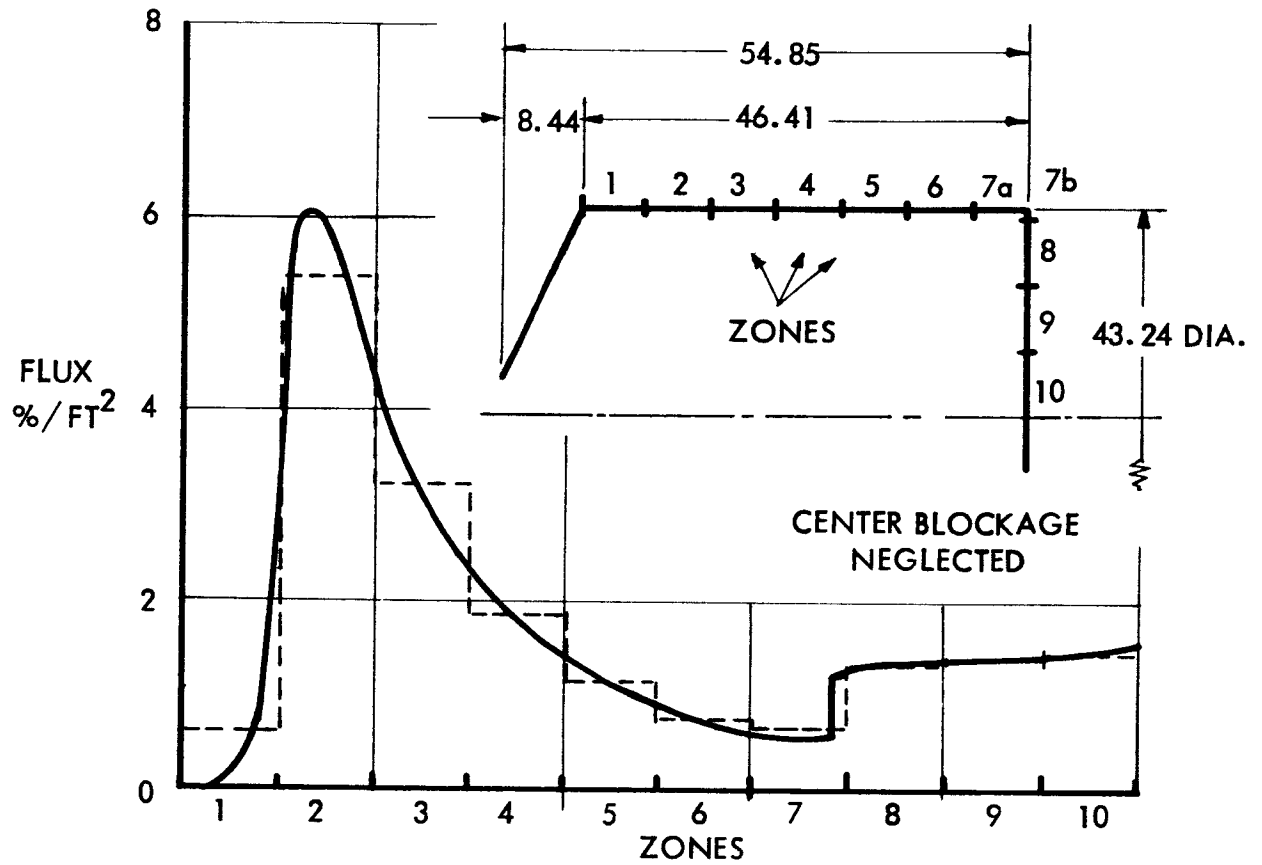


FIGURE 4.3-4b
CYLINDER VIEW FACTOR

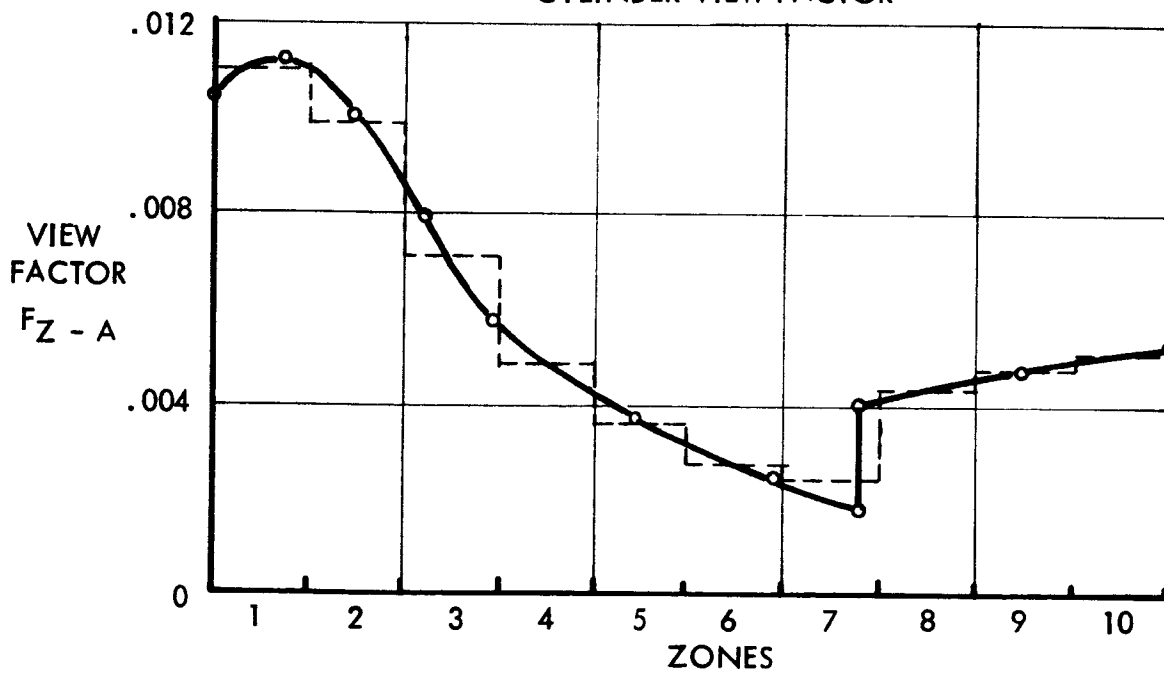


FIGURE 4.3-5
 REVERSE - CONE NO. 1 VIEW FACTOR

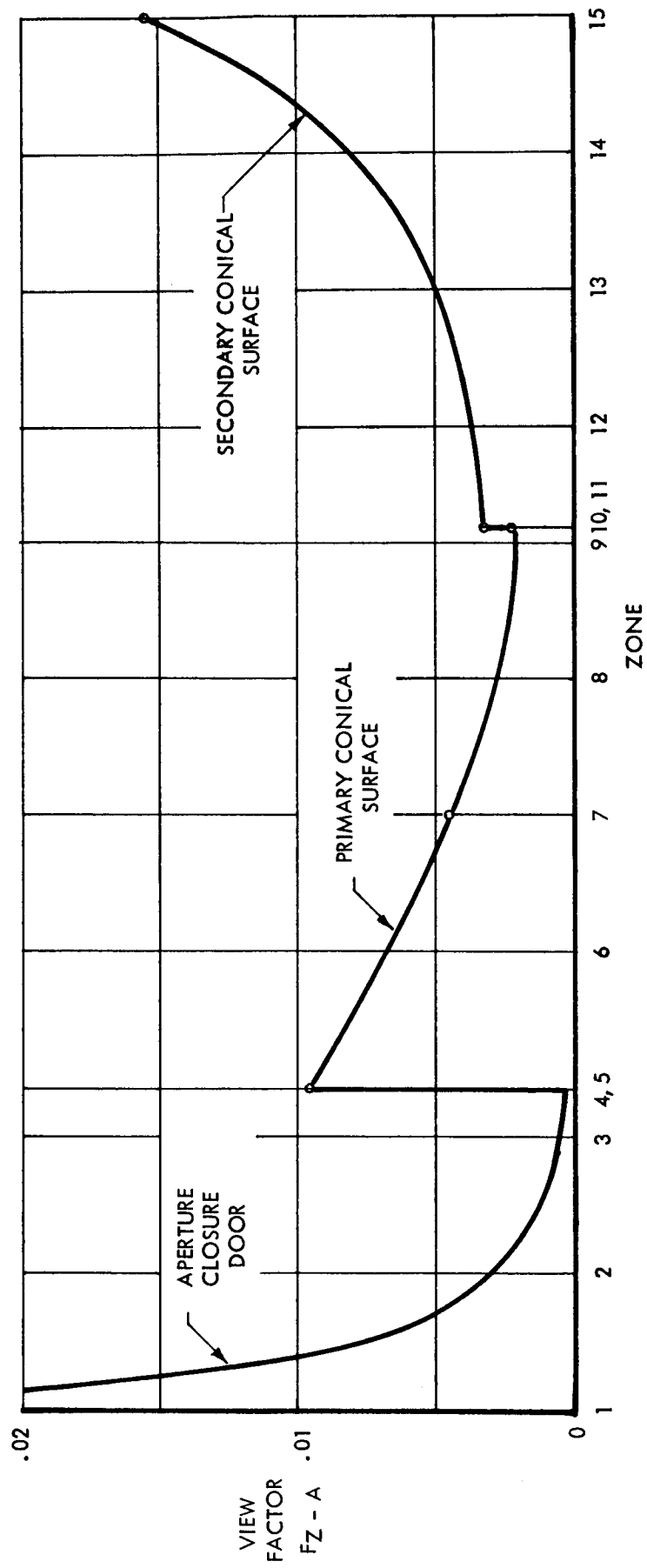


FIGURE 4.3-6
REVERSE - CONE NO. 3 VIEW FACTOR

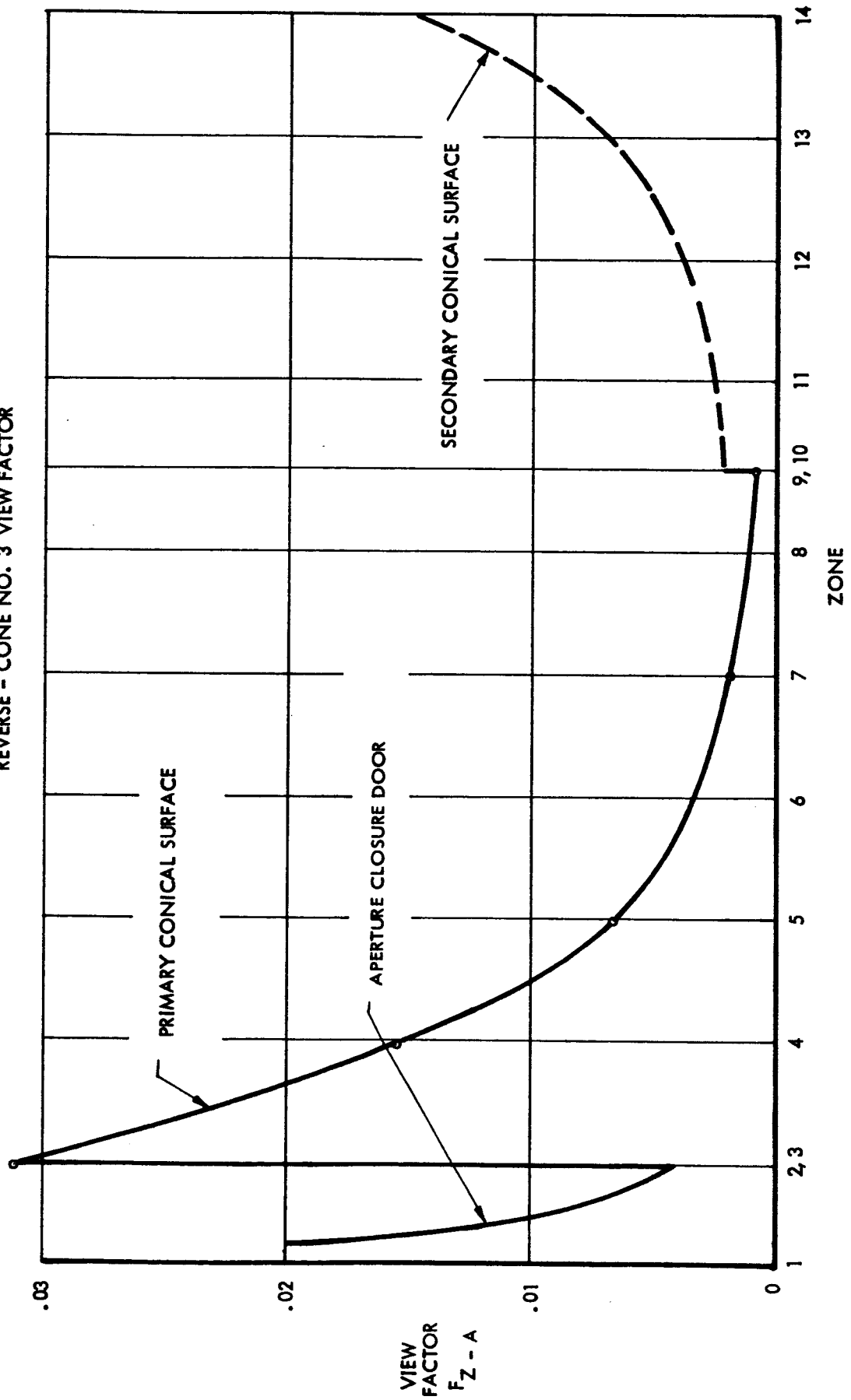
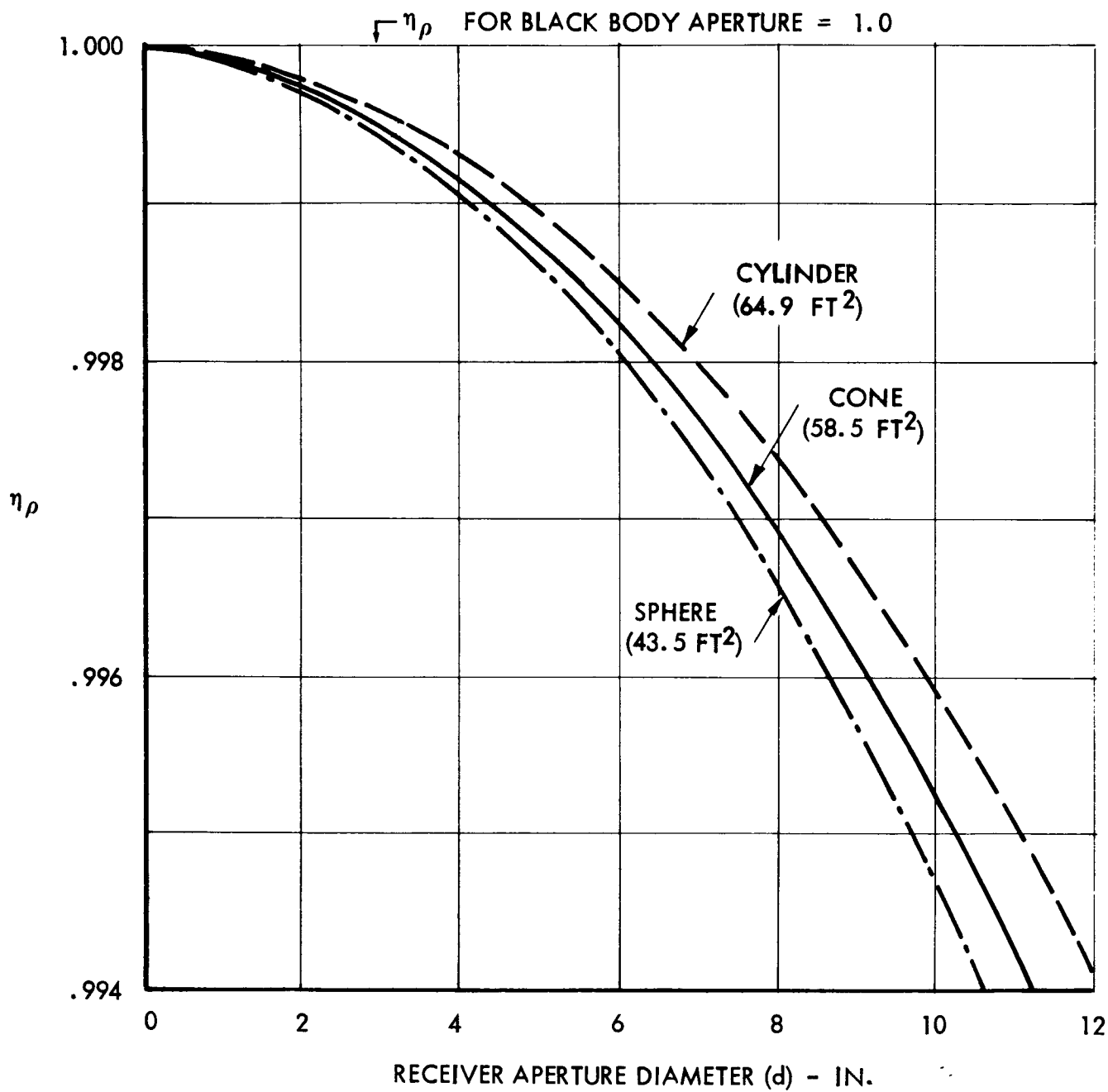


FIGURE 4.3-7

RECEIVER REFLECTIVITY EFFICIENCY FACTOR
VERSUS APERTURE DIAMETER

$$\alpha_s = .73$$



For an 8 inch aperture and an incident flux of 250,000 BTU/hr the reflection loss is 650, 775, and 850 BTU/hr for the cylinder, cone and sphere respectively. For comparison, if a uniform incident solar flux on the receiving surface were assumed, these same 8 inch aperture losses would have been 500, 550 and 740, respectively. There is no significant difference compared with the actual intercepted flux case because the reflection loss is not too large to begin with. However, the treatment of reflection loss by zones results in as much as a 40% greater loss in the case of the conical surface. Zonal treatment of the radiation loss, when the temperature profile is known, may increase that loss by a like value and this becomes significant.

Although it would appear that the cylinder is the best choice for minimum reflection loss, two points should be made. First, the interior areas of the three geometries are not equal, and the zonal view factors are a function of geometry and aperture-to-receiver surface ratio. To properly evaluate the reflection loss therefore, the geometries should be compared on an equal area basis if possible. Second, the incident concentrated solar flux profile on the receiver surface is not uniform and varies with geometry; thus the lower ratio of maximum-to-minimum incident solar flux of the sphere may result in a more uniform temperature profile and less tendency for hot spots, depending on the heat transfer properties of the receiver.

4.3.2 Cavity Radiation Losses

For the radiation loss, the cavity surface was assumed to be isothermal, although the temperature level was varied between 1500 and 2000 degrees F. The isothermal case is not expected, but it will be close because of the heat storage media boundary conditions.

The radiation loss is computed from equation (4.3-4).

$$L_E = A_R F_R \sigma T_R^4$$

The factor F_R is computed as

$$F_R = \frac{\epsilon_t F_{R-A}}{1 - (1 - \epsilon_t)(1 - F_{R-A})} \quad (4.3-8)$$

For the spherical receiver, the loss (L_E) is plotted versus aperture diameter with temperature (T_R) as a parameter in Figure 4.3-8. Figure 4.3-9 shows the radiation loss (L_E) plotted versus cavity surface emissivity to thermal radiation (ϵ_t) at 1700°F.

4.3.3 Total Cavity Loss

Also plotted on Figure 4.3-9 is the reflection loss (L_p) versus surface emissivity (where α_s equals absorptivity to solar flux). The combined loss is shown ratioed to black aperture loss (assuming solar absorptivity equals thermal emissivity). These curves should be used carefully, however. The reflection loss (L_p) assumes a uniform incident concentrated solar flux on the receiver surface. Based on the previous discussion the reflection loss is larger, thus the ratio Y would be slightly greater than shown. However, it is apparent that the solar absorptivity should approach zero. Since most surfaces do not deviate widely from gray body thermal radiation properties, the surface with the highest absorptivity (and therefore highest emissivity) is a better choice. The data in Figures 4.3-7 and 4.3-8 were based on measured values for molybdenum at high temperature with a solar absorptivity of 0.73 and a thermal emissivity of 0.60 (Reference 7). More recent results for high temperature metals measured in a vacuum (Reference 8) show that the solar absorptivity is higher (.70) than the thermal emissivity (.40); thus the loss would be $980 + 12,890 = 13,870$ BTU/hr or $Y = 1.062$. The total receiver loss is not too sensitive to surface emissivity above 0.5. If the final receiver surface is found to deviate from these values, then the Figure 4.3-9 data can be used to modify the losses.

4.4 Combined Concentrator Receiver Performance

The combined performance can be obtained from the results of Sections 4.2 and 4.3. The equation which represents this combined performance is equation (4.3-1),

$$\eta = \eta_B \rho \eta_G \eta_R \quad (4.3-1)$$

FIGURE 4.3-8
RECEIVER RADIATION LOSS VERSUS APERTURE DIAMETER

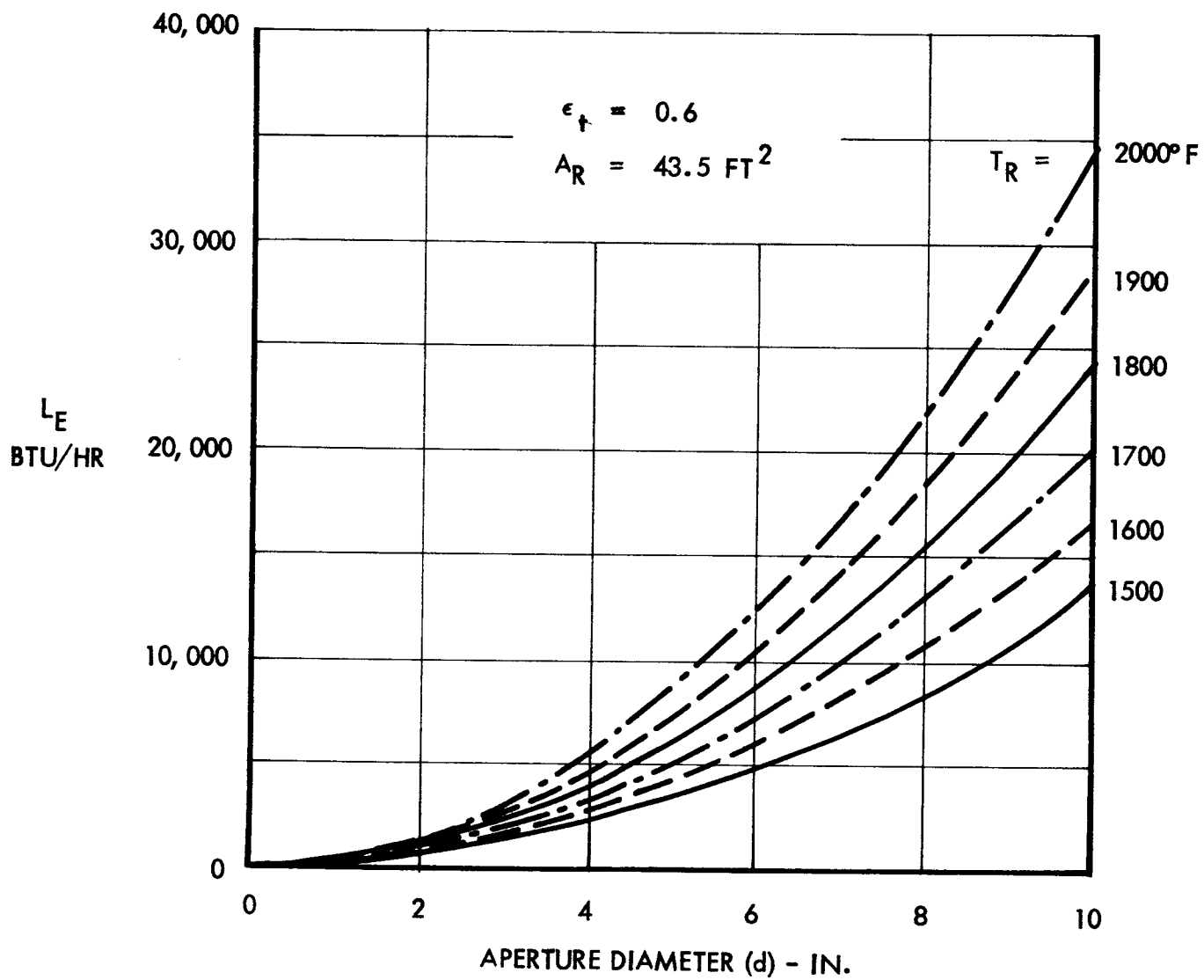


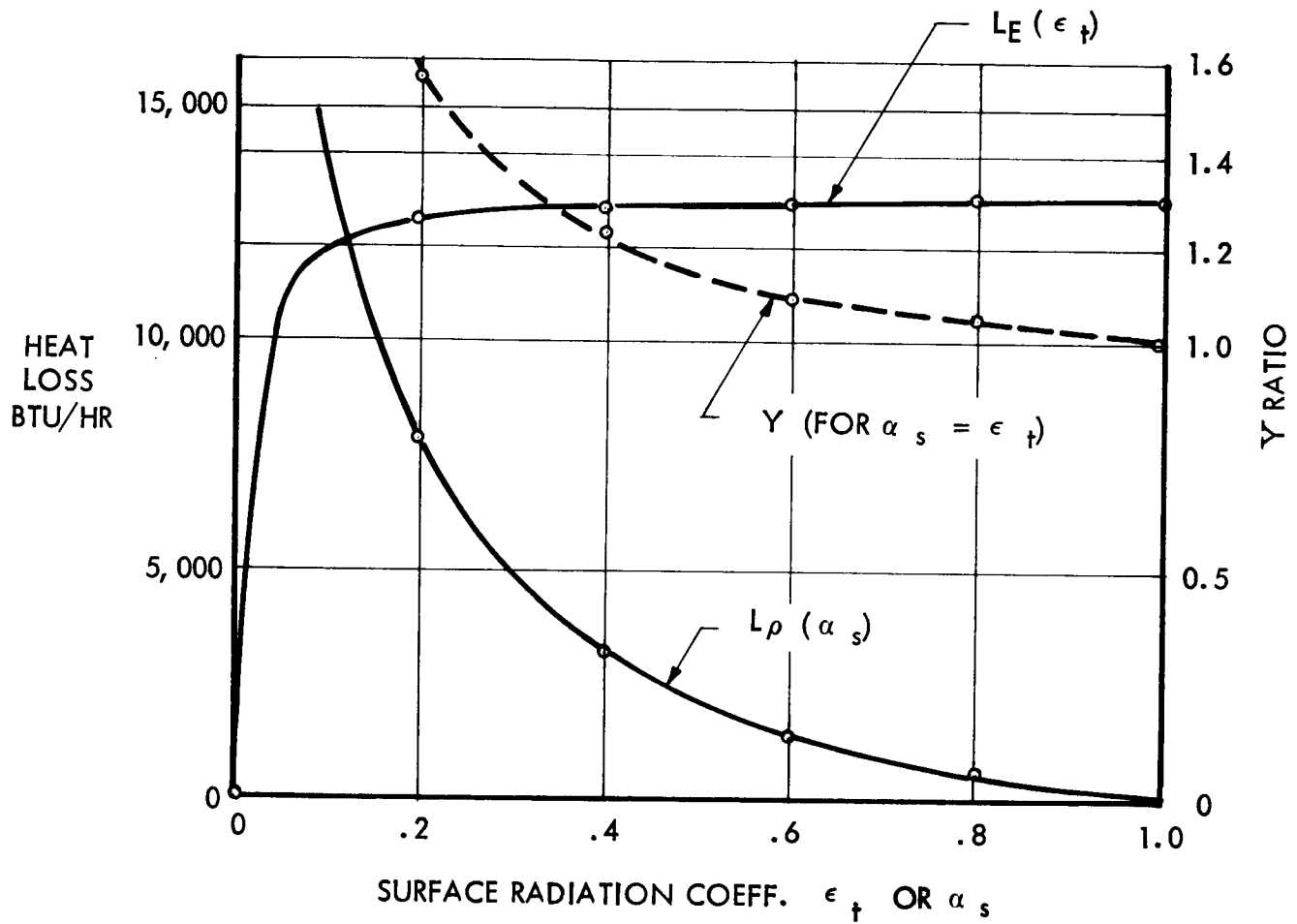
FIGURE 4.3-9
CAVITY LOSSES VERSUS SURFACE EMISSIVITY

$$T_R = 1700^\circ\text{F}$$

$$d = 8 \text{ IN.}$$

$$q_i = 250,000 \text{ BTU/HR}$$

$$A_R = 43.5 \text{ FT}^2 \text{ (SPHERE)}$$



$$Y = \frac{\text{CAVITY LOSS}}{\text{BLACK APERTURE LOSS}} = \frac{L_\rho + L_E}{A_A \sigma T_R^4}$$

It has been shown that both η_G and η_R vary with the aperture size. Thus to determine the maximum combined efficiency and thereby establish the optimum aperture size, equation (4.3-1) must be plotted over a range of aperture diameters.

Figure 4.4-1 presents the combined performance curves for several cases which were analysed. The parameters which were used in these cases are shown in Table 4.4-1 as well as the resulting optimum aperture size and corresponding maximum efficiency. These cases are for the anticipated Brayton collector optical quality ($\sigma_r = 6'$, $\sigma_c = 3'$); and the solar orientation and receiver temperature parameter are varied to determine the predicted performance of the recommended design configuration.

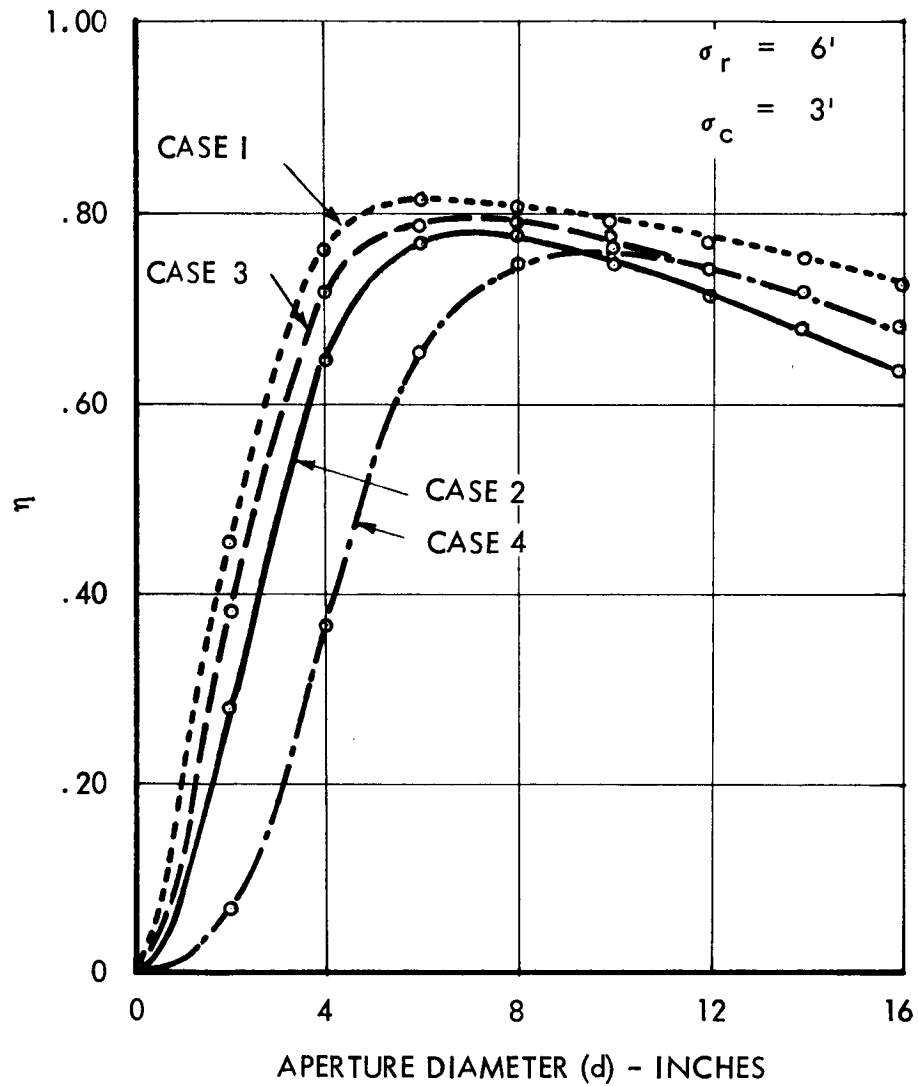
It is seen that the performance peaks in the efficiency range of 0.77 to 0.81. An aperture size of 7.0 inches diameter is selected as the optimum for the probable time averaged operating conditions of 6 minutes misorientation and 1700°F receiver temperature and results in a predicted time averaged efficiency in the sun of 0.79. Case 4 which considered a one half degree misorientation shows only a three per cent decrease in efficiency over the six minute case and indicates that the misorientation parameter may require optimization by the system designer when weighted against orientation control considerations. An orientation control system must be designed and analysed to establish a proper tradeoff criterion.

As mentioned previously, the analysis thus far has not considered the external receiver surface heat losses. For the spherical receiver shape considered here, these losses are estimated to be approximately an additional one per cent - resulting in an overall time average efficiency of 78% in the sun.

Since the concentrator operates only in the sun phase while the system operates continuously, the complete orbit time useful heat can be obtained from the following relationships.

$$q_s t_o + L_x t_o + L_E t_N = q_r t_s \quad (4.4-1)$$

FIGURE 4.4-1
CONCENTRATOR-RECEIVER EFFICIENCY IN THE SUN
VERSUS APERTURE DIAMETER



PARAMETRIC PERFORMANCE STUDY CASES

TABLE 4.4-1

| Case | CONCENTRATOR | | | | | | RECEIVER | | | | | COMBINED | |
|------|---------------|------------|-----------------------------|---------------------------------------------|----------------------------|----------------------------|----------------|----------------------------|------------------------|-------------------------------|---------------------------------|-------------|---------------------|
| | Surface Model | | Surface Reflectivity ρ | Surface Misorientation θ Min. of Arc | Blockage Factor γ_B | Rim Angle θ Degrees | Receiver Shape | Area A_R Ft ² | Surface Temp. T_R °F | Solar Absorptivity α_s | Thermal Emissivity ϵ_t | η Max. | d(in.) @ Max η |
| | Min. of Arc | θ_c | | | | | | | | | | | |
| 1 | 3 | 6 | 0.9 | 0 | 0.945 | 55 | Sphere | 43.5 | 1550 | 0.73 | 0.60 | 0.81 | 6.0 |
| 2 | 3 | 6 | 0.9 | 15 | 0.945 | 55 | Sphere | 43.5 | 1850 | 0.73 | 0.60 | 0.77 | 6.8 |
| 3 | 3 | 6 | 0.9 | 6 | 0.945 | 55 | Sphere | 43.5 | 1700 | 0.73 | 0.60 | 0.79 | 7.0 |
| 4 | 3 | 6 | 0.9 | 30 | 0.945 | 55 | Sphere | 43.5 | 1700 | 0.73 | 0.60 | 0.76 | 10.0 |

$$\eta = \rho \gamma_B \gamma_0 \gamma_R = \gamma_B \gamma_C \gamma_R$$

$$\gamma_B \gamma_C = 0.9 \times 0.945 \gamma_0 = .851 \gamma_0$$

$$\gamma_R = \gamma_p - \frac{I_B}{I_0 \rho A \gamma_B \gamma_0}$$

where the useful heat is

$$q_s t_o = Q_s = q_r t_s - L_x t_o - L_E t_N \quad (4.4-2)$$

The useful heat into the system and heat storage material can be obtained from equation (4.1-2)

$$q_r = AI_o \eta = AI_o \rho \eta_B \eta_G \eta_R \quad (4.4-3)$$

or in terms of only the unshadowed collector area it can be obtained from equation (4.3-2),

$$q_r = q_1 \eta_R = I_o \rho A_c \eta_G \eta_R \quad (4.4-4)$$

Thus equation (4.4-2) becomes,

$$Q_s = AI_o \eta t_s - L_x t_o - L_E t_N \quad (4.4-5)$$

Thus the useful heat to the system can be calculated for any orbital altitude and inclination by using the heat rate values established in this study and the proper orbit times.

5.0 SURFACE ERROR EVALUATION TESTING

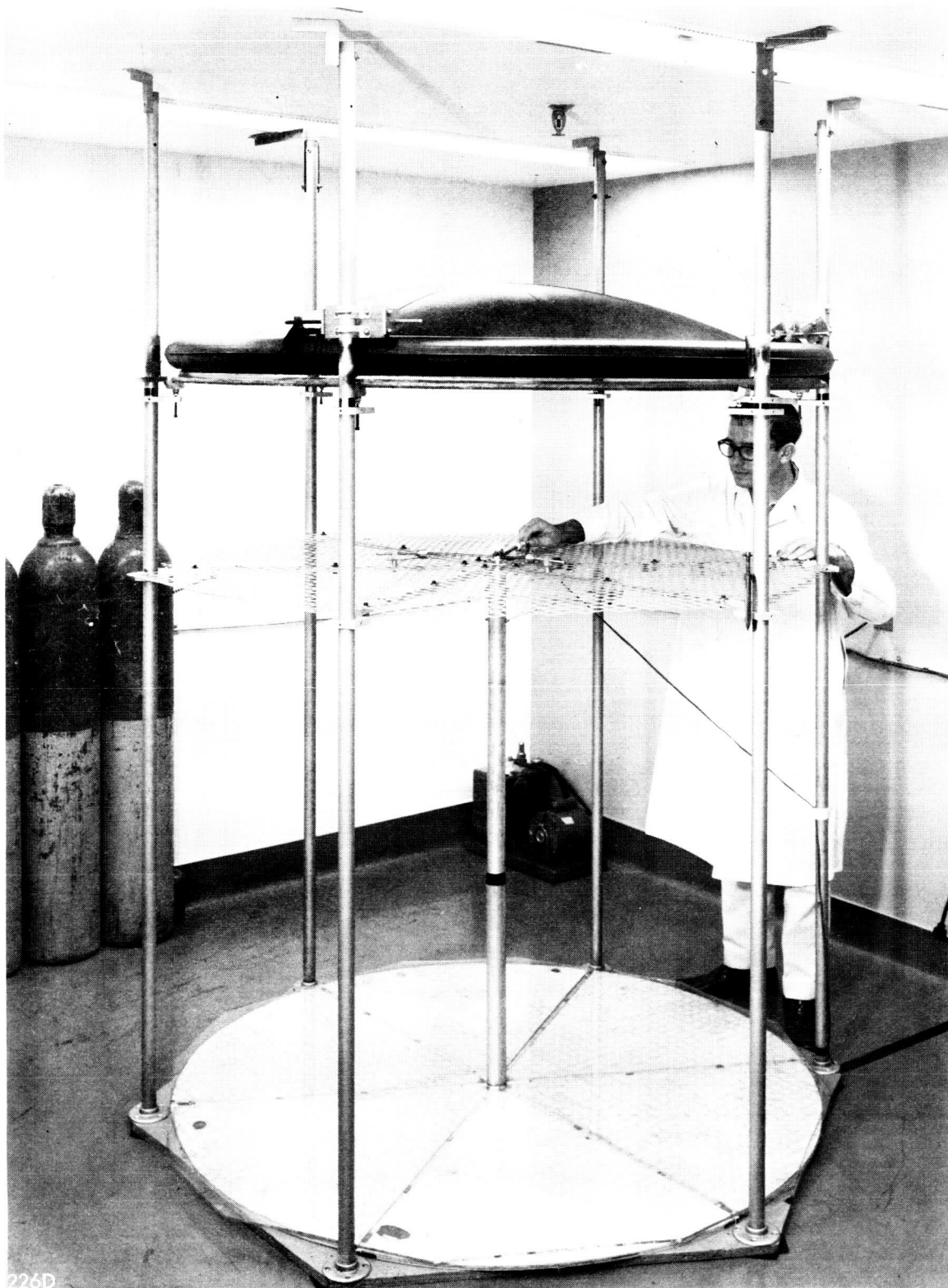
A portion of the program efforts were directed toward evaluating available hardware and fabrication techniques so that practical and accurate estimates of optical accuracy could be used in the Brayton cycle collector performance predictions. These evaluations consisted of optical inspections of five foot diameter stretch formed concentrators which were being fabricated on a NASA Langley contract. Also, adhesive bonded honeycomb sandwich specimens were fabricated and tested under various thermal gradients to determine geometric quality. In conjunction with the investigation of the effects of orbital environments, reflective specimens were fabricated; and after simulated micro-meteoroid erosion tests by NASA Lewis these specimens were evaluated for surface degradation.

5.1 Five Foot Diameter Concentrator Inspections

Geometric surface error inspections were performed on a five foot diameter concentrator fabricated under Contract NAS 1-3216. This concentrator is typical of the stretch formed sector type construction which is contemplated for the Brayton system.

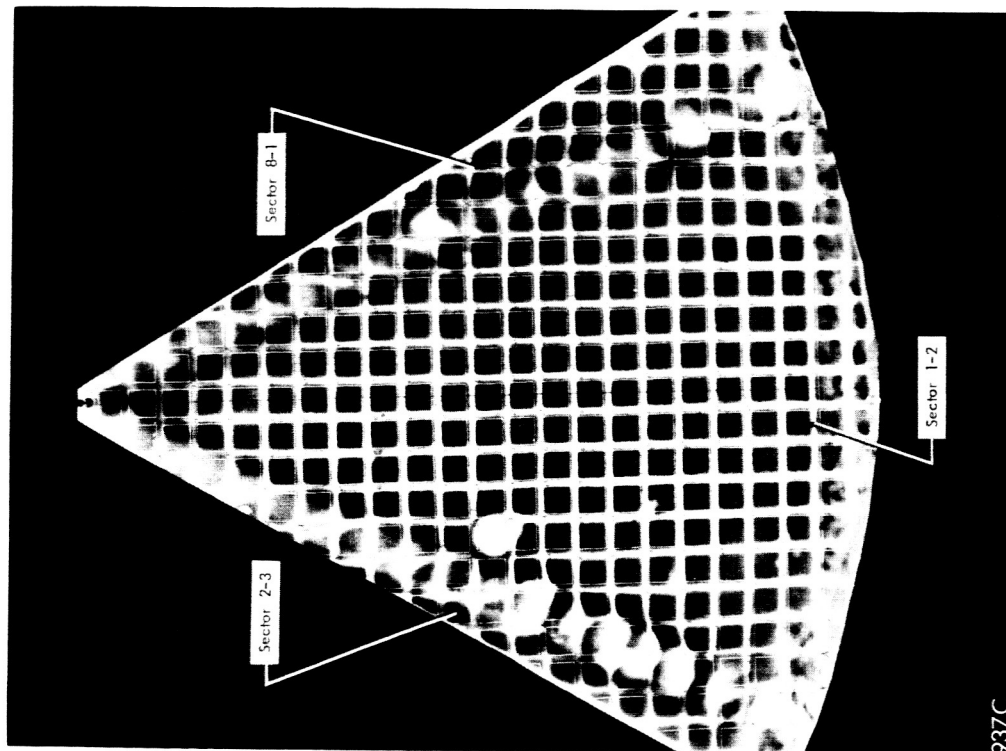
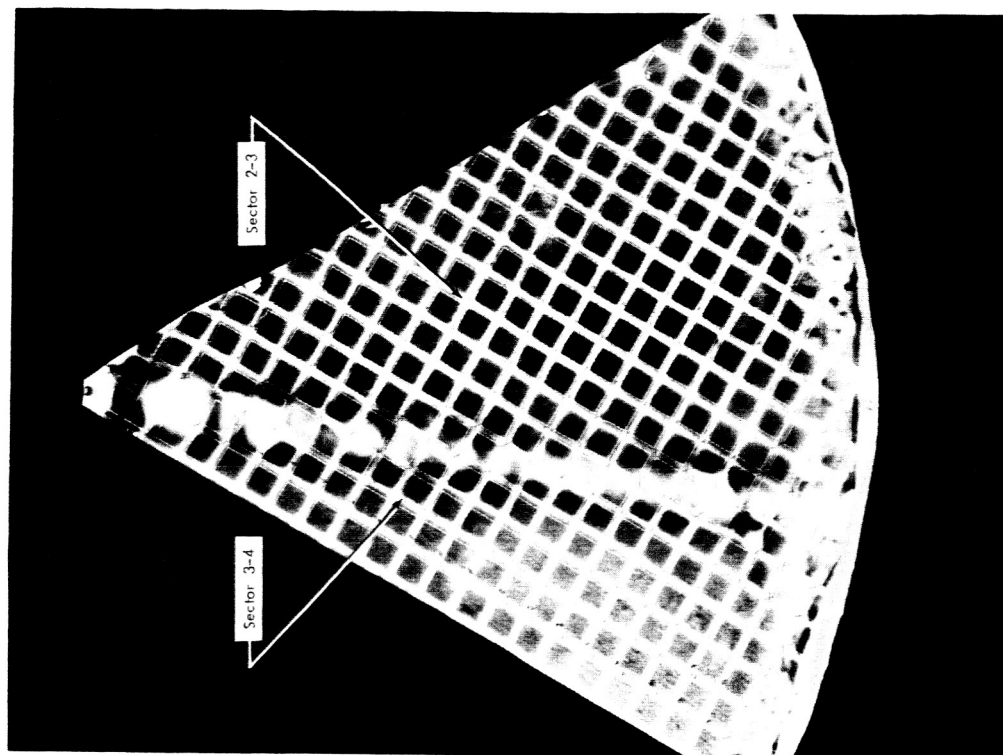
The inspection setup is shown in Figure 5.1-1 and it utilizes the optical characteristics of a paraboloid to detect any gross deviation from a true parabolic surface. Located at the focal point is a small light source which illuminates the concentrator. The reflected light from the mirror is nominally parallel to the optic axis by virtue of the optical characteristics of a paraboloid. By viewing the grid-screen arrangement which is aligned to be parallel, deviations of the reflecting surface are observed as misalignment of the grid shadow on the screen. Since the screen in this arrangement is a plexiglass sheet with the grid pattern outline on it, rapid inspection and a permanent record is made by placing photographic paper underneath the plexiglass for short period exposure. Typical inspection photographs are shown in Figure 5.1-2.

Each grid increment represents an inspection data point for which a specific surface deviation is obtained from the inspection photograph by measuring the



GEOMETRIC SURFACE ERROR INSPECTION RIG

FIGURE 5.1-1



INSPECTION PHOTOGRAPH'S

mismatch (Δ) of the grid shadow with respect to the grid pattern on the screen. The geometric relationships by which the surface rotation is calculated is shown schematically in Figure 5.1-3. Surface translation is neglected in this calculation since, for this quality concentrator, translation effects are very small compared to surface normal rotations.

These data points (approximately 1600 grid increments per collector) were then investigated statistically to determine the distribution of errors. Figure 5.1-4 shows a histogram of the data and the corresponding statistically determined normal distribution representation.

Inspections were performed at various stages of fabrication to identify specific sources of error and to aid in accurate extrapolation to a 20 and 30 foot diameter collector. The following sequence of optical inspections was performed:

1. Glass master tool with silvered convex surface. This inspection did not evaluate the glass tool errors since the effects of refraction through the glass distorted the true surface condition. However, this inspection represented a reference to be used as the basis for evaluating observed changes in subsequent inspections of stretched parts through the glass with the silvering removed.
2. All aluminized panels as stretched and before trimming. This evaluates the replication accuracy of the stretch forming process.
3. All aluminized trimmed sectors. This evaluates the effects of the trimming operation.
4. The final assembly of sectors and joints under vacuum bagging before curing.
5. Same as 4, but after adhesive curing.
6. Same as 5, but without vacuum bag. Inspections 4, 5, and 6 provide comparisons from which error induced by the shell assembly can be evaluated.

FIGURE 5.1-3
GEOMETRIC SURFACE ERROR INSPECTION RIG SCHEMATIC

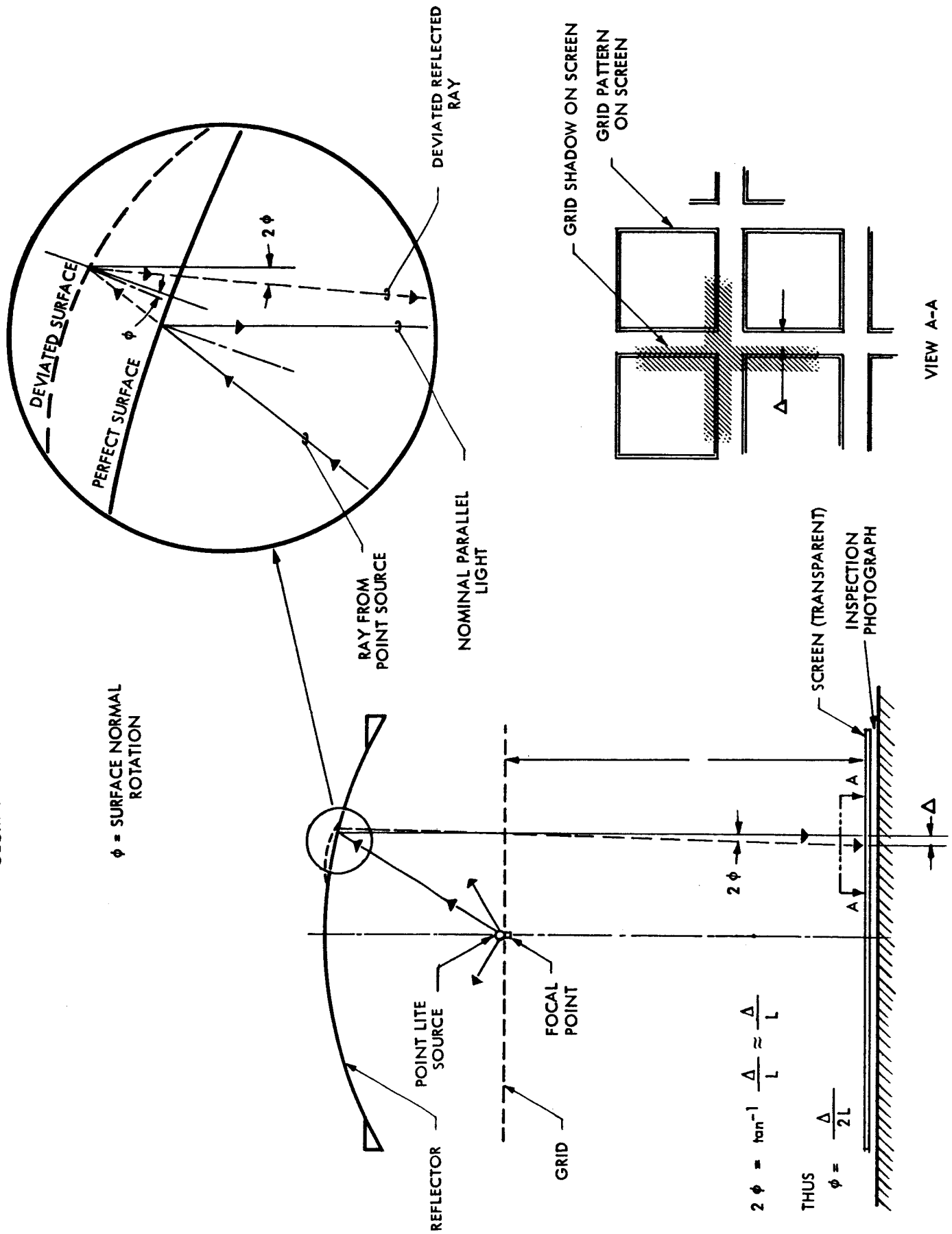
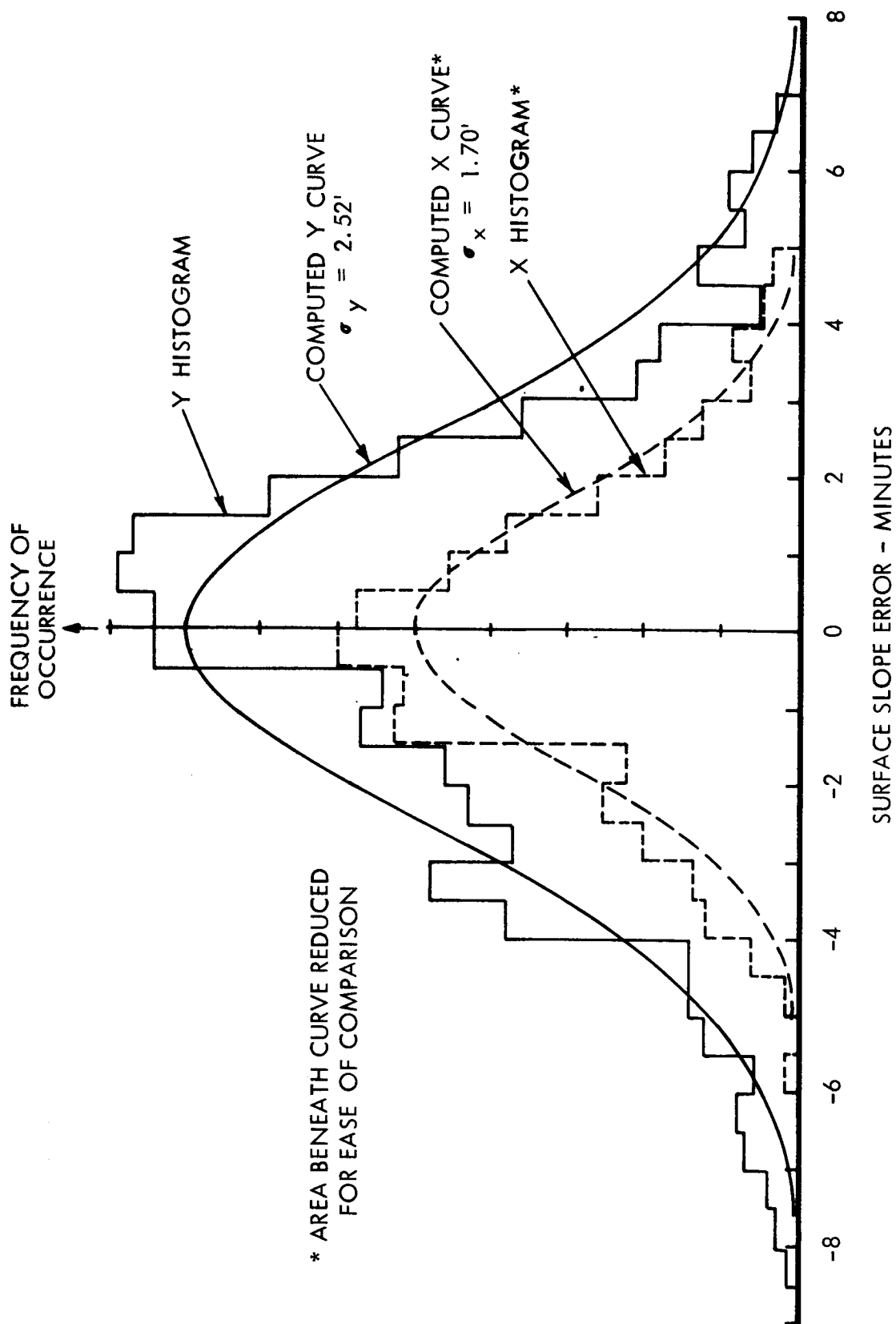


FIGURE 5.1-4
DISTRIBUTION OF SURFACE SLOPE ERRORS IN
X AND Y COORDINATE DIRECTIONS



7. Cured shell and support ring assembly. This evaluates the effects of bonding the torus to the shell.
8. Same as 7, but without the glass master in place. This provides an absolute measure of surface errors since the effects of light refraction through the glass master is eliminated.

Statistical investigation of the data resulting from this series of optical inspections resulted in the identification of the error sources shown in Table 5.1-1.

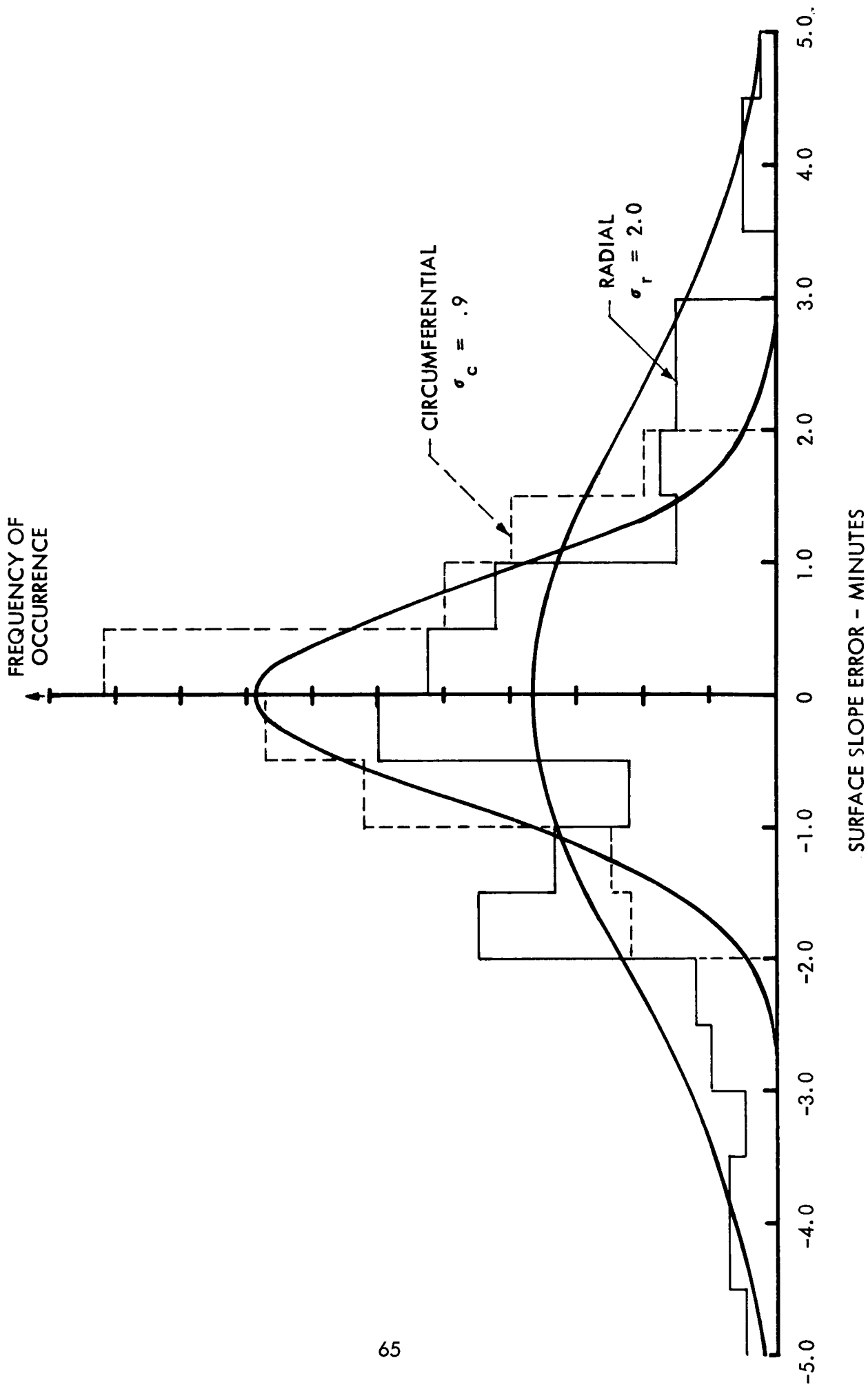
TABLE 5.1-1
MEASURED SURFACE ERROR CHARACTERISTICS

| | <u>$\Delta \sigma$</u> |
|-------------------------------------------------|-----------------------------------|
| Stretch replication | .82' |
| Trimming | .09' |
| Assembly (including torus) | .48' |
| Tooling (glass master) | .70' |
| Total measured standard deviation $\sigma =$ | 2.09' |

These results were extrapolated to the large diameter collector values shown in Table 4.2-1. It is seen that the measured trimming errors (.09') are very small when represented as a normal distribution. For this reason they were combined with measured seam distortions in the final assembly and they are considered as a localized error involving 2% of the total surface area as measured from the five foot diameter inspection photographs.

In addition to these comparison inspections and the final assembly inspection as represented in Figure 5.1-4, the results were analysed in the radial and circumferential directions to get a direct application to the two dimensional surface error model used in the theoretical performance analysis discussed in Section 4.2.2.2. This representation of results is shown in Figure 5.1-5. Again the normal distribution is approximated and the two dimension characteristic is apparent.

FIGURE 5.1-5
CIRCUMFERENTIAL AND RADIAL ERROR DISTRIBUTION



For additional discussion of the inspection procedure and results see reference (9).

In summary, the results of these five foot diameter stretch formed mirror inspections which are of direct value to the Brayton study are as follows:

1. The normal or Gaussian distribution of surface errors as represented by the standard deviation parameter (σ) is a valid model for analytical investigations.
2. A non-symmetric two dimensional model with $\sigma_c = 1/2 \sigma_r$ was the approximate relationship which was observed (see Figures 5.1-4, 5.1-5).
3. Sources of error and their magnitudes ($\Delta\sigma$) were determined as related to the various manufacturing steps.

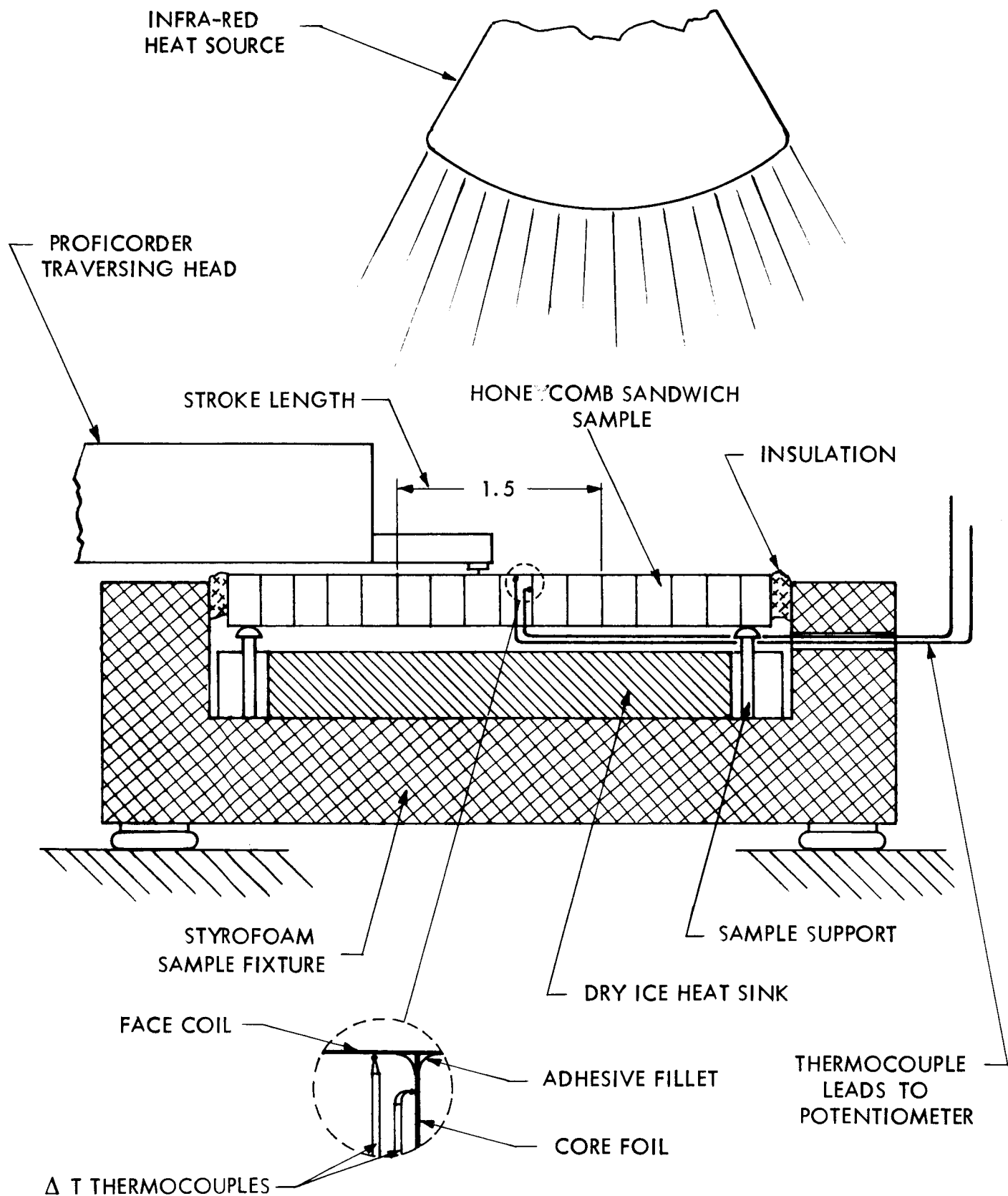
5.2 Honeycomb Markoff Investigation

The use of honeycomb sandwich material in the structural design presents the possibility of core cell markoff or "show-thru" on the mirror face. Also, the use of epoxy adhesives presented differential thermal expansion conditions which could lead to optical distortions. To investigate and eliminate these effects, small specimens of honeycomb sandwich material having various facing thicknesses were fabricated and inspected under thermal gradient conditions.

The specimen holder, shown in Figure 5.2-1, was designed to apply anticipated thermal environments to the specimens while mounted on a Proficorder waviness inspection instrument as shown in Figure 5.2-2. A heat lamp was used as the heat source and dry ice in an insulated enclosure was used as the heat sink. Temperature measurements were made using copper-constantan thermocouples with potentiometer readout. The thermocouples were applied to the front face and to the core walls during sandwich fabrication so that the temperature differential across the adhesive bond could be measured.

Typical Proficorder waviness traces are shown in Figure 5.2-3 for the "as fabricated" specimens. A typical trace obtained at estimated orbital equili-

FIGURE 5.2-1
HONEYCOMB MARK-OFF INSPECTION SCHEMATIC

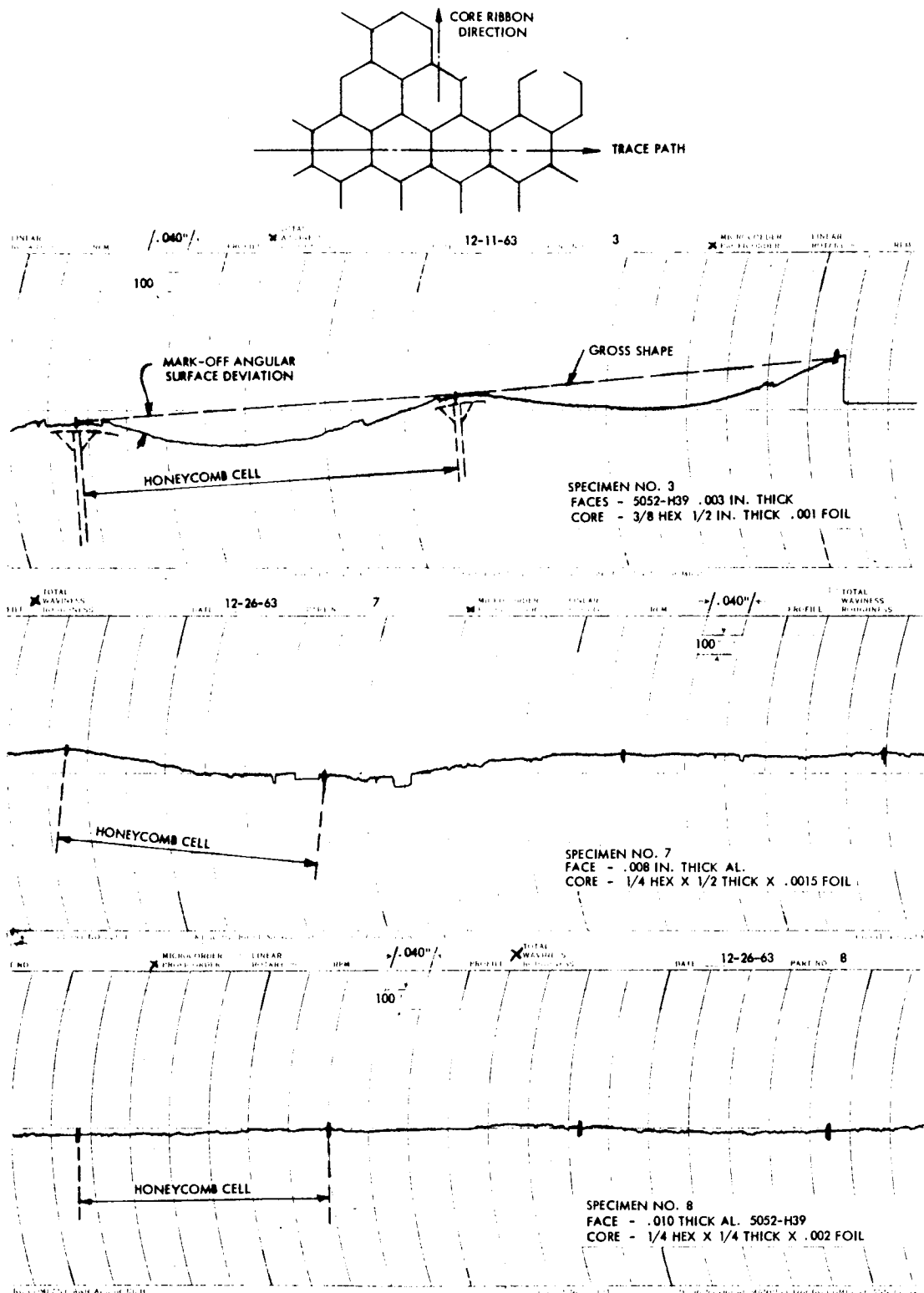




PROFICORDER WAVINESS INSPECTION INSTRUMENT

FIGURE 5.2-2

FIGURE 5.2-3
PROFICORDER WAVINESS TRACES "AS FABRICATED" CONDITION
ROOM TEMPERATURE



brium temperature and with a temperature differential across the bond is shown in Figure 5.2-4. These traces were used to investigate only the cell markoff characteristics. Some traces display what appears to be large amplitude waviness but this is due to the general curvature of the specimen.

The maximum slope for each cell was averaged from the specimens and plotted in Figure 5.2-5 to show the markoff characteristic versus face thickness for honeycomb sandwich materials. It is seen that very little distortion is encountered even under anticipated orbital thermal environments, when the face thickness is in the .008 to .010 inch range.

Based upon these observations, an .008 inch optical face has been selected for the Brayton collector design and the values measured have been used in the discussions of Section 4.2.1.1 and in the performance calculations. Final selection of the optical face thickness must be based upon development hardware evaluations where the markoff effects on a full panel can be determined.

5.3 Micrometeoroid Erosion Investigation

In the design of a solar concentrator for space applications, all the elements of the orbital environment-vacuum, penetrating and ultra-violet radiation, and meteoroids must be carefully considered. The extremely small meteoric particles are of particular concern with respect to optical surfaces due to the potentially large number of impacts involved. Experimental investigations (10) have been conducted at NASA Lewis in an attempt to predict the effect of micrometeoroids upon optical surfaces.

During the Brayton cycle concentrator study program reflective specimens were prepared by TRW and delivered to NASA Lewis for simulated micrometeoroid erosion testing. Reflectivity measurements were performed on the specimens before and after testing for comparison. Analysis and computations were performed to investigate the test results and the various parameters of the orbital micrometeoroid environment as related to the specific Brayton Cycle concentrator design.

5.3.1 Specimen and Test Description and Results

Six different types of reflective specimens were prepared which covered the range of possible aluminum solar mirror surfaces. Descriptions and test

FIGURE 5.2-4

PROFICORDER WAVINESS TRACES AT ORBITAL EQUILIBRIUM TEMPERATURE

SPECIMEN NO. 6

FACES - .010 THICK AL. 5052-H39

CORE - 1/4 HEX. X 1/4 THICK X .002 FOIL

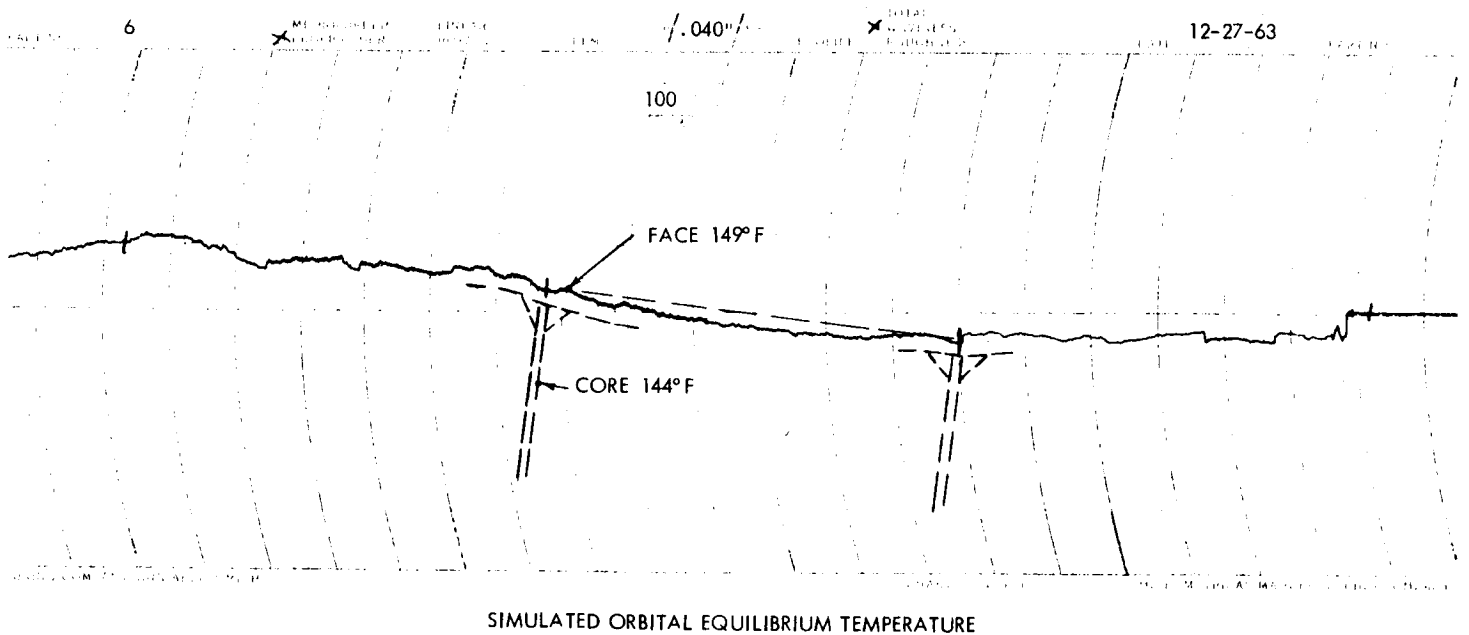
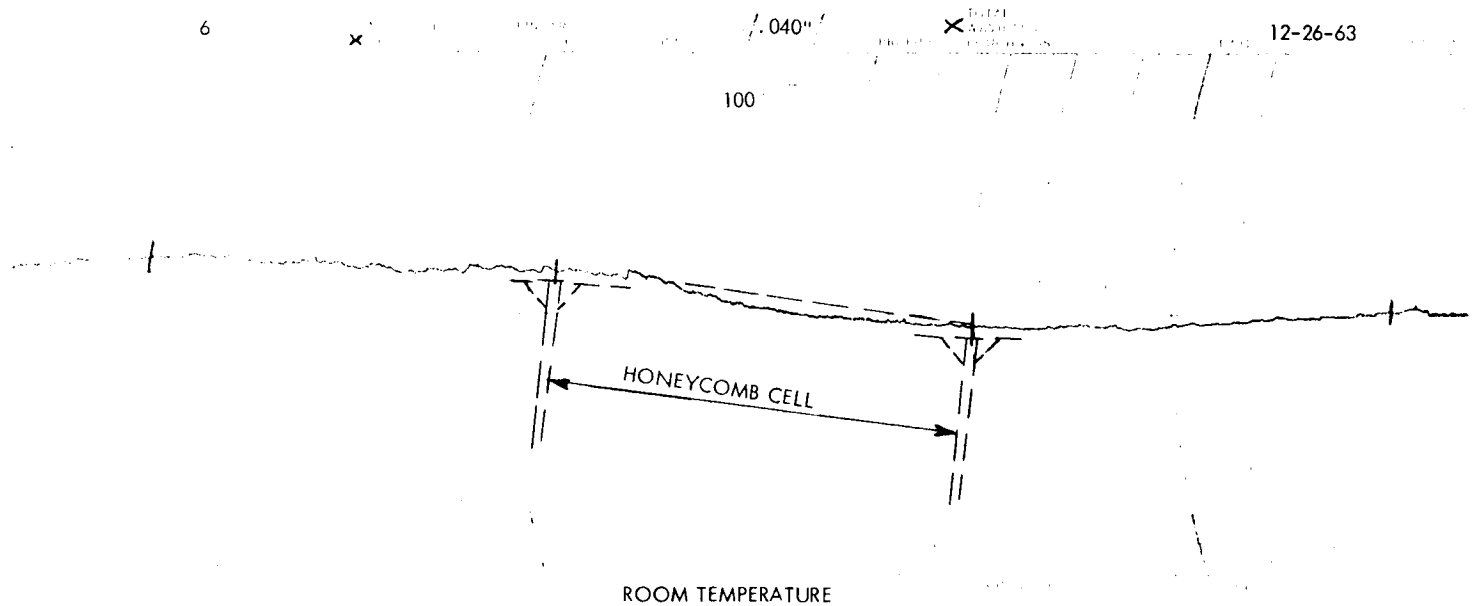
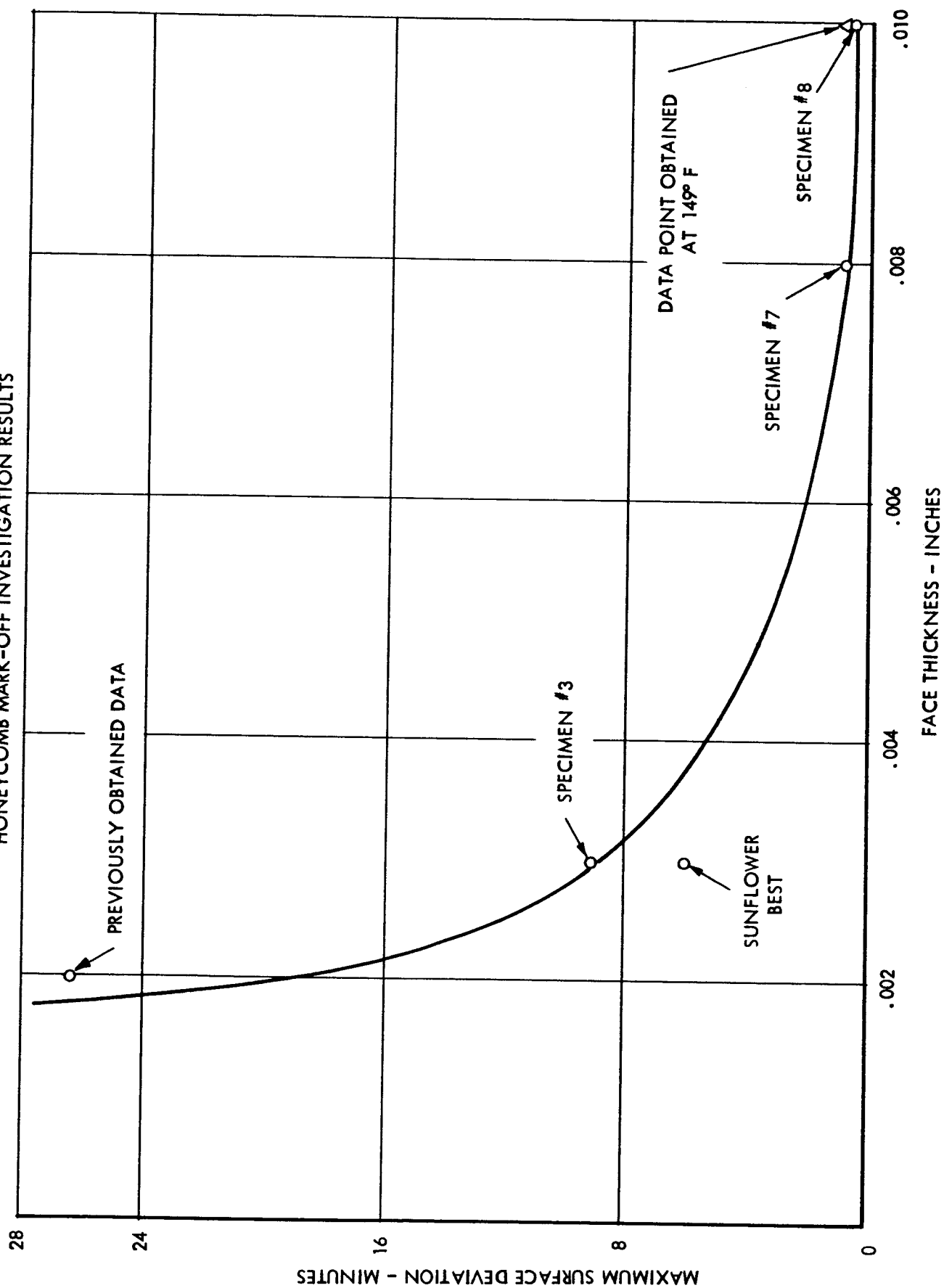


FIGURE 5.2-5
HONEYCOMB MARK-OFF INVESTIGATION RESULTS



results are shown in Table 5.3-1. Typical specimen details are shown in Figure 5.3-1.

These specimens were impacted by micron-size particles of SiC which were accelerated by aerodynamic drag to gas speeds in a 3 inch shock tube. For a description of the experimental equipment and procedure see reference 10.

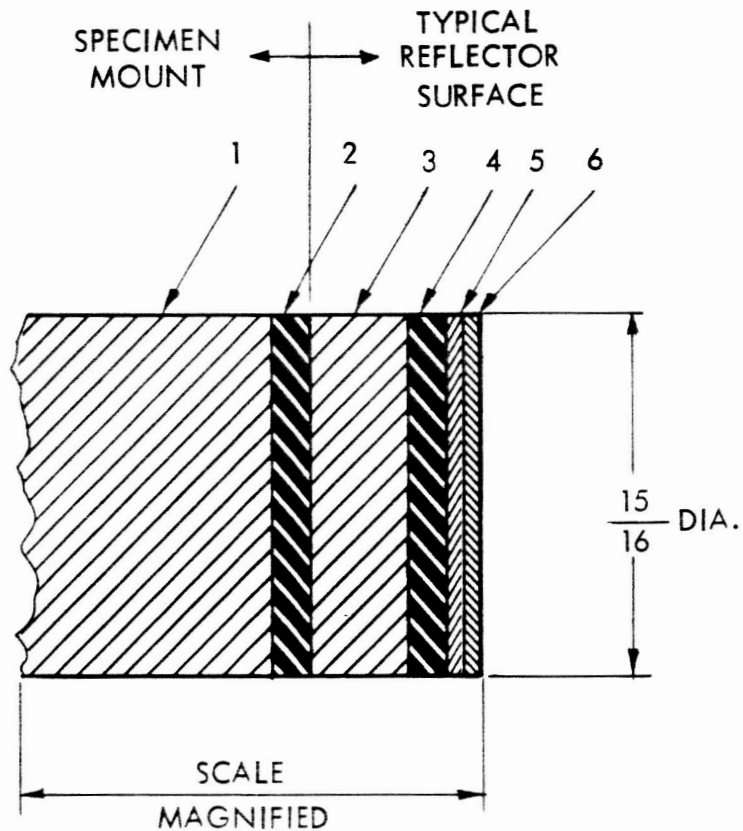
In Table 5.3-1, it is seen that the erosion environment which each specimen has seen is characterized by the total kinetic energy ($\sum 1/2 M_i V_i^2$) of the cloud of SiC particles impinging on the 15/16 inch diameter specimen. The reflectance measurements before and after testing were made at the Thermal Radiation Laboratories of TRW Space Technology Laboratories Inc. Typical spectral results for specimen No. 12 are shown in Figure 5.3-2. The measurements consist of the near normal directional total reflectance which includes all reflected light, and separately, the diffuse component which is only the non-specular or scattered light. The specular reflectance, then, is the difference between the total and the diffuse component and is shown as the dashed curve in Figure 5.3-2 for the "after" test condition. The "before" testing specular reflectance is very close to the total reflectivity.

Since these reflectance measurements are in the wave length range of the solar spectrum and the solar energy contribution varies with wave length, an integrated value of solar reflectance can be obtained from these measurements which characterizes the surface as a solar energy mirror. These integrated solar reflectance values are presented in Table 5.3-1 and from them the comparative degradation of the surfaces can be determined.

5.3.2 Experimental Results Discussion

The shock tube experimental results for the epoxy coated solar mirrors shown in Table 5.3-1 cannot be accurately extrapolated to the space environment from the limited testing which was performed. One reason for this is because of the nature of the craters formed by the SiC particles. The nature of the reflective degradation can be seen in Figures 5.3-3 and 5.3-4 which are photomicrographs of a portion of the 15/16 inch diameter specimen. Figure 5.3-3 shows the typical appearance of a specimen before testing and specimen No. 12 after testing. The damage, in most cases, can be observed as resulting from individual

FIGURE 5.3-1
SHOCK TUBE EROSION SPECIMEN NO. 12



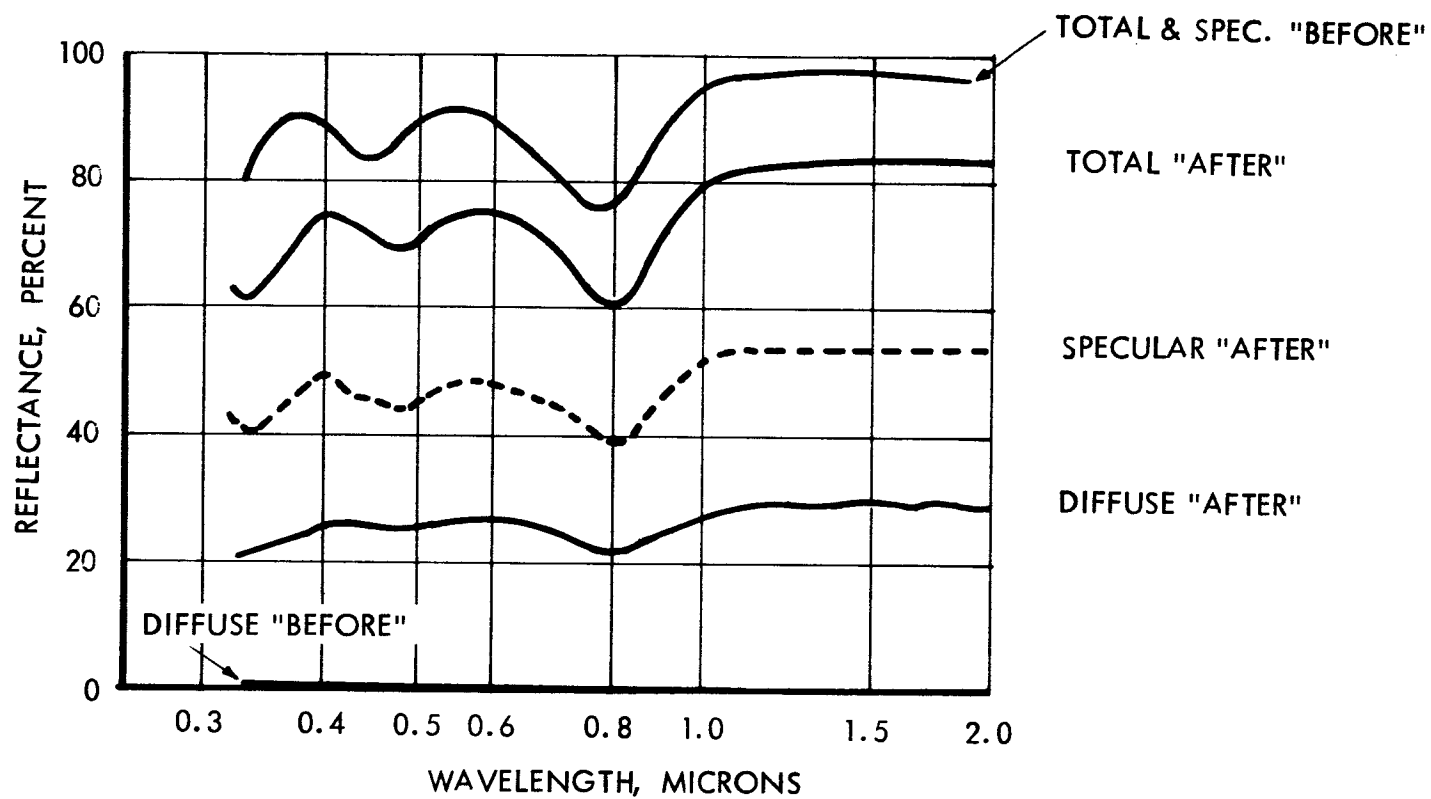
- LAYER 1: .063 THICK ALUMINUM BACKING
 2: EPOXY ADHESIVE - BONDMASTER 773
 3: .016 THICK ALUMINUM ALLOY 3003-0
 4: EPOXY COAT. .0003 - .0005 THICK - BEE CHEM. D5H-30004
 5: OPAQUE ($\sim 600 \text{ \AA}$) VACUUM EVAPORATED PURE ALUMINUM
 6: 2300 \AA THICK SiO_x VACUUM EVAPORATED

TABLE 5.3-1

SHOCK TUBE EROSION RESULTS

| Specimen Test No. | TRW Part No. | Description | Total Kinetic Energy of Shock Tube Cloud (joules) | Solar Reflectance Before Test | Solar Reflectance After Test | Degradation | Degradation per joule |
|----------------------|-----------------|------------------------------------------------------------------------------------------|---------------------------------------------------------------|-------------------------------------|------------------------------------|-------------|-----------------------------|
| 1 | 818090 | Al substrate .016/600 Å vac. deposited | .58 | .91 | .70 | .21 | .362 |
| 4 | 818091 | Al(.016)/Epoxy coat (.0005)/ 600 Å vac. dep. Al | 1.01 | .93 | .68 | .25 | .248 |
| 8 | 818092 | Al (.016)/Epoxy coat (.0005)/ 2000 Å vac. dep. Al | 1.12 | .93 | .71 | .22 | .196 |
| 12 | 818093 | Al (.016)/Epoxy (.0005)/ 600 Å vac. dep. Al/2300 Å SiO _x | .9 | .89 | .75 | .14 | .155 |
| 14 | 818094 | Al (.016)/Epoxy (.0005)/ 3000 Å SiO _x /600 Å Al/2300-Å SiO _x | 1.01 | .89 | .71 | .18 | .178 |
| 16 | 818095 | Al (.016)/Epoxy (.0005)/ 3000 Å SiO _x /600 Å al/ 2 μ SiO _x | 1.26 | .86 | .64 | .22 | .175 |

FIGURE 5.3-2
SPECIMEN NO. 12 REFLECTANCE



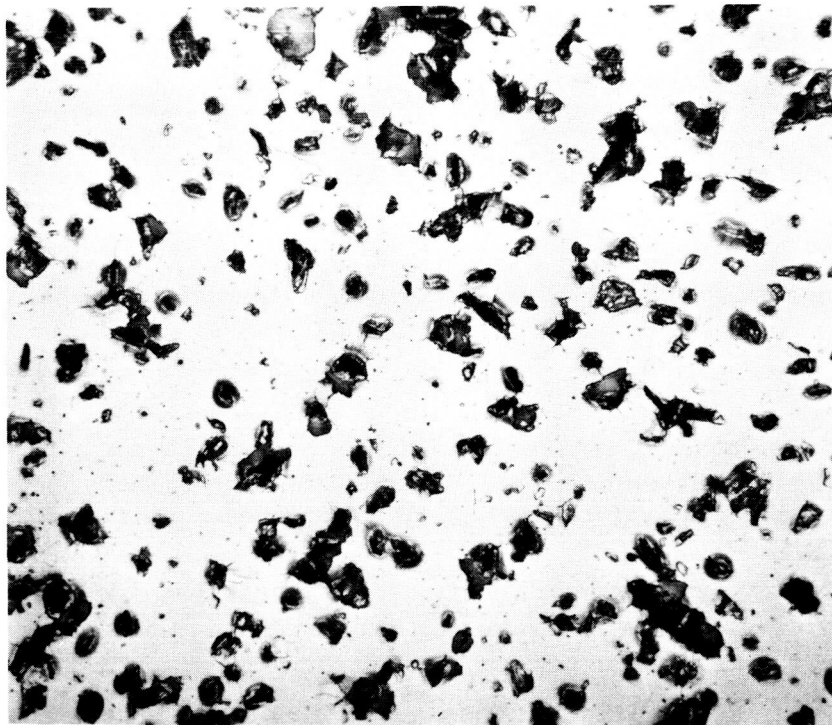
SOLAR ABSORPTANCE, $\alpha_s = 0.11$ (BEFORE)
 $\alpha_s = 0.25$ (AFTER)



Typical
"Before"

Scale - .1097 in = 1

Specimen No. 11 500 X



Typical
"After"

Scale - .0197 in = 1

Specimen No. 12 500 X

PHOTOMICROGRAPHS (500 X)

FIGURE 5.3-3



PHOTOMICROGRAPH SPECIMEN NO. 12 (1800 X)

FIGURE 5.3-4

craters. These craters are more like pits or chips in the hard epoxy and SiO_x coatings. Due to this irregular shape, the shock tube test results cannot be extrapolate to the space environment as in reference 10 nor even accurately utilized in cratering energy density determinations as in reference 12 because both these require a hemispherical cratering mechanism as is obtained in soft and ductile metals.

However, to associate the shock tube erosion environment and the measured degradation for comparisons, the degradation per unit of energy (joule) was calculated and is also shown in Table 5.3-1. On this degradation per joule basis it can be seen that the specimens which were coated with SiO_x displayed less degradation and therefore they may be more stable in the micrometeoroid environment of space. Of the specimens which were not SiO_x overcoated, it might be said that the epoxy substrate specimens (No. 4 and 8) displayed less degradation than the aluminum substrate specimen (No. 1).

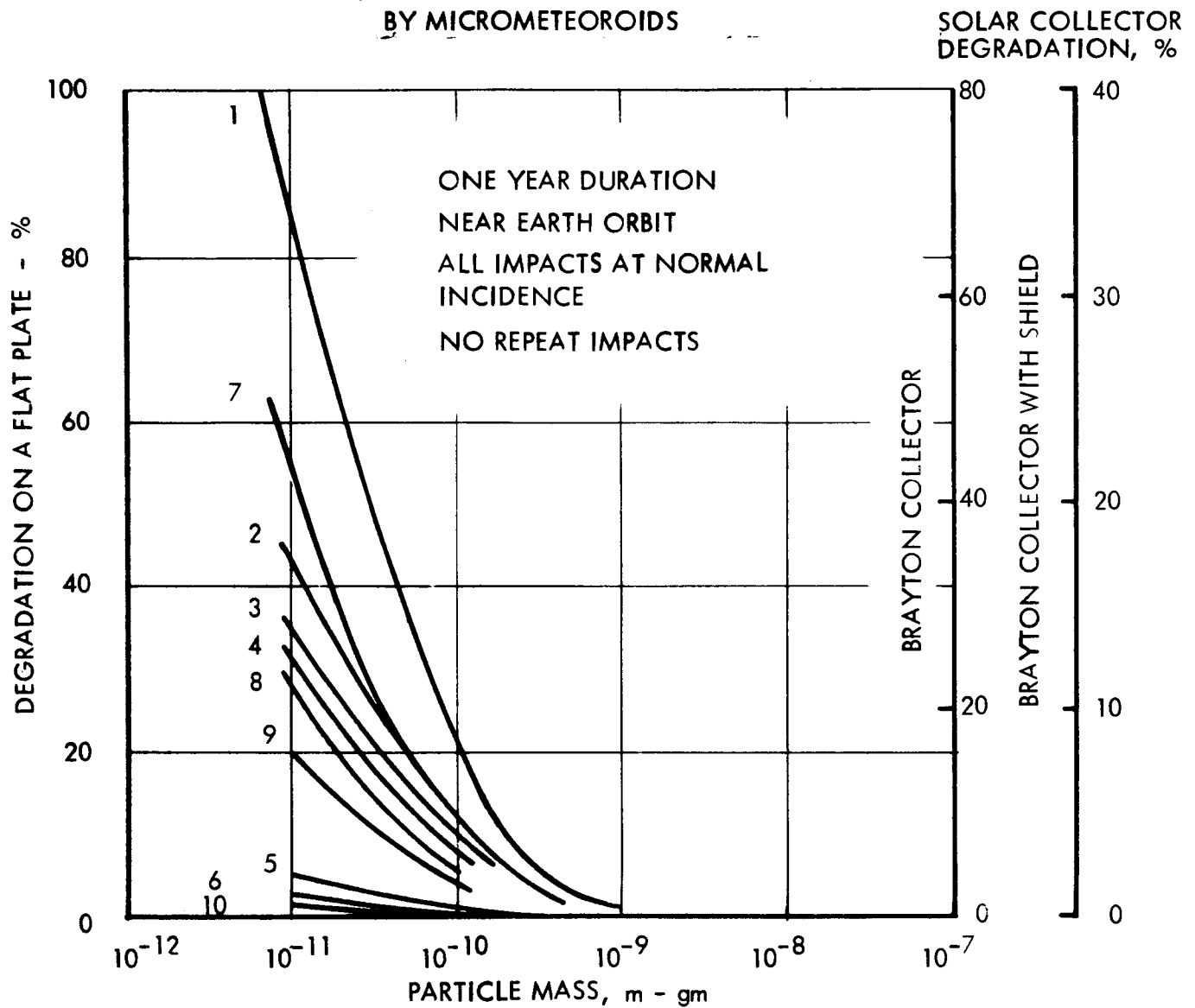
5.3.3 Predictions of Solar Mirror Degradation Due to Micrometeoroids

In considering the detailed cratering phenomena and its effects upon specular reflectors of solar radiation, the general approach has been to consider the crater areas as representative of the reflector damage. Here again assumptions of hemispherical cratering must be made. For the high velocity of micrometeoroids this may be an accurate model for even hard and brittle surfaces, such as the epoxy substrates, since at sufficiently high speeds a fluid impact region has been observed (11) where a hydraulic model describing impact is applicable.

Any predictions of degradation are highly approximate due to the many assumptions which must be made. The analysis of micrometeoroid effects upon surfaces is complicated by considerations of smaller mass particle limits, exact velocities, angles of incidence, particle density, substrate characteristics, and the actual cratering mechanism. Some discussion of these factors is presented in reference 29. Several variations of the micrometeoroid environment parameters and the possible penetration-cratering characteristics are investigated with respect to the specific Brayton Cycle concentrator geometry. The resulting range of possible degradation is shown in Figure 5.3-5 including the reduction of degradation possible with a simple mylar shield (as shown in the sketch) which

is particularly suited to the NASA Lewis Brayton system configuration. The resulting conclusion is that the unknowns of the exact space environment and the associated penetration-cratering phenomenon produce a wide range of predictable degradation. Because of this wide range, orbital experiments are necessary to provide an accurate basis for design and utilization of optical surfaces in the space environment.

FIGURE 5.3-5
PREDICTION AREA DEGRADATION
BY MICROMETEORIODS



| CURVE NO. | DEN-SITY | INFLUX DATA | PENETRATION EQUATION |
|-----------|----------|-------------|----------------------|
| 1 | 3.2 | Lewis | Bruce |
| 2 | 0.44 | " | " |
| 3 | 0.25 | " | " |
| 4 | 3.2 | Lewis | Herrmann-Jones |
| 5 | 0.44 | " | " |
| 6 | 0.25 | " | " |
| 7 | 3.2 | Whipple | Bruce |
| 8 | 0.44 | " | " |
| 9 | 3.2 | " | Herrmann-Jones |
| 10 | 0.44 | Whipple | Herrmann-Jones |
| 11 | 0.25 | " | " |

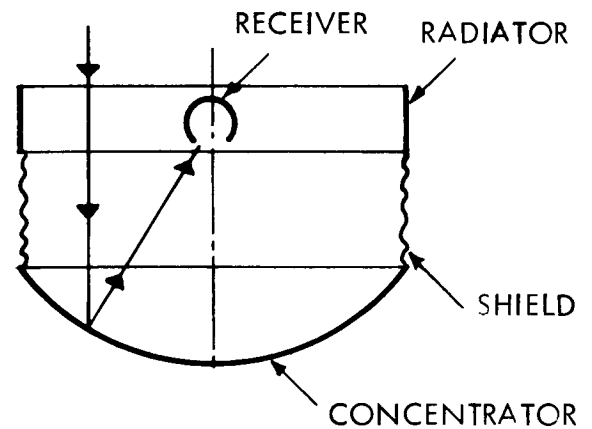
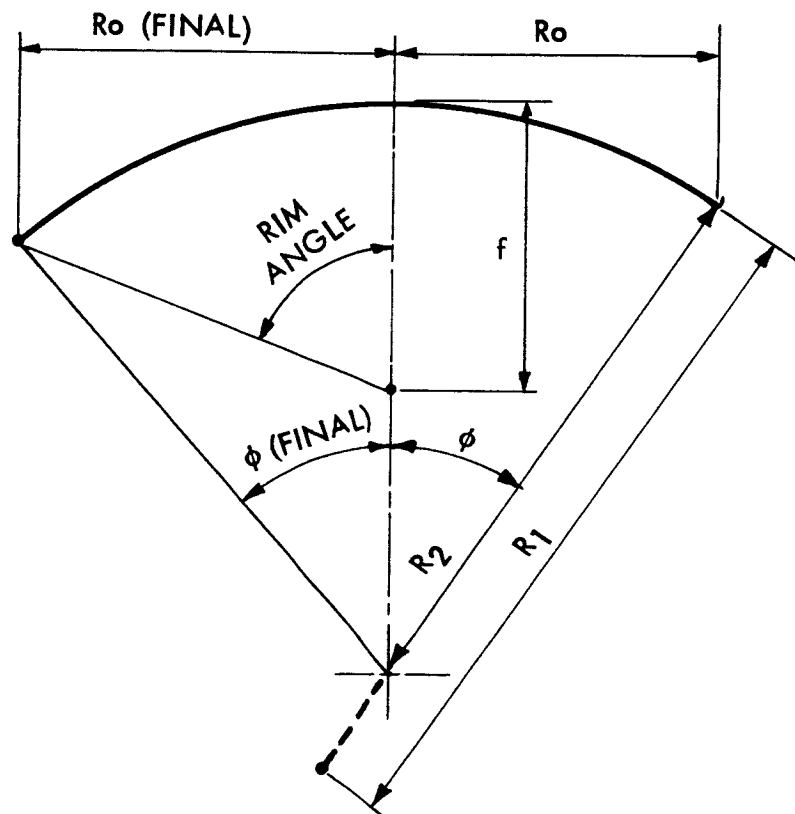


FIGURE 6.1-1
PARABOLOID GEOMETRY



- R_o = RADIUS OF PARALLEL CIRCLE = $2f \tan \phi$
 R_1 = RADIUS OF CURVATURE OF PARABOLOID ALONG MERIDIAN = $2f / \cos^3 \phi$
 R_2 = RADIUS OF CURVATURE NORMAL TO MERIDIAN = $2f / \cos \phi$
 ϕ = ANGLE BETWEEN AXIS OF SYMMETRY AND NORMAL TO THE SURFACE

6.0 STRUCTURAL ANALYSIS AND DESIGN

Analytical investigations were conducted to determine the structural design considerations which are required for the Brayton cycle solar concentrator. Both single thickness membrane and honeycomb sandwich design concepts were compared and evaluated for the required launch and orbital environment loading and a shell design was selected. Various support conditions were investigated and a structural support ring was designed.

6.1 Shell Membrane Analysis

6.1.1 Geometry

The concentrator shell geometry is indicated in Figure 6.1-1 and the membrane force notation in Figure 6.1-2. Where it has been necessary to approximate the paraboloid by a partial sphere, the radius of the sphere has been taken equal to the average of the meridian radius of curvature at the vertex and at the rim of the concentrator. For a 30 foot diameter concentrator of 60° rim angle, the radius of curvature is 312 inches at the vertex and 480 inches at the rim. The partial sphere would have a radius of curvature (R) equal to 396 inches. An expression which also can be used to approximate the paraboloid by a partial sphere is the equation for a circle passing through the collector vertex and end points;

$$R = \frac{D^2 + 4h^2}{8h}$$

where h is the depth of the paraboloid.

6.1.2 Membrane Stresses

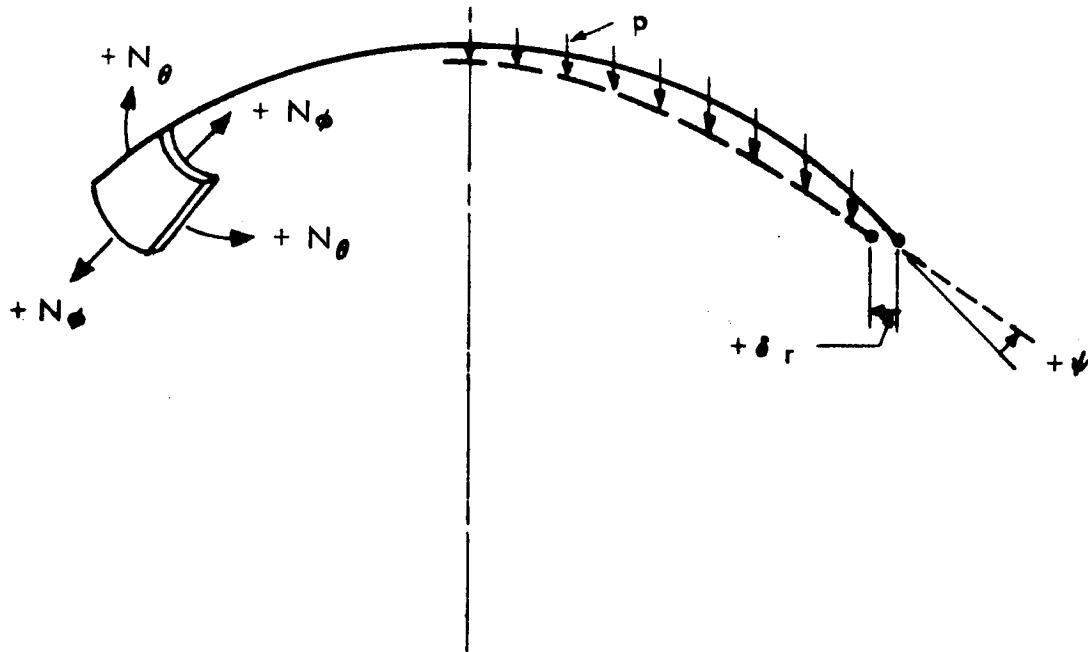
Membrane force equations for axisymmetrical body or inertial loads can be determined by considering the equilibrium of the shell. These membrane forces for both a spherical shell and a paraboloid are given by the equations shown in Figure 6.1-3; and from this plot the forces for any size concentrator may be determined.

Membrane stresses are computed by dividing by the shell thickness. For honeycomb sandwich construction, only the thickness of the faces is used in this calculation. Thus ,

$$\sigma = \frac{N}{t} \tag{6.1-1}$$

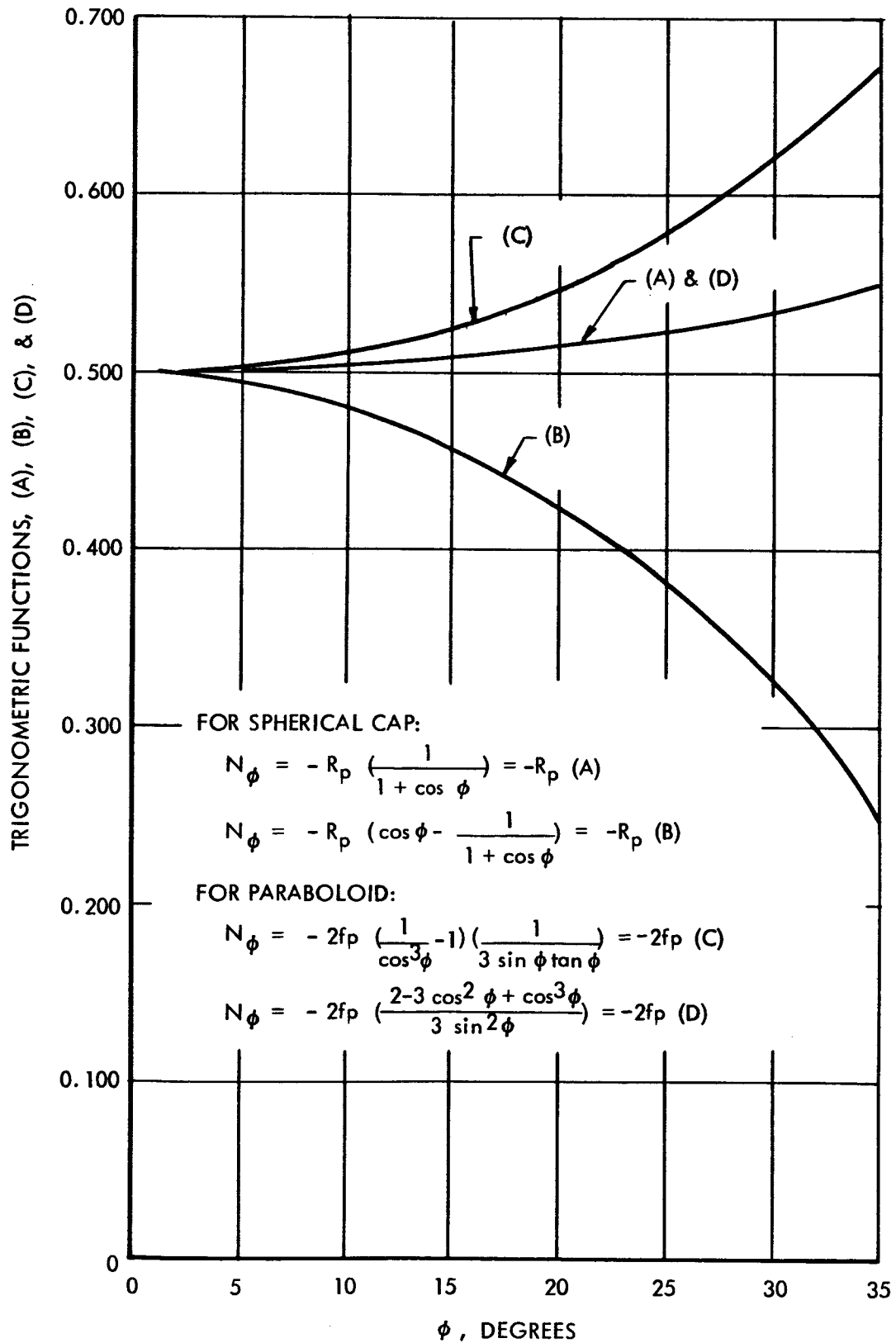
where t is the effective stress supporting thickness.

FIGURE 6.1-2
FORCE & DEFLECTION NOTATION



- N_ϕ = MEMBRANE MERIDIANAL FORCE PER UNIT LENGTH
- N_θ = MEMBRANE CIRCUMFERENTIAL FORCE PER UNIT LENGTH
- p = WEIGHT OR FORCE PER UNIT AREA
- δ_r = RADIAL DISPLACEMENT
- ψ = MERIDIANAL ROTATION

FIGURE 6.1-3
MEMBRANE FORCES FOR
SPHERICAL CAPS AND PARABOLOIDS



For inertially generated loadings (acceleration), the loading p is directly proportional to the thickness of the shell and the material density. Thus in equation 6.1-1 the thickness term cancels and the membrane stresses for an acceleration loading are independent of thickness - and only functions of material density and acceleration level. For example for the 30 foot diameter aluminum concentrator, p/t per G of acceleration is approximately 0.10 lb. per cubic inch; thus using Figure 6.1-3 ($\phi = 30^\circ$) and equation 6.1-1, the meridional stress is,

$$\sigma_\phi = \frac{N_\phi}{t} = -19.4 \text{ psi per "G"}$$

These membrane stresses are seen to be very low for aluminum concentrators.

6.1.3 Membrane Deflections

Notation and sign convention is indicated in Figure 6.1-2. The radial displacement of the parallel circle is

$$\delta_r = -\frac{R_o}{E_t} (N_\theta - \mu N_\phi) \quad (6.1-2)$$

For the spherical shell, the substitution of N_ϕ and N_θ in terms of ϕ into this expression results in

$$\delta_r = \frac{p R^2}{E_t} \sin \phi \left(\cos \phi - \frac{1 + \mu}{1 + \cos \phi} \right) \quad (6.1-3)$$

which is plotted in Figure 6.1-4. For the 360 inch diameter aluminum concentrator,

$$R = 396 \text{ inches}$$

$$E = 10 \times 10^6 \text{ psi}$$

$$\mu = 0.36$$

so that the maximum radial displacement is

$$(\delta_r)_{\max} = .00131 p/t \quad (6.1-4)$$

FIGURE 6.1-4
MEMBRANE DISPLACEMENT OF SPHERICAL CAP LOADED
BY ITS OWN WEIGHT

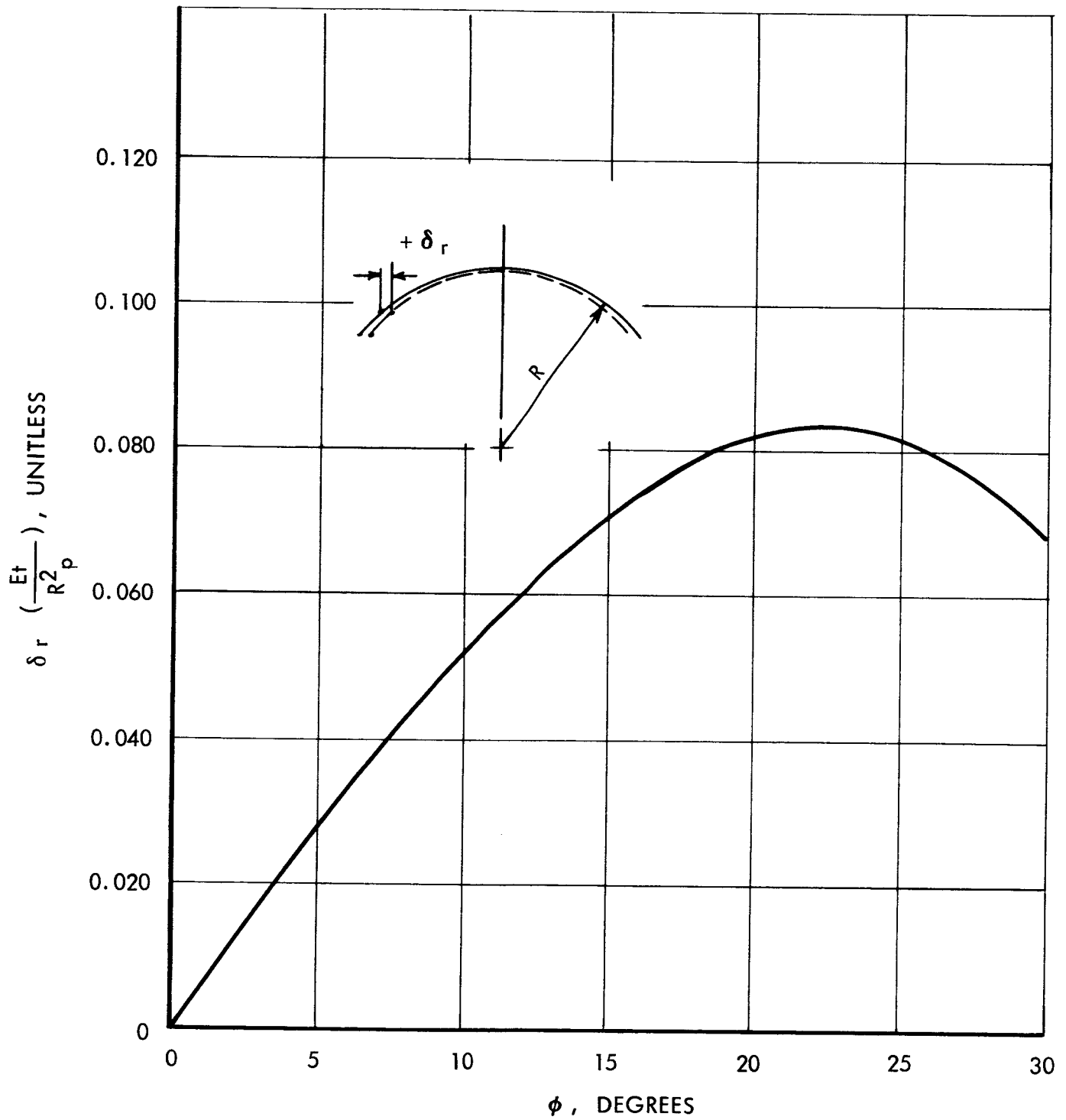
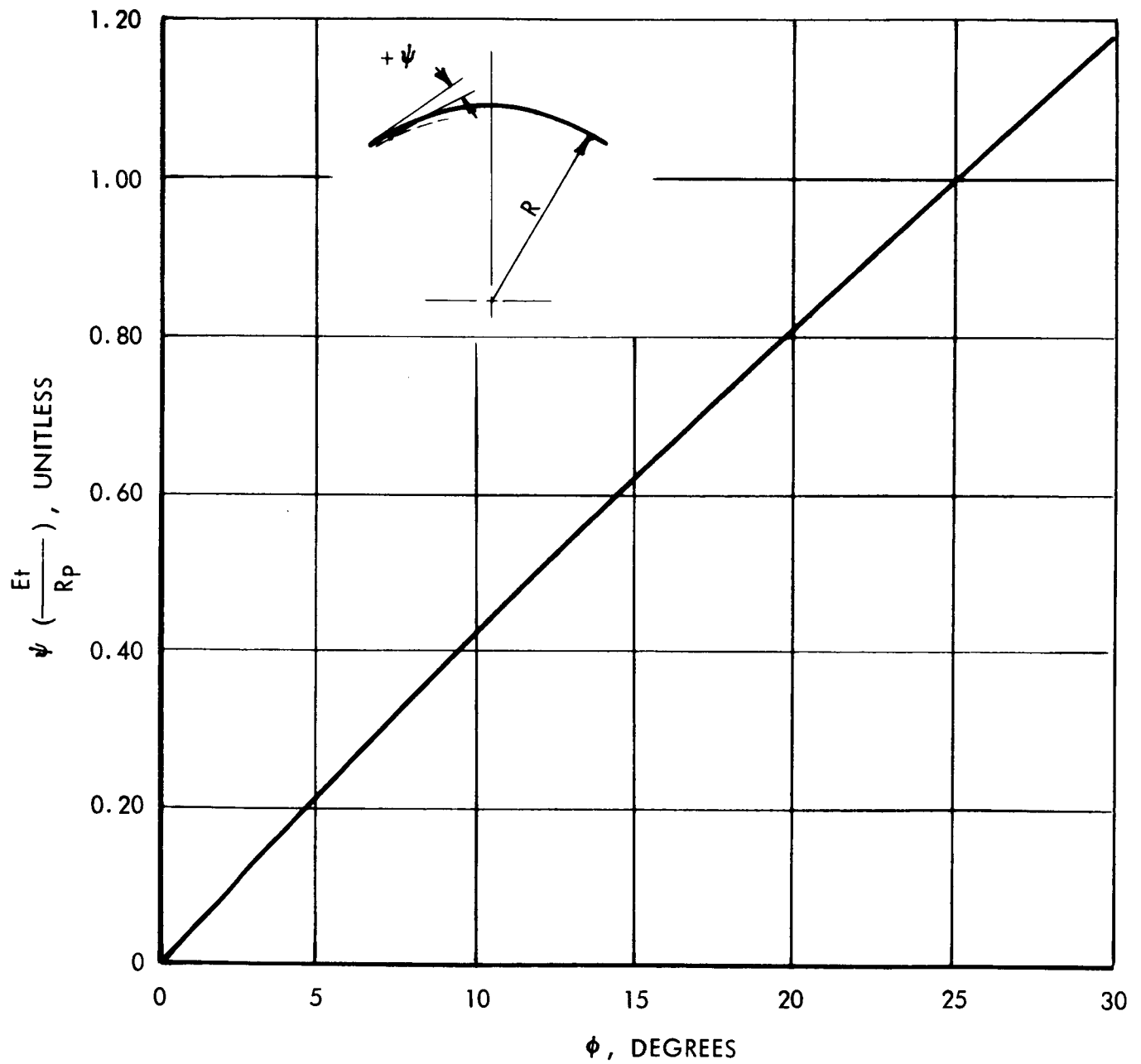


FIGURE 6.1-5
MEMBRANE ROTATION OF SPHERICAL CAP LOADED
BY ITS OWN WEIGHT



In a 1G environment, $p/t = 0.10$ or there results only a negligible deflection. Rotations are more difficult to determine. This requires the substitution into the general expression for the rotation of the meridian as obtained from reference 30.

$$\psi = \frac{\cot \phi}{R_1 Et} \left[(R_1 + \mu R_2) N_\phi - (R_2 + \mu R_1) N_\theta \right] - \frac{1}{R_1} \frac{d}{d\phi} \left[\frac{R_2}{Et} (N_\theta - \mu N_\phi) \right] \quad (6.1-5)$$

N_ϕ and N_θ in terms of ϕ must be differentiated before being evaluated. The calculation has been made only for the spherical case where $R_1 = R_2$ and where N_ϕ and N_θ are less cumbersome than for the paraboloid.

The equation reduces to

$$\psi = \frac{R_p}{Et} \left[\cot \phi (1 + \mu) \left(\frac{-2}{1 + \cos \phi} + \cos \phi \right) - \frac{\sin \phi}{(1 + \cos \phi)^2} (1 + \mu) - \sin \phi \right] \quad (6.1-6)$$

which is plotted in Figure 6.1-5. The maximum value for the 360 inch concentrator is less than 1 second of rotation for a 1G environment. As with the stresses, it will be independent of thickness in that the weight or load increased in direct proportion to t .

6.1.4 Validity of Membrane Solution

The shell must be of large radius compared to thickness - a requirement that is easily satisfied in solar concentrator design.

At the edge of the concentrator, support must be provided that will allow only a tangential meridian force to be developed. A properly sized support ring will provide the necessary reaction but not without restraining the shell normal to its edge. The result is discontinuity stresses which will be discussed in Section 6.2.

6.2 Support Ring Shell Discontinuity Considerations

6.2.1 Compatibility Equations

A shallow shell would like to do one thing under load while the support ring would like to respond differently. This is shown in Figures 6.2-1 and 6.2-2.

Under the action of positive pressure on the convex side of the shell, the membrane equations indicate a radial inward displacement of the shell edge. The membrane force reaction on the ring, on the other hand, causes the ring to displace radially outward. These two displacements must be compatible - the same is true, of course, for the shell edge and ring rotation under load. To bring the deformation of the shell edge into accordance with the deformation of the ring requires that redundant moments and forces exist at the junction. These are most conveniently determined by writing the compatibility equations in terms of edge influence coefficients.

These are defined as follows:

δ_H^S and Θ_H^S = displacement and rotation of shell due to a unit force acting in the direction of the unknown force H.

δ_M^S and Θ_M^S = displacement and rotation of shell due to a unit moment acting in the direction of the unknown moment M.

Similar coefficients with a superscript R are defined for the ring. Sign convention for the redundant moment M and force H as well as the displacement and rotation is indicated in Figure 6.2-3. The effect of a 1 pound force per inch of shell circumference is shown in Figure 6.2-4 as an example of an edge influence coefficient.

Let the total horizontal displacement of the shell under load be δ_T^S and that of ring be δ_T^R . In order that the displacement of the ring be compatible with that of the shell,

$$\delta_T^R = \delta_T^S$$

or

$$-\delta_H^R H + \delta_M^R M - \delta_p^R p = \delta_H^S H - \delta_M^S M + \delta_p^S p \quad (6.2-1)$$

FIGURE 6.2-1
EDGE FORCE AND DISPLACEMENTS
ACCORDING TO MEMBRANE THEORY

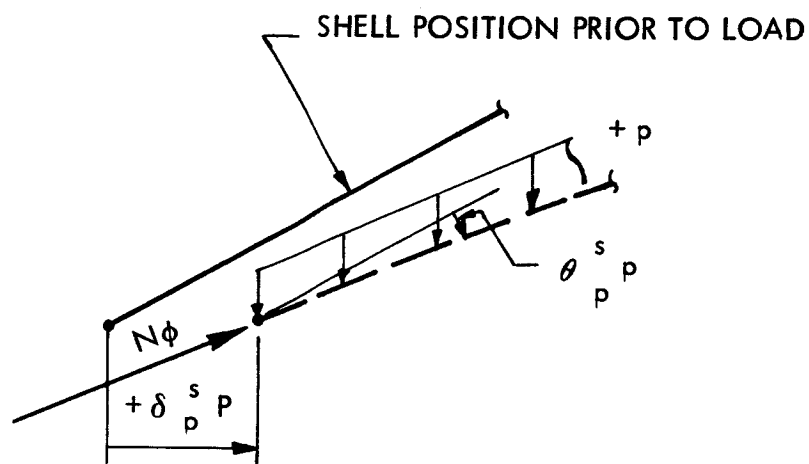


FIGURE 6.2-2
MEMBRANE REACTION ON RING

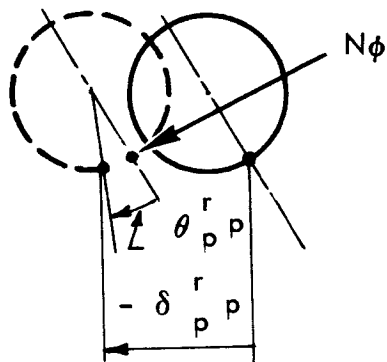


FIGURE 6.2-3
SIGN CONVENTION ATTACHED TO
REDUNDANT MOMENT AND FORCE

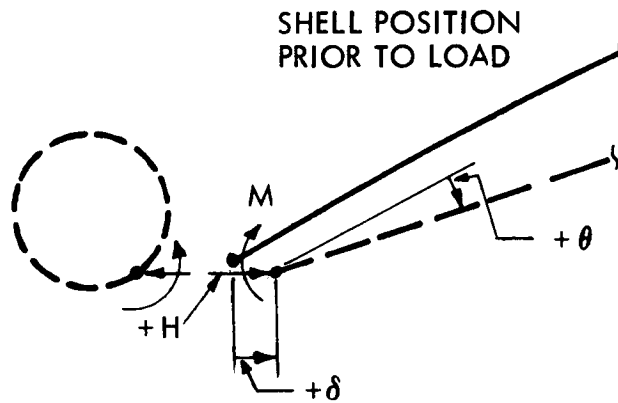
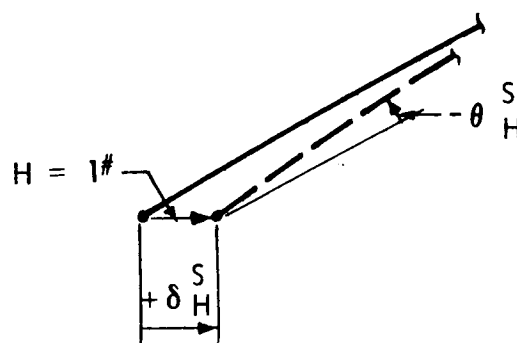


FIGURE 6.2-4
EXAMPLE OF EDGE
INFLUENCE COEFFICIENT



δ_p^S is the horizontal displacement of the shell in accordance with membrane theory when the shell is under the action of the applied pressure p . The direction of loading is chosen so as to cause a positive (radial inward) displacement of the shell edge; that is, the pressure is acting positively on the convex side of the shell. δ_p^R is the displacement of the ring when loaded by the membrane force reaction.

Rotation compatibility requires that

$$\theta_T^R = \theta_T^S$$

or

$$\theta_H^R - \theta_M^R + \theta_p^R = -\theta_H^S + \theta_M^S + \theta_p^S \quad (6.2-2)$$

The response of the ring to the membrane force can be written in terms of edge coefficients as follows:

$$\delta_p^R = \delta_H^R \cos \phi + \delta_M^R \cdot r N_\phi \quad (6.2-3)$$

and

$$\theta_p^R = \theta_M^R \cdot r N_\phi + \theta_H^R \cdot N_\phi \cos \phi \quad (6.2-4)$$

The moment going into the ring is $r N_\phi$ where r is the radius of the ring cross section. The force that displaces the ring is taken to be $N_\phi \cos \phi$. The vertical deflection of the ring, either simply supported or on a limited number of supports, is neglected in this analysis.

Substitution of Equations 6.2-3 and 6.2-4 into Equations 6.2-1 and 6.2-2 and rearranging results in:

$$H (\delta_H^R + \delta_H^S) - M (\delta_M^R + \delta_M^S) + \delta_H^R N_\phi \cos \phi + \delta_M^R r N_\phi + \delta_p^S p = 0 \quad (6.2-5)$$

$$-H (\theta_H^R + \theta_H^S) + M (\theta_M^R + \theta_M^S) - \theta_H^R N_\phi \cos \phi - \theta_M^R r N_\phi + \theta_p^S p = 0 \quad (6.2-6)$$

From these two simultaneous equations, the redundants M and H can be determined. The influence coefficients are evaluated using expressions provided in standard strength of material texts. The section to follow applies the method to a specific geometry.

6.2.2 Shell Influence Coefficients

Roark (13) has formulas for radial displacement and edge rotation of shells of revolution when loaded with either a uniform radial force or moment. For a 30 foot diameter paraboloid of 0.128 inch equivalent thickness, there results

$$\delta_H^S = .00943$$

$$\theta_H^S = \delta_M^S = .00358$$

$$\theta_M^S = .00268$$

The equality of θ_H^S and δ_M^S follows from equal work being done when a unit moment acts on displacement δ_M^S as when a unit force acts on a rotation θ_H^S .

6.2.3 Ring Influence Coefficients

Consider first the displacement of the ring due to a unit force acting in the direction of H, δ_H^R . Assuming the ring is tangent to the shell, the displacement at the ring-shell junction is actually made up of two components. The first is the displacement resulting from 1 pound passing through the center of rotation of the section. The second results from the moment that is imposed on the ring cross section because of the eccentricity of the ring-shell junction to the center of rotation.

For thin rings of circular cross section, the two components together equal, approximately

$$\delta_H^R = \frac{3 R_o^2}{2 E \pi h r}$$

The displacement due to a unit moment and the rotation due to a unit force will equal

$$\delta_M^R = \theta_H^R = \frac{R_o^2 \cos \phi f}{E \pi h r^2}$$

The ring rotation due to a unit moment is

$$\theta_M^R = \frac{R_o^2}{E \pi h r^3}$$

These influence coefficients are evaluated for an aluminum ring of circular cross section where $r = 2.35$ inch and $h = .095$ inch. For this specific geometry, then,

$$\delta_H^R = .00695$$

$$\delta_M^R = \theta_H^R = .00171$$

$$\theta_M^R = .000825$$

6.2.4 Shell Membrane Displacement and Rotation

The displacement and the rotation of the edge of the shell according to membrane theory is required before the redundant moment and force can be determined from the two simultaneous equations. Figures 6.1-4 and 6.1-5 provide the required information so that for the above example

$$\theta_p^S = .0039 p$$

$$\delta_p^S = .0898 p$$

In honeycomb sandwich construction, the flanges carry the membrane forces. Therefore, in the displacement and rotation equations, the thickness t has been taken equal to 0.012 inch for the example cited.

6.2.5 Solving the Compatibility Equations

Substituting the influence coefficients of Section 6.2.2 and 6.2.3 into the simultaneous equations of Section 6.2.1 and simplifying results in

$$.01638 H - .00529 M + .00695 N_{\phi} \cos \phi + .00171 r N_{\phi} + .0890p = 0$$

and

$$-.00529 H + .00351 M - .00171 N_{\phi} \cos \phi - .000825 r N_{\phi} + .00390p = 0$$

If N_{ϕ} for the specified shell is written in terms of p, the equations are

$$.01638 H - .00529 M + 2.040 p = 0$$

and

$$-.00529 H + .00351 M - .663 p = 0$$

These yield for the redundant forces

$$M = 3.6 p$$

and

$$H = -123 p$$

which must be considered in computing total stresses near the ring-shell junction. Using the shell equations of reference 13 and these loadings, results in a stress of 270 psi per G of loading at the shell edge.

The final displacement and rotation of the ring shell junction can now be computed by considering the forces and moments on either the ring or shell alone. For the shell, for example,

$$\theta_T^S = -\theta_H^S H + \theta_M^S M + \theta_p^S p$$

and

$$\delta_T^S = + \delta_T^S H - \delta_M^S M + \delta_p^S p$$

which yield

$$\theta_T^S = .456 p$$

and

$$\delta_T^S = -1.08 p$$

These deflections must agree with those of the ring; this affords at least a partial check of the equations.

For a pressure $p = 0.100$ psi the rotation and displacement are:

$$\theta_T^S = .0456 \text{ radians}$$

or

$$\theta_T^S = 2.6 \text{ degrees}$$

and

$$\delta_T^S = -.108 \text{ inches}$$

The shell edge under the imposed load would like to move inward according to the membrane theory. The ring and shell together, however, will grow in diameter at the edge because of the edge force reaction on the ring.

6.2.6 Shell Distortion Resulting from Temperature Difference Between the Ring and the Shell

The equations of compatibility can be used to determine the edge distortion due to a ΔT between the ring and the shell. The shell in the free state that sees a constant temperature above that of the ring will not rotate but will grow at the edge

$$\delta_{\Delta T}^S \Delta T = R_o \alpha \Delta T$$

where α is the coefficient of thermal expansion and ΔT is the shell to ring temperature difference. If the ring is attached to the shell, it resists this displacement with the result that redundant moment and force are set-up at the ring-shell junction. The compatibility equations (equations 6.2-5 and 6.2-6) take the form

$$H(\delta_H^R + \delta_H^S) - M(\delta_M^S + \delta_M^R) - \delta_{\Delta T}^S \Delta T = 0$$

$$-H(\theta_H^R + \theta_H^S) + M(\theta_M^R + \theta_M^S) = 0$$

Substituting the numerical values for the coefficients for the example concentrator there results

$$.01638H - .00529 M - .00234 \Delta T = 0$$

$$-.00529 H + .00351 M = 0$$

α has been taken equal to 13×10^{-6} per $^{\circ}\text{F}$ and R_0 is 180 inches. The equations yield

$$H = 0.279 \Delta T$$

and

$$M = 0.422 \Delta T$$

The edge rotation is

$$\theta_{\Delta T}^S = -\theta_H^S H + \theta_M^S M$$

or

$$\theta_{\Delta T}^S = .00013 \Delta T$$

which is equivalent to

$$\theta_{\Delta T}^S = 0.45 \text{ minutes per } ^{\circ}\text{F temp. differential}$$

6.3 Shell Stability

The concentrator shell is susceptible to buckling if compressively loaded. Overall shell buckling is a consideration as well as wrinkling and monocell buckling should the shell be constructed of honeycomb sandwich.

Several stability criteria are applied in this section. In addition, methods to counteract shell instability through the use of external supports are discussed.

6.3.1 Equivalent Single-Thickness Shell for Honeycomb Construction

Often it is useful to think in terms of an equivalent single-thickness rather than the built-up section when discussing stability or other shell characteristics. The discussion to follow indicates the equivalent thickness to be used depending on whether stresses and buckling or displacements and rotations are of interest.

Neglecting the stiffness of the core and assuming the beam or section is straight, the centroid of the honeycomb section will be located a distance \bar{Y} from the t_2 facing, where

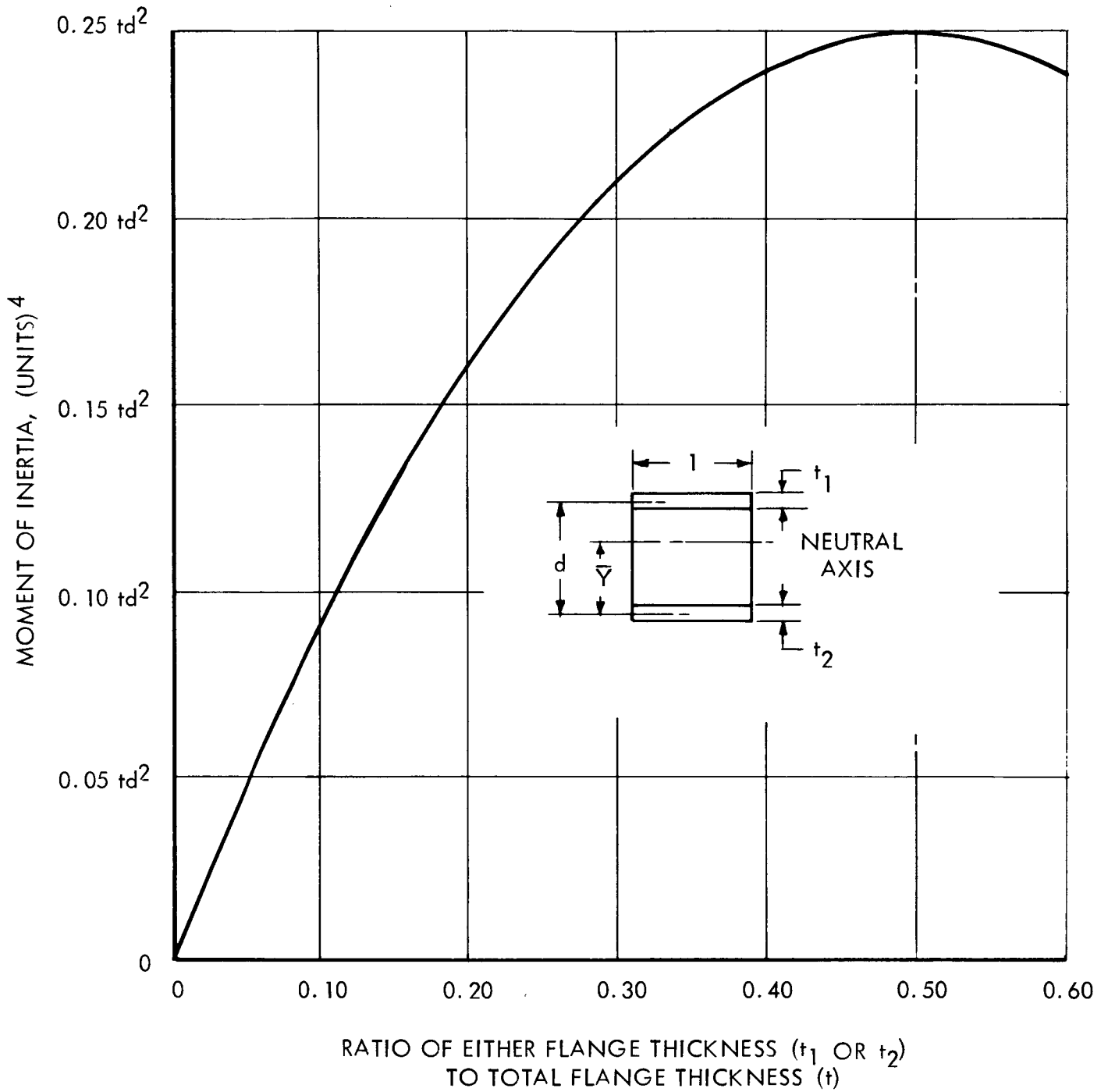
$$\bar{Y} = \frac{\int Y dA}{\int dA} = \frac{dt_1}{t_1 + t_2}$$

Neglecting the flexural rigidity of each face about its own centroid, the moment of inertia of the composite section will be the area of each flange times the square of the distance to the centroidal axis. This reduces to

$$I = \frac{d^2 t_1 t_2}{t_1 + t_2}$$

Moment of inertia as a function of the ratio of either flange thickness to the total flange thickness has been represented in Figure 6.3-1; this shows the obvious result that the more nearly equal the flange thickness, the higher the structural efficiency of the section.

FIGURE 6.3-1
MOMENT OF INERTIA AS A FUNCTION OF THE RATIO
OF EITHER FLANGE THICKNESS TO THE TOTAL
FLANGE THICKNESS



For beam-type deflections or rotations - these are inversely proportional to I - the thickness of the single-thickness section is

$$t^3 = \frac{12 d^2 t_1 t_2}{t_1 + t_2}$$

If stresses or stability are of interest, the section moduli for the two sections should be equated. The single-thickness equivalent for the t_1 face is

$$t^2 = 6dt_1$$

whereas for the t_2 face,

$$t^2 = 6dt_2$$

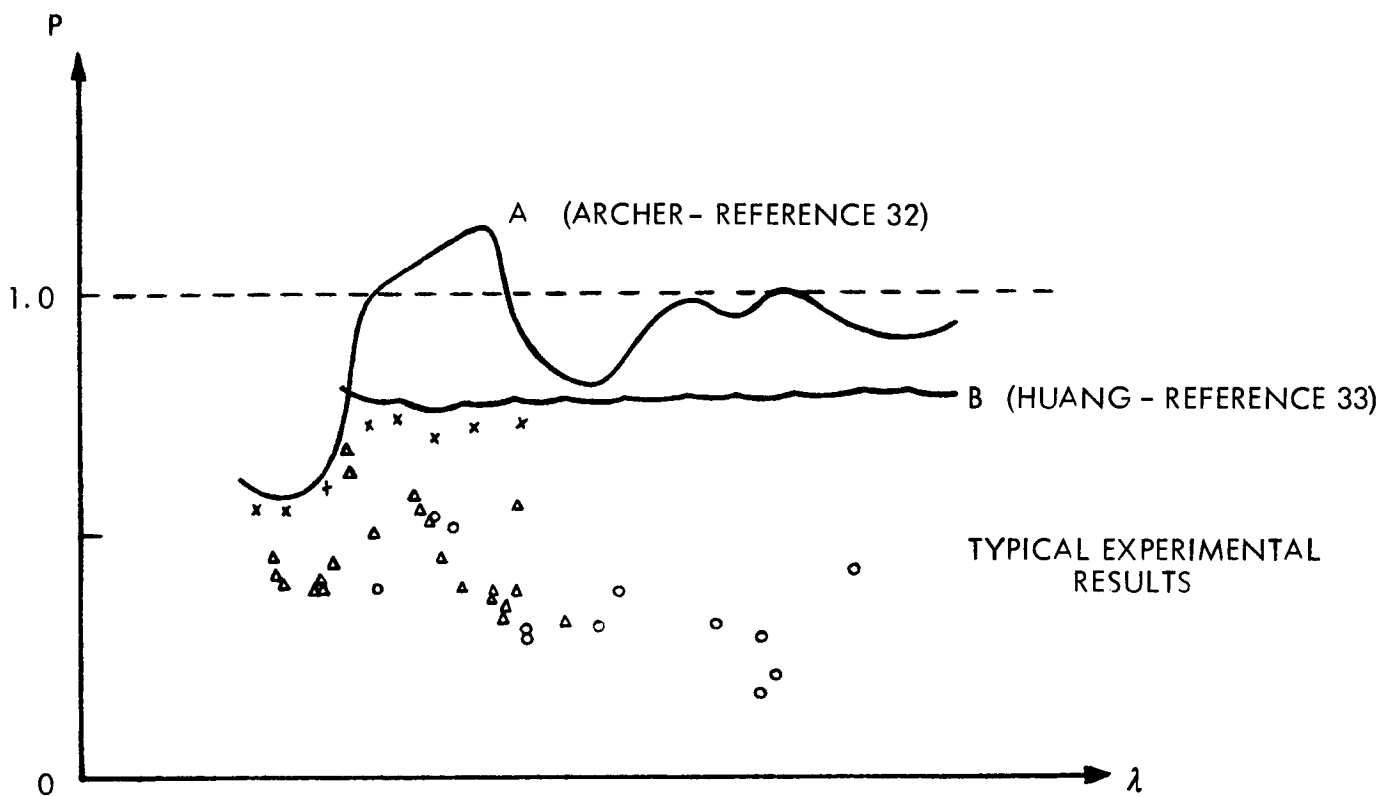
For example, consider a honeycomb sandwich of 0.25 inch core thickness. One flange is .008 inch thick; the other is .004 inch. For deflections and rotations, it looks like a single thickness shell of 0.128 inch thickness. For stability and stresses, the average equivalent single-thickness is 0.09 inches.

6.3.2 Overall Shell Stability

The detailed theoretical analysis of the buckling of the mirror is a problem in nonlinear shell stability. Most of the analytical work which has been done on this problem has considered the spherical shell, and therefore the paraboloidal mirror will be approximated by a partial sphere in the stability discussion.

The theoretical approaches which have been considered in shallow spherical shell stability can be summarized by Figure 6.3-2 (this sketch and discussion have been presented in reference 31). The dashed line represent the limit of the classical buckling solution for axisymmetrical deformation of the spherical shell. Experimental results show that buckling occurs at pressures much lower than the classical solution predicts. Investigations of the axisymmetric snap-through mode of buckling by Archer (32) have resulted in the solution represented by curve A. The asymmetric buckling of axisymmetrically deformed shells has been investigated by Huang (33) and the results, which

FIGURE 6.3-2
STABILITY OF SHALLOW SPHERICAL SHELLS



$$P = \frac{P_{cr}}{P_o}$$

WHERE $P_o = \frac{2Et^2}{R^2 \sqrt{3(1-\mu^2)}}$ CLASSICAL BUCKLING PRESSURE

$$\lambda^2 = \frac{4H}{t} \sqrt{3(1-\mu^2)}$$

predict the interaction of the circumferential and radial modes of buckling, are represented as curve B. It is seen that portions of these curves tend to form an envelope for the experimental results which are normally observed. The wide scatter of the experimental values of critical pressure might be accounted for by the large effect which even small initial imperfections will have due to the post buckling characteristics of spherical shells. The prediction of these effects requires the solution of the full nonlinear differential equations considering asymmetric post buckling with initial imperfections. This type solution is beyond the scope of the present study program and, in fact, is not justified for the initial design study since various empirical stability criteria are available.

The previous theoretical analysis discussions do provide some insight as to the buckling phenomena which might be expected for the large, thin shell configurations of space solar mirrors. First, imperfections in the shell geometry will have a large effect upon the stability; and second, a highly "wavy" mode of overall deformation can be expected in both the radial and circumferential directions due to the large value of λ .

One of the simplest empirical stability criteria is that the shell is assumed to buckle when the pressure reaches one-third the classical buckling pressure for the complete sphere (14). The limiting or critical pressure is,

$$p_{cr} = \frac{1}{3} \cdot \frac{2 E t^2}{R^2 \sqrt{3 (1 - \mu^2)}} \quad (6.3-1)$$

The limitations on the radius to thickness ratio are such that honeycomb sandwich construction for large diameter concentrators will be covered by the criterion. Pressures resulting from axial accelerations are assumed to buckle the shell at the same pressure as the uniform normal pressure.

For aluminum construction, the equation reduces to

$$p_{cr} = \frac{4.13 \times 10^6 t^2}{R^2} \quad (6.3-2)$$

This relationship is plotted as a function of shell radius of curvature for 10 G acceleration and for 0.050 psi constant pressure in Figure 6.3-3. These data may be used to size various diameter concentrators by taking, as an approximation, the intercepted diameter ($2R_0$) equal to the radius of curvature (R).

Restricting our attention to shells of 30 foot diameter and assuming $R = 396$ inches, equation 6.3-2 becomes

$$p_{cr} = 26.4 t^2 \quad (6.3-3)$$

The specific weight of aluminum is 0.10 lbs per cubic inch, or $p/t = 0.10G$; where G is the number of gravity units of acceleration. For critical buckling values, the substitution of this into equation 6.3-3 results in,

$$G_{cr} = 264 t$$

These limiting loads are presented as a function of shell thickness in Figure 6.3-4.

The equations assume shells of single thickness aluminum. For built-up sections, a thickness based on the equivalent section moduli as per Section 6.3-1 should be used in the critical pressure equation. For example, for .008 inch and .004 inch facings and 0.250 inch thick core, the single-thickness for equivalent stability is 0.090 inch. From Figure 6.3-4 the critical pressure is 0.214 psi.

The acceleration as a function of shell thickness curves are, of course, no longer valid for built-up or honeycomb sections. These assume a weight to pressure ratio of 0.10 psi; obviously, the honeycomb section will not weigh as much as the equivalent single-thickness aluminum.

It should be pointed out that the criterion used (Equation 6.3-1) is none too conservative. If the limiting stress as determined by the Von Karman Equation (15)

$$\sigma_{cr} = 0.154 E \left(\frac{t}{R} \right)$$

FIGURE 6.3-3
SHELL THICKNESS AS A FUNCTION OF RADIUS OF CURVATURE FOR
PRESSURE & ACCELERATION FOR OVERALL SHELL BUCKLING

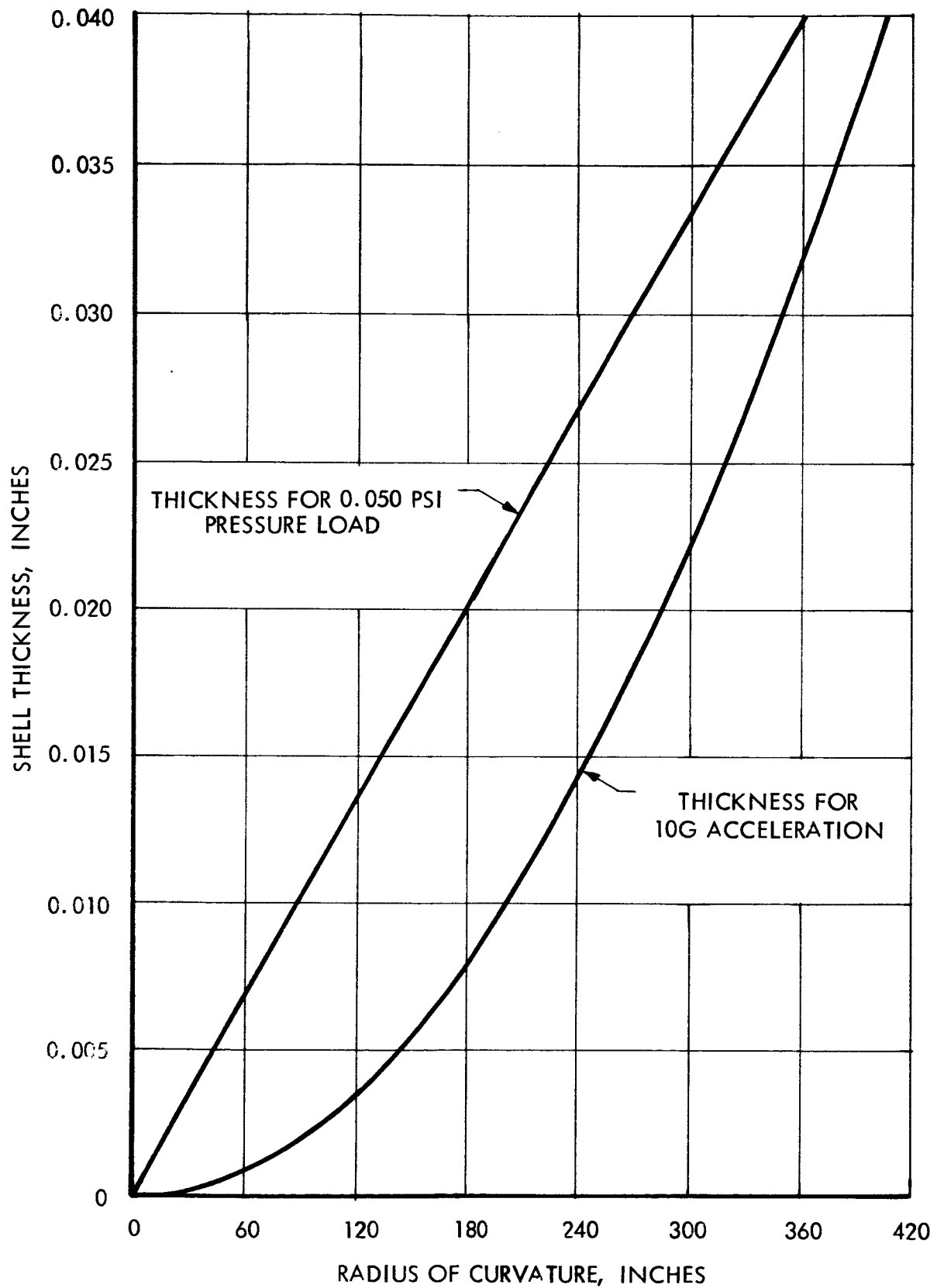
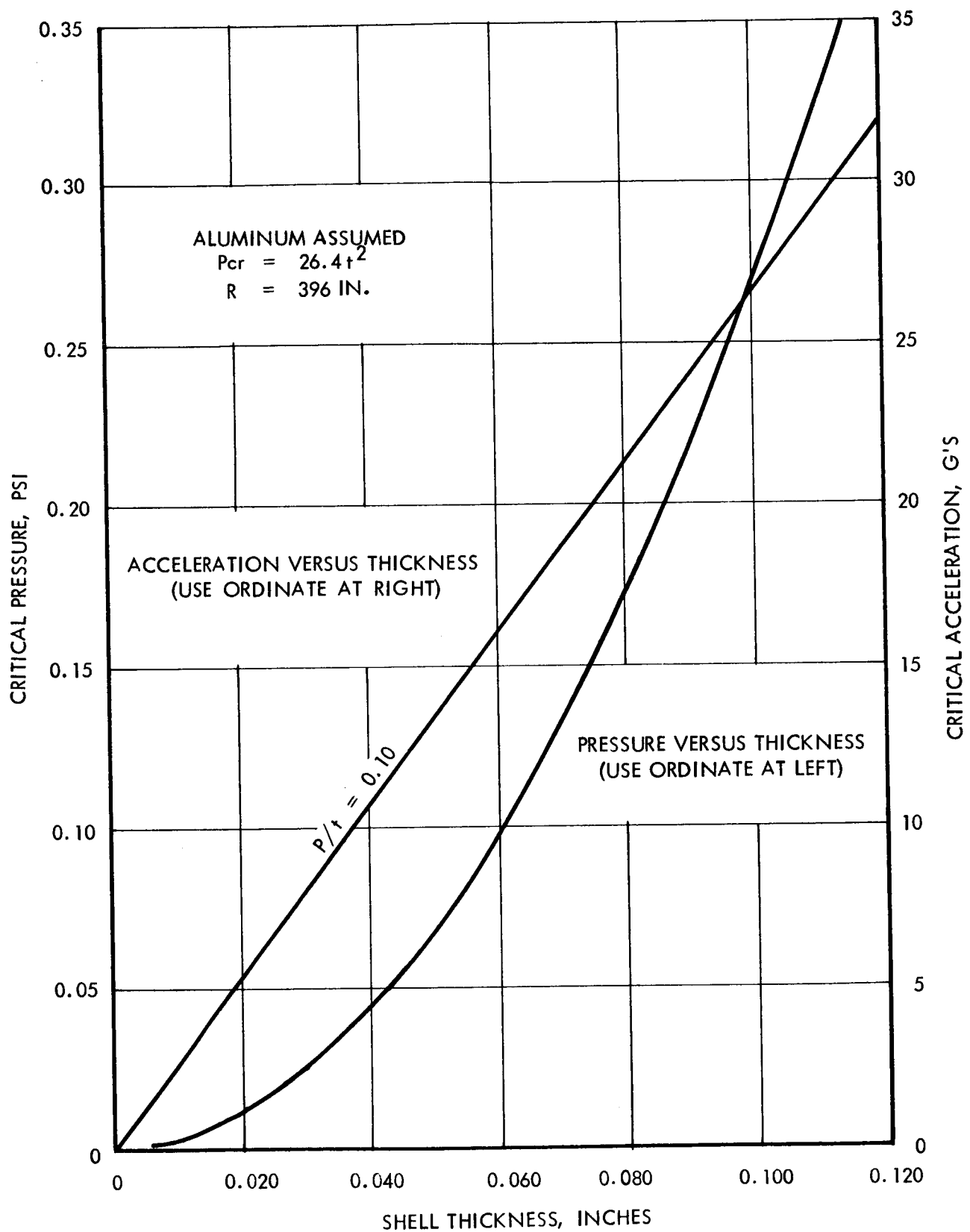


FIGURE 6.3-4
CRITICAL LOADS FOR
LARGE DIAMETER CONCENTRATORS



is related to a pressure load, the shell thickness required for a given pressure will be 30 per cent greater than that determined by equation 6.3-1. Another source (16) suggests using a coefficient of 0.2 in the classical formula rather than 0.33; the thickness, again, would be greater than that determined by equation 6.3-1. As discussed previously these empirical criterions are based upon experimental results which may be highly influenced by shell or load imperfections. Also, very little data are available for large-thin shells. Thus due to the nature of these stability criterions, marginal design loadings should be avoided and probable combined environment loadings should be used in the initial design.

High lateral loads will also cause instability. Data and applicable criteria are scarce; however, it should be obvious that if the shell is able to withstand 50 or 100 G axial acceleration, 1 or 2 or even 10 G's applied laterally will be no problem assuming the support ring is able to provide the right edge reaction. This may not be true if single-thickness shells are sized for a minimum 5 or 10 G axial loading.

6.3.3 Other Approaches to Counteracting Shell Instability

Several approaches to externally providing shell stabilization have been considered. These are listed here as well as their disadvantages or limitations in solar concentrator design.

6.3.3.1 Stabilization with Bag and Differential Pressure

The bag must be blown free of the system prior to operation. The pressure system must respond rapidly and accurately to small changes in pressure associated with changes in altitude. Most importantly, the response of the contained volume of air to noise and vibration and the input this will impart to the concentrator are largely areas of unknowns.

6.3.3.2 Stabilization with Many Supports

Donnell (17) indicates the size of the buckling dimple assuming an external pressure loading and large deflection theory. It is

$$\beta = 7.00 \sqrt{\frac{t}{R}} \text{ radians}$$

where β = the total angle subtended by the dimple. For $R = 396$ inches, the arc length affected is

$$S = 139 \sqrt{t} \text{ inches}$$

For $t = .015$ inches, $S = 16.7$ inches; for $t = .030$ inches, $S = 24.1$ inches. The conclusions are that local conditions on only a small portion of the shell surface are important and that many supports would have to be provided to increase the resistance of the shell to instability.

6.3.3.3 Stabilization with Central Column

It has been suggested that during launch the shell could be column loaded through an inner ring. This would put the shell membrane in tension and, consequently, would permit a larger compressive load before failure through elastic instability. Analysis indicates, however, that one can expect:

- a) Extremely high stress near the shell vertex for a small gain in stability near the edge.
- b) Excessive weight penalty on other flight components due to the column load reaction.

6.3.3.4 Rib-Stiffened Shells

Such shells would be difficult to fabricate and less efficient from a weight-load point of view than honeycomb sandwich construction.

6.3.4 Local Buckling Considerations

Honeycomb sandwich construction requires that local modes of failure be considered. One form is monocell buckling of the individual cells within the honeycomb core. As reported by Cunningham and Jacobson (18), the criterion is

$$\sigma_{cr} = 0.9 \eta E \left(\frac{t_1}{a} \right)^{3/2}$$

where a = diameter of circle inscribed within a honeycomb cell
and η = plasticity reduction factor (equals 1 in elastic region)

In Figure 6.3-5, the limiting compressive stress is plotted as a function of facing thickness with cell size represented parametrically. The analysis has been developed for flat plates; compressive stresses should, therefore, be kept well below those allowed by the criterion for concentrator shells that have initial curvature. The curves indicate that .008 inch facings with 1/4 inch cells should not buckle under a compressive edge load until the stress reaches 49,000 psi.

Wrinkling or distortion over a series of honeycomb cells may occur if the core does not have sufficient ability to stabilize the faces. Several criteria have been applied and none indicate an unstable condition for the honeycomb sections for large diameter concentrators. These would include sections of .004 inch to .012 inch facing thickness bonded to 1/4 inch thick cores of 1/4 inch cell size. The core foil thicknesses considered were .001 to .004 inch.

6.4 Thermal Stress and Distortion Considerations

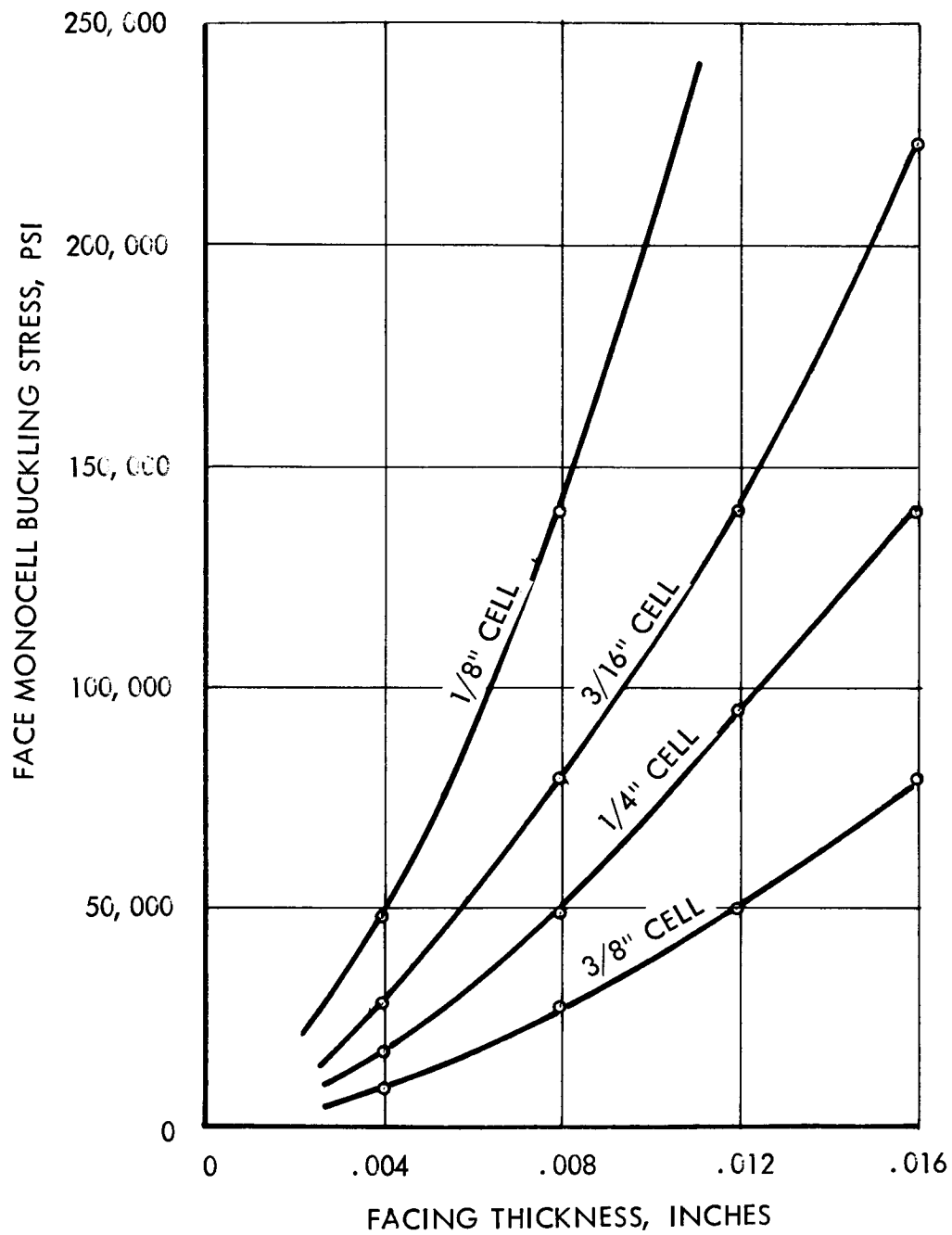
The concentrator shell sees temperatures that may be nonuniform in both the meridional and thickness directions. Honeycomb sandwich construction requires additional consideration in that the bonding agent will have different thermal properties than either the honeycomb core or facing. The approach here has been to consider the various effects separately and to assume the principle of superposition. The temperature conditions which are used in this portion of the analysis were established in a separated detailed study of the concentrator thermal environment which will be discussed in Section 7.0.

6.4.1 Shell With Uniform Increase in Temperature

Consider first that the concentrator shell is free at the edge and that it undergoes a uniform increase in temperature, ΔT . Free thermal strain

$$\epsilon_{\phi} = \epsilon_{\theta} = \alpha \Delta T$$

FIGURE 6.3-5
MONOCELL BUCKLING STRESS



exists everywhere, and there will be no thermal stress. The shell has not distorted but has merely grown slightly in size. The magnitude of growth can be determined by considering a point of x and y coordinate on the shell that grows Δx and Δy due to ΔT . Before the increase in temperature, the parabola can be represented by the equation

$$y = \frac{x^2}{4f}$$

where f the focal length is a constant for a particular shell. With ΔT increase, x grows to $x + \Delta x$ where $\Delta x = x \alpha \Delta T$ and similarly for the y coordinate. The parabola is represented now by

$$y = \frac{x^2}{4f} \left(\frac{1 + 2\alpha \Delta T}{1 + \alpha \Delta T} \right)$$

if $(\Delta x)^2$ terms are neglected compared to $x \Delta x$ terms. The shell is still parabolic but, whereas, the focal length was f it is now

$$f' = f \left(\frac{1 + 2\alpha \Delta T}{1 + \alpha \Delta T} \right)$$

For aluminum and a 100°F increase in shell temperature

$$f' = f \left(\frac{1 + 2 \times 13 \times 10^{-6} \times 100}{1 + 13 \times 10^{-6} \times 100} \right)$$

or

$$f' = f \left(\frac{1.00260}{1.00130} \right) = 1.0013 f$$

For $f = 156$ inches (a 30 foot diameter concentrator) the increase in focal length will be 0.20 inches.

If the concentrator shell is attached to a support ring of lower temperature, the support-ring will resist this free growth of the shell and redundant force and moment will be imposed on each at the ring-shell junction. The resulting edge distortion can be determined as indicated in Section 6.2. This distortion decays rapidly, and, as an approximation, the arc length (S) affected can be taken equal to

$$S = 1.20 \sqrt{Rt}$$

This is the arc length at which a spherical shell is first distortion free when under the action of an edge moment. The equations used in this determination are from Novozhilov (35). For the 30 foot diameter concentrator ($R = 396$ inches and $t = 0.128$ inches equivalently for the 1/4 inch honeycomb section)

$$S = 8.5 \text{ inches}$$

6.4.2 Shell With Thickness Temperature Gradient

The parabolic shell acts like a partial hollow sphere rather than an unrestrained flat plate. That is, the thickness temperature gradient produces stresses in the shell but not distortion. Symmetry alone would not permit one surface element to rotate with respect to another in the circumferential direction for shells of revolution.

The magnitude of stress can be computed as follows; if the surface was flat and unrestrained and subjected to a thickness gradient, it would assume a curvature

$$\frac{1}{R} = \frac{\alpha \Delta T}{t}$$

Moment also produces constant curvature such that

$$M = \frac{\alpha E I \Delta T}{t (1 - \mu)}$$

Relating stress to moment results in

$$\sigma = \frac{\alpha E \Delta T}{2 (1 - \mu)} \quad (6.4-1)$$

The distribution of stress is similar to that of the temperature gradient. In honeycomb sandwich construction, the temperature drop occurs almost entirely across the adhesive with constant but different face temperatures; the hot face, therefore, is in almost uniform compression while the cold face is in tension. The requirements on the core are only to keep the two faces acting as an integral unit.

For aluminum, Equation 6.4-1 yields facing stresses equal to

$$\sigma = \pm 100 \text{ psi per } ^\circ\text{F}$$

Adhesive bonding results in 5 to 10⁰F gradients; stresses are, therefore, small. If the edge of the shell is free, it is not able to develop the stresses necessary to prevent distortion under the temperature gradient. A requirement of the support-ring, then, is that it provides the required support without excessive deformation. For further discussion of the shell stresses and small local distortions including the specific case of the parabolic geometry, see reference 34.

6.4.3 Honeycomb Facing - Adhesive Considerations

The brief analysis that follows considers the adhesive bond-line and the aluminum facing and neglects the effect of the core material on either. This is consistent with the properties of honeycomb core in that it is rigid only in the thickness dimension and gives with the panel rather than resisting its deflection.

A ring of adhesive bounds a honeycomb cell face of aluminum. Should the composite material see a rise in temperature or should there exist a temperature gradient, stresses will be produced in the aluminum and the adhesive due to the difference in thermal expansion coefficients. This stress can be determined by equating the radial growth of the adhesive ring and the aluminum while each is in the thermal environment and is acted on by the unknown but equal edge force. Assuming no eccentricity and letting subscript A refer to the adhesive and M to the aluminum metal, the force is

$$F = \frac{T_A \alpha_A \frac{r}{E_A A_A} - T_M \alpha_M \frac{l}{t E_M}}{\frac{r}{E_A A_A} + \frac{l}{t E_M}} \quad (6.4-2)$$

where

T = temperature

α = coefficient of thermal expansion

r = radius of honeycomb ring or cell

E = modulus of elasticity

A_A = one-half the cross section area of the adhesive

t = thickness

Assuming characteristic adhesive properties and a realistic cross-section area, the edge force will be about 1 pound per inch per 100°F change in temperature for .008 inch aluminum and $3/8$ inch cells. This force will actually be developed as a shear in the adhesive and will result in stresses of less than 100 psi. This stress is small but the direction to go if improvement is required is as follows: try to match coefficients of thermal expansion; then, select an adhesive with a low modulus so that it can deform with the metal without high stress at the interface.

Equation 6.4-2 indicates that temperature gradients of 5 to 10°F have a negligible effect on adhesive bonded aluminum structures compared to operating temperatures that differ from the bonding temperature by 100 to 200°F . Solar concentrators should be bonded at a temperature lower than the operating temperature; this will put the aluminum face in a small tensile field which should tend to reduce any honeycomb mark-off or other irregularities in the reflecting surface.

6.5 The Brayton Cycle Environmental Specification

Structural analysis considerations as they relate to general solar concentrator development have been presented in the preceding sections. The sections to follow utilize these considerations in the design of a 30 foot diameter single piece paraboloid and support ring. This section discusses the Solar Brayton Cycle Environmental Specification which covers the anticipated environment for the 30 foot diameter concentrator.

The environmental specifications were reviewed and two categories of loading were defined, (1) buckling loads and (2) loads which produce large stresses but not a buckling mode. Combinations of loads derived from the simultaneous application of environments are considered in both categories.

6.5.1 Shell Instability Loads

The loads during launch and lift-off govern the structural design of the reflector. If the concentrator is oriented such that the 7G launch acceleration causes tensile membrane loading, then the inertial load that may buckle the shell can be taken equal to 3G minimum (reverse acceleration). To this should be added any other simultaneous loadings which may cause buckling.

To evaluate the effects of the specified acoustical noise environment upon the reflector, a literature survey was conducted with the primary purpose of establishing a loading and failure criterion. It was found that two general types of failures should be considered; fatigue failures and static failures (19)(20).

Vibrations can be induced in structures by acoustic waves which may lead to fatigue failures. These vibrational loadings along with other dynamic loadings are not considered as buckling loads and will be discussed in Section 6.5-2. However, for lightweight structures an equally important criterion is static failure which can occur at rocket-engine ignition or as the noise level is increased to a critical intensity. Tests to investigate the structural requirements for acoustically induced transient overpressure occurring during engine start-up have been reported (21). It was determined in these tests that to meet structural requirements imposed by overpressure, long unsupported skin panels had to be supported by additional framing.

In the light of these static failure mode possibilities, the Brayton system noise specification was interpreted as follows. The sound pressure level of 148 d.b. is a result of the rocket engine noise which originates near ground level and is directed upward into the vehicle compartments. The differential in sound pressure between one side of the concentrator and the other will depend upon the reverberation characteristics of the vehicle skin as well as the mass, stiffness, and damping associated with the concentrator. Because of the complexity of the problem as well as the many unknowns, it has been assumed that 0.050 psi acts so as to compressively load the shell. This is equivalent to a 10 d.b. differential from 148 d.b. which is felt to be in the range of absorption for the structure. Ordinarily this low pressure differential would not be significant in the design of air frame, bulkhead, or tankage members;

however, for the large concentrator surface area and the thin shell construction, this pressure loading in combination with the previously mentioned 3G reverse acceleration loading constitute the primary structural design criterion for the Brayton solar concentrator. It should be realized that this pressure loading does not have to be present over the entire back side of the concentrator to cause a buckling failure since, as discussed previously, the size of a buckling dimple is small compared to the diameter of the concentrator. Thus, even if a directionality cannot be assumed for the acoustic environment, the possibility exists of a local attenuation across the structure which could produce a localized buckling failure.

The complexity of the required analytical techniques makes a detailed acoustic and dynamic analysis of the structure beyond the scope of this contract. Also, the lack of a detailed specification of the acoustic environment and the reality of combinations of environment as presented in specification No. P0055-1 precludes the necessity of sophisticated methods of analysis in this phase of the study. Thus the combined pressure and reverse acceleration loading criterion is considered to be an adequate initial design basis.

Because of the unknowns involved in defining the environment and the complex nature of the response phenomena of the structure to the loadings, a considerable amount of environmental testing is anticipated upon which final design refinements can be based.

6.5.2 High Stress Load

Stresses developed in the shell and support ring results from the assumed sound pressure differential, shock, vibration, and reverse acceleration. The approach has been to analytically size upward the response loads associated with shock and vibration and then to consider the static condition only. The buckling mode of failure is not considered imminent; the assumption here is that the periodic inputs occur rapidly and then only for a short duration of time.

6.5.2.1 Shallow Shell Fundamental Frequency

Even a nominal shock and vibration analysis will require that the natural frequency of the shell is known. Reissner (22) indicates an approximate expression

for clamped shallow spherical shells. A 30 foot diameter aluminum shell approximating a parabolic solar concentrator will have a fundamental frequency of about 150 cps. For the shell depths and thicknesses of interest, frequency changes only negligibly with thickness. Experimental evidence (23) confirms this, as well as the fact that frequencies for clamped-edge and momentless edge conditions are nearly equal. Therefore no modification has been made in the Reissner formulation to allow for actual edge conditions.

6.5.2.2 Shock

The specification indicates a 35G shock during launch and lift-off. Because of the shell's high fundamental frequency, it will actually see an equivalent static acceleration several times 35G at the first response peak. This intolerably high input can be substantially reduced by incorporating isolators into the system. Properly selected isolators should result in the shell not seeing more than about 25G acceleration at the first response peak. The isolator, itself, will respond with sufficient deflection so that any additional supports provided the shell must spring from the supporting structure between the isolator and the shell.

6.5.2.3 Vibration

Assuming the use of isolators, the lowest frequency of the shell-ring-isolator system will be in the 16-100 cps range. Isolators normally amplify by a factor of 3 at resonance so one may expect the structure to see 18 G peak at resonance.

6.5.3 Load Summary

The shell is sized under a buckling load of 3G plus 0.050 psi. Stresses the ring and shell see result from 0.050 psi plus 50 G acceleration; this acceleration level results from approximately 25 G shock, 18 G vibration, and 7 G reverse acceleration.

6.6 Sizing the Concentrator Shell

Stability rather than stresses will govern the design. For acceleration or pressure alone, Figure 6.3-4 could be used to size a single-thickness 30 foot

diameter concentrator. For the combined acceleration and pressure design loads (3 G plus 0.05 psi), the shell can be sized by writing the acceleration in terms of equivalent pressure as a function of thickness and limiting the total pressure to the critical value according to the buckling equation. Thus the equivalent pressure acting on the shell is,

$$p = p_1 + p_2$$

where p_1 is due to acceleration and p_2 due to acoustic noise. For 3 G acceleration and solid aluminum construction, $p_1 = 0.30 t$ so that the total buckling load is $p = 0.30 t + 0.05$. Substituting into equation 6.3-3 results in a limiting shell thickness of $t = 0.05$ inches. The shell would weigh about 535 pounds or 0.76 psf. The ring weight will approximately equal that of the shell so that the total weight would be near 1000 pounds. It will be seen that the weight of this single thickness design is excessive when compared to a sandwich material design concept.

Consider honeycomb sandwich construction. The reflecting face thickness is chosen to insure no "mark-off" resulting from adhesive bonding. Based upon the inspection and tests of honeycomb sandwich specimens as discussed in Section 5.2, an .008 inch optical face has been selected. After selecting a core thickness of 0.25 inch for practical fabrication and handling plus low weight and high heat transfer, the back face thickness could be determined by writing the section modulus of the section in terms of the back face thickness and the total pressure in terms of the section weight, loading, and back face thickness. Equating the two using the stability criterion, results in a required back face thickness of only about 0.001 inch for 3G + 0.050 psi. However, 0.004 inch as a minimum is recommended because of fabrication limitations. The weight of the section is 0.0022 psi or 235 pounds total. From Figure 6.3-3 the critical pressure is 0.214 psi using an equivalent single thickness of 0.090 inch. Applying a safety factor of 2 to the constant 0.050 psi pressure, the shell could withstand an additional 52G rather than the specified 3G. Thus, a nominally sized honeycomb cross section provides a considerable factor of safety to account for the previously mentioned limitations of the empirical stability criterions and the unknown of the environmental loadings.

Membrane stresses are small. For 50G plus 0.050 psi, the equivalent pressure is

$$p = 50 (0.0022) + .050$$

or

$$p = 0.160 \text{ psi}$$

The maximum membrane force will be the meridian force at the edge of the concentrator. Referring to Section 6.1, it will have a value

$$N_{\phi} = -194 p$$

or

$$N_{\phi} = 31.1 \text{ pounds per inch}$$

Dividing by the thickness of the honeycomb facings,

$$\sigma_{\phi} = \frac{31.1}{.012}$$

or

$$\sigma_{\phi} = 2600 \text{ psi}$$

This is well within the design limit for aluminum alloys.

The maximum circumferential force for $p = 0.160$ psi would require an adhesive shear strength of less than 50 psi for a $3/4$ inch lap.

6.7 Sizing the Support Ring

6.7.1 The Inner Ring

Consider first the inner support ring which is really just a close-out in that it transfers no load into supporting structure. Near the vertex the meridional force will be $160 p$ or 26 pounds per inch. For a ring of 15 inch radius, the hoop force is 390 pounds, or if the cross-sectional area of the ring is 0.10

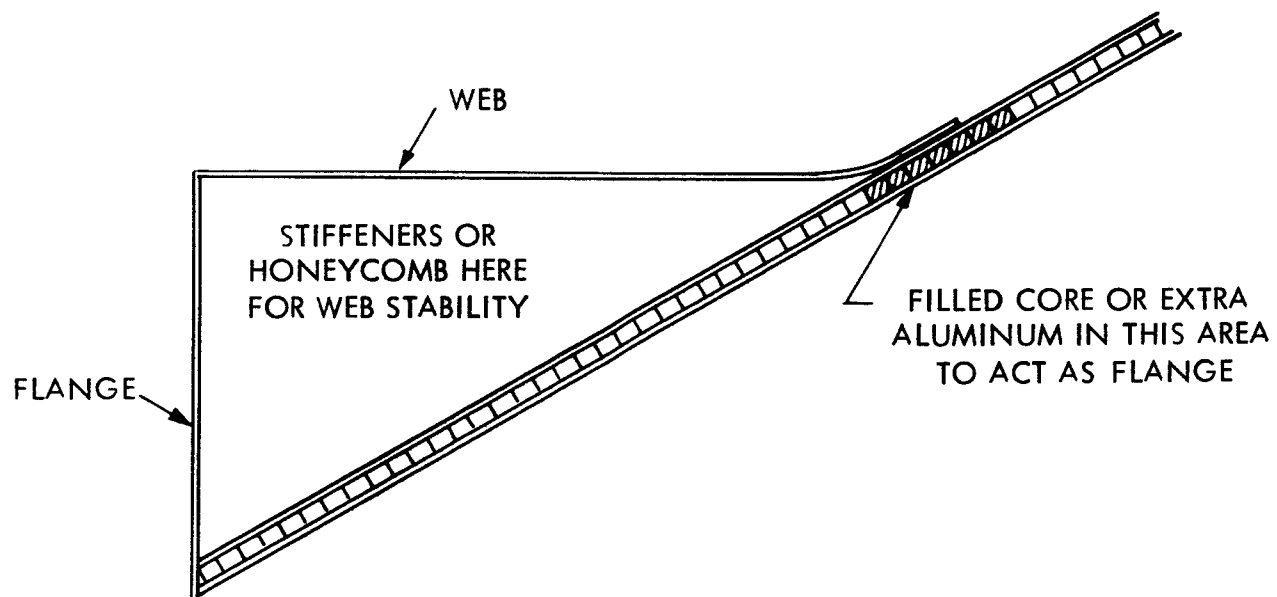
square inches, the stress is 3900 psi. If the edge or meridional force is compressive, the stability of the section must be checked. One-half inch of depth in the direction of the edge force will provide sufficient resistance to instability.

6.7.2 The Edge Support Ring

The proposed Brayton cycle concentrator support ring is shown in Figure 6.7-1. Analyses of many sections as well as practical considerations led to this design. The thin-walled triangular shaped torus has the following characteristics:

- a) The section is closed; this provides ample torsional rigidity.
- b) The support ring has good strength in the direction of the high shell edge load. In fact, its stiffness in this direction will be more than 5 times as large as a circular ring of equal material area and of equal torsional rigidity. Consider, for example, the ring on eight supports and under the action of the 31.1 pound per inch shell edge load of Section 6.6. The maximum bending stress will be about 10,000 psi if the triangular section has stiffness equivalent to two 0.040 square inch flange areas 12 inches on center. Aluminum alloys with yield strengths of 30,000 - 40,000 psi are not uncommon and will have sufficient strength to counteract additional discontinuity stresses.
- c) Because the section has a high moment of inertia in the direction of the shell edge load, its stability in this direction is good.
- d) The center of rotation of the section is closer to the edge of the shell than it would be for a circular section of comparable beam strength; the moment due to an edge force and the eccentricity is, therefore, less than it would be for the circular cross section.
- e) The section is easy to fabricate. The outer flange is a circular cylinder. The one web is a flat plate; the other is the shell itself.

FIGURE 6.7-1
SUPPORT RING CONCEPT



- f) Sufficient bond area is provided for the ring to shell attachment. In addition, the transition from shell to ring is gradual. This should allow the full strength of the section to be developed as well as inhibiting shell instability near the edge during compressive loading.
- g) The ring is on the back of the concentrator and will not intercept any solar energy. The ring does not extend beyond the rim of the concentrator; the full specified diameter can, therefore, be utilized to concentrate solar flux.

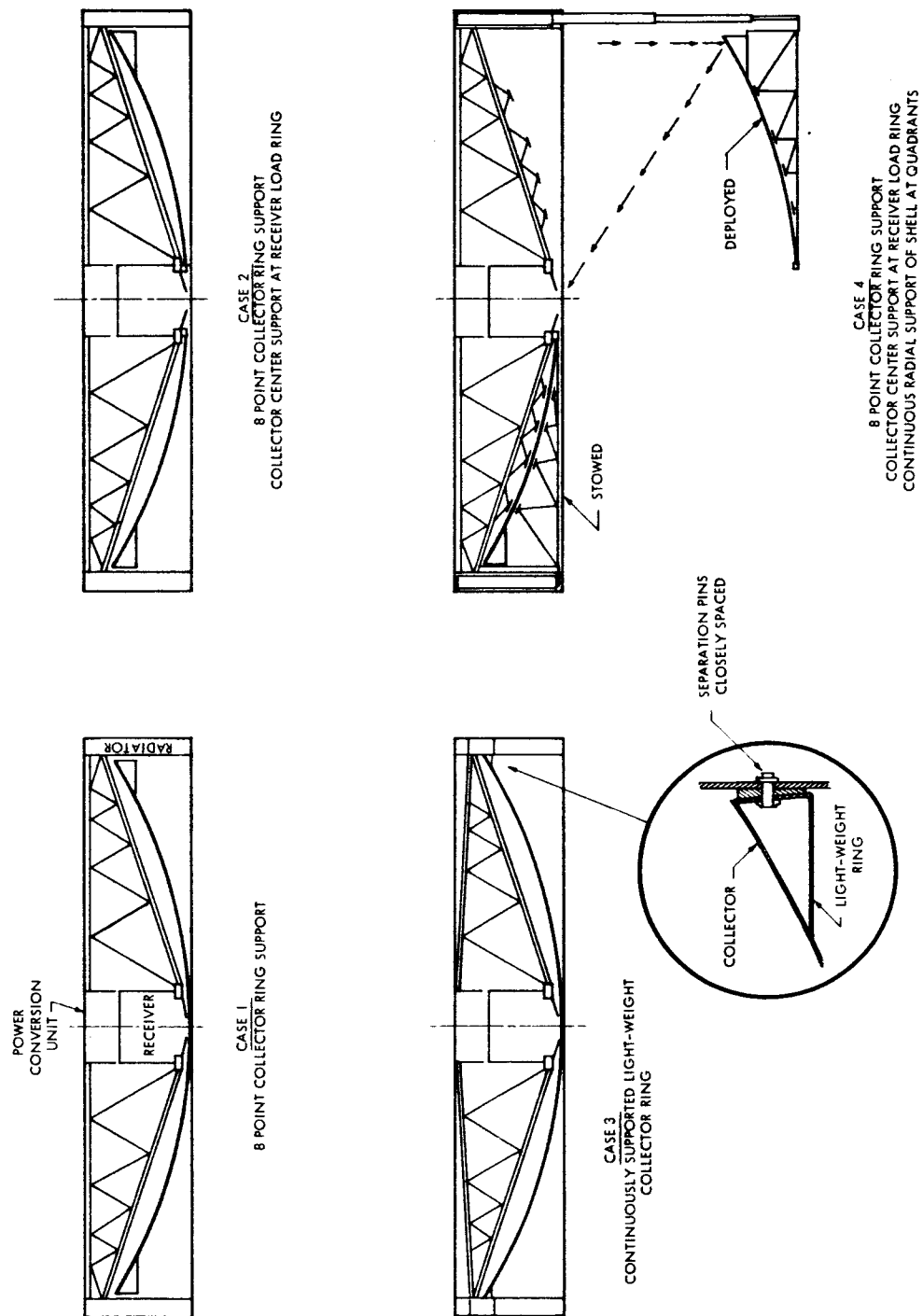
6.8 Overall Structural Support Considerations

Early in the study program, several possible concentrator support configurations were proposed for system packaging considerations. Figure 6.8-1 shows four such support arrangements which are within the Brayton cycle system stowing concept. Case 1 is the originally specified support condition which was used throughout this study and in the detailed design layout. Case 2 includes a center support point for the shell at the receiver load ring. This type support is not recommended for the present design because the center support does not appreciably improve the buckling stability and may cause unfavorable dynamic inputs from the receiver structure.

Since the general packaging configuration indicates that the concentrator loads must be transferred and supported by the radiator structure, a highly efficient structural support arrangement is shown in Case 3. Here the shell would get essentially continuous rim support from the radiator for the launch loadings. Calculation indicates that a lightweight ring designed as a load transfer section and for the lower deployed orbital loads would be approximately one half the weight of the support ring which has been designed for a eight point support. This is possible because the large launch load bending is eliminated from the ring design criterion.

Case 4 does not appreciably improve the buckling problem and requires considerable additional weight.

FIGURE 6.8-1
CONCENTRATOR SUPPORT CONFIGURATION



As mentioned previously, Case 1 is used in the present design; however, Case 3 could be incorporated if system and packaging considerations indicate this to be a more favorable design arrangement.

6.9 Detailed Design Considerations

Based upon the performance optimization studies and the structural and thermo-elastic analysis of the previous sections, the concentrator design shown in drawing 818180 is recommended for the Brayton cycle solar power system. This design utilizes the advanced state of technology which has been demonstrated on previous NASA contracts - NAS 1-3216 (Langley) involving stretch forming techniques and NAS 5-462 (Sunflower) involving lightweight honeycomb sandwich design for large diameter concentrators.

6.9.1 Design Description

The design consists of a shell reflector made up of twenty segments which are fabricated and mirror coated individually. The shell material is an adhesive bonded aluminum honeycomb sandwich construction. The individual segments are spliced together and an outer structural ring is added to form a rigid single-piece concentrator. The support ring is a built-up cross section which is internally stiffened by honeycomb core material. This approach also improves the heat transfer from shell to ring. Other fabrication and design considerations are discussed in Section 8.0.

It might be mentioned here that other design concepts as well as honeycomb fabrication techniques were considered. The following concepts were briefly considered during the study program:

Single Thickness Membrane Concepts

1. Segmented shell using adhesive bonded splices.
2. Segmented shell using seam welded joints.
3. Membrane shell with sublimating foam backing structure.

Honeycomb Sandwich Concepts

1. Brazed aluminum honeycomb construction.
2. Sublimating plastic honeycomb and back face.

Most of these concepts have specific advantages but they involve a considerable amount of applied research and development before a reliable design could be made. Also, tooling and fabrication costs become extremely large.

The recommended adhesive bonded aluminum sandwich material construction provides an efficient and reliable structural design as well as being within the present capabilities of fabrication technology.

6.9.2 Concentrator Weight

Based upon the recommended design as presented in drawing 818180, the weight estimate shown in Appendix F was compiled.

This weight estimate may be summarized as follows:

| | |
|---------------------------|--------------|
| Honeycomb sandwich shell | 224.0 lbs. |
| Joints and splices | 33.5 |
| Support ring | <u>170.0</u> |
| Total concentrator weight | 427.5 lbs. |

In terms of specific weight, this is approximately 0.60 lb. per square foot of total area (707 sq. ft.). For the continuously supported ring design previously mentioned (Case 3, Figure 6.8-1) the estimated total weight is 340 lbs. which is approximately 0.48 lb. per square foot.

7.0 ORBITAL THERMAL CHARACTERISTICS ANALYSIS

The solar concentrator must be capable of satisfactory operation in earth orbits between 300 miles and 20,000 nautical miles. Due to the heating and cooling characteristics associated with the sun and shade operation and due to nonsymmetrical radiation characteristics of the collector, variation in temperature level and thermal gradients will occur. Thermal gradients in any structure will produce deflections or stresses or a combination of both. Analysis and calculations were performed during the study program to establish the temperature characteristic of the Brayton concentrator in the orbital radiation environment. These temperature calculations were then used, as described in Section 6 to calculate thermoelastic deflections and stresses, and to establish a satisfactory thermal control design.

7.1 Concentrator Radiation Environment

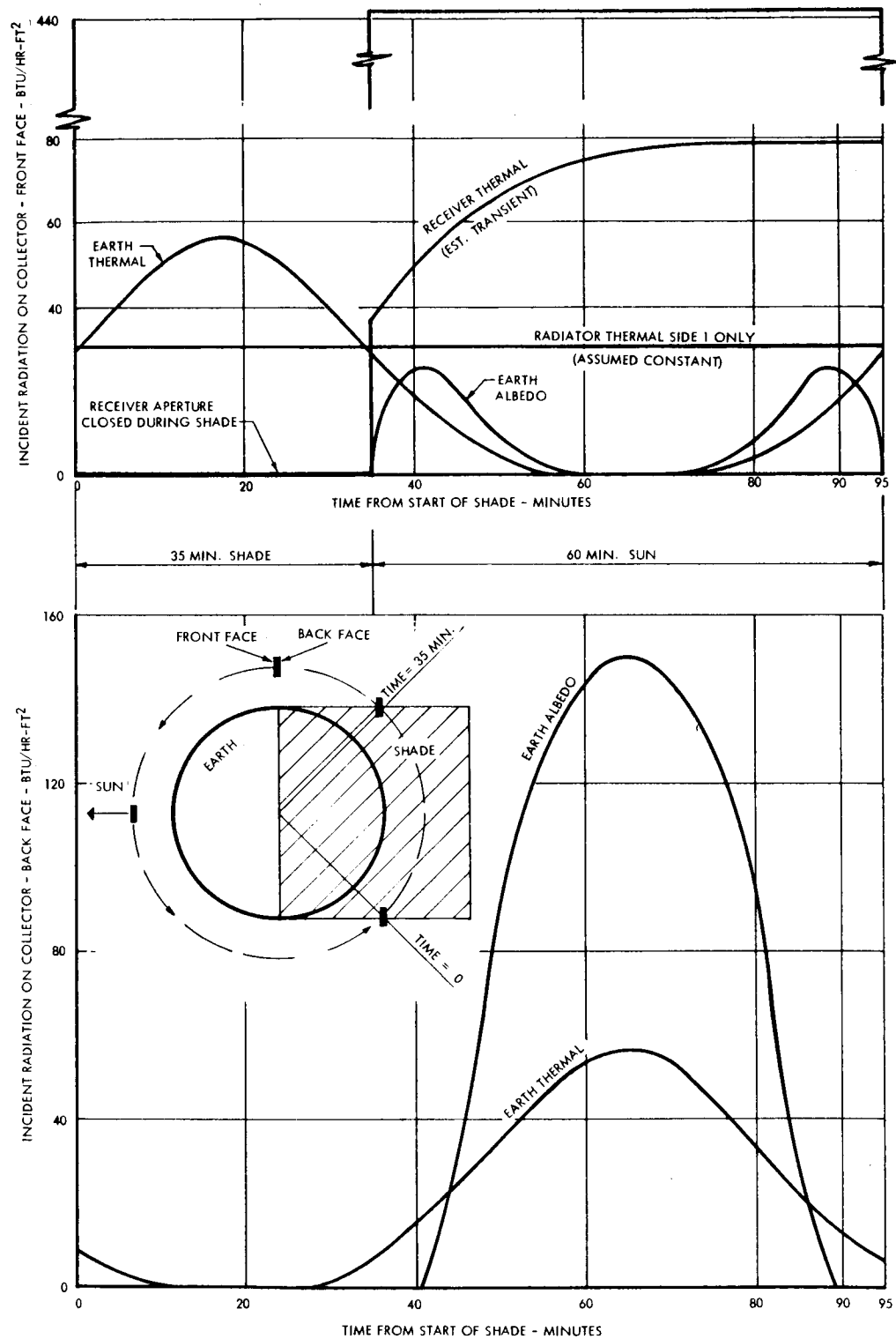
The sources of radiation interchange which were considered in the heat balance calculations are listed below.

- Direct solar radiation
- Planetary thermal radiation
- Planetary albedo
- System radiator thermal radiation
- System receiver reradiation

Typical variations associated with these sources during an orbital period are shown in Figure 7.1-1. These incident flux intensities are for an idealized flat collector facing the sun and in a 300 nautical mile zero inclination orbit. View factor and intensities were calculated using the methods described in reference (6) and (24).

Irradiation in a 20,000 mile orbit consists primarily of direct solar and the radiator and receiver contributions on the front side. Because of the small view factor for radiation interchange with the earth, the earth thermal and albedo contributions are negligible on both sides.

FIGURE 7.1-1
INCIDENT ENERGY LEVELS FOR 300 MILE ORBIT
SURFACE PERPENDICULAR TO OPTIC AXIS - ZERO ORBITAL INCLINATION



It is seen that the radiation environment is defined as to the type of radiation (solar or thermal) and the specific surface upon which it impinges. In this way, the appropriate surface radiation characteristic (α_s/ϵ) for a specific thermal control design can be used in heat balance calculations.

When the paraboloidal shape of the reflector is considered, variation of the incident flux environment will occur for different radial locations. A typical radial variation for the paraboloidal geometry is seen in Figure 7.1-2 which also shows the variation caused by the receiver heat-up in the sun phase.

The circumferential variation characteristics of the incident flux environment caused by anticipated radiator temperature variations is seen in Figure 7.1-3. It is seen that very little variation occurs and therefore this circumferential effect is neglected in heat balance calculations.

7.2 Absorbed Radiation

For a paraboloid shape which is continuously sun oriented in the previously described radiation environment, the structure will absorb a certain portion of the incident energy. The amount which is absorbed depends upon the absorptivity of the surfaces and the radiation interchange view with respect to the source.

Calculated absorbed energy for various locations on the Brayton cycle reflector are shown in Figure 7.2-1. The surface radiation constants which were used are shown on the figure and they are typical for a high reflectivity aluminum front side and an α_s/ϵ coating of 0.5 on the back. Also used in these calculations were the varying view factors for the specific location on the paraboloid. The view factor of an incremental area on the concentrator is a function of the orbital position, surface slope, orbital altitude and shadowing effects caused by other system components. Figure 7.2-1 is for a rotating power system (4 RPM) where time averaged view factors were used for any radiation source which is not co-axial with the concentrator. This spacecraft spin thus eliminates circumferential gradients from the temperature calculations. For the non-rotating system the calculated view factors shown in Figures 7.2-2 and 7.2-3 must be used.

FIGURE 7.1-2
INCIDENT RECEIVER RADIATION RADIAL LOCATION AT ORBIT TIME

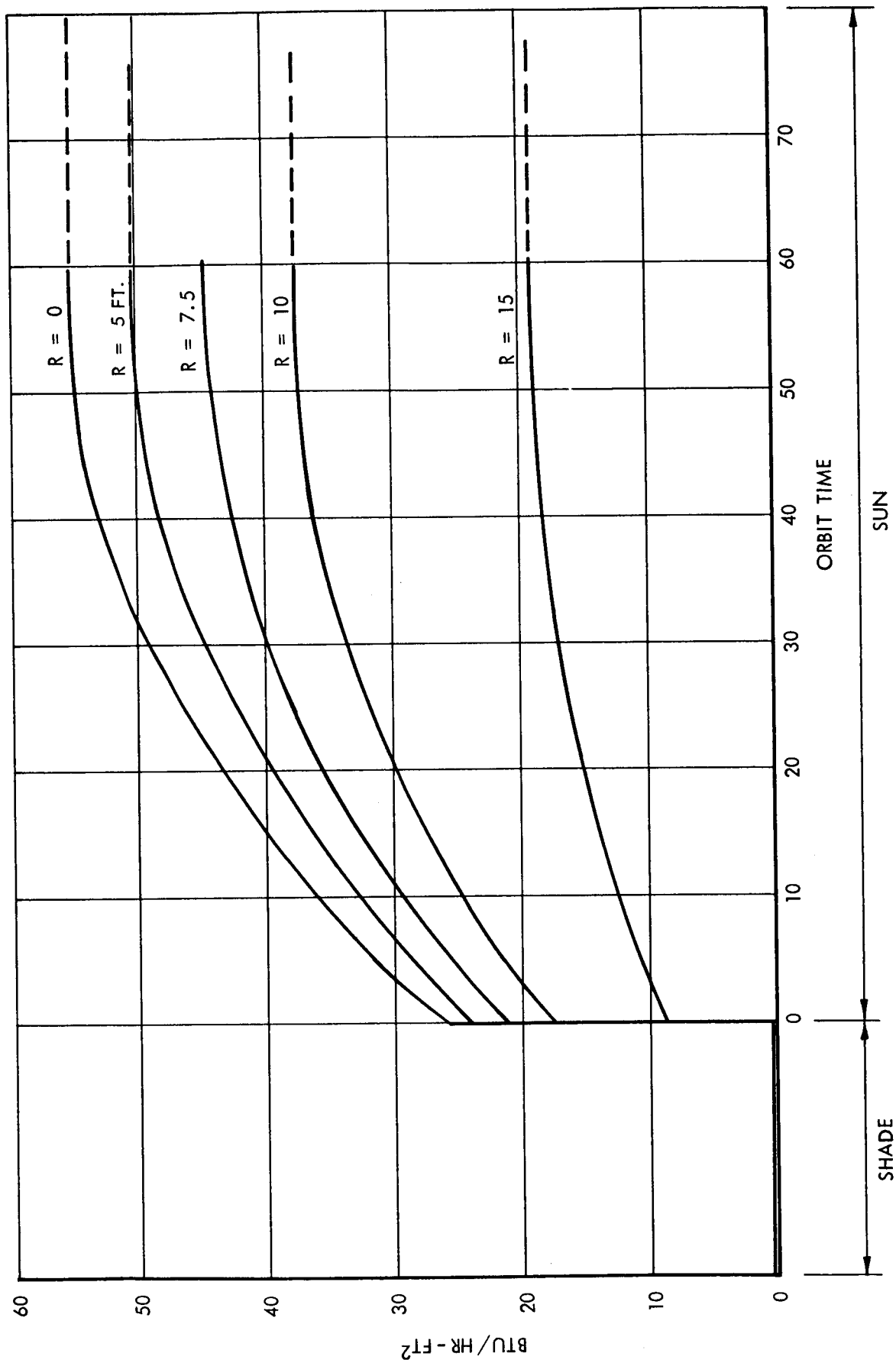


FIGURE 7.1-3
INCIDENT RADIATOR ENERGY VERSUS RADIUS

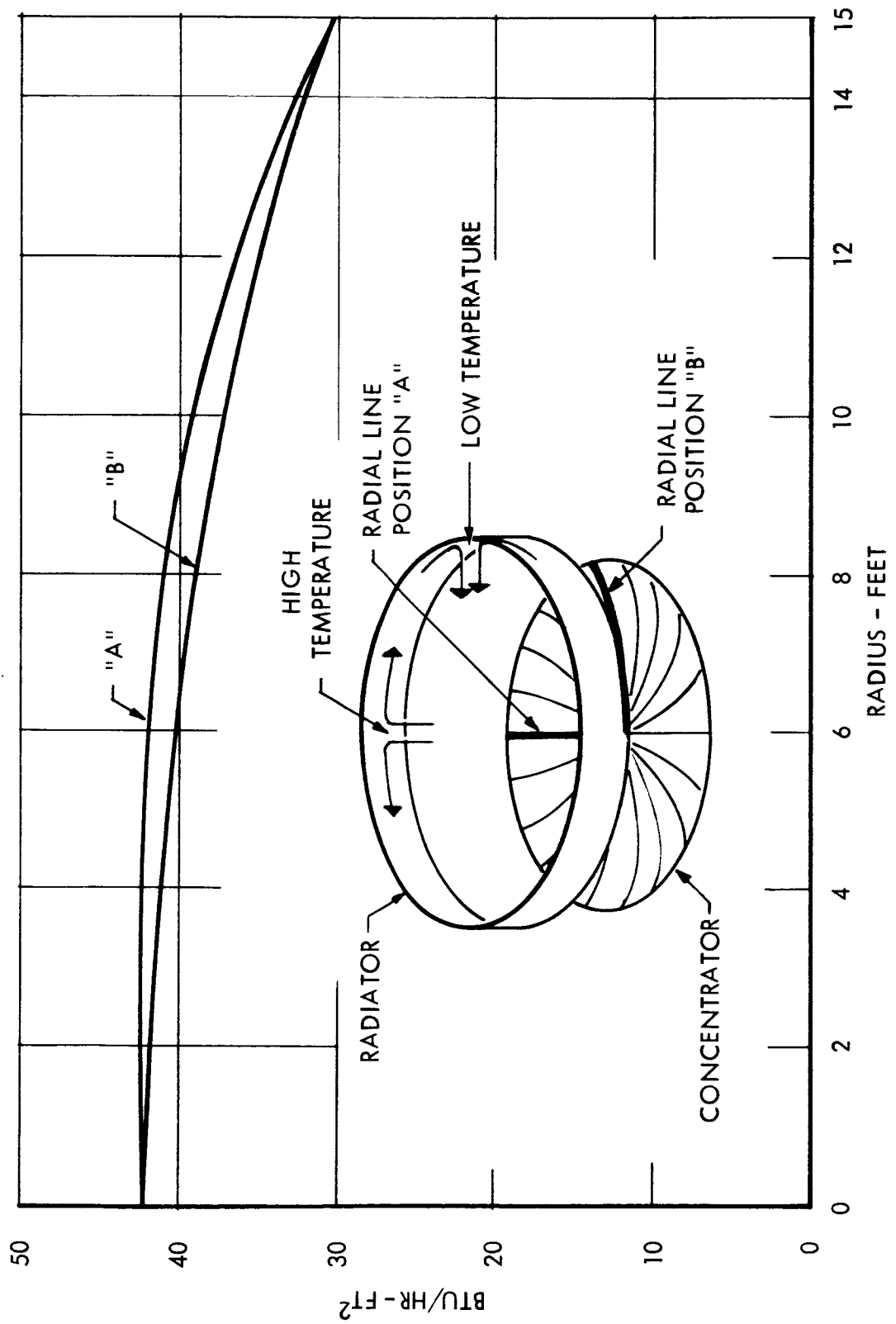


FIGURE 7.2-1a
 TOTAL ABSORBED RADIATION - BTU/HR FOR UNIT AREA AT CENTER OF CONCENTRATOR
 OF 30' DIAMETER, 60° RIM ANGLE, 300 NM ORBIT

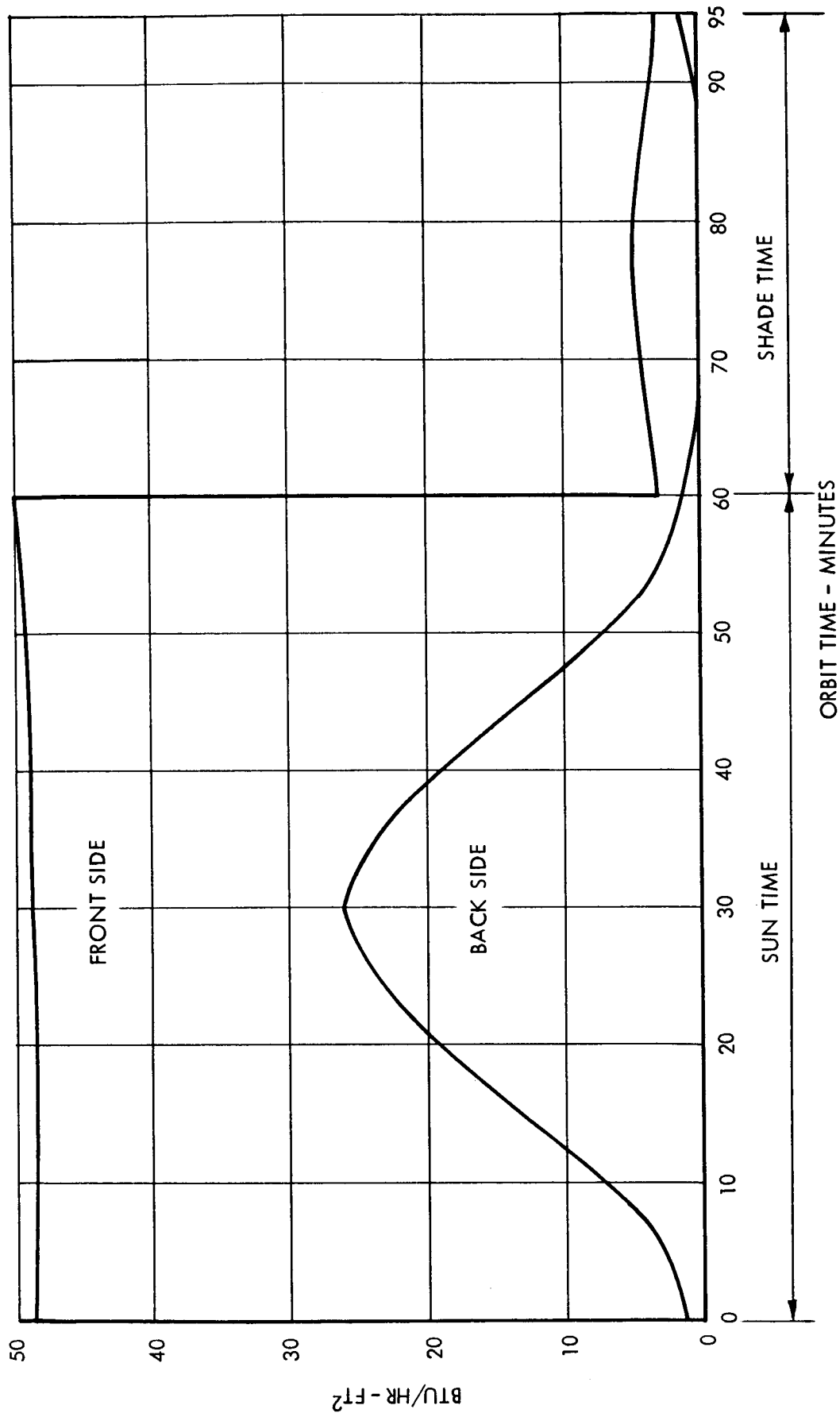


FIGURE 7.2-1b
 TOTAL ABSORBED RADIATION - BTU/HR FOR UNIT AREA AT 7.5°R OF CONCENTRATOR
 OF 30' DIAMETER, 60° RIM ANGLE, 300 NM ORBIT

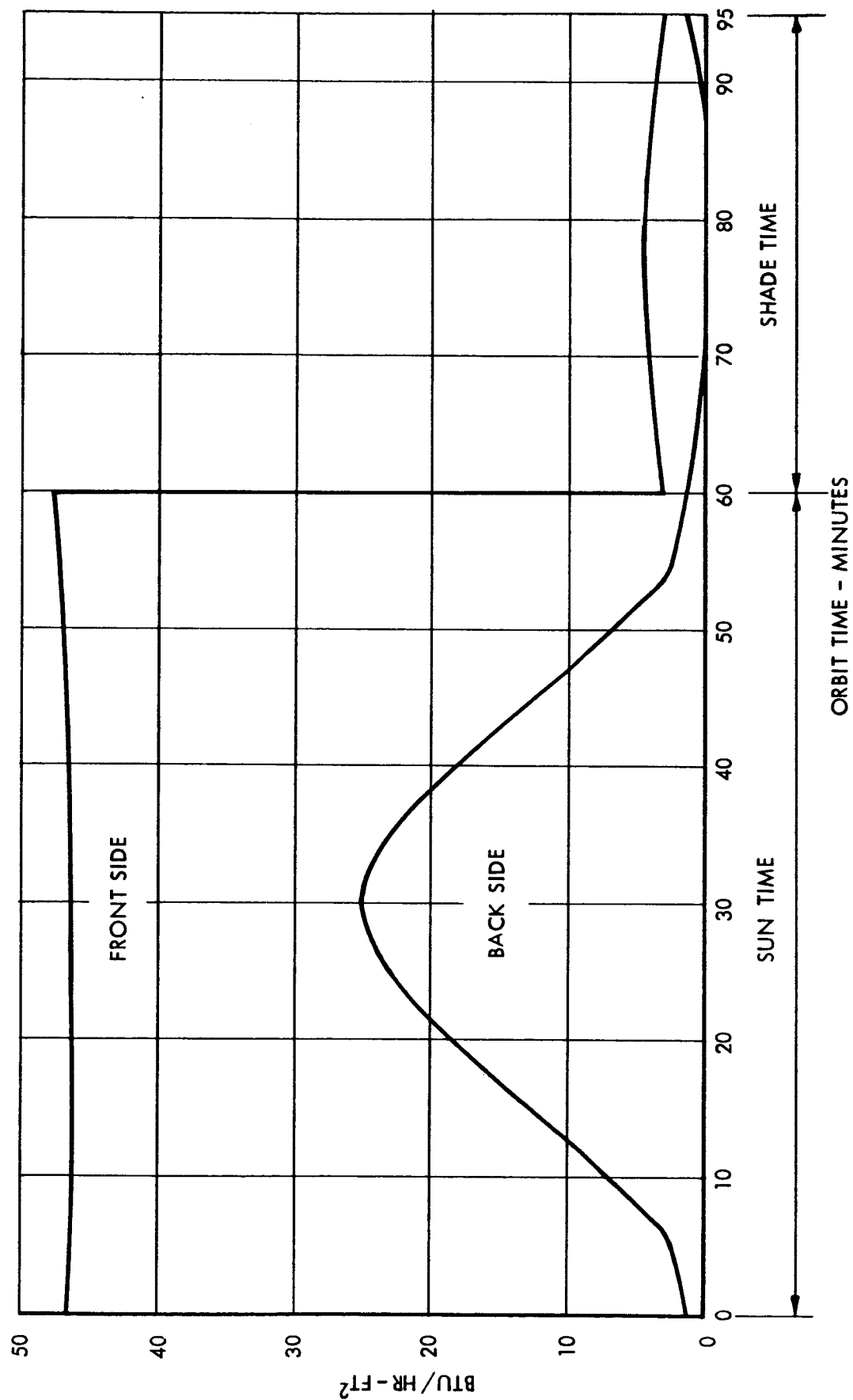


FIGURE 7.2-1c
TOTAL ABSORBED RADIATION - BTU/HR FOR UNIT AREA AT RIM OF CONCENTRATOR
OF 30' DIAMETER, 60° RIM ANGLE, 300 NM ORBIT

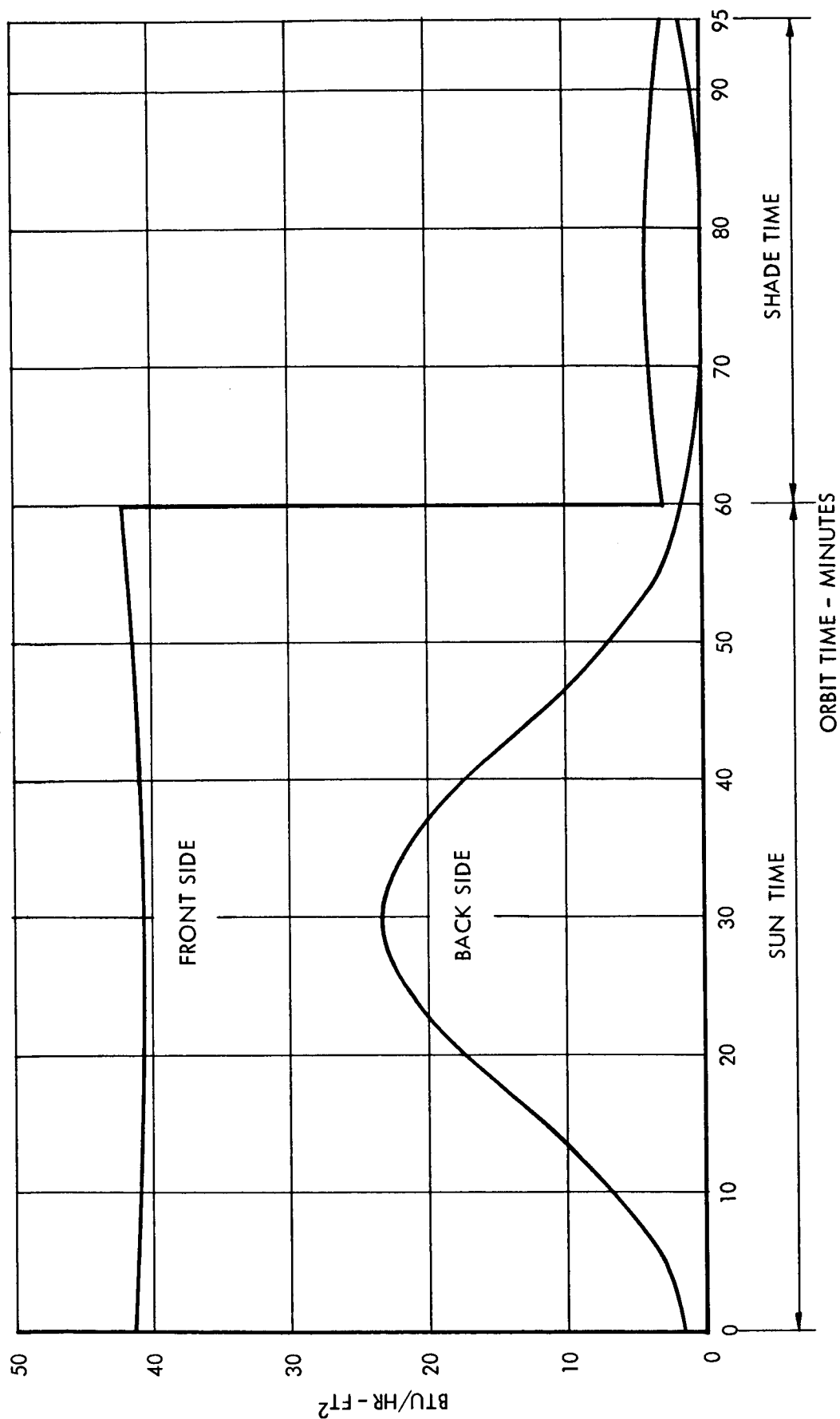


FIGURE 7.2-2
 PLANETARY RADIATION VIEW FACTOR FOR UNIT AREA AT RIM OF CONCENTRATOR
 30' DIAMETER, 60° RIM ANGLE, 300 NM ORBIT
 FRONT SIDE

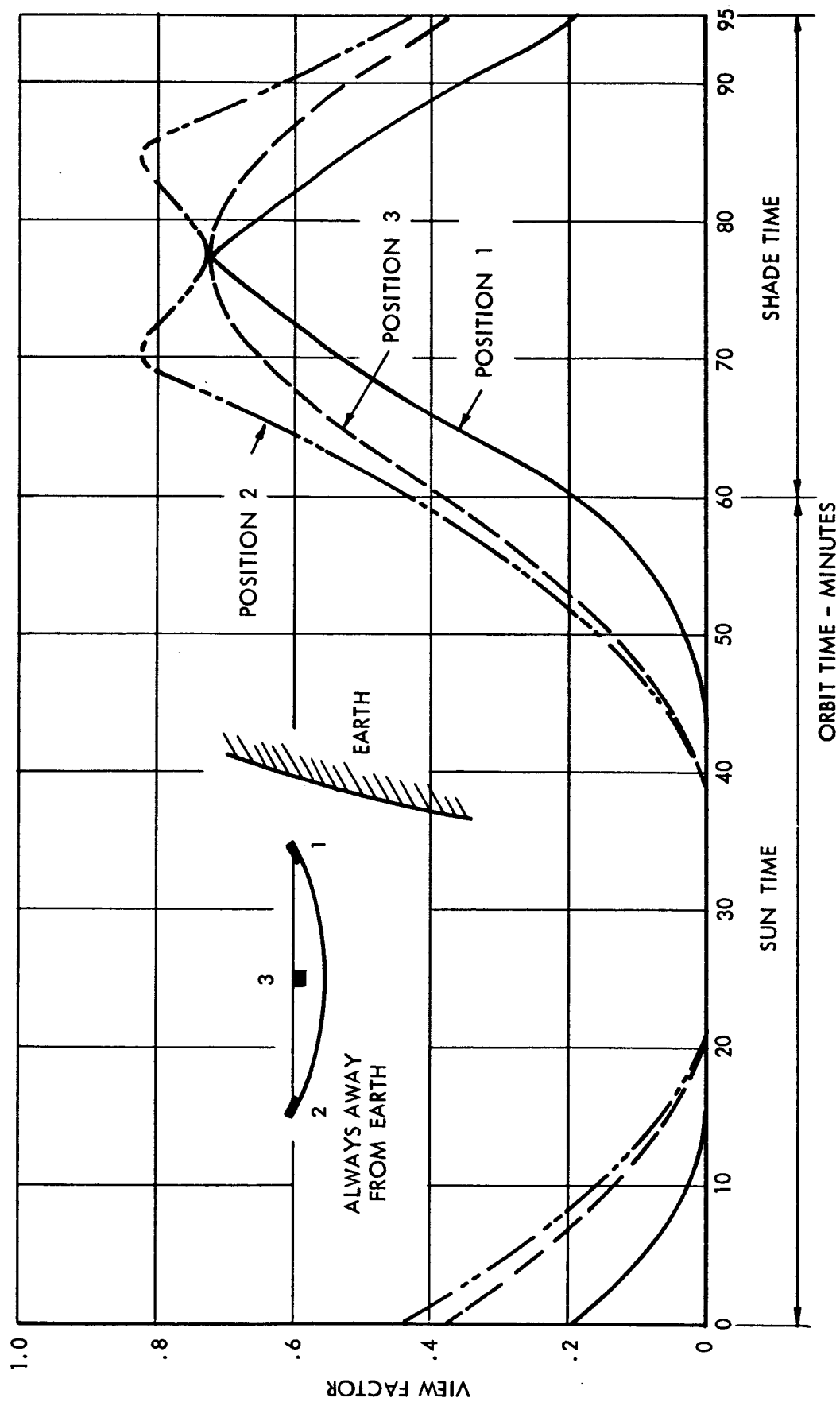
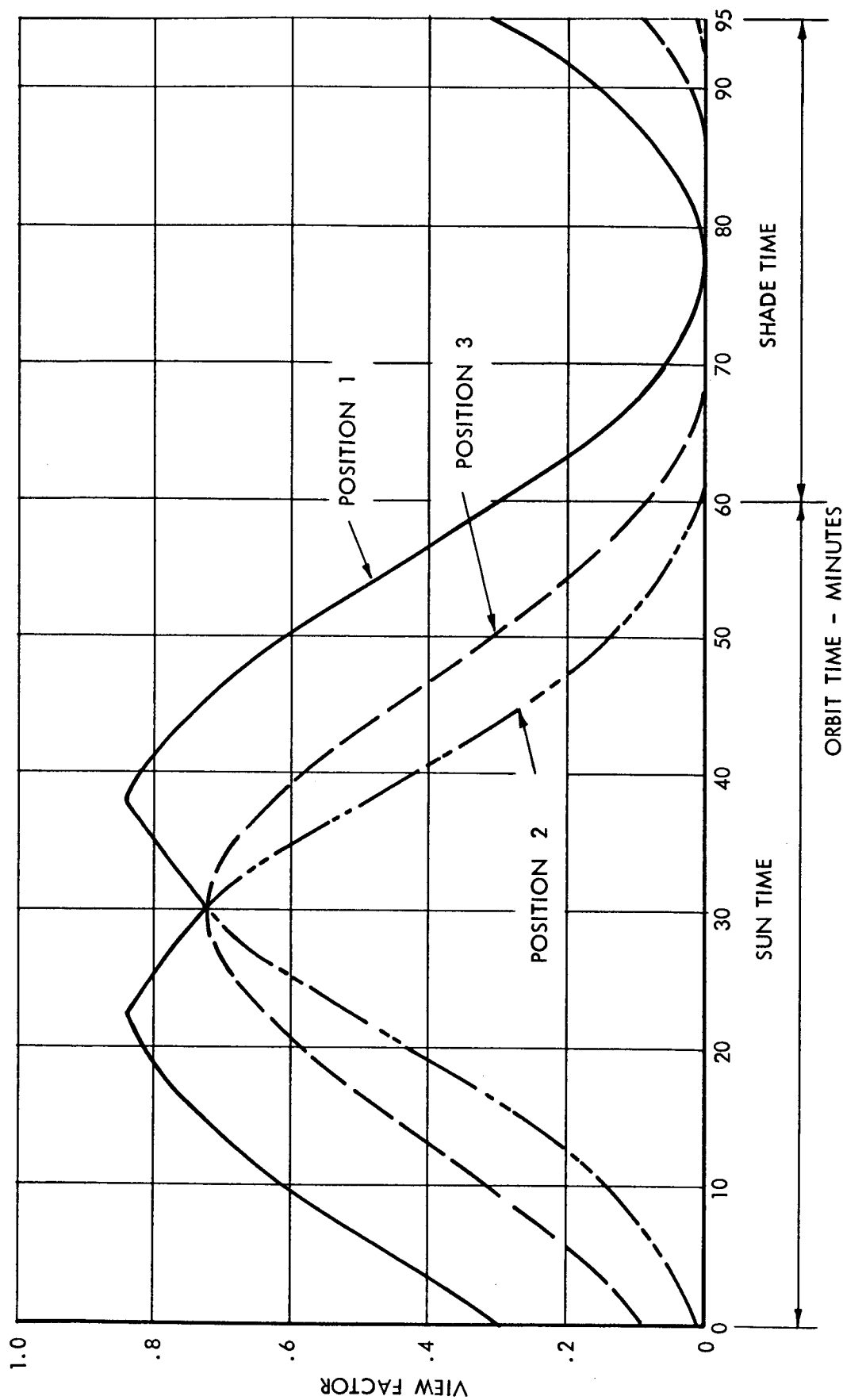


FIGURE 7.2-3
 PLANETARY RADIATION VIEW FACTOR FOR UNIT AREA AT RIM OF CONCENTRATOR
 30' DIAMETER, 60° RIM ANGLE, 300 NM ORBIT
 BACK SIDE



7.3 Transient Heat Balance

The temperature experienced by an object in space will be determined completely by the balance between the radiation absorbed and that radiated when there is no internally generated heat. The expression which was used to calculate the transient temperature characteristics is,

$$\frac{dT}{dt} = \frac{I_A - I_R}{mc}$$

Using absorbed heat (I_A) values presented in Section 7.2 the heating and cooling characteristics of the reflector material were calculated. Transient calculations were started from a calculated equilibrium temperature which was assumed to occur at the end of the sun period. An iteration about this temperature was required until the calculated transient temperature at the end of the orbital variation matched the assumed initial temperature.

Typical results for various membrane weights are shown in Figures 7.3-1 and 7.3-2.

When the transient heat balance of the honeycomb sandwich material is considered, the problem becomes complicated by the possible temperature differential between the front and back face masses. To obtain a solution, the thermal conductivity of the honeycomb sandwich material must be known. Vacuum heat transfer test data obtained during the Sunflower program was used to estimate the conductance of the 1/4 inch hex core used in the Brayton structural design. These results are shown in Figure 7.3-3. Since the major portion of the heat transferred thru the sandwich material in a vacuum is by conduction thru the core foil walls, the extrapolation was based upon the ratio of core sizes.

Using this thermal connection between the masses of the front and back faces, the transient heat balance (including the iterative consideration previously mentioned) was calculated. The resulting transient thermal gradient map is shown in Figure 7.3-4 for the rotating spacecraft condition where only a radial gradient is significant.

A point of particular interest in the orbital variations is the end of the sun

FIGURE 7.3-1
TRANSIENT TEMPERATURES
300 MILE ORBIT
IDEALIZED FLAT COLLECTOR

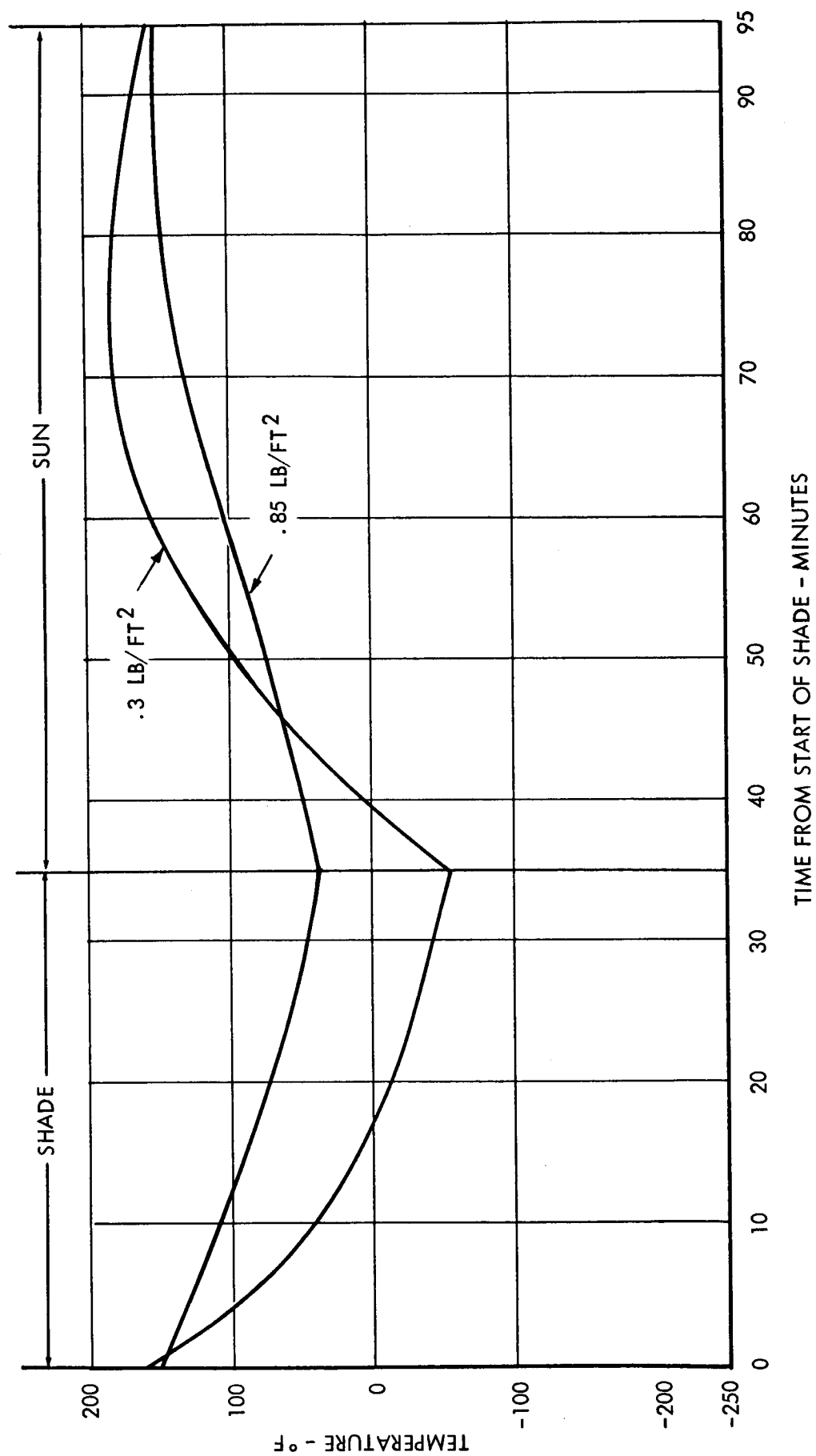


FIGURE 7.3-2
TRANSIENT TEMPERATURES
24 HOUR ORBIT
IDEALIZED FLAT COLLECTOR

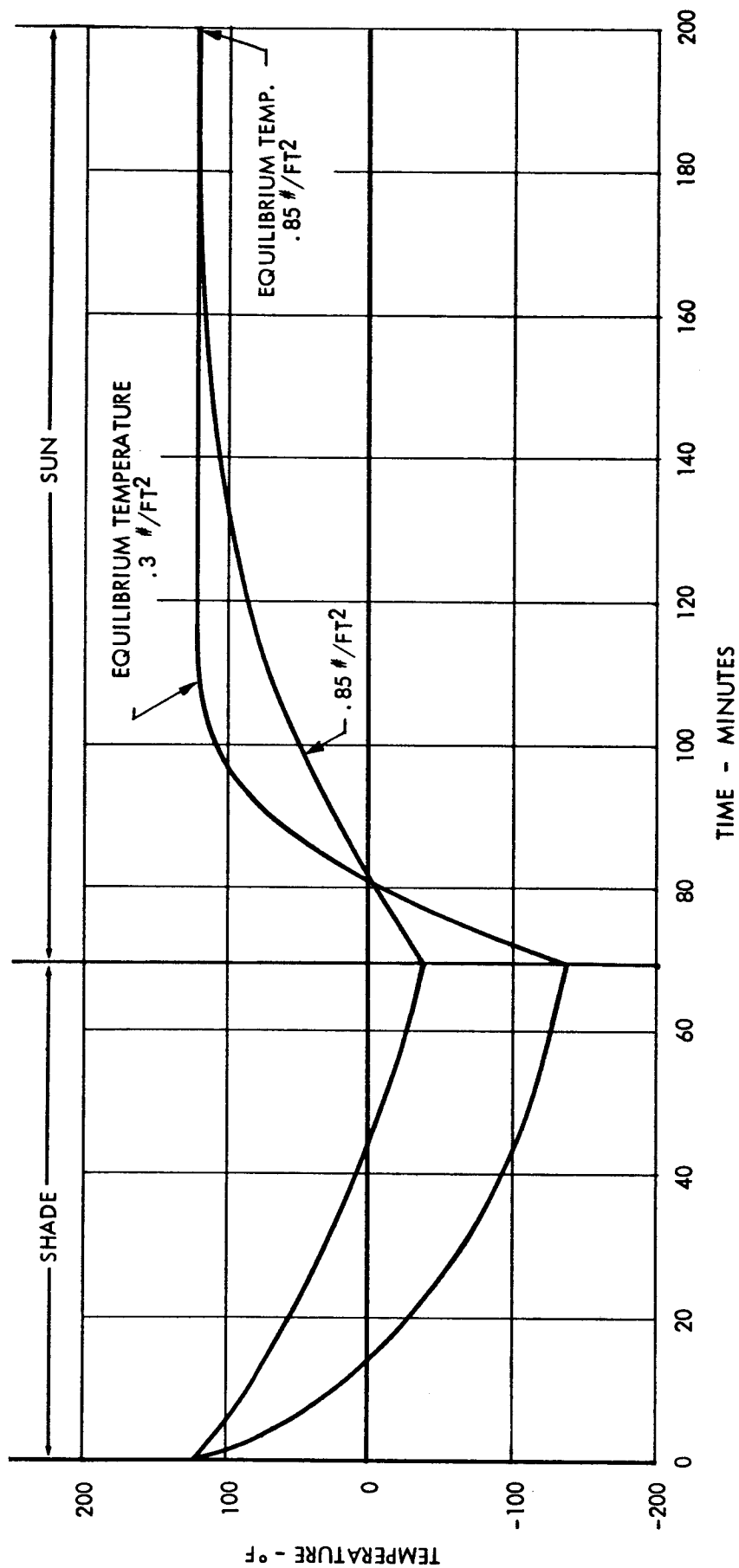


FIGURE 7.3-3
 ΔT VERSUS HEAT RATE THROUGH HONEYCOMB IN VACUUM

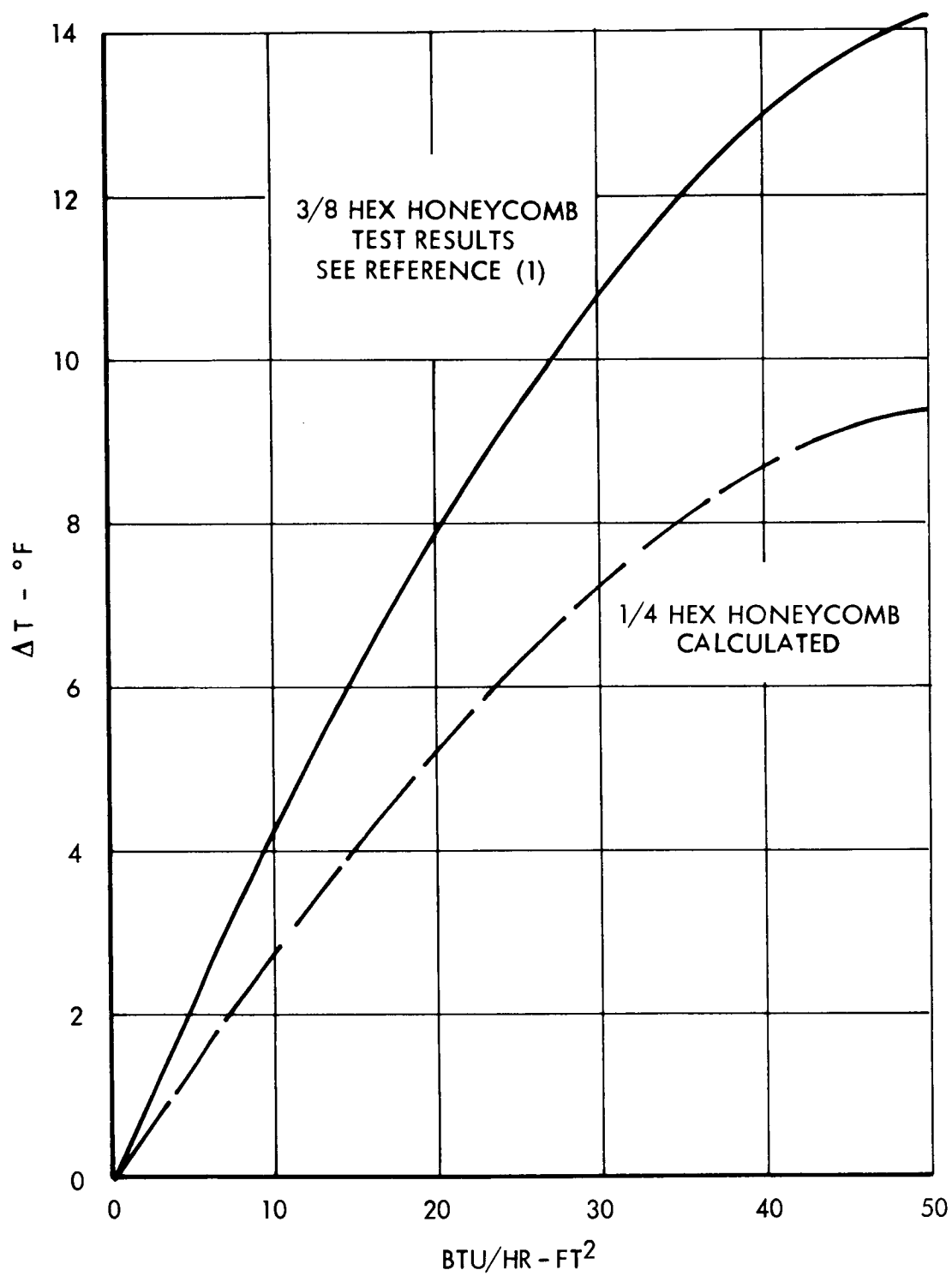
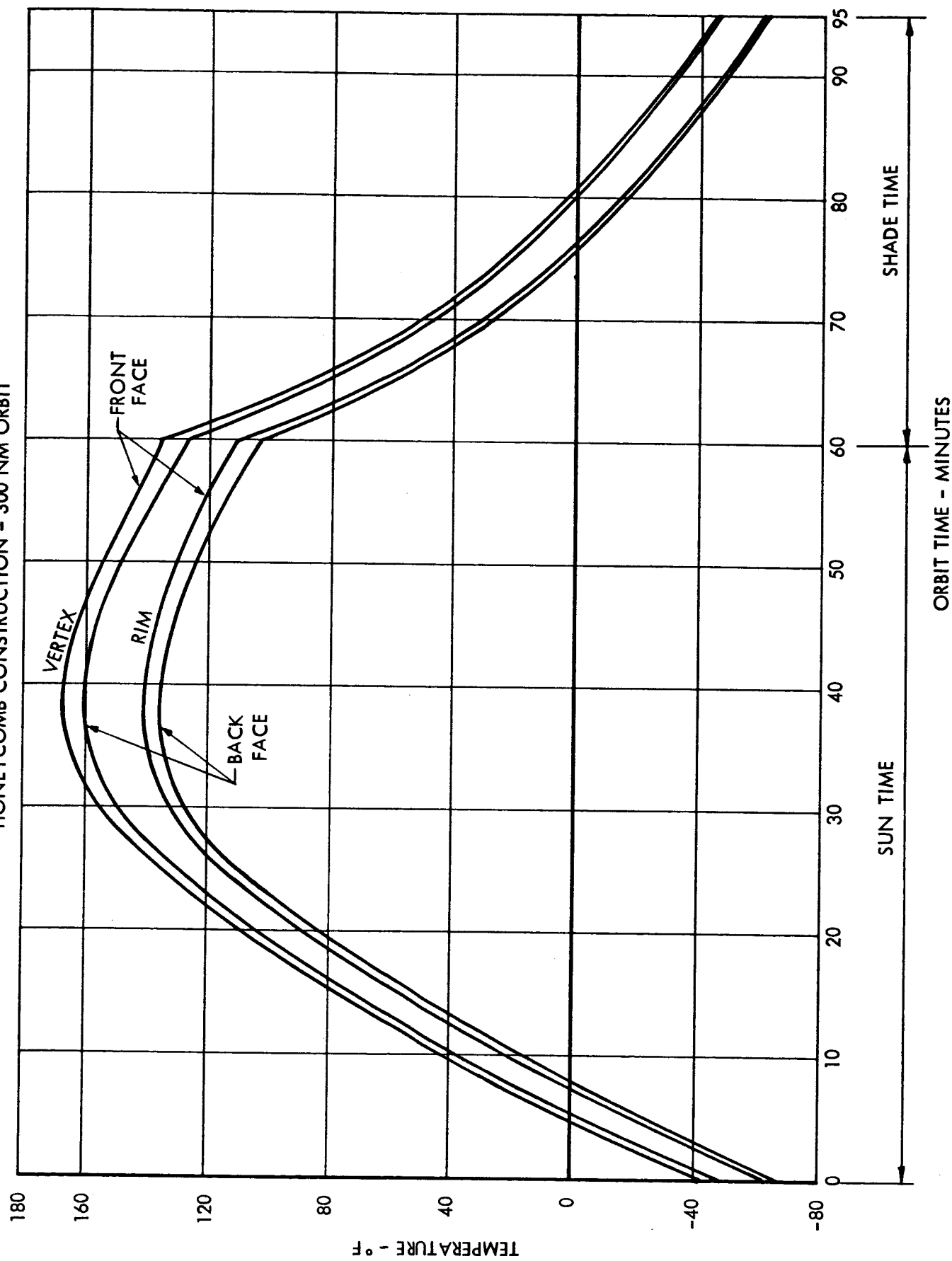


FIGURE 7.3-4
TRANSIENT TEMPERATURES OF CONCENTRATOR
HONEYCOMB CONSTRUCTION - 300 NM ORBIT



phase. At this point the thermal gradients tend to be a maximum because the greatest unbalance occurs between the absorbed energy on the front and back sides. A detailed plot of the gradients at this point is shown in Figure 7.3-5. Also displayed in the figure are the effects of lateral conduction of heat in the collector materials. Due to the thin materials and the low mass, very little gradient "leveling" is accomplished by conduction.

For the non-rotating spacecraft similar calculations can be made for this point in orbit using the data presented in Figures 7.2-2 and 7.2-3.

These temperature variations were used as input parameters for evaluating the thermoelastic deflections of the concentrator as discussed in Section 6.0. Since these temperatures were arrived at by using typical radiation coefficients for aluminum reflectors, improved temperature characteristics can be obtained by proper use of thermal control coatings.

7.4 Thermal Control Design

As was noted in Figure 7.3-5, lateral conduction of heat in the collector materials has only a small affect on the temperature. Thus it may be concluded that the temperature of various areas of the concentrator will be primarily a function of the local radiation characteristics in that specific area. This leads to the possible use of thermal control coatings or materials in the collector design.

One such possibility which was investigated briefly during the study program is the use of a commercially available (25) multiple radiation barrier material on the back side of the concentrator. For example, the radial temperature gradient shown in Figure 7.3-5 can be eliminated by varying the total emissivity of the back side with respect to radial location. This could be accomplished by covering portions of the area with multiple radiation barriers. Reducing the emissive surface would result in a higher overall temperature level; however, covering 5% of the area at mid radius and increasing to 20% at the rim would result in the constant face temperature shown in Figure 7.4-1. The added weight would be approximately 5 lbs.

FIGURE 7.3-5
STEADY STATE RADIAL TEMPERATURE OF CONCENTRATOR
AT END OF SUN TIME - 300 NM ORBIT

- I SINGLE SHELL
- II HONEYCOMB - NO SIDE CONDUCTION
- III HONEYCOMB - WITH SIDE CONDUCTION
- IV SUPPORT RING - WITH CASE III

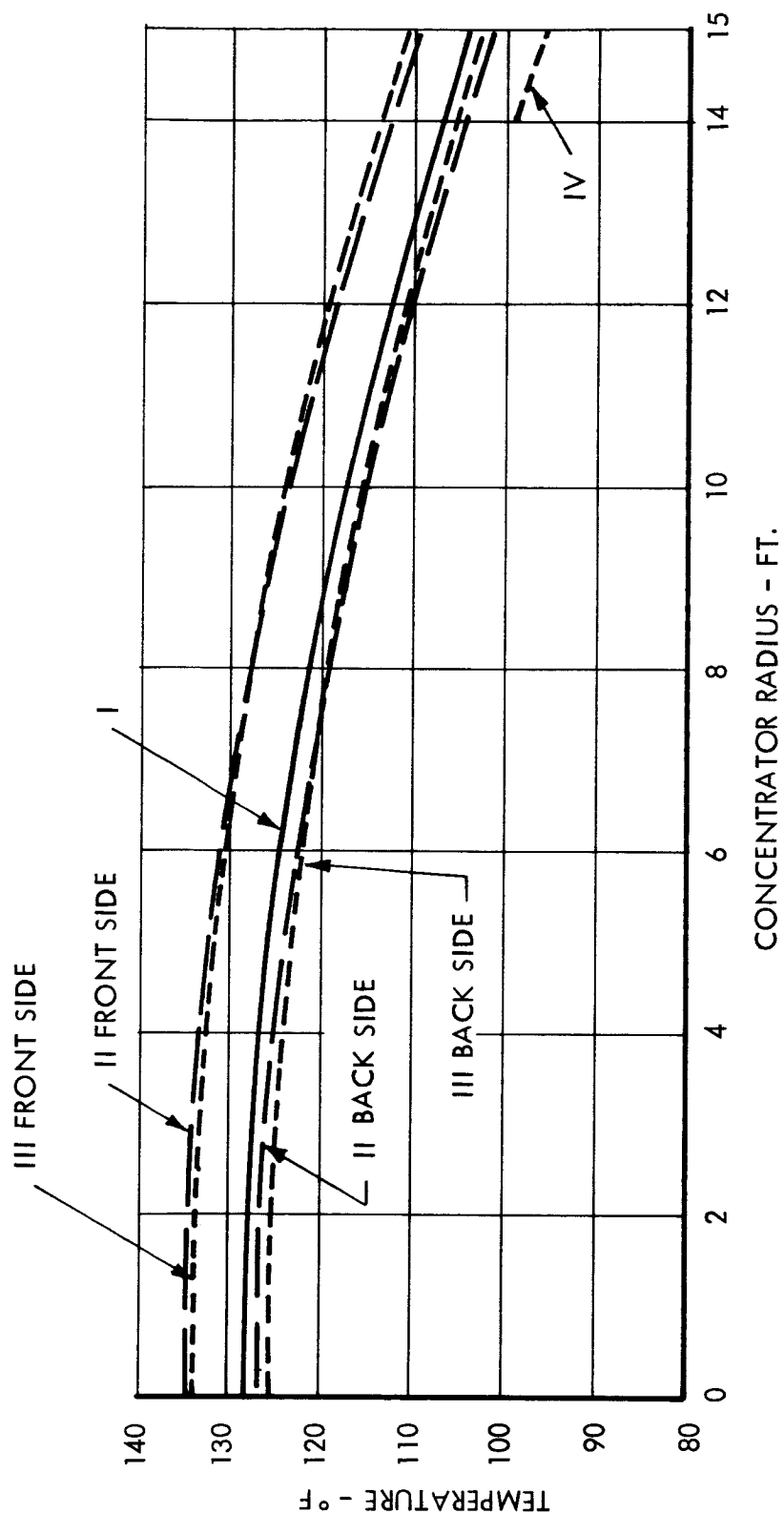
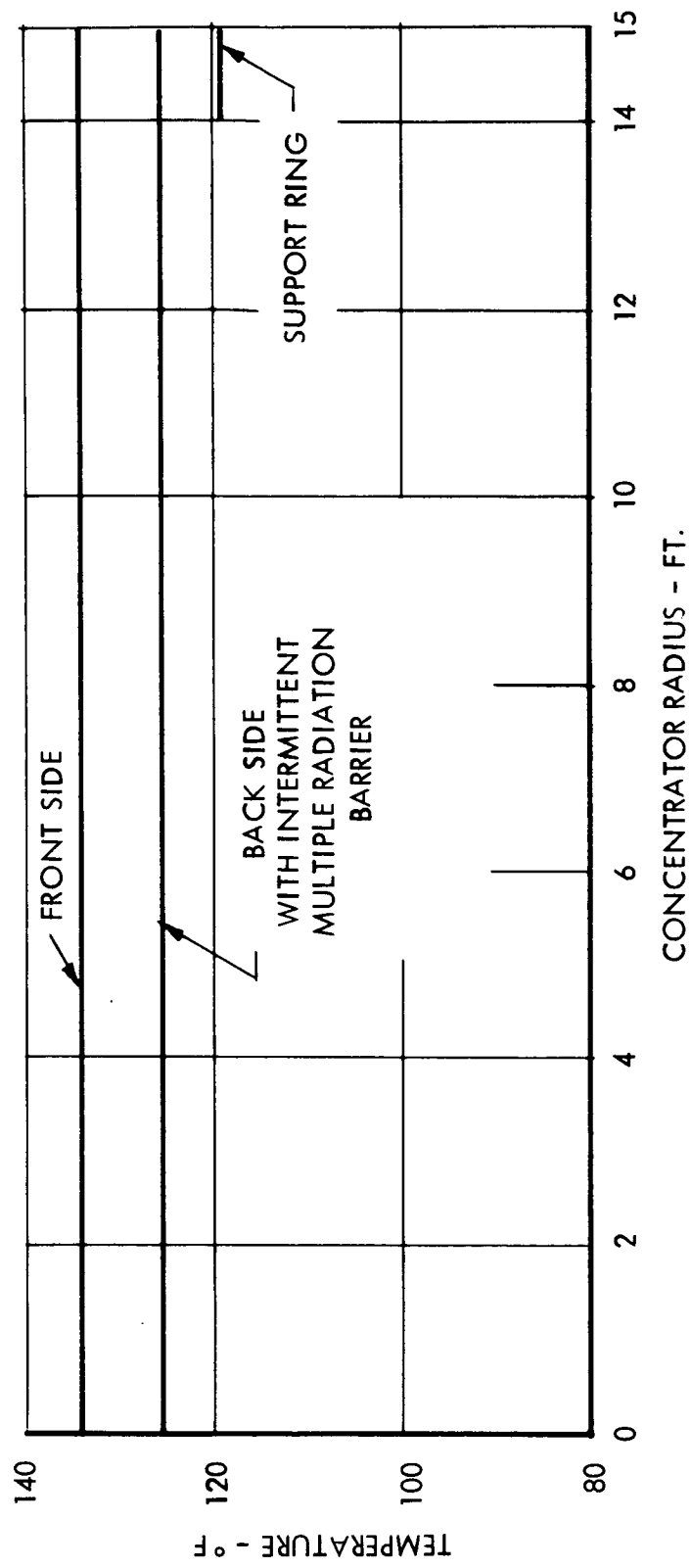


FIGURE 7.4-1
STEADY STATE RADIAL TEMPERATURE OF CONCENTRATOR
AT END OF SUN TIME - 300 NM ORBIT



The selection of emissive characteristics for the back face and the overall thermal control design concept must be based upon finalized calculations and tests which include the specific orbital mission trajectory and the influences of heat loads and shadowing of the finalized spacecraft and system geometry. However, to maximize system performance the use of transparent selective radiation control films on the mirror face is not recommended due to the associated reduction in reflectivity.

8.0 FABRICATION CONSIDERATIONS

As presented in Section 6.0, the recommended Brayton concentrator structural design utilizes adhesive bonded aluminum honeycomb sandwich construction. Although the primary advantage of this design concept is its structural efficiency, another major advantage is the highly developed fabrication technology which has grown out of numerous design applications of adhesive bonded construction in the aircraft, missile, and space industry (26), (27), (28). These applications and many others have demonstrated the superior structural efficiency of adhesive bonded honeycomb sandwich construction.

What is required for successful fabrication of sandwich material reflectors is the utilization of aircraft standard fabrication practices within the requirements for high geometric quality. This high degree of geometric and optical quality can only be obtained by detailed control of tooling error, fabrication processing, assembly, and handling. Adequate inspection is also required to insure quality.

8.1 Sector Fabrication Process

The fabrication concept of the Brayton concentrator involves the fabrication of individual segments which are then assembled into the complete one piece concentrator. The segment approach is necessary due to the available aluminum stock size limitations. Also, this allows vacuum aluminizing the mirror surface in the presently available NASA facility (1); where a higher degree of quality control can be obtained compared to mirroring the full paraboloid.

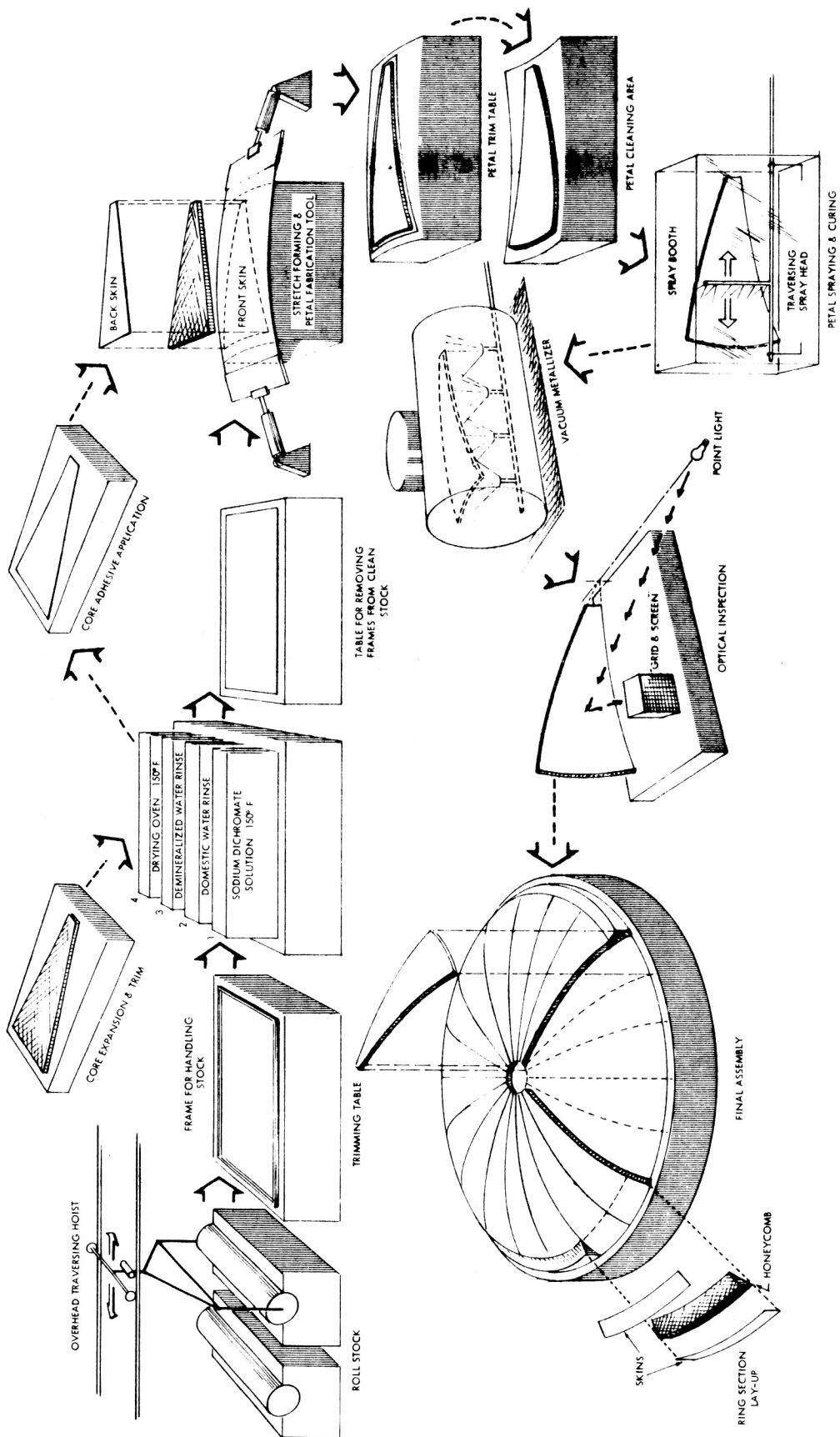
The following is a detailed description of the recommended Brayton concentrator fabrication procedure. Refer to Figure 8.1-1 for sequence of operations and to the concentrator design layout (drawing 818180) for parts descriptions.

Sector Fabrication Procedure

1. Backface Stock - 4 mil aluminum

- .1 Roll out stock on table. Trim to length (Table raised to take one-half of handling frame). Clamp stock into handling frame.
- .2 Transfer to cleaning area. Run thru acid tank, two rinse tanks, and drying oven.

FIGURE 8.1-1 FABRICATION SEQUENCE



- .3 Transfer to clean room where handling frame is removed.
 - .4 Vacuum clean surface of stretch form tool. Treat tool surface with lubricant. Reclean tool surface and place back-face stock on tool. Perform final inspection of tool and stock surfaces. Perform final cleaning. Stretch back-face. Punch locating holes and rough trim back-face. (same size as core)
 - .5 Remove back-face from tool using contoured handling frame (and tape to hold stock). Protect faying surface and store temporarily.
2. Front face stock - 8 mil aluminum
- .1 Roll out stock, reflective side up on trim table. Trim to length. (Here again half of handling frame is around trim table raised center). Place a thin sheet of rubber or plastic (Viton or Mylar) over the reflective face of the aluminum. Clamp remaining half of handling frame in place.
 - .2 Transfer to cleaning area. Run thru cleaning and drying sequence.
 - .3 Transfer to clean room where handling frame is removed. Remove with protective face toward table.
 - .4 Clean stretch form tool surface. Recoat with lubricant. Vacuum clean and place front face stock on tool. Perform final inspection and vacuum cleaning of tool and stock surfaces. Stretch front face. Punch locating holes in stock. Trim stock oversize. Put pins in locating holes.
3. Core - 1/4 hex - .250 thk - .0015 foil
- .1 Have HOBE faces machined to provide a flat cell edge and required .250 thickness.
 - .2 Partially expand HOBE and run thru degreaser.
 - .3 Fully expand HOBE and check for defects.
 - .4 Trim HOBE a few inches oversize except at the small end using a pattern.

Also cut out areas for handling fasteners and locating hole bushings.

4. Sector Lay-up

- .01 Seal front face to tool and pull full vacuum. Put blind bushings over locating pins.
- .02 Lightly coat front face faying surface with adhesive (1 to 2 mil using a glass cloth swab)
- .03 Dip core to provide for a fillet having a .036 throat (.025 high)
- .04 Place core on front face. Pot handling fasteners and locating bushings in place.
- .05 Locate I.D. Channel cut out core, and pot channel tie-ins in place.
- .06 Put back-face on locating pins and locate handling fastener holes.
- .07 Lightly coat faying surface of back-face (1 or 2 mils) with adhesive and roll coat or spray coat core back-face with a thixotropic adhesive.
- .08 Put back-face in place. Put core supports all around petal edge. Bag back-face and pull partial vacuum. (Only enough pressure to hold parts in intimate contact).
- .09 Cure assembly at room temperature for required length of time.
- .10 Post cure assembly at 120°F for required length of time.
- .11 Remove from assembly tool and place on trimming tool. Trim to required size. Protect new faying surfaces along radial edges and outer circumference.
- .12 Using handling frame take trimmed petal from trimming tool. Use handling frame as a support while cleaning the front face.
- .13 Clean petal front face for specular coating.

- .14 Epoxy coat petal front face, dry or cure or both in a very clean environment. This treatment is termed a specularly coating because it provides a glass-like epoxy coating (one half to one mil thick) which improves the surface specularly over that obtained from the stretch formed aluminum.
- .15 Take finished and coated petal to vacuum metalizing tank and vacuum deposition coat as per drawing 818180. (All faying surfaces must be protected. Radial joints and outer circumference of back-face).
- .16 Inspect finished petal and put in storage area until final assembly. Petals wrapped for storage. (See Section 8.4 for a description of the inspection technique).

8.2 Final Assembly of Full Paraboloid

Upon completion of the twenty individual sectors, the final assembly is accomplished on a full paraboloidal male assembly tool. Two major steps are involved - bonding of the segments into a continuous shell, and application of the outer structural support ring.

The following is a detailed description of the final assembly procedure. Refer to drawing 818180.

Collector Final Assembly Procedure

1. Shell Assembly

- .01 Move finished petals into collector assembly area one at a time.
- .02 Locate center support ring "T" section on assembly tool. (Approximate location).
- .03 Vacuum clean and clean each sector of assembly tool surface before placing petal in position.
- .04 Remove general protective cover from petal before placing on tool. However, the faying surface protection should not be removed until the time of layup.

- .14 Epoxy coat petal front face, dry or cure or both in a very clean environment. This treatment is termed a specularity coating because it provides a glass-like epoxy coating (one half to one mil thick) which improves the surface specularity over that obtained from the stretch formed aluminum.
- .15 Take finished and coated petal to vacuum metalizing tank and aluminize. (All faying surfaces must be protected. Radial joints and outer circumference of back-face).
- .16 Inspect finished petal and put in storage area until final assembly. Petals wrapped for storage. (See Section 8.4 for a description of the inspection technique).

8.2 Final Assembly of Full Paraboloid

Upon completion of the twenty individual sectors, the final assembly is accomplished on a full paraboloidal male assembly tool. Two major steps are involved - bonding of the segments into a continuous shell, and application of the outer structural support ring.

The following is a detailed description of the final assembly procedure. Refer to drawing 818180.

Collector Final Assembly Procedure

1. Shell Assembly

- .01 Move finished petals into collector assembly area one at a time.
- .02 Locate center support ring "T" section on assembly tool. (Approximate location).
- .03 Vacuum clean and clean each sector of assembly tool surface before placing petal in position.
- .04 Remove general protective cover from petal before placing on tool. However, the faying surface protection should not be removed until the time of layup.

- .05 All petals will be placed on tool to check fit-up.
- .06 Half the petals will be removed and the center support "T" section bonded into the half shell.
- .07 The remaining petals can then be bonded to the "T" section.
- .08 Silastic RTV-731 will be used to seal all radial seams full length. Cure at room temperature for 24 hours and trim flush with front face faying surface. (A pre-bond coating for the faying surfaces may be required due to the extended time lapse between cleaning of the faying surfaces and the final assembly lay-up).
- .09 Lay-up front face doubler with glass cloth cut 1/4" oversize along each edge.
- .10 Cut joint core 1/8" oversize on width. Dip core to provide for a fillet having a .036 throat.
- .11 Lightly coat back or front face doubler with adhesive (1 - 2 mils).
- .12 Overexpand core slightly to allow side clearance when inserting into joint. Release core to take up side clearance. If required pull core to sides to insure contact between it, the adhesive impregnated glass cloth, and the petal core.
- .13 Lay up back-face glass cloth and back-face doubler and outer circumference doubler for rim ring. (Back face doubler extends only to edge doubler where they butt).
- .14 Dead weight joints and outer edge.
- .15 Room cure bonded joints and edge for required length of time.
- .16 Post cure bonded joints and edge at 120°F using heating blankets for required length of time.

2. Outer Support Ring Assembly

- .01 Have outer ring HOBE machined to proper contour and surface finish.

- .02 Partially expand HOBE and run thru degreaser.
- .03 Have ring web and ring flange sections cut and formed to required shape. Clean as described previously.
- .04 Rout edge of shell assembly to accept bent up tabs of ring skirt.
- .05 Fill routed edge of shell with adhesive and insert tabs of ring skirt.
- .06 Assemble complete ring skirt to shell in this manner and assemble skirt sections together using doublers and rivets. Hold in place and in correct position using fixtures on assembly tool. Allow to cure at room temperature and post cure at 120°F.
- .07 Cover inside surface of skirt with adhesive impregnated glass cloth.
- .08 Fully expand ring HOBE and examine for defects.
- .09 Dip expanded core in adhesive to provide a .096 fillet throat.
(Dip contoured face only).
- .10 Coat faying surfaces lightly with adhesive (1 - 2 mils).
- .11 Put core in place inside ring skirt. Stagger the core joints relative to the skirt joints.
- .12 Place adhesive impregnated glass cloth between the core faces in the core joints.
- .13 Place adhesive impregnated glass cloth over the top of the ring core to act as an adhesive holder between the ring flange and core.
- .14 Put ring flange on and join the ends of the flange sections using doublers and rivets. Inside edge of ring flange is to coincide with the inside edge of the ring back race doubler. Stagger joints.
- .15 Bag the entire assembly.

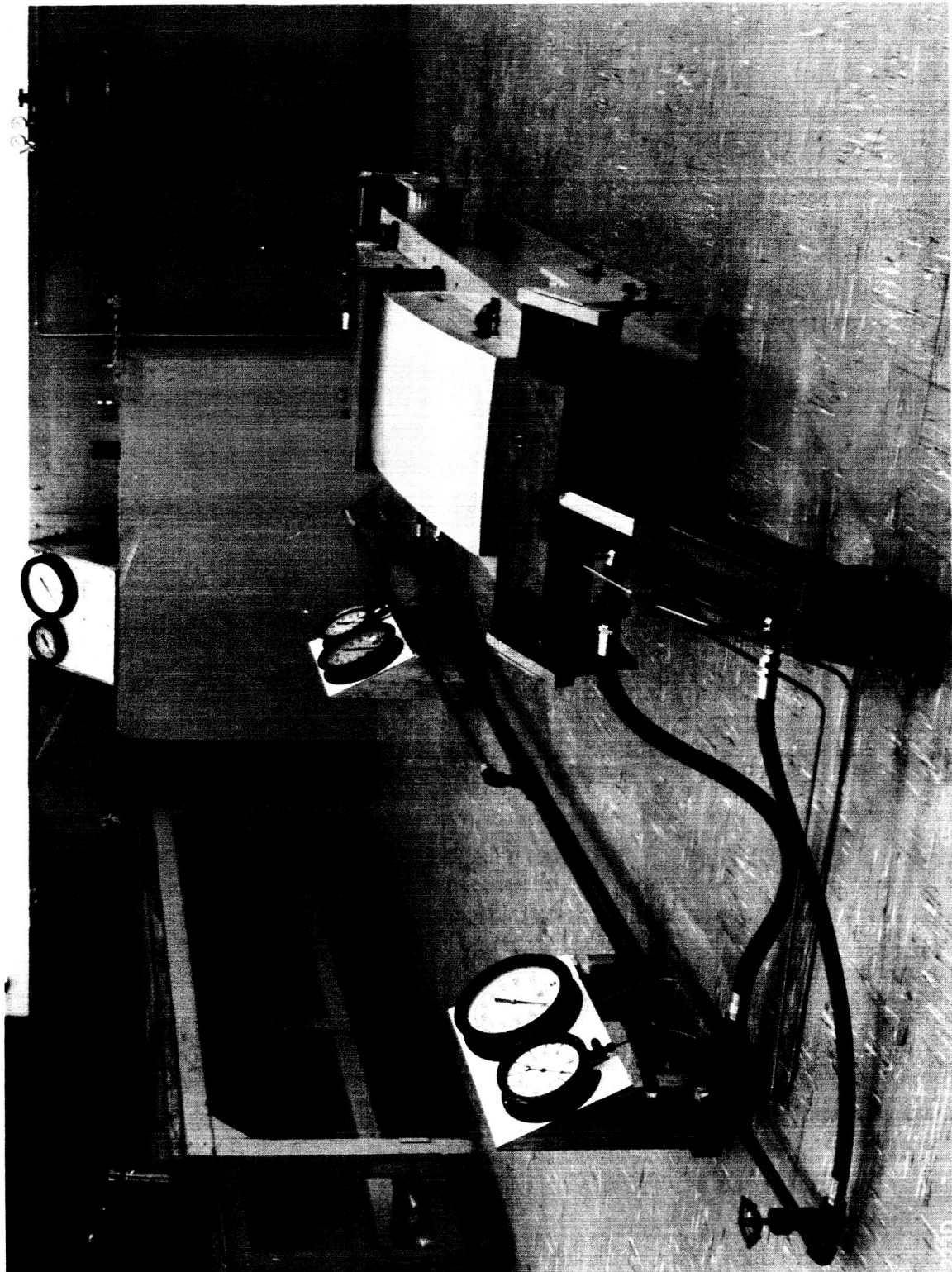
- .16 Allow ring assembly to room cure and then post cure the assembly at 120^oF.
- .17 Rout out edge of ring assembly for extruded close out section.
- .18 Fill routed edge of ring with a thixotropic adhesive and place adhesive impregnated glass cloth on edge of skirt and flange.
- .19 Put extruded close out section in place. Join ends of close out using doublers and rivets. Stagger joints relative to joints in skirt and flange. Vacuum bag the assembly and rivet at intervals. Room cure and heat cure.
- .20 Locate launch support fasteners from assembly tool.
- .21 Adhesive bond in place and room cure. Post cure at 120^oF.
- .22 Clean and paint or treat all back side surfaces for required space thermal control.
- .23 Remove complete collector from assembly tool.

8.3 Tooling

The major tooling requirements for the Brayton cycle solar concentrator consists of the paraboloidal surface patterns. For the optical accuracy requirements of the Brayton cycle concentrator, a highly accurate pattern is required for the replication. The sector fabrication techniques requires that the master tooling be only a segment of the full paraboloidal surface.

Thus, the master tool is a segment of the full paraboloid which is used as the stretch forming pattern for the reflector faces. Figure 8.3-1 shows a typical master tooling and stretch forming set-up at TRW.

The other major tooling requirement is the assembly pattern which must be a full paraboloid of revolution. The accuracy of this full tool is not as critical as the master tool since it is used for positioning and fixturing of the already formed sectors, and no surface replication is involved.



TYPICAL MASTER TOOL AND STRETCH FORMING FACILITY AT TRW

FIGURE 8.3-1

8.3.1 Master Tool

To satisfy the high geometric accuracy requirements of the Brayton cycle concentrator design and to be compatible with fabrication techniques, an all metal master tool is recommended. This tool, although approximately fifteen feet long and six feet wide, can be fabricated from a single piece aluminum casting. Highly accurate geometric shapes can be produced using numerically controlled profile milling. Computer controlled machines of the capacity required for this single piece tooling approach are being used in the aircraft and missile industry and several machines are available for use. A typical large capacity numerically controlled milling machine installation is shown in Figure 8.3-2.

This master tooling approach has been used successfully by TRW in a concentrator fabrication program for the Air Force (Contract AF 33(657)8101). Refer to Figure 8.3-1.

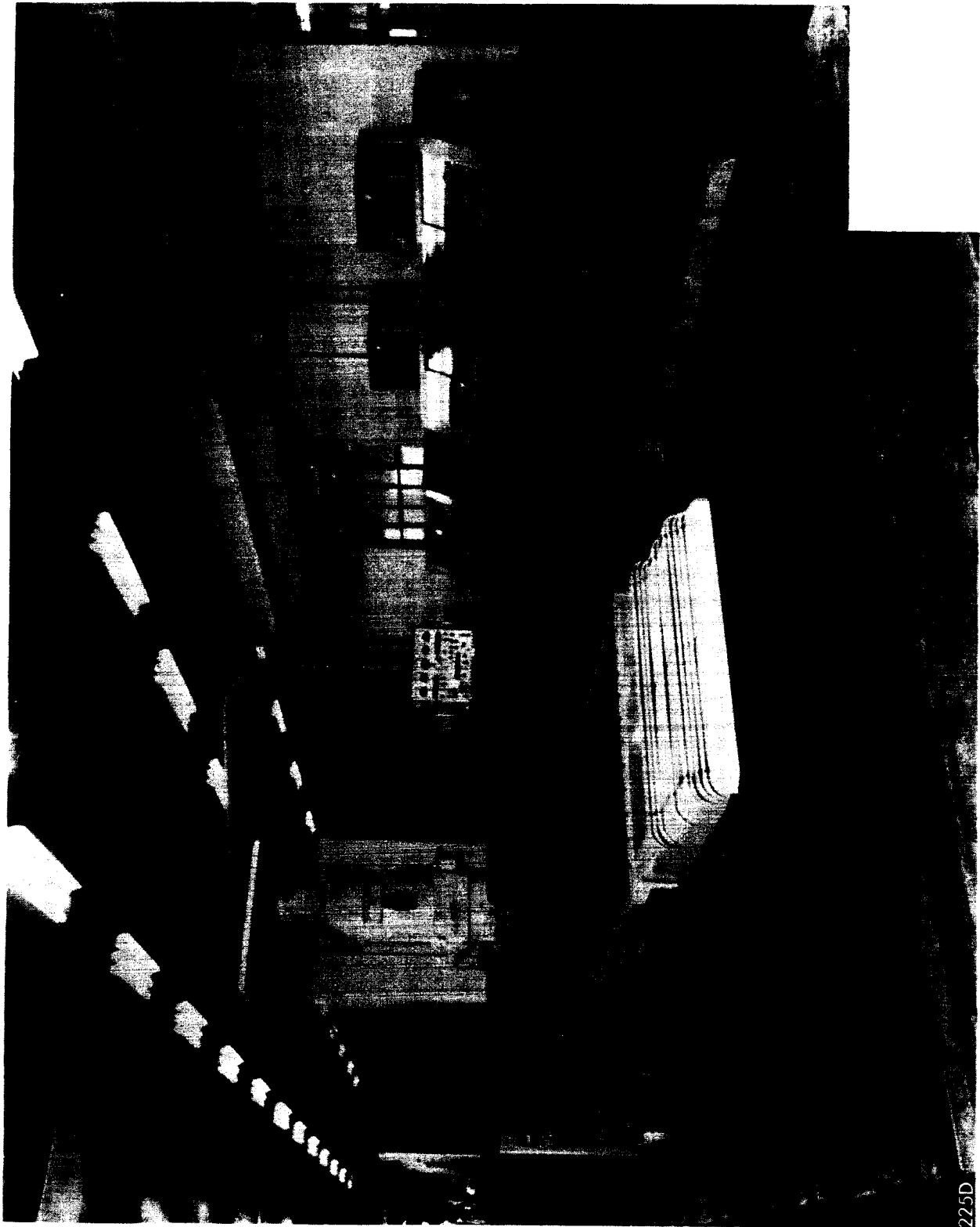
Other methods of providing master tooling (such as spin casting) were considered; however, they generally required a replication step to get the male stretch forming tool. This replication step is a source of error which is avoided by the profile milling approach.

8.3.2 Assembly Tool

Since the full paraboloidal assembly tool surface quality specifications and temperature requirements are not as critical as the master tool, plastic replication techniques can be used.

The metal master tool can be used to generate the full assembly tool by a plastic segment replication technique shown schematically in Figure 8.3-3. A female plastic pattern would be made on the metal master tool from which male segments for the full assemble tool would in turn be cast. Accurate alignment and final finishing of the segments would result in the full paraboloidal assembly fixture.

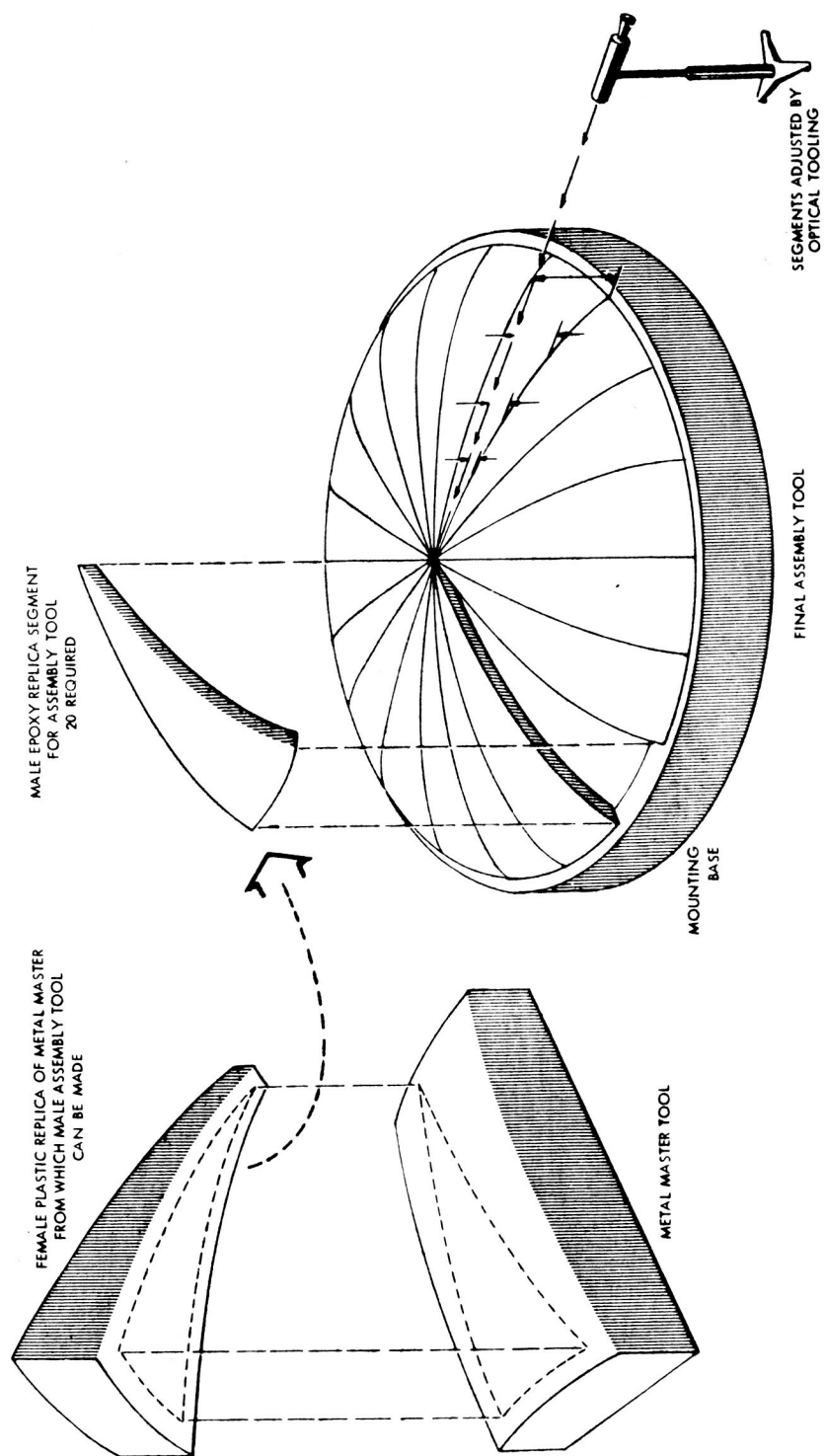
Another approach to obtaining an assembly tool is to numerically machine radial support ribs which would support individual mirror segments along their edges while being spliced. A spin casting approach is also possible.



TYPICAL LARGE CAPACITY NUMERICALLY CONTROLLED
MILLING MACHINE INSTALLATION

225D

FIGURE 8.3-3 ASSEMBLY TOOLING CONCEPT



8.4 Inspection

To insure the highest optical quality, thorough inspection is required in every step of the concentrator fabrication.

Two of the primary optical inspections are: (1) inspection of individual sectors as they are fabricated and (2) final optical inspection of the complete assembly. The evaluation of paraboloidal mirrors is normally based upon the optical focusing properties associated with the parabolic shape. Most of the optical test methods which are available can be categorized by the nature of the light source. The two general approaches are:

1. A collimated light source or actually the solar source (with incidence parallel to the optic axis) which will ideally reflect to the focal point. Examples of this type test are the ray trace test or Hartmann test.
2. A point source of light at the focal point which illuminates the mirror and ideally reflects collimated light. Grid tests use this type light source.

Generally, ray trace type tests are not suited for large mirrors because of the accurate alignment and traversing equipment which is required and because it is a time consuming process. Also, inspection data is obtained in the focal plane, and while this provides excellent insight as to the ultimate performance of the paraboloid, it does not provide a direct measurement of the surface errors.

It has been shown in the Sunflower collector development program (1) that gross waviness inspections of large surface areas can be rapidly and accurately performed by using a point light source - grid screen method. This method has also been used in inspecting five foot diameter mirrors. The point source grid method requires a single accurate alignment of the grid and screen and the point source of light. If the grid is designed to cover the entire collector surface, this provides an excellent overall picture of the paraboloid surface characteristics and also minimizes the actual test time since the grid screen can be photographed to provide a permanent record of the total surface

accuracy. As described in Section 5.1, each grid increment represents a data point and this information can be handled statistically to establish a standard deviation value σ for comparison with the mathematical model discussed in Section 4.2.

A more direct use of this type inspection information in predicting concentrator performance can be made by incorporating the measured surface deviations at each data point directly into the generalized theoretical analysis computer program. In this manner, the reflector is no longer considered as a paraboloid but, instead, as an arbitrarily shaped reflector surface based upon actual measured data. In other words, the mathematical model is eliminated from the computer program and the actual measured surface is used.

It is believed that this approach to optical inspection and utilization of resulting data will provide an accurate means of predicting orbital optical performance under a variety of environmental conditions.

8.5 Handling and Shipping Considerations

In the utilization of large-minimum weight structures designed for space applications, special considerations of handling and shipment become necessary. For solar concentrators an additional critical consideration is the protection of the reflecting surface from abrasive or corrosive environments.

8.5.1 Fabrication, Assembly, and Test Handling

During each step of the fabrication and assembly process, special techniques and fixtures must be used to insure against damage to the geometric and optical quality of individual components. Once the concentrator is assembled any handling operations should be performed using the eight point support system for which the structural support ring was designed. This will require a rigid handling frame for operations such as removal of the concentrator from the assembly tool, optical inspection or other test setups.

Protection of the mirror surface can be accomplished successfully by top coating the aluminized surface with approximately 2300 Angstroms of vacuum deposited silicon oxide. This protection is specifically recommended for the Brayton

developmental and ground test units. Since this coating results in a 3% to 4% reduction in reflectivity, development of a peel coating or sublimating coating for the flight units should be considered. The peel coating could be removed prior to launch or a sublimating coating would evaporate after a short period in the vacuum orbital environment. Selection of a protective coating depends to a great extent upon the finalized launch and start-up logistics of the Brayton cycle system.

8.5.2 Shipping

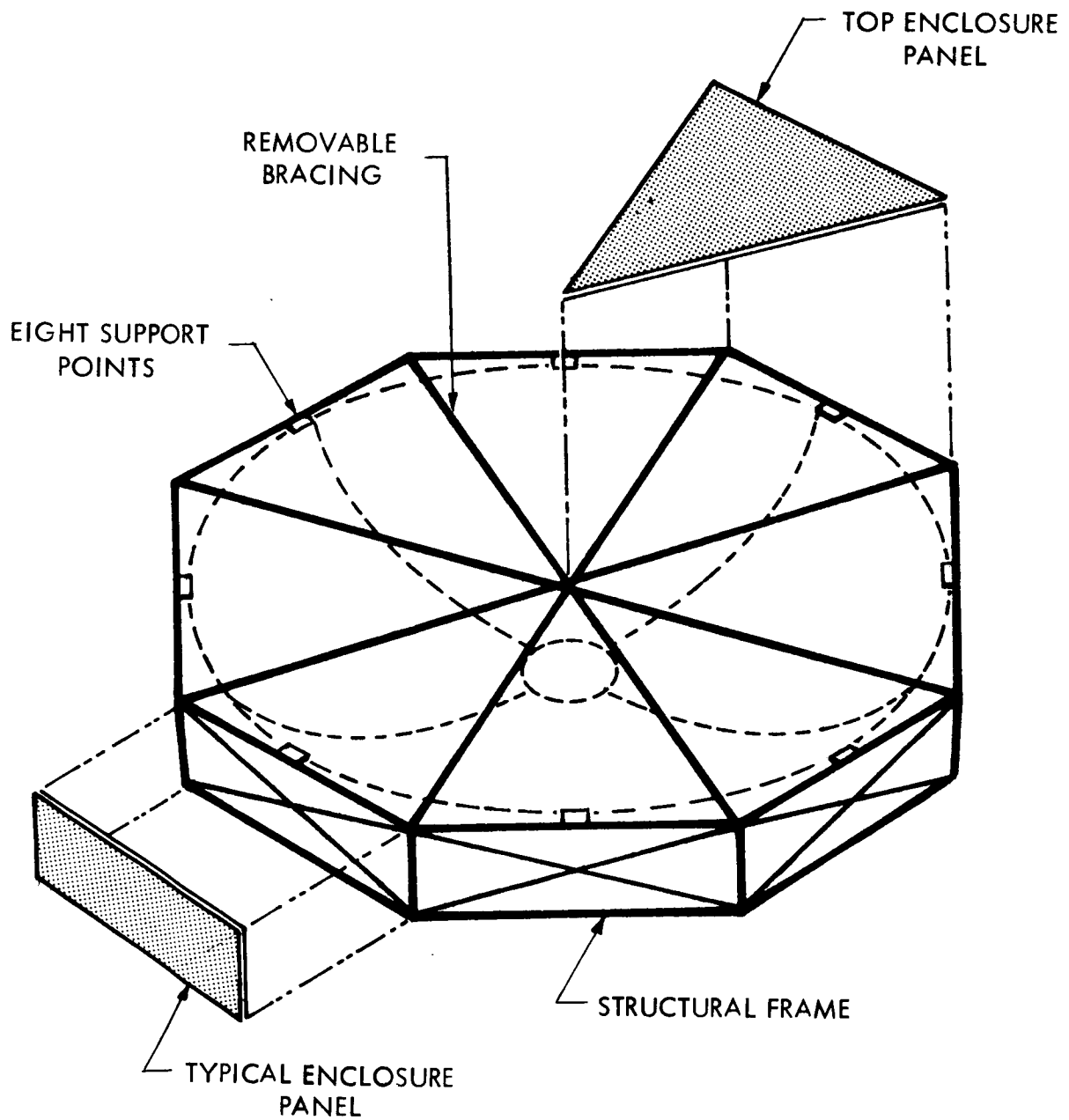
Shipment of the single piece 20 or 30 foot diameter concentrators can be accomplished by several methods. For any method which is chosen, an adequate shipping container must be provided. A typical crating concept is shown in Figure 8.5-1. Here an aluminum structural frame provides eight point support to the concentrator including vibration mountings. Removable cross bracing members give in-plane rigidity and they support panels for complete enclosure of the concentrator. With this concept, the basic structural frame could be designed to serve also as the fabrication and handling fixture discussed in Section 8.5.1.

Since the estimated weight of such a container is 3000 lb to 4000 lb it could be transported for short distances by helicopter or lighter-than-air craft. Shipment to launch or test areas in Florida or the West Coast, however, can be made by barge or ship.

Depending upon finalized logistics, other methods can be implemented. For example, shipment of the concentrator segments individually and establishment of the final assembly and inspection facilities at the site of launch and test could be used.

Another practical possibility is shipment of the concentrator in two halves. This would allow the major portion of the assembly to be fabricated on the master tooling. The final assembly of the two halves at the site would require nominal fixturing and alignment. With this approach, the halves could be shipped by conventional means - such as, "low boy" trailers. Thus several method of shipment are feasible. The selection of a specific method can be made at a time when system logistics are defined.

FIGURE 8.5-1
TYPICAL CRATING CONCEPT



9.0 DISCUSSION AND CONCLUSIONS

The solar concentrator shown in drawing 818180 is the conceptual design resulting from this study program.

The optical geometry is a direct result of the parametric performance analysis which utilizes a normal or Gaussian distribution as an analytical model of surface errors. Possible surface errors and combinations of errors which were estimated from existing state-of-art information for stretch-formed concentrators resulted in a prediction of 18' maximum combined slope error over 95% of the surface area. With anticipated advances in tooling and fabrication techniques this can be reduced to 12' or less. A concentrator rim angle between 53° and 55° was shown to maximize geometric efficiency for this type error model.

To establish overall performance capabilities an analysis was made of the several cavity geometries under consideration in the Brayton receiver study contract (NAS 3-2779). For the hemispherical cavity shape, an optimum aperture of 7.0 inches was established and the performance of this solar energy collection system was computed. The average concentrator-receiver efficiency in the sun is 78% (including misorientation effects) which results in the collection of 71.7 KW for one hour of sun. It should be noted that the major losses in this collection system are the mirror absorption loss and the structure shadowing loss. The concentrator geometric efficiency is very high (97%); and therefore, only small improvements in performance can be anticipated with more accurate and expensive master tooling.

One of the major conclusions of this design study is that a lightweight reinforcement of the reflector face is required to provide structural reliability and efficient weight design such that the precise optical geometry of the mirror is preserved throughout the launch environment.

The recommended honeycomb sandwich construction provides this structural efficiency and is based on a broad background in fabrication technology. The load support ring at the external diameter of the mirror has been designed for eight point load transfer to the adjoining structure. This ring is the structural interface of the concentrator to other components and its design and weight is

largely affected by the design of these other system components. The ring construction and attachment to the mirror is such that the cross section can be easily modified for other support conditions.

The effects of the orbital environment were investigated analytically and experimentally. For the cases investigated, thermal distortions were shown to be small and controllable. A detailed thermal control design analysis will be required when space station heat loads are known and specific orbital inclination angles are determined from mission objectives. The life of the optical surface in the orbital environment cannot be accurately predicted at the present time and continued experimental effort is required in the laboratory and space.

The overall design study has resulted in a structurally reliable component with an optimized geometry, and the design represents a large stretch-formed aluminum concentrator concept which is suitable for use with a Brayton cycle power system.

REFERENCES

1. "Sunflower Solar Collector" Topical Report, TRW ER-5555, September 1963.
2. Silvern, D. H., "An Analysis of Mirror Accuracy Requirements for Solar Power Plants," ARS Paper 1179-60.
3. Schrenk, G. L. "Theoretical Analysis of Solar Reflectors," GMC EDR 3193, 1 July 1963.
4. Schrenk, G. L., Gritton, D. G., "Analysis of Solar Reflectors - Mathematical Theory and Methodology for Simulation of Real Reflectors", Final Report Contract AF 04(695)-335, GMC EDR 3693, 16 December 1963.
5. "Sunflower Boiler/Heat Storage", Topical Report, TRW ER-4869, April 1963.
6. Eckert, E. R. G., Introduction to the Transfer of Heat and Mass, McGraw-Hill, New York.
7. "High Temperature, High Emittance Intermetallic Coatings", ASD TDR 63-657, Part I, August 1963.
8. Butler, C. P., Jenkins R. J., Parker W. J., "Absorptance, Emittance, and Thermal Efficiencies of Surfaces for Solar Spacecraft Power", Solar Energy Vol. 8, No. 1, 1964.
9. "60 Inch Stretch Formed Aluminum Solar Concentrator" Final Report, Contract NAS 1-3216, TRW ER-5638, 11 November 1963.
10. Mark, H., Mirtich, M. J., "Alternation of Surface Optical Properties by High-Speed Micron Size Particles", NASA Lewis TP-63.
11. Summers, J. L., "Investigation of High-Speed Impact: Regions of Impact and Impact at Oblique Angles", NASA TN D-94, October 1959.
12. Mark, H., Goldberg, G., Mirtich, M. J., "Determination of Cratering Energy Densities for Metal Targets by Means of Reflectivity Measurements", Prepared for American Institute of Aeronautics and Astronautics Journal, December 5, 1963.

13. Roark, R. J., Formulas for Stress and Strain, McGraw Hill Book Company, Inc., 1954.
14. Reiss, E. L., "Axially Symmetric Buckling of Shallow Spherical Shells Under External Pressure", Transactions, Am. Soc. Mechanical Engrs., Vol. 80, December 1958, pp. 556-560.
15. Turner, D. A., NASA-Lewis, in "Preliminary Review of Analytic Methods for Solar Collector Design".
16. Abraham, L. H. and Lowy, M. J., "Shell Instability Problems as Related to Design", Collected Papers on Instability of Shell Structures, NASA TN D-1510, p. 3.
17. Donnell, L. H. "Shell Theory", Proceedings of the Fourth Midwestern Conference on Solid Mechanics, 1959, p. 11.
18. Cunningham, J. H. and Jacobson, J. J., "Design and Testing of Honeycomb Sandwich Cylinders Under Axial Compression", Douglas Aircraft Company, Inc., 1962, p. 7.
19. Harris, C. M., Crede, C. E., Shock and Vibration Handbook, Vol 3, McGraw-Hill, 1961, p. 48-3.
20. Wiener, F. M., "Rocket Noise of Large Space Vehicles", STAR Document N63-18244.
21. McGregor, H. N., "Acoustic Problems Associated with Underground Launching of a Large Missile", Office of the Secretary of Defense Research and Engineering, Bulletin No. 29, Shock, Vibration and Associated Environment, Part IV, June 1961.
22. Reissner, E. "On Vibration of Shallow Spherical Shells", Journal of Applied Physics, December 1946, p. 1042.
23. Hoppmann, and Baronet, "A Study of the Vibrations of Shallow Spherical Shells", Journal of Applied Mechanics, Vol. 30, September 1963, p. 329.

24. Ballinger, J. C., Elizalde, J. C., Christensen, E. H., "Thermal Environment of Interplanetary Space", SAE Report 344B, 1961.
25. NRC-2 Insulation, Technical Brochure, National Research Corporation, Cambridge, Massachusetts, 1962.
26. "A Report on Structural Adhesive Bonding in the Boeing 707", Boeing Transport Division, February 1959.
27. Foral, R. F., "Sandwich Construction for Primary Structure of Ballistic Missiles and Space Vehicles, Aerospace Engineer, Vol. 20, July 1961.
28. Sharpe, L. H. Schonhorn, H., Lynch, C. J., "Adhesives," International Science and Technology, April 1964.
29. "Micrometeoroid Considerations in Solar Collector Design", TRW TM-3841-68, December 5, 1963.
30. Timoshenko, S., Woinowsky-Krieger, S., Theory of Plates and Shells, McGraw-Hill Book Company, Inc., 1959, pg. 538.
31. Archer, R. R., "Some Nonlinear Elastic Stability Problems", Lectures in the Theory of Structural Stability, Case Institute of Technology, Spring 1964.
32. Archer, R. R., "On the Numerical Solution of the Nonlinear Equations for Shells of Revolution", Journal of Mathematics & Physics, Vol. XLI No. 3, September 1962.
33. Huang, N. C., Technical Report 15, Div. Eng. Appl. Physics, Harvard University, March 1963.
34. Stern, G. S., "Thermoelastic Analysis of a Parabolic Shell", Technical Report No. 32-479, Jet Propulsion Laboratory, August 1, 1963.
35. Novozhilov, V. V., "The Theory of Thin Shells," Translated by P. G. Lowe, The Netherlands, 1959, pp. 292-295.
36. Dunsby, J. A., "Cyclic Temperature Effects on Materials and Structures", AGARD Report 410, July 1962.

NOMENCLATURE

| | |
|------------------|-------------------------------------------------------------------------------------------------|
| A | $\frac{\pi D^2}{4}$ = nominal area of the reflector |
| A _c | A - A _r - A _s = net concentrator area |
| A _r | projected area of receiver plus insulation which shades the concentrator |
| A _R | internal surface area of receiver cavity |
| A _s | projected area of structure or components other than the receiver which shades the concentrator |
| A _x | external surface area of receiver |
| c | specific heat |
| d | aperture diameter |
| d | distance between centroids of honeycomb flanges |
| D | outer diameter of the reflector |
| E | modulus of elasticity |
| f | focal length |
| F _R | receiver radiation loss factor |
| F _{R-A} | average view factor from cavity interior to aperture opening |
| F _{Z-A} | increment view factor of a zonal area to the aperture opening |
| G | acceleration due to gravity |
| h | thickness of circular support ring |
| H | redundant force |
| H | spherical shell depth |

NOMENCLATURE (CONTINUED)

| | |
|------------|----------------------------------------------------------------|
| I | moment of inertia |
| I | energy per unit area on a focal surface |
| I_A | absorbed energy per unit area |
| I_O | incident solar energy per unit area 442 BTU/Hr Ft ² |
| I_R | radiated energy per unit area |
| L | concentrator-receiver losses |
| m | mass per unit area |
| M | redundant moment |
| N_ϕ | Meridional membrane force |
| N_θ | circumferential membrane force |
| p | weight or force per unit area |
| q_A | total solar flux absorbed by receiver walls |
| q_i | input heat rate from collector thru aperture |
| q_r | net heat rate into the receiver and heat storage material |
| q_s | heat rate required by the power system |
| q_x | heat loss rate from receiver external surface |
| q_z | solar flux incident on a receiver zone |
| Q_s | total useful heat to the power system during a complete orbit |
| r | radius of circular support ring |
| r | radial location in the focal plane |
| R | radius of approximate spherical shell |
| R | radial location on the paraboloid |
| R_O | radius of parallel circle |
| R_1 | radius of curvature of paraboloid along meridian |

NOMENCLATURE (CONTINUED)

| | |
|-------------------------------|-----------------------------------------------------------------------------------------------------|
| R_2 | radius of curvature of paraboloid normal to meridian |
| t | shell thickness (for honeycomb sandwich construction, constitutes total thickness of flanges, only) |
| t_1 | thickness of one honeycomb flange or facing |
| t_2 | thickness of other honeycomb flange or facing |
| t_N | night (shade) portion of orbit time |
| t_O | total orbital period time |
| t_S | sun portion of orbit time |
| T | temperature |
| T_R | internal surface temperature of receiver |
| ΔT | temperature difference between support ring and shell or across shell thickness |
| X_z | $(1 - \alpha_s) (1 - F_{Z-A})$ |
| Y | ratio of combined receiver loss to black aperture loss |
| α' | coefficient of thermal expansion |
| α | solar disc angle, $32'$ |
| α_c | mirror absorptivity to solar radiation |
| α_s | absorptivity to solar radiation |
| β | misorientation angle of concentrator optic axis from the center of the solar disc |
| δ | relative translation between collector and focal plane |
| δ_R | radial displacement of parallel circle |
| δ_H^R and θ_H^R | displacement and rotation of ring due to a unit force acting in the direction of unknown force H |

NOMENCLATURE (CONTINUED)

| | |
|-------------------------------|-----------------------------------------------------------------------------------------------------|
| δ_M^R and θ_M^R | displacement and rotation of ring due to a unit moment acting in the direction of unknown moment M |
| δ_P^R and θ_P^R | displacement and rotation of ring when loaded by the membrane force reaction |
| δ_T^R and θ_T^R | total displacement and rotation of ring |
| $\delta_{\Delta T}^S$ | displacement of shell due to a unit change in temperature |
| δ_H^S and θ_H^S | displacement and rotation of shell due to a unit force acting in the direction of unknown force H |
| δ_M^S and θ_M^S | displacement and rotation of shell due to a unit moment acting in the direction of unknown moment M |
| δ_P^S and θ_P^S | displacement and rotation of shell in accordance with membrane theory |
| δ_T^S and θ_T^S | total displacement and rotation of shell |
| ϵ_t | thermal emissivity of receiver surface at temperature T_R |
| η | concentrator-receiver efficiency (Brayton system) |
| η_B | total blockage efficiency |
| $\eta_c = \rho \eta_G$ | nominal concentrator efficiency |
| η_{CR} | concentrator-receiver efficiency (Idealized collector) |
| η_G | concentrator geometric efficiency as computed from IBM 7094 |
| η_r | receiver blockage efficient |

NOMENCLATURE (CONTINUED)

| | |
|-----------------|--------------------------------------------------------------------|
| η_R | receiver retention efficiency |
| η_s | structure blockage efficiency |
| η_x | receiver external surface loss efficiency |
| η_ρ | receiver reflection efficiency factor |
| θ | concentrator rim angle |
| ρ | mirror reflectivity to solar radiation |
| σ | Stefan-Boltzmann constant |
| σ_c | circumferential direction standard deviation of surface errors |
| σ_r | radial direction standard deviation of surface errors |
| σ_θ | circumferential membrane stress |
| μ | Poisson's ratio |
| σ_ϕ | meridional membrane stress |
| ϕ | concentrator surface rotation from true paraboloid |
| ϕ | angle between axis of symmetry and normal to surface |
| ϕ_f | angle between axis of symmetry and normal to surface at shell edge |
| ψ | rotation of meridian |

APPENDIX A
EFFICIENCY DERIVATION BY LOSS ANALYSIS

The derivation is started by defining the overall efficiency of the concentrator receiver as

$$\eta = \frac{\text{Net power (in sun) to the system and heat storage material}}{\text{Maximum power available}}$$

$$\eta = \frac{P}{P_{\max}} = \frac{AI_o - L}{AI_o} \quad (1)$$

where,

P = Net power in the sun

$$P_{\max} = AI_o = \frac{\pi D^2}{4} I_o$$

I_o = solar constant

L = total losses in the sun

The losses are defined as:

$L_s = A_s I_o$ = power lost due to structure blockage

$L_r = A_r I_o$ = power lost due to receiver blockage

L_x = rec. external surface loss = surface area x loss rate

$L_c = A_c \alpha_c I_o$ = power lost due to absorptivity of concentrator

L = power lost due to geo. inaccuracy scattering outside aperture

$L_R = L_E + L_\rho$ = power lost due to reradiation and refl. from cavity

where

$A = \frac{\pi D^2}{4}$ = max. projected area available to Brayton cycle

A_s = projected area of structure or components other than receiver which shade the concentrator

A_r = projected area of receiver and insulation which shades the concentrator

$A_c = A - A_s - A_r$ = actual concentrator area which intercepts solar energy

Two other stipulations will be made in developing the efficiency equations, and they are the following definitions:

$$\eta_G = \frac{\text{Power thru the aperture}}{\text{Power at the focal plane}} \quad (2)$$

η_G = concentrator geometric eff. computed from IBM 7094

and

$$\eta_R = \frac{\text{net power into cavity walls incl. ext. losses}}{\text{input power from concentrators}} \quad (3)$$

η_R = receiver reradiation and reflection eff.

These definitions are inherently based upon the existing methods of calculating them.

Consider equation (2).

Power at the focal plane is

$$\begin{aligned} I_O & \left[A - A_s - A_r - \alpha (A - A_s - A_r) \right] \\ &= I_O (A - A_s - A_r) (1 - \alpha) \\ &= I_O (A - A_r - A_s) \end{aligned}$$

Thus,

$$\eta_G = \frac{\text{Power thru aperture}}{I_O \rho (A - A_r - A_s)} = \frac{I_O \rho (A - A_r - A_s) - L_G}{I_O \rho (A - A_r - A_s)}$$

From which,

$$L_G = (1 - \eta_G) I_O \rho (A - A_r - A_s) \quad (4)$$

Similarly L_R is obtained from equation (3).

input power from concentrator $\times \eta_R$ = power absorbed

input $\times \eta_R$ = input - L_R

$$L_R = \text{input} (1 - \eta_R)$$

but the input to the cavity is the maximum available, less the losses to that point

$$\text{input} = A I_O - L_s - L_r - L_c - L_G$$

thus,

$$L_R = (A I_O - L_s - L_r - L_c - L_G) (1 - \eta_R) \quad (5)$$

From eq. (5)

$$L_R = (A I_O - L_s - L_r - L_c - L_G) - (A I_O - L_s - L_r - L_c - L_G) \eta_R$$

The total losses therefore are

$$L = L_s + L_r + L_x + L_c + L_G + L_R$$

Substituting in eq. (1)

$$\eta = \frac{A I_O - L_s - L_r - L_c - L_G - L_R - L_x}{A I_O} \quad (6)$$

Equation (6) can be further modified by substituting the equalities for the various losses as defined for equation (1).

$$\eta = \frac{I_O \left[A - A_s - A_r - A_c \alpha_c - (1 - \eta_G) \rho (A - A_r - A_s) \right] \eta_R - \frac{L_x}{A I_O}}{A I_O}$$

using $(A - A_s - A_r) = A_c$ and, $\alpha_c = 1 - \rho$

$$\eta = \frac{[A_c \rho - (1 - \eta_G)] \eta_R - \frac{L_x}{AI_o}}{A}$$

$$\eta = \frac{\rho A_c}{A} \left[1 - (1 - \eta_G) \right] \eta_R - \frac{L_x}{AI_o}$$

$$\eta = \frac{\rho A_c}{A} \eta_G \eta_R - \frac{L_x}{AI_o} \quad (7)$$

Let $\frac{A_c}{A} = \eta_B$ = total blockage eff.

$$\frac{A_c}{A} = \frac{A - A_r - A_s}{A} = 1 - \frac{A_r}{A} - \frac{A_s}{A}$$

Thus,

$$\eta_B = 1 - (1 - \eta_r) - (1 - \eta_s)$$

where,

$$\eta_s = \frac{A - A_s}{A}, \quad \eta_r = \frac{A - A_r}{A}, \quad \eta_x = \frac{AI_o - L_x}{AI_o}$$

Thus using these in equ. (7)

$$\eta = \rho \eta_B \eta_G \eta_R - (1 - \eta_x) \text{ Brayton Collector equation}$$

or using

$$\eta_c = \rho \eta_G$$

$$\eta = \eta_B \eta_C \eta_R - (1 - \eta_x)$$

In idealized collector analysis

$$\eta_s = 1 \quad \therefore \quad \eta_B = 1 - 1 + \eta_r = \eta_r = \frac{A_c}{A}$$

$$\eta_x = 1$$

$$\eta_{cR} = \frac{P_{out}}{I_o A_c}$$

$$\eta = \frac{P_{out}}{AI_o} = \frac{I_o A_c}{I_o A} \quad \eta_c \quad \eta_R = 0$$

thus

$$\frac{P_{out}}{I_o A_c} = \eta_c \quad \eta_R = \eta_{cR} \quad \text{Idealized Collector equation}$$

APPENDIX B
EXTENSION OF SILVERN'S ANALYSIS

Reference: "An Analysis of Mirror Accuracy Requirements for Solar Power Plants" by David H. Silvern - ARS Paper 1179-60

In the reference, the following equation is developed and given at the bottom of Page 6.

$$K' (r, \alpha) = K \int_{\beta=0}^{2\pi} \int_{\gamma=0}^{\gamma_o} \int_{X=X_1}^{X_o} \int_{\theta=0}^{2\pi} \left[\frac{\gamma d\gamma d\beta}{\pi \gamma_o^2} \right] \left[\frac{X dX d\theta}{f_1 f_2 X_o^2} \right]^{P_1 P_2}$$

where*: $K' (r, \alpha)$ is the flux on the focal plane at a point whose coordinates with respect to the focal point are (r, α)

K is the solar constant

β and γ are the angular coordinates of a point on the solar disc
(γ_o is the angular radius of the solar disc)

X and θ are the coordinates of a point on the collector (X_1 and X_o are the inner and outer radii of the collector)

$$f_1 = 2 \frac{\left(\frac{X}{X_o}\right)^2 + \left[\frac{\tan \theta_o}{2} \left(1 - \frac{X^2}{X_o^2}\right) + \frac{1}{\tan 2 \theta_o} \right]^2}{\frac{\tan \theta_o}{2} \left(1 - \frac{X^2}{X_o^2}\right) + \frac{1}{\tan 2 \theta_o}}$$

$$f_2 = 2 \left\{ \left(\frac{X}{X_o}\right)^2 + \left[\frac{\tan \theta_o}{2} \left(1 - \frac{X^2}{X_o^2}\right) + \frac{1}{\tan 2 \theta_o} \right]^2 \right\}^{\frac{1}{2}}$$

*Note - nomenclature used in this appendix is that of the noted reference and applies only to this section of the report.

θ_0 is the ideal slope of the collector surface tangent at the outer rim.
 (The "rim angle" of the collector is $2 \theta_0$) Note that θ_0 is not a particular value of θ , but refers to an entirely different angle.

$$P_1 P_2 = \frac{1}{2 \pi \sigma^2} \exp \left(-\frac{1}{2} \left\{ \left[\frac{r}{\sigma f_1 X_0} \cos (\theta - \alpha) - \frac{\phi}{2 \sigma} \cos \theta - \frac{\gamma}{2 \sigma} \cos (\theta - \beta) \right]^2 + \left[\frac{r}{\sigma f_2 X_0} \sin (\theta - \alpha) - \frac{\phi}{2 \sigma} \sin \theta - \frac{\gamma}{2 \sigma} \sin (\theta - \beta) \right]^2 \right\} \right)$$

σ is the standard deviation of the collector surface slope errors.

ϕ is the angle of misorientation of the collector axis from the center of the solar disk.

The exponential in the expression for $(P_1 P_2)$ can be put in more advantageous form by expanding the squared terms and simplifying the result, as follows:

$$\exp \left(-\frac{1}{2} \left[\frac{\phi^2}{4 \sigma^2} + \frac{\gamma^2}{4 \sigma^2} + \frac{\phi \gamma}{2 \sigma^2} \cos \beta + \frac{r^2}{\sigma^2 f_1^2 X_0^2} \cos^2 (\theta - \alpha) + \frac{r^2}{\sigma^2 f_2^2 X_0^2} \sin^2 (\theta - \alpha) - \frac{r \phi}{\sigma^2 f_1 X_0} \cos (\theta - \alpha) \cos \theta - \frac{r \phi}{\sigma^2 f_2 X_0} \sin (\theta - \alpha) \sin \theta - \frac{r \gamma}{\sigma^2 f_2 X_0} \cos (\theta - \alpha) \cos (\theta - \beta) - \frac{r \gamma}{\sigma^2 f_2 X_0} \sin (\theta - \alpha) \sin (\theta - \beta) \right] \right)$$

Further simplification of the expression for $K'(r, \alpha)$ is possible if f_1 and f_2 are replaced by an average value f_m .

First, substituting f_m in the exponential, it becomes

$$\begin{aligned} & \exp \left(-\frac{1}{2} \left\{ \frac{\phi^2}{4\sigma^2} + \frac{\gamma^2}{4\sigma^2} + \frac{\phi\gamma}{2\sigma^2} \cos \beta + \frac{r^2}{\sigma^2 f_m^2 X_o^2} \left[\cos^2(\theta - \alpha) \right. \right. \right. \\ & \quad \left. \left. + \sin^2(\theta - \alpha) \right] - \frac{r\phi}{\sigma^2 f_m X_o} \left[\cos(\theta - \alpha) \cos \theta + \sin(\theta - \alpha) \sin \theta \right] \right. \\ & \quad \left. \left. - \frac{r\gamma}{\sigma^2 f_m X_o} \left[\cos(\theta - \alpha) \cos(\theta - \beta) + \sin(\theta - \alpha) \sin(\theta - \beta) \right] \right\} \right) \\ & = \exp \left(-\frac{\phi^2}{8\sigma^2} - \frac{\gamma^2}{8\sigma^2} - \frac{\phi X}{4\sigma^2} \cos \beta - \frac{r^2}{2\sigma^2 f_m^2 X_o^2} \right. \\ & \quad \left. + \frac{r\phi}{2\sigma^2 f_m X_o} \cos \alpha + \frac{r\gamma}{2\sigma^2 f_m X_o} \cos(\alpha - \beta) \right) \end{aligned}$$

and the form for $K'(r, \alpha)$ becomes

$$K'(r, \alpha) = \frac{K}{2\pi^2 \gamma_o^2 X_o^2 \sigma^2 f_m^2} \int_{\beta=0}^{2\pi} \int_{\gamma=0}^{\gamma_o} \int_{X=X_1}^{X_o} \int_{\theta=0}^{2\pi}$$

$$\gamma d\gamma d\beta x dx d\theta \exp()$$

where the terms in the exponential are those in the preceding equation.

Rearranging factors

$$K'(r, \alpha) = \frac{K}{2\pi^2 \gamma_o^2 X_o^2 \sigma^2 f_m^2} \exp \left(-\frac{\phi^2}{8\sigma^2} - \frac{r^2}{2\sigma^2 f_m^2 X_o^2} + \frac{r\phi \cos \alpha}{2\sigma^2 f_m X_o} \right) \int_{X=X_1}^{X_o} X dX \int_{\theta=0}^{2\pi} d\theta \int_{\beta=0}^{2\pi} \int_{\gamma=0}^{\gamma_o} \gamma d\gamma d\beta \exp \left(-\frac{\gamma^2}{8\sigma^2} - \frac{\phi\gamma}{4\sigma^2} \cos \beta + \frac{r\gamma \cos(\alpha-\beta)}{2\sigma^2 f_m X_o} \right)$$

Evaluating the first two integrals

$$K'(r, \alpha) = \frac{K(X_o^2 - X_1^2)}{2\pi \gamma_o^2 X_o^2 \sigma^2 f_m^2} \exp \left(-\frac{\phi^2}{8\sigma^2} - \frac{r^2}{2\sigma^2 f_m^2 X_o^2} + \frac{r\phi \cos \alpha}{2\sigma^2 f_m X_o} \right) \int_{\beta=0}^{2\pi} \int_{\gamma=0}^{\gamma_o} \exp \left(-\frac{\gamma^2}{8\sigma^2} - \frac{\phi\gamma}{4\sigma^2} \cos \beta + \frac{r\gamma \cos(\alpha-\beta)}{2\sigma^2 f_m X_o} \right) \gamma d\gamma d\beta$$

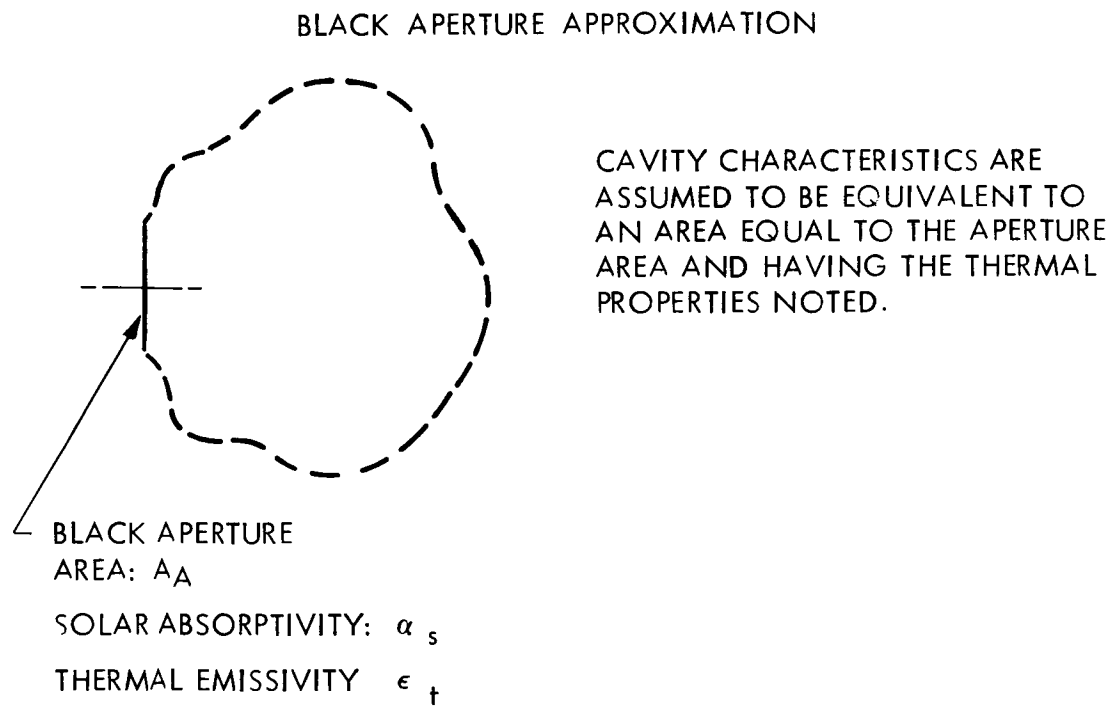
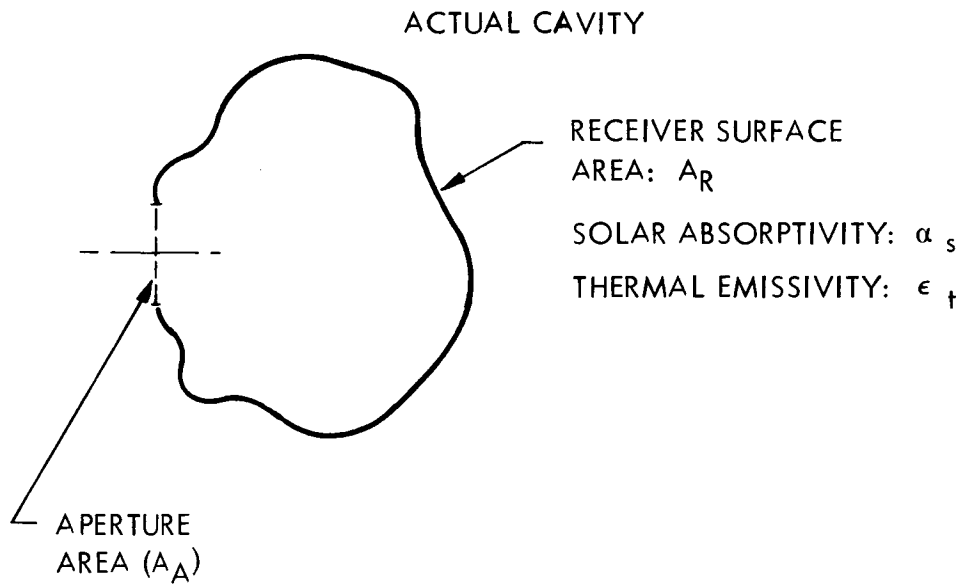
The remaining double integral is an integration over the solar disk, and its approximate value for any set of values of $r, \alpha, \phi, \sigma, f_m$, and X_o was found by dividing the solar disk into sixty-four equal areas, evaluating the integrand at the center of each area, averaging the integrand values, and substituting this value in the integral.

A program for an LGP-30 computer was written to calculate the approximate value of the integral, and to multiply this value by the other factors in the equation to give a factor $C(r, \alpha, \sigma, \phi, X_o, X_1, f_m, \gamma_o)$ such that

$$K' (r, \alpha) = C (r, \sigma, \alpha, \phi, X_0, X_1, f_m, \gamma_0) K$$

Parametric computations were successfully carried out varying σ , ϕ , and f_m , using fixed values for X_0 , X_1 , and γ_0 .

FIGURE C-1



APPENDIX C
AN EXAMPLE OF ACTUAL VERSUS BLACK
APERTURE RECEIVER LOSSES

Assume the two receiver configurations shown in Figure C-1. A comparison between black aperture loss and actual cavity loss is made on Table C-1. Six different cases of cavity parameters are chosen. Note that in all cases the ratio of cavity loss to black aperture loss is greater than one; and for the two cases where the cavity surface is the aperture area, the ratio is large.

The reason for the large ratio is that the incident concentrated solar flux is 250,000 BTU/hr divided by 0.35 ft² or 715,000 BTU/hr-ft²; whereas the thermal radiation at an emissivity of 1.0 is 37,300 BTU/hr-ft². There is a potentially greater energy flux to be reflected than is emitted by black body radiation.

The integrated view factor from the cavity surface to the aperture (F_{R-A}) is obtained as follows. Assume that the aperture is a plane surface which emits inward to the cavity surface. The law of reciprocity therefore establishes that,

$$(1) \quad A_A F_{A-R} = A_R F_{R-A}$$

Since the cavity surface intercepts all radiation emitted by the aperture, then the view factor of the aperture to the cavity interior is,

$$(2) \quad F_{A-R} = 1$$

Then the average view factor of cavity surface to the aperture is,

$$(3) \quad F_{R-A} = \frac{A_A}{A_R}$$

Thus the view factor (F_{R-A}) is independent of cavity geometry and equal to the ratio of aperture area to cavity surface area. As the interior surface area increases, with the aperture remaining constant, the receiver loss becomes smaller; and in fact, approaches the black aperture loss as a limit.

TABLE C-1 (APPENDIX C)

| CASE | A_R RECEIVER SURFACE AREA SQ. FT. | A_A/A_R AREA RATIO | α_s SOLAR ABSORPTIVITY OF RECEIVER SURFACE | ϵ_t THERMAL EMISSIVITY OF RECEIVER SURFACE (AT 1700° F) | L_p SOLAR FLUX REFLECTED BACK OUT OF APERTURE BTU/HR. | L_E THERMAL RADIATION PASSING OUT OF APERTURE BTU/HR. | L_R TOTAL LOSS PASSING THRU APERTURE BTU/HR. | $\frac{L_R}{A_A \sigma T_R^4}$ ACTUAL LOSS LR TO BLACK APERTURE LOSS RATIO BTU/HR. |
|------|-------------------------------------------------|-------------------------|------------------------------------------------------------|------------------------------------------------------------------------------|------------------------------------------------------------------------|------------------------------------------------------------------------|------------------------------------------------------------|---------------------------------------------------------------------------------------------------|
| 1 | 0.35 | 1.0000 | 0.5 | 0.5 | 125,000 | 6,530 | 131,530 | 10.07 |
| 2 | 10 | .0350 | 0.5 | 0.5 | 8,450 | 12,610 | 21,060 | 1.613 |
| 3 | 45 | .0078 | 0.5 | 0.5 | 1,930 | 12,960 | 14,890 | 1.141 |
| 4 | 0.35 | 1.0000 | 0.5 | 1.0 | 125,000 | 13,060 | 138,060 | 10.57 |
| 5 | 10 | .0350 | 0.5 | 1.0 | 8,450 | 13,060 | 21,510 | 1.648 |
| 6 | 45 | .0078 | 0.5 | 1.0 | 1,930 | 13,060 | 14,990 | 1.149 |
| 7 | 0.35 | 1.0000 | 1.0 | 1.0 | 0 | 13,060 | 13,060 | 1.000 |

EQUATIONS: A. $\eta_R = \eta_p = \frac{A_R F_R \sigma T_R^4}{I_o A_C \eta_C}$

B. $L_R = L_p + L_E = q_i (1 - \eta_p) + A_R F_R \sigma T_R^4$

C. $F_R = \frac{\epsilon_t (F_R - A)}{1 - (1 - \epsilon_t) (1 - F_R - A)}$

D. $\eta_p = \frac{\alpha_s}{1 - (1 - \alpha_s) (1 - F_R - A)}$

CONDITIONS: $T_R = 1700^\circ \text{F}$; $q_i = 250,000 \text{ BTU/HR}$; $A_A = 0.35 \text{ SQ. FT.}$ ($d_A = 8 \text{ IN.}$)

APPENDIX D
COMPUTATION OF CONCENTRATED SOLAR FLUX
INCIDENT ON A RECEIVER SURFACE

The following procedure for computing the incident solar flux profile is accurate for large ratios of receiver dimensions to cavity aperture diameter.

For the Brayton receiver and aperture dimensions it is quite adequate.

Procedure

Assume point source and incident energy is perfectly collimated.

Divide the concentrator into area formed by equal increments of angle $\Delta\theta$, Figure D-1, and determine the per cent of total intercepted energy in each of the zones formed.

Project the same incremental angles ($\Delta\theta$) into the receiver, Figure D-2, and compute the intercepted area of the same zones on the receiver surface. Divide the per cent of intercepted solar flux in each zone by the area of each zone, Figure D-2. This provides the incident flux intensity for a point source. For the example (25.5" sphere; off-focal point 11.5") the profile is as in Figure D-3.

The effect of concentrator surface imperfections and aperture vignetting is to modify the profile in the end zones, usually only one on either end.

The effect can be approximated by projected lines of maximum ray deviation from the concentrator OD and ID into the receiver and intersect the surface, Figure D-4. The zones X and Q are formed by the maximum deviated rays and provide the new boundaries for the imperfect concentrator surface. This results in the modified receiver flux profile curve in Figure D-4.

The profile in Figure D-4 was compared with a profile calculated by the generalized theoretical analysis of solar reflectors developed by Dr. G. L. Schrenk wherein a computer program is available to compute profiles on an arbitrary surface in the focal area. The two curves were coincident indicating good accuracy from this graphical method for the high degree of optical accuracy and small vignetting of the Brayton collector system.

FIGURE D-1

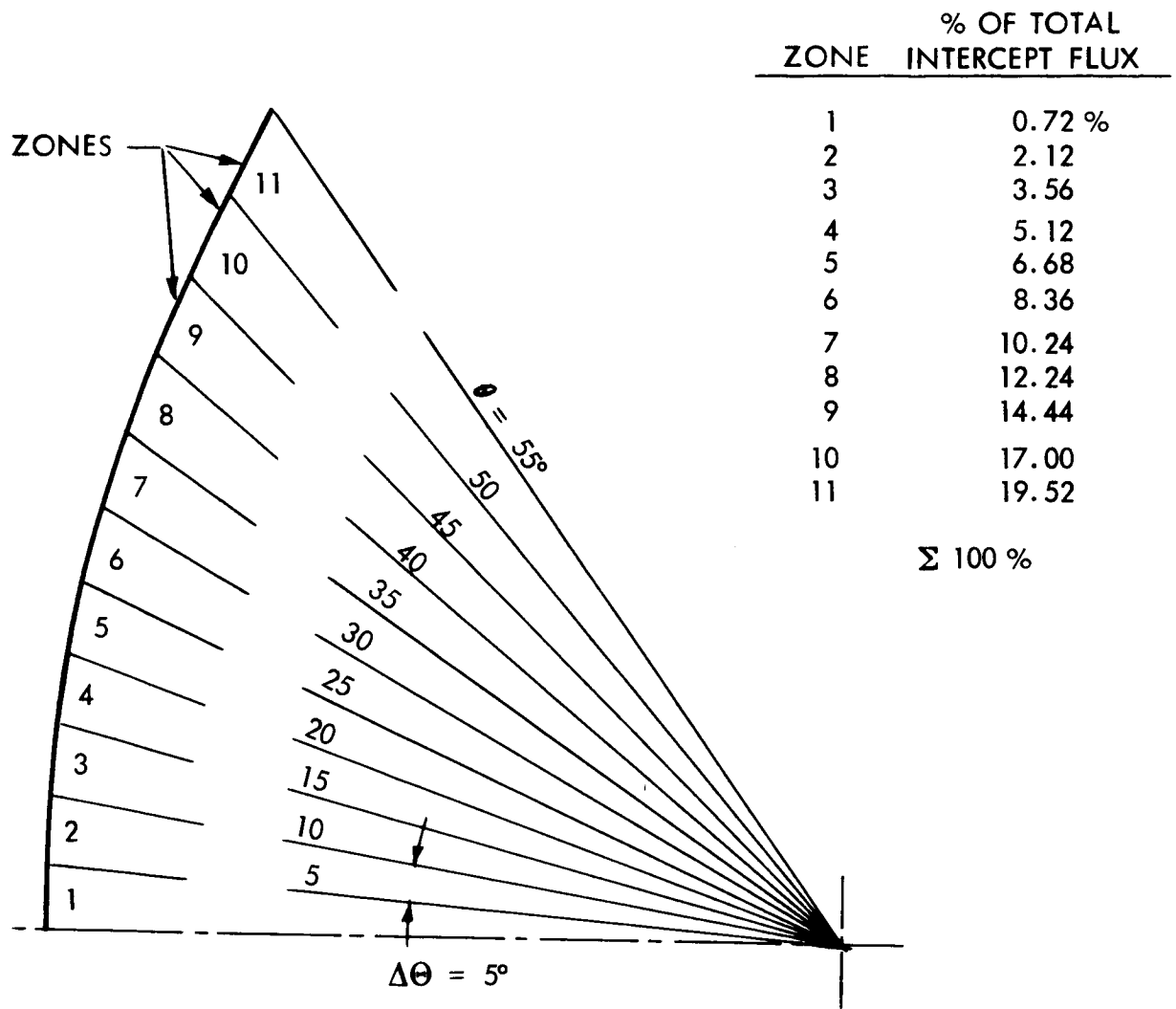


FIGURE D-2

| ZONES | %/FT ² |
|-------|-------------------|
| 1 | .0310 |
| 2 | .0321 |
| 3 | .0324 |
| 4 | .0346 |
| 5 | .0359 |
| 6 | .0375 |
| 7 | .0410 |
| 8 | .0448 |
| 9 | .0500 |
| 10 | .0578 |
| 11 | .0632 |

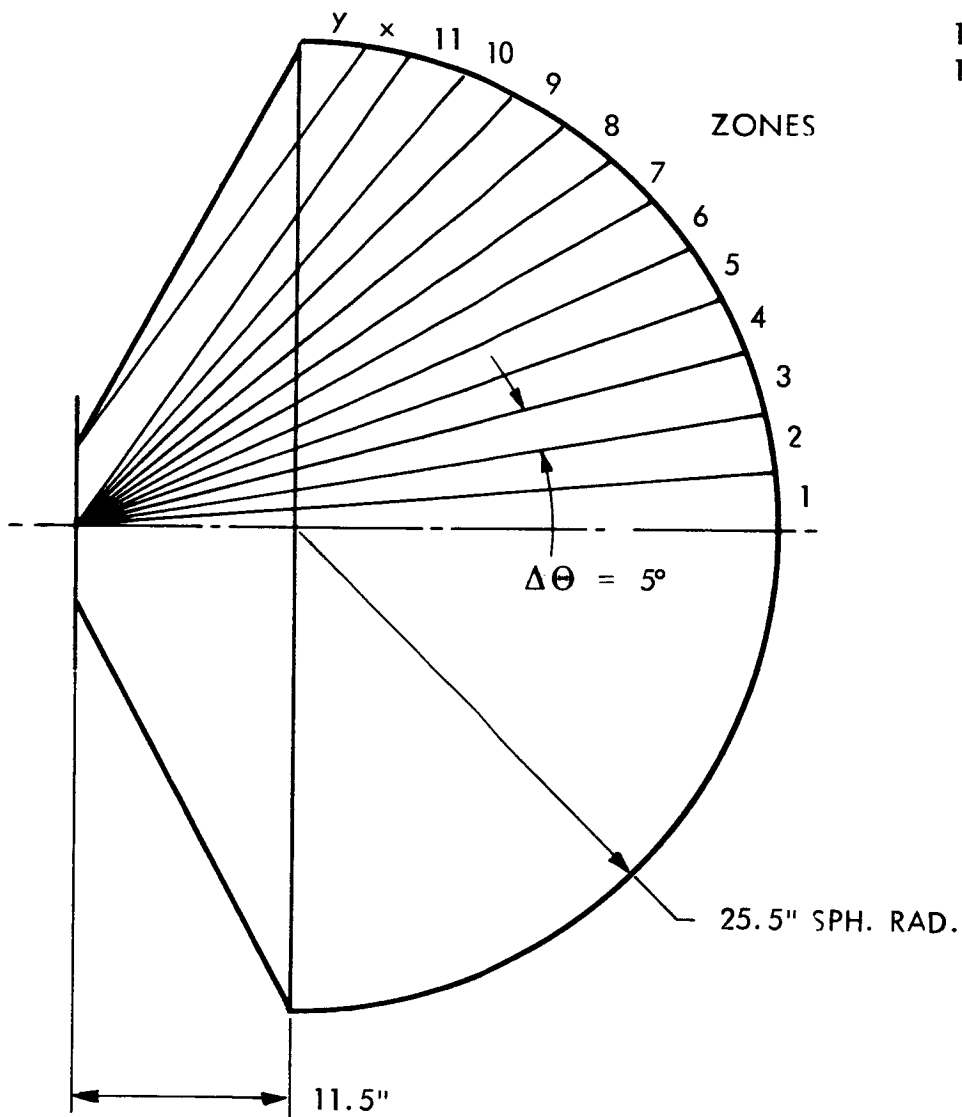


FIGURE D-3

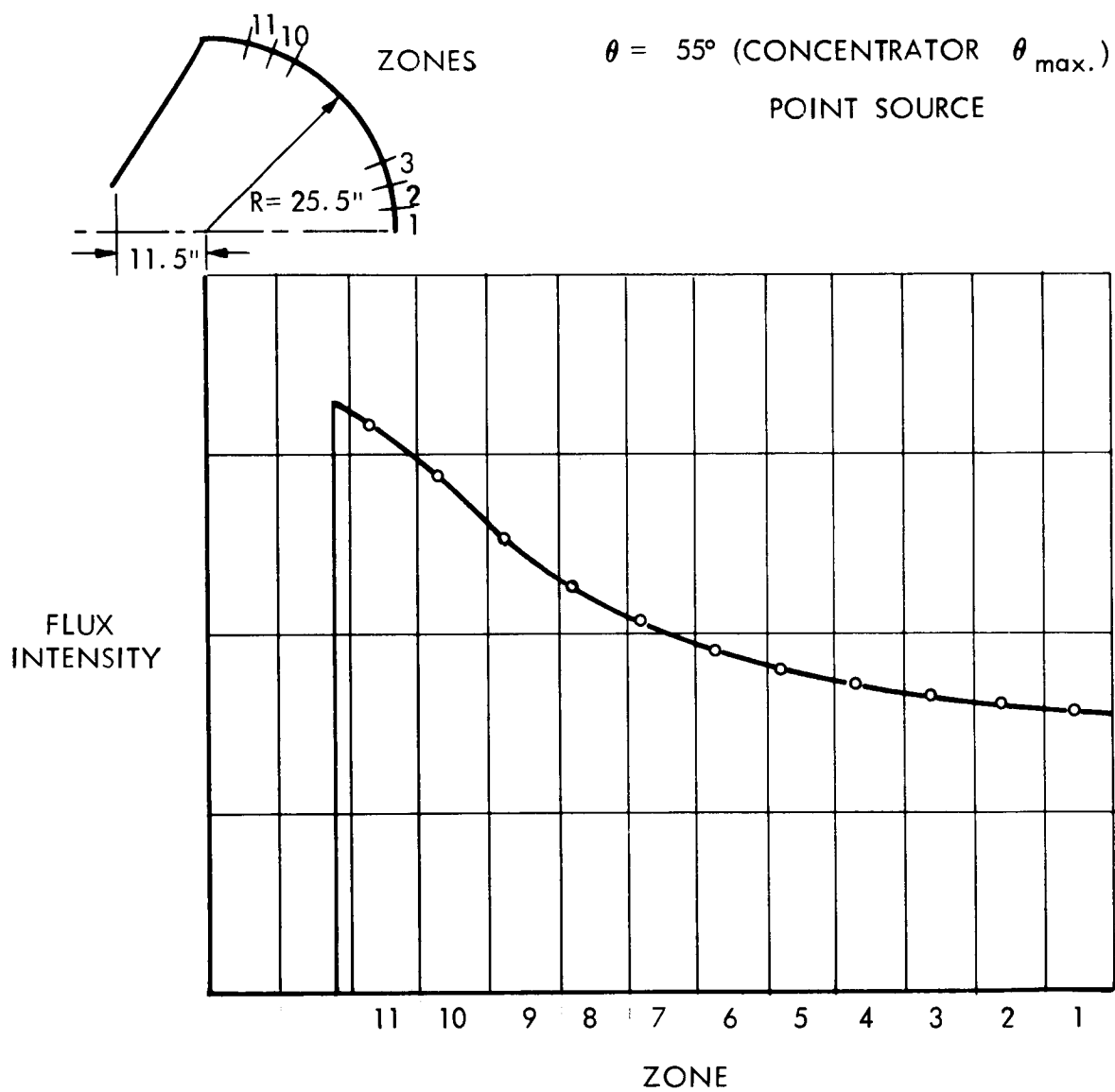
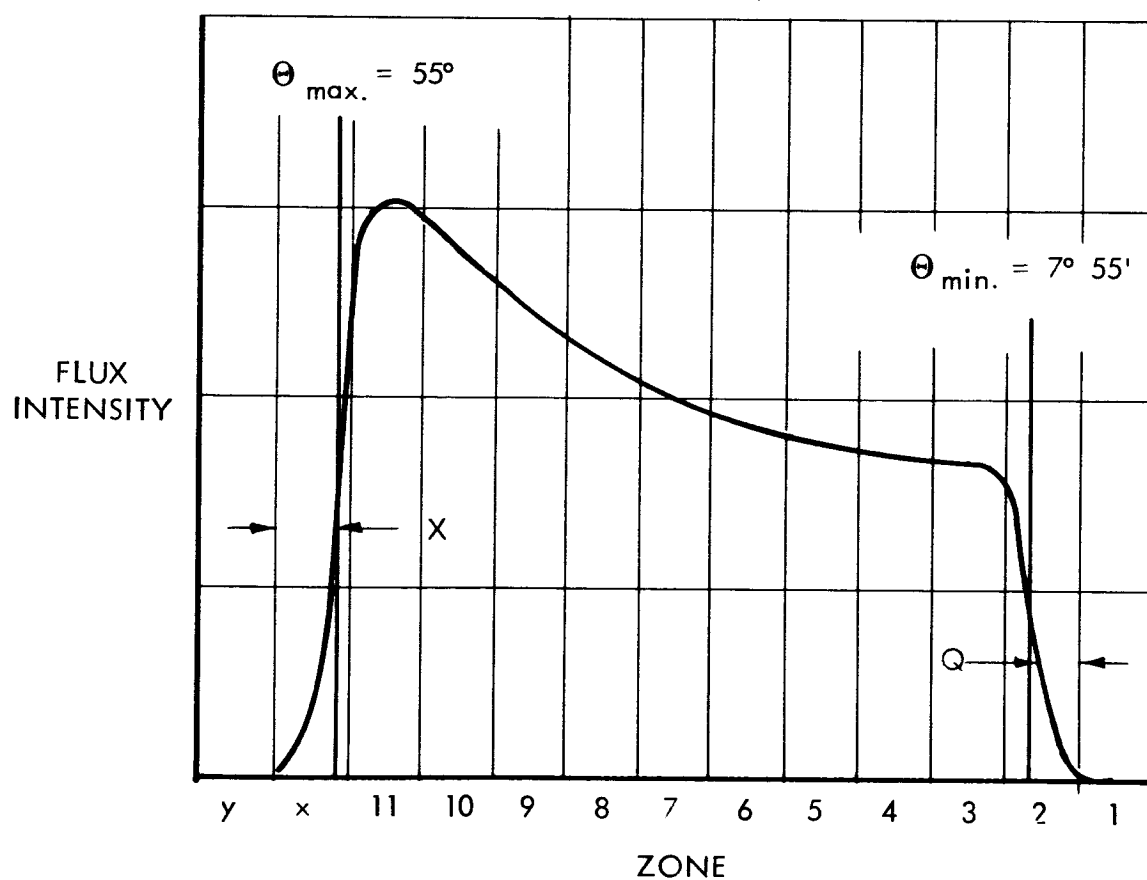
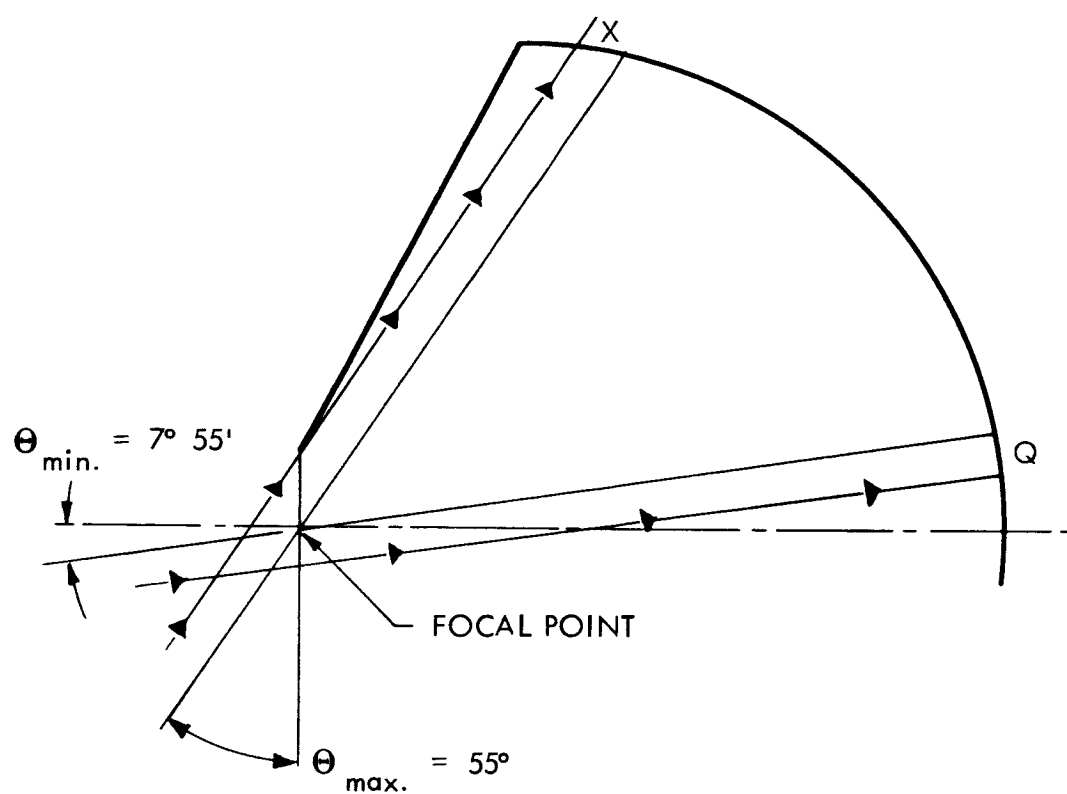


FIGURE D-4



APPENDIX E
REFLECTION EFFICIENCY FACTOR DERIVATION

For a given zone on the receiver surface

at first incidence of solar flux:

| | |
|-----------------------------------|-------------------------------------|
| $q_Z \alpha_s$ | is absorbed |
| $q_Z (1 - \alpha_s)$ | is reflected, of which |
| $q_Z (1 - \alpha_s) F_{Z-A}$ | passes directly out aperture |
| $q_Z (1 - \alpha_s)(1 - F_{Z-A})$ | is reflected to remainder of cavity |

at second incidence:

| | |
|--------------------------------------------------------------|--------------------------------------|
| $q_Z (1 - \alpha_s)(1 - F_{Z-A}) \alpha_s$ | is absorbed |
| $q_Z (1 - \alpha_s)(1 - F_{Z-A})(1 - \alpha_s)$ | is reflected, of which |
| $q_Z (1 - \alpha_s)(1 - F_{Z-A})(1 - \alpha_s) F_{R-A}$ | passes directly out of aperture, and |
| $q_Z (1 - \alpha_s)(1 - F_{Z-A})(1 - \alpha_s)(1 - F_{R-A})$ | is reflected to remainder of cavity |

at third incidence:

| | |
|-----------------------------------------------------------------|--------------------------------------|
| $q_Z (1 - \alpha_s)^2 (1 - F_{Z-A})(1 - F_{R-A}) \alpha_s$ | is absorbed |
| $q_Z (1 - \alpha_s)^2 (1 - F_{Z-A})(1 - F_{R-A})(1 - \alpha_s)$ | is reflected, of which |
| $q_Z (1 - \alpha_s)^2 (1 - F_{Z-A})(1 - F_{R-A}) F_{R-A}$ | passes directly out of aperture, and |
| $q_Z (1 - \alpha_s)^3 (1 - F_{Z-A})(1 - F_{R-A})^2$ | is reflected to remainder of cavity |

The total absorbed solarflux is then,

$$q_A = q_Z \alpha_s + q_Z (1 - \alpha_s)(1 - F_{Z-A}) \alpha_s + q_Z (1 - \alpha_s)^2 (1 - F_{Z-A}) \alpha_s (1 - F_{R-A}) + q_Z (1 - \alpha_s)^3 (1 - F_{Z-A})(1 - F_{R-A})^2 \alpha_s + \dots$$

or

$$q_A = q_Z \alpha_s \left[1 + (1 - \alpha_s) (1 - F_{Z-A}) + \sum_{n=1}^{\infty} (1 - \alpha_s)^n (1 - F_{R-A})^n \right]$$

if,

$$X_Z = (1 - \alpha_s) (1 - F_{Z-A})$$

then,

$$q_A = q_Z \alpha_s + q_Z \alpha_s X_Z \left[1 + \sum_{n=1}^{\infty} (1 - \alpha_s)^n (1 - F_{R-A})^n \right]$$

$$= q_Z \alpha_s + q_Z \alpha_s X_Z \left[\frac{1}{1 - (1 - \alpha_s) (1 - F_{R-A})} \right]$$

$$q_A = q_Z \alpha_s + q_Z X_Z \left[\frac{\alpha_s}{1 - (1 - \alpha_s) (1 - F_{R-A})} \right]$$

if,

$$F_R = \frac{\alpha_s}{1 - (1 - \alpha_s) (1 - F_{R-A})}$$

then, for a given zone on the receiver surface

$$q_{A-Z} = q_Z \alpha_s + q_Z X_Z F_R = q_Z (\alpha_s + X_Z F_R)$$

For a ten zone surface the total absorbed solar flux is,

$$q_A = \sum_{Z=1}^{Z=10} q_Z (\alpha_s + X_Z F_R)$$

APPENDIX F
BRAYTON CYCLE COLLECTOR WEIGHT ESTIMATE

| <u>Item</u> | <u>Description</u> | <u>Unit Weight</u> | <u>No. Required</u> | <u>Total Weight</u> |
|-------------|-----------------------------------------------------|-------------------------|------------------------|---------------------|
| 1. | Shell Face Material .008 AL | .113 lb/ft ² | 748.76 ft ² | 84.61 lb. |
| 1(a) | Shell Face Adhesive | 72 lb/ft ³ | .312 ft ³ | 22.5 lb. |
| 2. | Shell Core 1/4 Hex 1/4 Thk. .0015 Foil | .07 lb/ft ² | 748.76 ft ² | 52.5 lb. |
| 3. | Shell Back Face Material .004 AL | .056 lb/ft ² | 748.76 ft ² | 41.93 lb. |
| 3(a) | Shell Back Face Adhesive | 72 lb/ft ³ | .312 ft ³ | 22.5 lb. |
| 4. | Shell Front Face Doubler .004 AL x 1.5" | .056 lb/ft ² | 36.2 ft ² | 2.03 lb. |
| 4(a) | Shell Front Face Doubler Glass Cloth .004 Thk. | .28 oz/ft ² | 48 ft ² | .84 lb. |
| 4(b) | Front Face Glass Cloth Doubler Adhesive | 72 lb/ft ³ | .028 ft ³ | 2.02 lb. |
| 5. | Petal Joint Core 1/4 Hex .242 Thk, .0015 Foil | .068 lb/ft ² | 36.2 ft ² | 2.44 lb. |
| 6. | Petal Joint Back Face Doubler .004 AL x 3.0 Wide | .056 lb/ft ² | 66.2 ft ² | 3.70 lb. |
| 6(a) | Petal Joint Back Face Glass Cloth .004 Thk. | .28 oz/ft ² | 66.2 ft ² | 1.16 lb. |
| 6(b) | Petal Joint Back Face Glass Cloth Adhesive | 72 lb/ft ³ | .0386 ft ³ | 2.78 lb. |
| 7. | Petal Thd'd Fasteners #10 THD. 6 per metal | | 120 | .25 lb. |
| 7(a) | Petal Thd'd Fasteners Adhesive | 72 lb/ft ³ | .006 ft ³ | .41 lb. |
| 8. | Center Ring "T" Section & "U" channel + Tie-ins | .262 lb/ft | 8.1 ft | 2.40 lb. |

| <u>Item</u> | <u>Description</u> | <u>Unit Weight</u> | | <u>No. Required</u> | | <u>Total Weight</u> | |
|-------------|--------------------------------------------------------|--------------------|--------------------|---------------------|-----------------|---------------------|-----|
| 8(a) | Tie-In Adhesive | 72 | lb/ft ³ | .0084 | ft ³ | .61 | lb. |
| 9. | Support Ring Back Face Doubler .004 AL | .056 | lb/ft ² | 128 | ft ² | 7.20 | lb. |
| 9(a) | Support Ring Back Face Doubler Glass Cloth .004 | .28 | oz/ft ² | 128 | ft ² | 2.25 | lb. |
| 9(b) | Support Ring Back Face Doubler Glass Cloth Adhesive | 72 | lb/ft ³ | .075 | ft ³ | 5.37 | lb. |
| 10. | Support Ring-Outer Ring .050 AL | .724 | lb/ft ² | 57 | ft ² | 41.3 | lb. |
| 10(a) | Support Ring - Outer Ring Glass Cloth .004 | .28 | oz/ft ² | 57 | ft ² | 1.00 | lb. |
| 10(b) | Support Ring - Outer Ring Glass Cloth | 72 | lb/ft ³ | .033 | ft ³ | 2.39 | lb. |
| 10(c) | Support Ring - Outer Ring Edge Potting Adhesive | 13 | lb/ft ² | .123 | ft ² | 1.6 | lb. |
| 10(d) | Support Ring - Outer Ring Doubler 5.5 x 2 x .050 AL | .724 | /ft ² | .38 | ft ² | .28 | lb. |
| 10(e) | Doubler Glass Cloth .010 | 1.0 | oz/ft ² | .38 | ft ² | .03 | lb. |
| 10(f) | Doubler Glass Cloth Adhesive | 72 | lb/ft ³ | .00038 | ft ³ | .03 | lb. |
| 10(g) | Doubler Rivets .190 Dia. 4 per Doubler | | | 20 | | .04 | lb. |
| 11. | Extruded Close Out Section | 160 | lb/ft ³ | .095 | ft ³ | 15.1 | lb. |
| 11(a) | Close Out Glass Cloth .004 | 28 | oz/ft ² | 7.8 | ft ² | .14 | lb. |
| 11(b) | Close Out Adhesive | 13 | lb/ft ³ | .1435 | ft ³ | 1.86 | lb. |
| 11(c) | Close Out Doubler .050 AL | .7241 | lb/ft ² | .235 | ft ² | .17 | lb. |
| 11(d) | Close Out Doubler | 1.0 | oz/ft ² | .235 | ft ² | .02 | lb. |
| 11(e) | Glass Cloth Adhesive | 72 | lb/ft ³ | .00024 | ft ³ | .02 | lb. |

| <u>Item</u> | <u>Description</u> | <u>Unit Weight</u> | <u>No. Required</u> | <u>Total Weight</u> |
|--------------|----------------------------------------------------|-------------------------|----------------------|---------------------|
| 11(f) | Doubler Rivets .190 Dia. 4 Required Per Doubler | | 20 | .03 lb. |
| 12. | Support Ring - Flange .025 Thk AL | .361 lb/ft ² | 83 ft ² | 30.0 lb. |
| 12(a) | Flange Glass Cloth .004 | .28 oz/ft ² | 83 ft ² | 1.5 lb. |
| 12(b) | Flange Glass Cloth Adh. | 72 lb/ft ³ | .051 ft ³ | 3.65 lb. |
| 12(c) | Flange Doubler 2 x 11 x .025 | .361 lb/ft ² | .765 ft ² | .28 lb. |
| 12(d) | Doubler Glass Cloth .010 | 1.0 oz/ft ² | .765 ft ² | .05 lb. |
| 12(e) | Doubler Glass Cloth Adhesive | 72 lb/ft ³ | .008 ft ³ | .06 lb. |
| 12(f) | Doubler Rivets .190 Dia. 6 Per | | 30 | .04 lb. |
| 13. | Support Ring Core 3/8 Hex x .0015 Foil | 2.25 lb/ft ³ | 21.8 ft ³ | 49.2 lb. |
| 13(a) | Support Ring Core Back Face Adhesive | 72 lb/ft ³ | .225 ft ³ | 16.2 lb. |
| 13(b) | Support Ring Core Splice Glass Cloth .010 | 1.0 oz/ft ² | 5 ft ² | .31 lb. |
| 13(c) | Splice Glass Cloth Adhesive | 72 lb/ft ³ | .005 ft ³ | .36 lb. |
| 14. | Launch Support Fasteners 1/4" Thd. | | 32 Pcs | .35 lb. |
| 14(a) | Fastener Adhesive | 13 lb/ft ³ | | 2.6 |
| 15. | Deployment Lug Fasteners 3/8 Thd. | | 16 | .47 lb. |
| 15(a) | Fastener Adhesive | 13 lb/ft ³ | | <u>1.0 lb.</u> |
| Total Weight | | | | 427.5 lb. |

DISTRIBUTION LIST

FINAL REPORT

| <u>Recipient</u> | <u>Address</u> |
|--------------------------------------------------------------------------------|------------------------------------------------------------------------------------------------------------------------------------------|
| T. S. Mroz NASA Lewis (7) Technical Manager (1) reproducible | NASA Lewis Research Center 21000 Brookpark Road Cleveland, Ohio 44135 Attention: T. S. Mroz |
| John E. Dilley NASA Lewis Contracting Officer (1) | NASA Lewis Research Center 21000 Brookpark Road Cleveland, Ohio 44135 Attention: John E. Dilley |
| Reports Control Office NASA-Lewis (1) | NASA Lewis Research Center 21000 Brookpark Road Cleveland, Ohio 44135 |
| Lewis Library (2) | NASA Lewis Research Center 21000 Brookpark Road Cleveland, Ohio 44135 Attention: Library |
| NASA Lewis Technology Utilization Office (1) | NASA Lewis Research Center 21000 Brookpark Road Cleveland, Ohio 44135 Attention: Technology Utilization Office |
| Dr. Bernard Lubarsky NASA Lewis Space Power System Division Chief (1) | NASA Lewis Research Center 21000 Brookpark Road Cleveland, Ohio 44135 Attention: Dr. Bernard Lubarsky |
| R. L. Cummings NASA Lewis Solar & Chemical Power Branch Chief (1) | NASA Lewis Research Center 21000 Brookpark Road Cleveland, Ohio 44135 Attention: R. L. Cummings |
| NASA Lewis Office of Reliability and Quality Assurance (1) | NASA Lewis Research Center 21000 Brookpark Road Cleveland, Ohio 44135 Attention: Office of Reliability and Quality Assurance |

DISTRIBUTION LIST

FINAL REPORT

| <u>Recipient</u> | <u>Address</u> |
|--------------------------------------------------------------------------------|------------------------------------------------------------------------------------------------------------------------------------------|
| T. S. Mroz NASA Lewis Technical Manager (7) | NASA Lewis Research Center 21000 Brookpark Road Cleveland, Ohio 44135 Attention: T. S. Mroz |
| John E. Dilley NASA Lewis Contracting Officer (1) | NASA Lewis Research Center 21000 Brookpark Road Cleveland, Ohio 44135 Attention: John E. Dilley |
| Norman T. Musial NASA Lewis Patent Counsel (1) | NASA Lewis Research Center 21000 Brookpark Road Cleveland, Ohio 44135 Attention: Norman T. Musial |
| Lewis Library (2) | NASA Lewis Research Center 21000 Brookpark Road Cleveland, Ohio 44135 Attention: Library |
| NASA Lewis Technology Utilization Office (1) | NASA Lewis Research Center 21000 Brookpark Road Cleveland, Ohio 44135 Attention: Technology Utilization Office |
| Dr. Bernard Lubarsky NASA Lewis Space Power System Division Chief (1) | NASA Lewis Research Center 21000 Brookpark Road Cleveland, Ohio 44135 Attention: Dr. Bernard Lubarsky |
| R. L. Cummings NASA Lewis Solar & Chemical Power Branch Chief (1) | NASA Lewis Research Center 21000 Brookpark Road Cleveland, Ohio 44135 Attention: R. L. Cummings |
| NASA Lewis Office of Reliability and Quality Assurance (1) | NASA Lewis Research Center 21000 Brookpark Road Cleveland, Ohio 44135 Attention: Office of Reliability and Quality Assurance |

| <u>Recipient</u> | <u>Address</u> |
|-------------------------------------------------------|--------------------------------------------------------------------------------------------------------------------|
| Scientific and Technical Information Facility (6) | NASA Scientific and Technical Information Facility Box 5700 Bethesda, Maryland |
| Arvin Smith, Code RNW (1) NASA Washington | National Aeronautics & Space Administration Washington, D. C. 20546 Attention: Arvin Smith, Code RNW |
| Preston Maxwell, Code RNW (1) NASA Washington | National Aeronautics & Space Administration Washington, D. C. 20546 Attention: Preston Maxwell, Code RNW (1) |
| Bernard Resnick, Code RNR (1) NASA Washington | National Aeronautics & Space Administration Washington, D. C. 20546 Attention: Bernard Resnick, Code RNR |
| Mr. H. Briceland (1) Institute of Defense Analysis | Institute of Defense Analysis 1666 Connecticut Avenue Washington, D. C. Attention: Mr. H. Briceland |
| Ames Research Center Library (1) | NASA Ames Research Center Moffett Field, California 94035 Attention: Library |
| Flight Research Center Library (1) | NASA Flight Research Center P. O. Box 273 Edwards, California 93523 Attention: Library (1) |
| Goddard Space Flight Center Library (1) | NASA Goddard Space Flight Center Greenbelt, Maryland 20771 Attention: Library |
| Jet Propulsion Laboratory Library (1) | Jet Propulsion Laboratory 4800 Oak Grove Drive Pasadena, California 91103 Attention: Library |
| Atwood Heath (1) NASA Langley Research Center | NASA Langley Research Center Langley Station Hampton, Virginia 23365 Attention: Atwood Heath |
| NASA Langley Research Center Library (1) | NASA Langley Research Center Langley Station Hampton, Virginia 23365 Attention: Library |

| <u>Recipient</u> | <u>Address</u> |
|--------------------------------------------------------------|-------------------------------------------------------------------------------------------------------------------------------------------|
| NASA Manned Spacecraft Center Library (1) | NASA Manned Spacecraft Center Houston, Texas 77001 Attention: Library |
| NASA Marshall Space Flight Center Library (1) | NASA Marshall Space Flight Center Huntsville, Alabama 35812 Attention: Library |
| NASA Western Operations Library (1) | NASA Western Operations 150 Pico Boulevard Santa Monica, California 90406 Attention: Library |
| Bernard Chasman (ASRCE) (1) Aeronautical Systems Division | Air Force Systems Command Aeronautical Systems Division Wright Patterson Air Force Base, Ohio Attention: Bernard Chasman (ASRCE) |